Quantum Controlled Collisions and Magnetic Trapping of Ultracold NaLi Molecules

by

Juliana Park

Submitted to the Department of Physics
in partial fulfillment of the requirements for the degree of

Doctor of Philosophy

at the

MASSACHUSETTS INSTITUTE OF TECHNOLOGY

February 2023

Author .....
Department of Physics
January 13, 2023

Certified by .....
Wolfgang Ketterle
John D. MacArthur Professor of Physics
Thesis Supervisor

Accepted by .....
Lindley Winslow
Associate Department Head of Physics

Quantum Controlled Collisions and Magnetic Trapping of Ultracold NaLi Molecules

by

Juliana Park

Submitted to the Department of Physics
on January 13, 2023, in partial fulfillment of the
requirements for the degree of
Doctor of Philosophy

Abstract

^{23}Na^{6}Li is a fermionic molecule that has weak singlet-triplet mixing, making it a suitable system to study the triplet rovibrational ground state ($a^3\Sigma^+, v = 0, N = 0$). It is notable for its both non-zero electric (0.175 Debye) and magnetic ($2\mu_B$) dipole moments and small two-body scattering rate, as predicted by the universal model for cold collision. Additionally, ^{23}Na^{6}Li is the lightest bi-alkali molecule, and the theoretical simulation of collisions is relatively feasible compared to other heavy molecules which makes it a promising benchmark system for theoretical quantum scattering calculations.

This thesis describes three experiments and a numerical/theoretical work on ^{23}Na^{6}Li molecules in the triplet ground state. The first two experiments are on molecular Feshbach resonances: in spin-polarized ^{23}Na^{6}Li+^{23}Na collisions and in ^{23}Na^{6}Li+^{23}Na^{6}Li collisions. The first experiment focuses on the spectroscopic study of Feshbach resonances in two possible spin-polarized ^{23}Na^{6}Li+^{23}Na collisions from near 0 to 1400 Gauss. This allows learning about the molecular interaction potential surface and intermediate collision complexes, benchmarking theory, and controlling reactive collisions. The second experiment is a report of an unpredicted p-wave Feshbach resonance in ^{23}Na^{6}Li+^{23}Na^{6}Li collisions and interpretations. The resonance occurs for molecules in the lower stretched hyperfine state near an open-channel degeneracy. The collision loss rate is enhanced by more than two orders of magnitude from the p-wave universal value at the background to near the 2D unitarity limit.

In addition to the search for magnetically tunable resonances, ^{23}Na^{6}Li molecules in the triplet potential are suitable for magnetic trapping. The third experiment describes building an improved experimental setup that allows magnetic trapping of ^{23}Na^{6}Li molecules and studying various collisions in the magnetic trap by quantum state control of molecules and atoms. The molecular density is a factor of 10^5 higher than that reported for magnetically trapped ultracold molecules, and the temperature is $\approx 1\mu K$. This condition enables observation of both atom-molecule and molecule-molecule collisions in the ultracold regime and sympathetic cooling of ^{23}Na^{6}Li by evaporative cooling of ^{23}Na in the magnetic trap.

Lastly, this thesis presents the numerical and theoretical approach to finding a window for an all-optical creation of molecules using Raman transitions from ^{23}Na and ^{6}Li atoms to ^{23}Na^{6}Li molecules. All-optical creation of molecules in which the magnetic association step near a Feshbach resonance is eliminated is expected to broaden the horizon of ultracold molecules to a larger pool and to eliminate the need for high magnetic fields.

Thesis Supervisor: Wolfgang Ketterle
Title: John D. MacArthur Professor of Physics

Acknowledgments

The time I spent as a Ph.D. candidate at MIT was full of tension, wonder, and excitement. I learned how much I can hate or love being an experimental physicist while trying to be a good one. I realized that the excitement of being a scientist that I had thought I lost long ago was not gone after all.

I am extremely grateful to Wolfgang Ketterle for offering me the opportunity to experience the whole world of AMO physics. Being his student and working next door to his first BEC machine has been a great honor. He was patient when I was being too careful or slow and guided me to become a good researcher. I enjoyed listening to his new ideas and often admired his insights and intuitions.

Only in my third year, I started to understand that some experiments are not designed for one or more ultimate scientific goals. The BEC3 machine, the NaLi experiment, is one of them. With the given toolbox, one rather finds what to do next. I had difficulty finding what to explore with NaLi molecules and my thesis topic. In my fourth year, when I came and talked to Wolfgang about this concern, he was not worried because he believed that new things and ideas will come as we go forward. Back then, I felt a bit of relief from his words, but I was also not fully convinced, and talked about it to Alan, a former research scientist in Ketterle's group. In the end, he was right that we will find exciting new things to do. What I achieved during my Ph.D. was possible thanks to his belief in BEC3.

When I first joined the BEC3 team, we were a team of five. Ariel Sommer, who was a postdoctoral researcher, taught me how to code with Python, and Timur Rvachov, who was a senior graduate student, often handed me a random broken electronic box to fix, which trained me to deal with everyday problems in the lab. Although they left about a year after I joined, I learned a lot from them. Alan had been like my co-supervisor. He gave me advice when I needed it when he was at MIT and also after he left for the University of Waterloo as a professor. Hyungmok Son, who is a former graduate student, spent the most time in the lab with me, keeping the 20-year-old lab from falling apart. My time here would not have been the same without them.

As the rest of the team members left, in the last couple of years of my graduate studies, I had to mostly work alone in the lab. I am grateful to have had the opportunity to connect and collaborate with Tijs Karman and Timur Tscherbul during this period, who allowed me to dive into the field of quantum chemistry and made me feel that I was not alone. Although Yukun Lu left for the BEC2 lab and Dypole lab, he was very helpful at certain moments when I was completely stuck in the lab. Li, Yiqi, Enrique, Airlia, Michael, and Cedric have been great friends. Every time I had to vent due to the amount of stress I had in the lab, I went to their lab or office just to relax and calm myself.

I would like to express my deepest appreciation to my relatives in America. My grandparents Sunsoon Kang and Sunhee Kang, aunt Miran, Clara, and Jean, and uncle Thomas, Woosung, and Jaedeok have been like my parents in America. Thanks to them and my cousins Andrew, Calvin, Daniel, Hannah, and Crispin, it did not feel like I was studying abroad but rather felt like I finally came back to my hometown.

Last but not least, I could not have undertaken this journey without the support of my husband Wonyl Choi, and my parents in South Korea, Choonkil Park and Miyoung Kang. Their belief in me has allowed me to face and overcome my challenges, and pursue my goals.

Contents

List of Figures

List of Tables

Chapter 1

Introduction

The field of ultracold polar molecules is driven by the success of ultracold atoms which provided many exciting and diverse applications such as atomic clocks, precision tests of fundamental physics, quantum simulations of many-body quantum phenomena, and new quantum information architectures. The underlying foundation is the advent of optical and magnetic trapping of atoms, various cooling methods including laser cooling and evaporative cooling, which have been the most effective ways to cool atoms to the submilli-Kevin and nano-Kelvin regimes, respectively, techniques to control the quantum states both at the internal and external level, and to manipulate interactions between atoms.

Extending these types of control to ultracold polar molecules offers exciting new directions of research. Molecules have a richer energy-level structure that includes rotation, vibration energy levels, and a relatively strong anisotropic interaction. In addition, they can have a long-range electric dipole-dipole interaction when they are polarized. Due to their additional properties, they can offer opportunities to study quantum state controlled chemistry [1, 2], quantum simulation [3–5], and quantum information processing [6–9] in a different regime.

However, even the simplest molecules in the quantum degenerate regime are extremely difficult to prepare because of the extra degrees of freedom. Due to the rotation and vibration energy levels, a closed set of electronic transitions normally does not exist, and it prevents us from performing laser cooling of molecules. Col-

lective efforts have been made to obtain molecules in a single quantum state and understand the interactions among them. There are two main streams toward ultracold molecules, which laid the foundation for achieving atom-like control of ultracold molecules: (i) direct cooling of molecules that are chemically prepared and (ii) ultracold assembly of precooled atoms. Cooling of chemically synthesized molecules became possible using direct laser cooling. This method is restricted to only a handful of molecules that form a near-closed transition, that is, CaF, SrF, and YO [10–12]. The ultracold association method was first demonstrated in 2008 by two groups with Cs_2 and KRb and has since been widely used to create other diatomic molecules as well [13–19].

1.1 Formation and properties of NaLi

The focus of this thesis is on the $^{23}Na^{6}Li$ molecules in their triplet ground state that are formed by the association of precooled Na and Li atoms. Although direct cooling has made significant advances in recent years [20–22], the highest density that can be reached is more than a few orders of magnitude lower than that of the ultracold association and the typical temperature that is achieved is tens of μK (never reached the nano-Kelvin regime). So far, ultracold association has been the most effective method for producing near-quantum degenerate gases of molecules [23]. Furthermore, it is natural to produce bialkali molecules using the ultracold association method, as the experimental apparatus, named BEC3, was designed for the production of ultracold Na and Li atom mixtures[1].

One of the most successful recipes for achieving ground-state molecules by ultracold assembly has two combined steps. The first step is the magnetic association of cold atoms to weakly bound molecules near a Feshbach resonance. The second step is the efficient formation of ground-state ultracold molecules via the stimulated Raman adiabatic passage (STIRAP). Although this recipe allowed the production of

[1]BEC3 was built in 2001 to produce ^{23}Na Bose-Einstein condensates and later upgraded in 2007 to coproduce ^{6}Li degenerate Fermi gases.

cold molecules as low as tens of nano-Kelvin, it also has some drawbacks. It requires a Feshbach resonance to be at an experimentally accessible bias field and to be strong compared to any decoherence rate for an efficient magnetic association. The Na + Li mixture has very narrow (∼mG) resonances only at high fields (>700 G), and using these resonances for molecule formation is technically challenging. Formation of weakly bound NaLi Feshbach molecules was first reported in 2012 [24] by the same BEC3 lab. Even after the success of the experiment, achieving the ground state of NaLi was also demanding because there was no prior spectroscopic data available for STIRAP. A detailed spectroscopic study of the excited and ground triplet potentials of NaLi was carried out using one- and two-photon photoassociation spectroscopy, providing the spectroscopic positions and strengths of the transitions to most of the vibrational states in the excited $c^3\Sigma^+$ and ground $a^3\Sigma^+$ potentials of NaLi [25, 26], and the first formation of an ultracold gas of NaLi molecules in the triplet ground state was achieved using the spectroscopic results in 2017. Initially, 3×10^4 molecules were formed at a density of $5 \times 10^{10}\text{cm}^{-3}$ and a temperature of 3 μK [13]. This was further improved, which is described in this thesis and in the thesis of Hyungmok Son [27].

Several parameters are important when discussing heteronuclear bialkali molecules. The two valence electrons on each alkali atom can pair in either a triplet or a singlet spin configuration. The triplet potential is much shallower than the deeply bound singlet potential, and thus energetically can be unstable. However, NaLi is unique compared to other heteronuclear bialkaline molecules and is particularly suitable for studying the triplet state. NaLi in the triplet ground state has weak coupling to the singlet manifold due to the weak spin-orbit coupling and thus is meta-stable. Indeed, they were measured to have a long lifetime ($\sim$ 4 s) at a density of $5 \times 10^{10}\text{cm}^{-3}$ and a temperature of 3 μK. Singlet molecules have anti-aligned electron spins and thus have a very small magnetic moment from the nuclear spin, while triplet molecules have aligned electron spins and thus have a magnetic moment of 2 μ_B. The non-zero magnetic moment enables magnetic trapping of molecules and can be used to tune collisional resonances in molecules.

Furthermore, although it has the smallest permanent electric dipole moment among all singlet ground state molecules, it has the fourth largest permanent electric dipole moment among triplet ground state molecules, as listed in Table 1.1. NaLi in the triplet ground state has both magnetic and electric dipole moments. These dipole moments provide $\sim 1/r^3$ character between molecules i and j as

$$V_{ij}^{dd} = \frac{1}{2\pi\epsilon_0} \frac{\vec{\mu}_i \cdot \vec{\mu}_j - 3(\vec{\mu}_i \cdot \vec{e}_{ij})(\vec{\mu}_i \cdot \vec{e}_{ij})}{r_{ij}^3} \tag{1.1}$$

where μ_i is the dipole moment and $\vec{r}_i$ is the position vector of the molecule i. Here, $\vec{r}_{ij} = |\vec{r}_i - \vec{r}_j|$, and $\vec{e}_{ij}$ is the unit vector in the direction of $\vec{r}_{ij}$. Note that the electric dipole interaction is typically much stronger than the magnetic dipole interaction. For example, for the electric dipole of value $d \approx 1D$ has a four orders of magnitude stronger interaction compared to the magnetic dipole of value $1\mu_B$. Tunable long-range interactions between spins through the electric dipole-dipole interaction in ultra-cold polar molecules can offer new possibilities for quantum simulation [3].

NaLi is fermionic since the total spin F (nuclear and electronic) of the molecule is half-integer. The states converge to 8 hyperfine thresholds in the zero-field limit due to the conservation of the total angular momentum $F = |\vec{F}| = |\vec{S} + \vec{I}_{\mathrm{Na}} + \vec{I}_{\mathrm{Li}}|$, where $S = |\vec{S}| = 1$ is the total electron spin of NaLi ($a^3\Sigma^+$) and $I_{\mathrm{Na}} = 3/2$ and $I_{\mathrm{Li}} = 1$ are the nuclear spins of Na and Li. With the method explained above, NaLi molecules are initially formed in the $|F = 7/2, m_F = 7/2\rangle$ hyperfine state, which is a stretched state in which all nuclear and electron spins are aligned to the direction of the bias field. Fermionic molecules including NaLi can only collide via p-wave collisions that are suppressed by the centrifugal barrier and therefore have much longer lifetimes than their bosonic counterparts if they exist.

Chemical reactivity is another property that needs to be considered when it comes to molecular collisions. Any collision that transfers internal energy into relative kinetic energy is likely to eject both collision partners from the trap. If both species are in their absolute ground state (singlet), inelastic collisions are impossible, but there remains the possibility of reactive collisions through atom exchange $AB + AB \rightarrow$

Molecule	PDM (Debye)	PDM* (Debye)	C_6 (a.u.)
LiNa	0.57	0.175	3709
LiK	3.58	0.312	411682
LiRb	4.18	0.359	884704
LiCs	5.59	0.462	30409406
NaK	2.78	0.0269	516606
NaRb	3.31	0.0594	1507089
NaCs	4.69	0.0914	6946696
KRb	0.62	0.0540	17720
KCs	1.84	0.101	469120
RbCs	1.25	0.0344	180982

Table 1.1: Permanent dipole moment of molecules in the ground state of the $X^1\Sigma$ potential (PDM) [28], permanent dipole moment of molecules in the ground state of the $a^3\Sigma$ potential (PDM*) [29], and long-range dispersion coefficients in atomic units [30]. permanent dipole moment

$A_2 + B_2$ [2]. For alkali-metal dimers $AB(a^3\Sigma^+)$ in the rovibrational ground state of the triplet potential, the following reaction processes may lead to collisional losses:

$$2AB(a^3\Sigma^+) \rightarrow A_2(a^3\Sigma^+) + B_2(a^3\Sigma^+) \tag{1.2}$$

$$2AB(a^3\Sigma^+) \rightarrow A_2B + B \tag{1.3}$$

$$2AB(a^3\Sigma^+) \rightarrow A_2(X^1\Sigma^+) + B_2(T) \tag{1.4}$$

$$2AB(a^3\Sigma^+) \rightarrow AB(X^1\Sigma^+) + AB(T) \tag{1.5}$$

where T is $X^1\Sigma^+$ or $a^3\Sigma^+$. Collisions of triplet ground state molecules could result in inelastic loss from decay to states in the much deeper singlet manifold as well mediated by nonadiabatic spin-dependent couplings. Thus in principle, singlet ground state, non-reactive molecules are the most desirable candidates for long sample lifetimes.

Collisions between two NaLi molecules in the triplet ground state are highly re-

[2]For singlet alkali-metal dimers in levels near the potential minimum, trimer formation reactions $2AB \rightarrow A_2B + B$ or $A + AB_2$ are always energetically forbidden [31].

active, although spin-dependent couplings are weak and reactions involving transitions to lower-spin states (Eq. 1.4 and Eq. 1.5) are suppressed. The reaction processes within the quintet potential (Eq.1.2 and Eq.1.3) are exothermic [29] for NaLi. However, the collisions between NaLi and Na are peculiar, unlike collisions between two NaLi. Collisions of $^{23}Na^{6}Li(a^{3}\Sigma^{+})$ with Na are generally chemically reactive ($^{23}Na^{6}Li(a^{3}\Sigma^{+}) + Na \rightarrow Na_2(X^{1}\Sigma_{g}^{+}) + Li + heat$). However, the dissociation energies for $^{23}Na^{6}Li$ and $^{23}Na_2$ in the lowest triplet state $a^{3}\Sigma^{+}$ are 208.0826(3) cm^{-1} [25] and 163.7(12) cm^{-1} [32], respectively. Therefore, the chemical reaction in the fully spin-polarized atom–molecule system is strongly suppressed due to the conservation of the total spin [29, 33], and stable long-lived states can be supported. Sympathetic cooling of NaLi molecules with Na atoms has been demonstrated in a 1-dimensional 1,596-nm optical lattice [34], which is a significant step forward to reaching quantum degeneracy with molecules.

1.2 Cold collisions in molecular systems

At low temperatures of micro- and nanokelvin, the collision occurs at low partial waves, and collision physics can be reduced to a few well-defined parameters. For many systems, these parameters are the s-wave scattering length and the two-body loss coefficients. However, because of the strong anisotropic interactions at short-range and multiple decay channels that are possible in collisions involving molecules, it is much more difficult to describe them. In relatively simple systems, such as pairs of alkali-metal atoms or light atom-molecule systems, it is possible to solve the Schrödinger equation using coupled-channel methods. However, for heavier and more complex systems, the number of channels needed for convergence is too large, and coupled channel approaches become prohibitively costly. In this regime, considerable success has been achieved with effective single-channel methods that take into account short-range inelastic/reactive loss with a single parameter [35, 36].

1.2.1 Universal loss model for reactive collisions

In particular, a single channel model by Zbigniew Idziaszek and Paul S. Julienne [35] introduces a complex potential to represent the long-range potential (van der Waals and centrifugal potential at $r \gtrsim R_0$) and short-range loss dynamics (at $r < R_0$): $U_l(r) = -\frac{C_6}{r^6} + \frac{\hbar^2 l(l+1)}{2\mu r^2} - i\frac{\gamma(r)}{2}$ and an energy-dependent complex scattering length $\tilde{a} = \tilde{\alpha} - i\tilde{\beta}$. R_0 denotes the range of short-range forces $\gamma(r)$ simulates all short-range coupling at $r < R_0$ to exoergic non-threshold exit channels that result in loss from the entrance channel. The van der Waals (vdW) potential is characterized by the length $\bar{a} = 4\pi R_6/\Gamma(\frac{1}{4})^2$ where $R_6 = \frac{1}{2}(2\mu C_6/\hbar^2)^{1/4}$. Long-range dispersion coefficients C_6 of bialkali molecules are given in Table 1.1. The model uses the analytic framework of generalized multichannel quantum defect theory (MQDT) and the two quantum defect parameters: phase parameter $s = a/\bar{a}$ and loss parameter y where a is the scattering length. These parameters represent the effects of complex short-range dynamics on the wave function $\Psi(r) \sim \frac{1}{\sqrt{k(r)}} e^{-i\int^r k(x)dx} - \left(\frac{1-y}{1+y}\right)\frac{1}{\sqrt{k(r)}} e^{i\int^r k(x)dx}$. The first term represents the flux of incident particles, whereas the second term gives the flux reflected from the short-range potential. The quantum defect parameter $0 \leq y \leq 1$ is related to the probability of irreversible loss of incoming scattering flux from the entrance channel due to dynamics at short-range. For $y = 1$ there is a unit probability loss, which corresponds to a special "universal" case and for $y = 0$ there is no loss (incident and reflected fluxes are equal). For arbitrary y the complex scattering length for s-wave and p-wave collisions are given by:

$$\tilde{a}_{l=0}(k) = a + \bar{a}y\frac{1 + (1-s)^2}{i + y(1-s)} \tag{1.6}$$

$$\tilde{a}_{l=1}(k) = -2\bar{a}_1(k\bar{a})^2\frac{y + i(s-1)}{ys + i(s-2)} \tag{1.7}$$

when $k\,|\tilde{a}| \ll 1$ and $kR_6 \ll 1$. In the case of $y = 1$ the elastic and inelastic or reactive collision rates depend only on the quantum scattering by the long-range potential at distances $R \gtrsim \bar{a}$. Any incoming scattering flux that penetrates inside $\bar{a}$ experiences no reflection back into the entrance channel as it is lost to inelas-

tic/reactive channels. Elastic rate constant $K^{el} = 2g\frac{hk}{\mu}\left|\tilde{a}(k)\right|^2 f(k)$ and inelastic rate constant $K^{ls} = 2g\frac{h}{\mu}\tilde{\beta}(k)f(k)$ where $k^2 = 2\mu(E - E_0)/\hbar^2$ with E denoting the total energy, μ the reduced mass, and E_0 the threshold energy. The function $f(k) = \left[1 + k^2\left|\tilde{a}(k)\right|^2 + 2k\tilde{\beta}(k)\right]^{-1} \approx 1$ is the saturation factor which deviates from 1 when $k\left|\tilde{a}\right| \ll 1$ is not satisfied. Then universal rate constants ($y \to 1$) for elastic and inelastic collisions are given as:

$$K^{el}_{l=0} = 4g\frac{h}{\mu}k\bar{a}^2 \qquad K^{ls}_{l=0} = 2g\frac{h}{\mu}\bar{a} \tag{1.8}$$

$$K^{ls}_{l=1} = 4\sigma g\frac{h}{\mu}k\bar{a}_1^2(k\bar{a})^4 \qquad K^{ls}_{l=1} = 2\sigma g\frac{h}{\mu}\bar{a}_1(k\bar{a})^2 \tag{1.9}$$

Here, $\bar{a}_1 = \bar{a}\Gamma(\frac{1}{4})^6/(144\pi^2\Gamma(\frac{3}{4})^2) \approx 1.064\bar{a}$. The factor $g = 1$ except that $g = 2$ when both particles are identical species in identical internal states, and the factor $\sigma = 3$ for $l = 1$ for molecules in the universal limit. This result implies that reactive collisions undergo universal loss, which is greater for larger C_6 and therefore NaLi is long-lived due to the small vdW coefficient despite its reactivity.

Ironically, most reactive collisions and even many non-reactive collisions involving one or more dimers that have been studied are known to go under fast collision loss and have loss rates saturated or close to their universal value [41–49]. There are proposed explanations for the fast loss of non-reactive molecules including formation of a long-lived collision complex during collision which is referred to as "sticky collision" [37,38] and photoassociation of intermediate complexes by the optical trap [39,40] as depicted in Fig.1-1. As new ideas emerge, collisional studies directed to intermediate complexes became an active research. The lifetime of the intermediate complex in RbCs + RbCs collision was estimated by shining pulsed optical excitation light [50] and long-lived intermediate complex was observed in KRb molecular systems [40,51].

1.2.2 Fabry-Perot interferometer model for collision resonances

The previously introduced single-channel model that uses the analytic framework of MQDT may not be so intuitive, although it has simple results. Therefore, we now

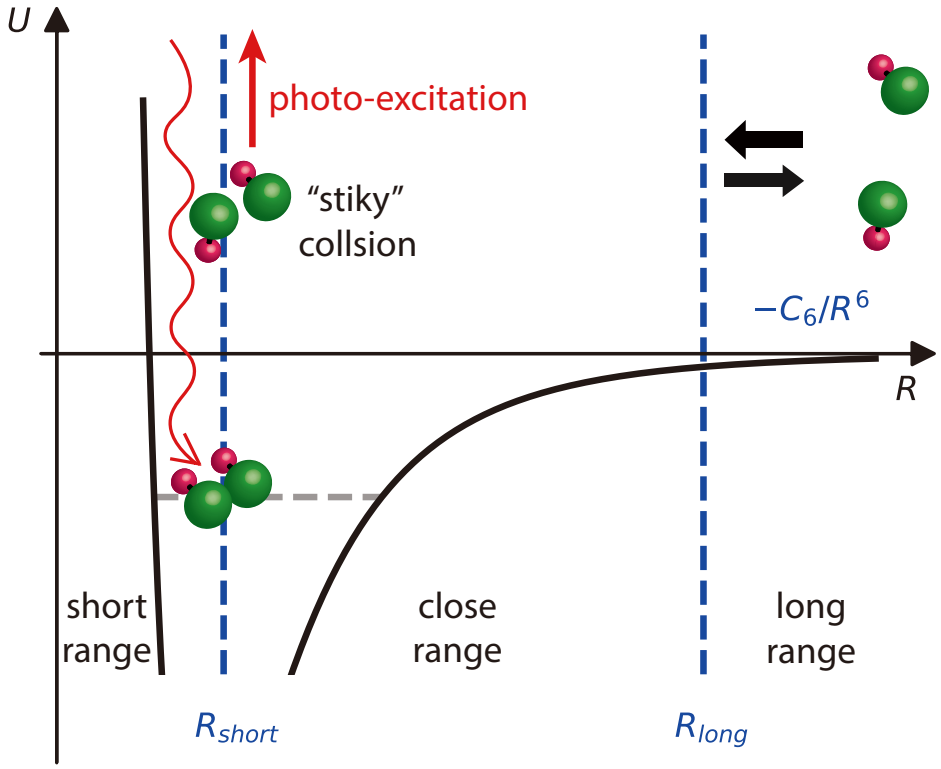

Figure 1-1: **Photo-induced collisional loss.** The collisions between two molecules (green and red sphere) occur in a potential which is the attractive vdW potential $-C_6/R^6$ at long-range $R>R_{\rm long}$ (R is the inter-particle distance) and a strongly repulsive potential at short-range $R<R_{\rm short}$. Most experiments on collisions involving one or more dimers show fast collision loss that are saturated or close to their universal value and it is proposed that the fast loss of non-reactive molecules involve long-lived intermediate complexes so called "sticky collision" [37, 38]. These complexes are photo-excited by optical trap, and near universal loss can be observed [39, 40].

focus on the simple picture of an optical Fabry-Perot interferometer with two mirrors developed in Ref. [33]. This picture is analogous to cold collisions that are explained by two reflectors, where the two reflections are from quantum reflection by the long-range vdW potential and reflection at short-range by the repulsive core potential as in Fig.1-1. The flux transmitted by the inner mirror M_2 in Fig.1-2 represents inelastic loss where mirror M_1 represents long-range reflection (quantum reflection or reflection by the centrifugal barrier) and mirror M_2 represents reflection at short-range. For an incoming flux I, the total transmission T through both reflectors is given by the flux transmitted in the absence of the second mirror $(I \cdot |t_1|^2)$ times the interference term (C):

$$T = (I \cdot |t_1|^2)\left(\frac{1-|r_2|^2}{|1-r_2 r_1 e^{-i\phi}|^2}\right) \equiv (I \cdot |t_1|^2)C \tag{1.10}$$

Here, r_i and t_i are the amplitude reflection and transmission coefficients for the mirror M_i and ϕ is the round-trip phase. The first term represents the universal loss since it assumes no reflection by the inner mirror ($r_2 = 0$). The inner reflection is directly related to the quantum defect parameter y introduced in the single channel model as: $r_2 = (1-y)/(1+y)$, $t_2 = 2\sqrt{y}/(1+y)$, which is 1 for complete transmission and 0 for 100 % reflection. Long-range reflection approaches unity at very low energies and $r_1 \sim 1$. In this limit, $C(y,\phi) = 2y/(1-\cos\phi+y^2(1+\cos\phi))$ and at $\phi = 0$ contructive interference leads to an enhancement of $C = 1/y$ and at $\phi = \pi$ destructive interference leads to a minimum transmission with $C = y$.

This Fabry-Perot interferometer model can explain collisional resonances as well. When a new bound state is added to the interparticle potential and the close-range potential is modified, the Fabry-Perot is tuned over one full spectral range. This takes the scattering length a over its full range between $\pm\infty$. The Fabry-Perot phase ϕ is directly related to the quantum defect parameter s by: $\cos\phi = 1-2/(1+(1-s)^2)$ and therefore we obtain $C(y,s) = y(1+(1-s)^2)/(1+y^2(1-s)^2)$ which exactly reproduces the results from Eq.1.6. The single channel model explained earlier can be extended for a Feshbach resonance, which occurs when the incoming scattering channel becomes resonant to a bound state by an external magnetic field. The Feshbach resonance at

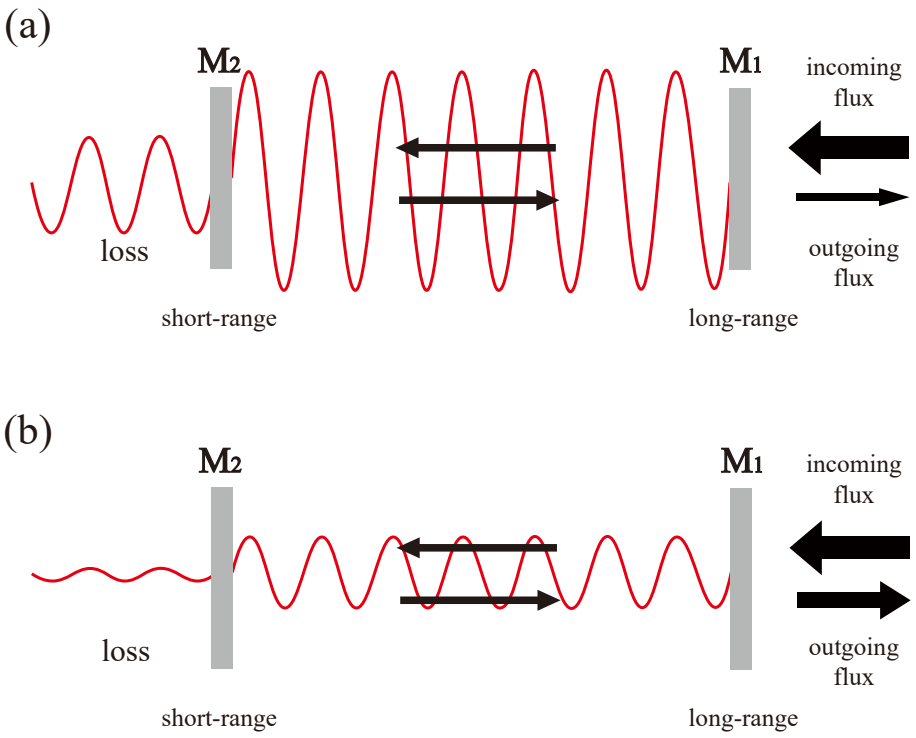

Figure 1-2: **Fabry-Perot interferometer model for reactive collisions.** The scattering dynamics can be fully described by quantum reflection off the vdW potential at $R{\sim}R_{\rm long}$ and reflection and transmission at $R{\sim}R_{\rm short}$. Transmission into short-range implies inelastic/reactive loss [35,52–54]. This situation is fully analogous to an optical Fabry-Perot interferometer with two partially reflective mirrors (M_1 and M_2). Reactive loss is proportional to the flux transmitted through both mirrors. Depending on constructive and destructive interference between multiple reflections, the loss can be highly enhanced (on resonance, Fig. (a)) or suppressed (Fig. (b)) than the transmission through mirror M_1 only, which represents the universal loss.

B=B_{res} acts as a lossless phase-shifter for the Fabry-Perot phase $s(B) = q\left(1 - \frac{\Delta}{B - B_{\text{res}}}\right)$ where, q characterizes the background scattering phase far away from the Feshbach resonance, and Δ is the width of the resonance.

The universal limit from the single-channel model assumes no short-range reflection and is given by all the flux that has not been reflected at long-range. The loss rates can be modified only if the background loss rate is below the universal limit ($y < 1$) and the backreflected flux at short-range destructively or constructively interferes with quantum reflection via Feshbach resonances. Spin-polaried NaLi+Na with low reactivity has the background loss rate more than an order of magnitude lower than the universal limit. Therefore, it can be a possible system for the realization of quantum chemistry controlled by an external field. In principle, due to its chemical reactivity, NaLi+NaLi is not a good candidate to observe magnetically tunable chemical reactions using Feshbach resonances. However, as we shall discuss shortly, the experimental evidence has not corroborated this hypothesis.

1.3 Thesis outline

The preceding discussion illustrates that the ground state NaLi in the triplet potential is an experimental system that has pushed the field of ultracold physics and quantum chemistry. Since the first signal of the triplet ground-state NaLi molecules [13, 25, 26] achieved on the first year of my Ph.D studies, I was involved in building the control circuits, STIRAP laser system, and imaging laser system at a high magnetic field for multiple hyperfine states of Na and Li atoms, which was necessary for two important experiments: collisional cooling of NaLi with Na in an optical lattice [34], and control of reactive collisions by quantum interference [33]. These two experiments are elaborated in the thesis of Hyungmok son [27].

This thesis focuses on three experiments that I led in the last two years of my Ph.D studies after the two experiments mentioned above, and numerical/theoretical work on a new approach of creating ground-state NaLi using a free-to-bound Raman

transition. Chapter 2 provides an overview of the experimental apparatus, focusing on recent modifications for the purpose of the formation and manipulation of molecules. Chapters 3, 4 and 5 discuss the three experiments: the spectrum of Na + NaLi Feshbach resonances, a Feshbach resonance in NaLi + NaLi collisions, and magnetic trapping and cooling of NaLi. These experiments use magnetic quantum control of NaLi in the triplet potential to understand molecular collisions and reactions at ultracold temperatures. Chapter 6 discusses two-photon Raman transfer from Na and Li atoms to NaLi molecules. Chapter 7 is a summary of the work with future prospects.

Chapter 2

Experimental apparatus

The experimental apparatus or the BEC3 machine was built in 2001 and was initially designed to produce ^{23}Na Bose-Einstein condensates. In 2007, the ^{6}Li atomic source was added to the apparatus and modified to study ^{6}Li degenerate Fermi gases. After upgrading, long efforts were made to create ^{23}Na^{6}Li molecules from ultracold atoms. The further development of the apparatus that was necessary for molecular spectroscopy [25, 26] and the first production of ^{23}Na^{6}Li in the triplet ground state [13] is given in the thesis of Timur Rvachov. This chapter focuses on significant improvements to the apparatus after the first signal of the ground state molecules, necessary for studying molecular collisions using magnetic quantum control.

2.1 Instrumentation for control

The control of the experiment is accomplished through the integration of commercial and home-built apparatus. We use Cicero word generator for our experimental control software, which can send messages to devices through RS-232, GPIB connections, and National Instruments (NI) digital and analog output cards. The purpose of this section is to describe the instrumentation developed to generate reliable TTL signals from the NI digital output and a circuit to buffer NI analog signals.

2.1.1 Digital control

To switch devices on and off during the experimental sequence, we use National Instruments (NI) PXI-6533 digital output cards, in which output signals are sent to home-built instrumentation to generate TTL compatible digital control signals. This TTL compatible signal generating device is used to constitute two parts: "an opto-isolator box" and "a switch board". The opto-isolator electronic box isolates the ground of the National Instrumentation cards from the rest of the system using a logic gate optocoupler (FOD0720) and converts NI output low voltages (< 0.4V) or high voltages (> 2.4V) to 0V or 5V via a digital buffer. After this stage, the converted signals are sent to the "switch board" circuitry, which allows for either computer or manual control of the digital output voltage. It has two toggle switches and two LEDs per channel. The first switch allows us to switch between computer and manual control mode, and the second switch, which is enabled only when the first switch is set to manual control mode, allows us to toggle between high and low output voltages. Two LEDs indicate computer or manual mode and high or low output voltage. This digital control instrumentation had a few problems, and redesigning was necessary for future molecule experiments. First, all the wires were hand-soldered and very old and would often fall apart. Second, it was not designed to isolate between different output channels, which caused cross-talk among them. Lastly, the LEDs were powered by an output signal itself, and the brightness of the LED significantly depends on the amount of current drawn by the device being controlled. In many cases, LEDs on a single "switch board" that contains eight output channels simultaneously light on and off during experimental runs as a result. Figure 2-1 is a simplified schematic of the old circuit design, and figure 2-2 is a simplified schematic of the new circuit design for a single digital channel. Parts inside the green dashed box in figure 2-1 were included in the old "switch boards" and the rest were in a separate "opto-isolator box". In the new design, eight duplicates of every part in figure 2-2 were built in a single "switch board". This was only possible by making the circuit compact by employing printed circuit boards (PCBs). All output signals share the same ground which corresponds

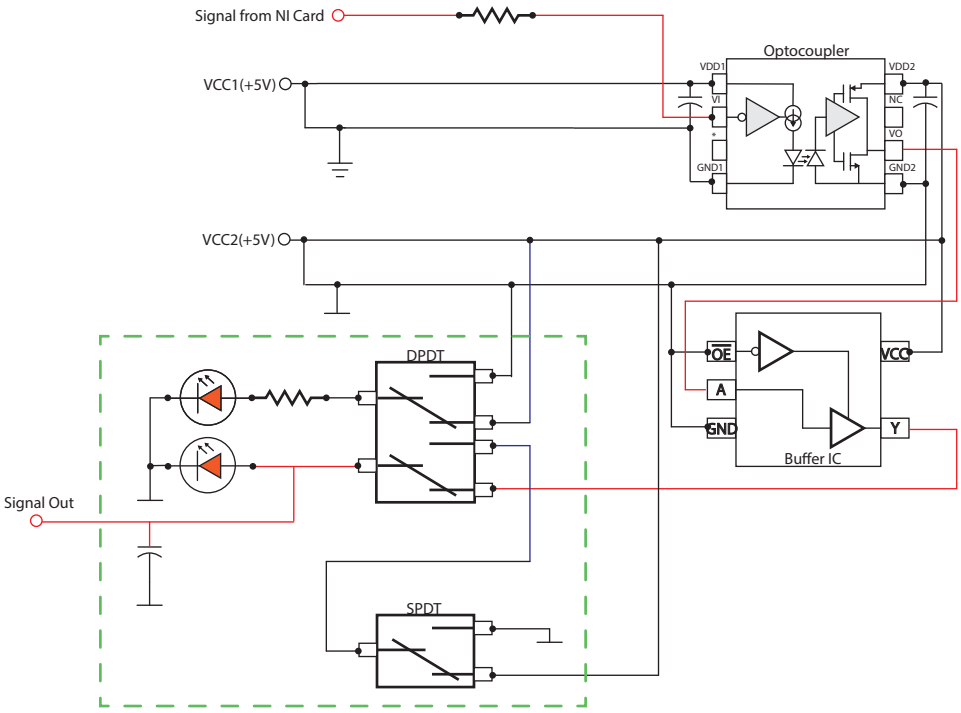

Figure 2-1: **Schematic of old digital control instrumentation circuit for single channel.** This is a simplified schematic for single control output. Only the parts inside the green dashed box were included in the old "switch boards" and the rest were in a separate "opto-isolator box".

to 'GND2' in figure 2-1 for the old design, while each output channel has individual floated ground by having a separate DC to DC converter for the new design. (See Appendix A.1 for the full eight-channel PCB schematic and board design.)

2.1.2 Analog control

Analog control voltages (ranging from 0V to 10V) are used to vary laser frequencies and intensities and magnetic fields in an experimental sequence. These voltages are generated by PXI-6733 analog output cards and a newly developed low-noise system using high-precision DACs and floating power supplies by Will Lunden [55]. We use the low-noise system to vary the intensity of our 1D optical lattice and the magnetic bias field for Feshbach resonances. For the rest of the analog control, we use the voltage signals generated by the analog output cards that are buffered by home-built

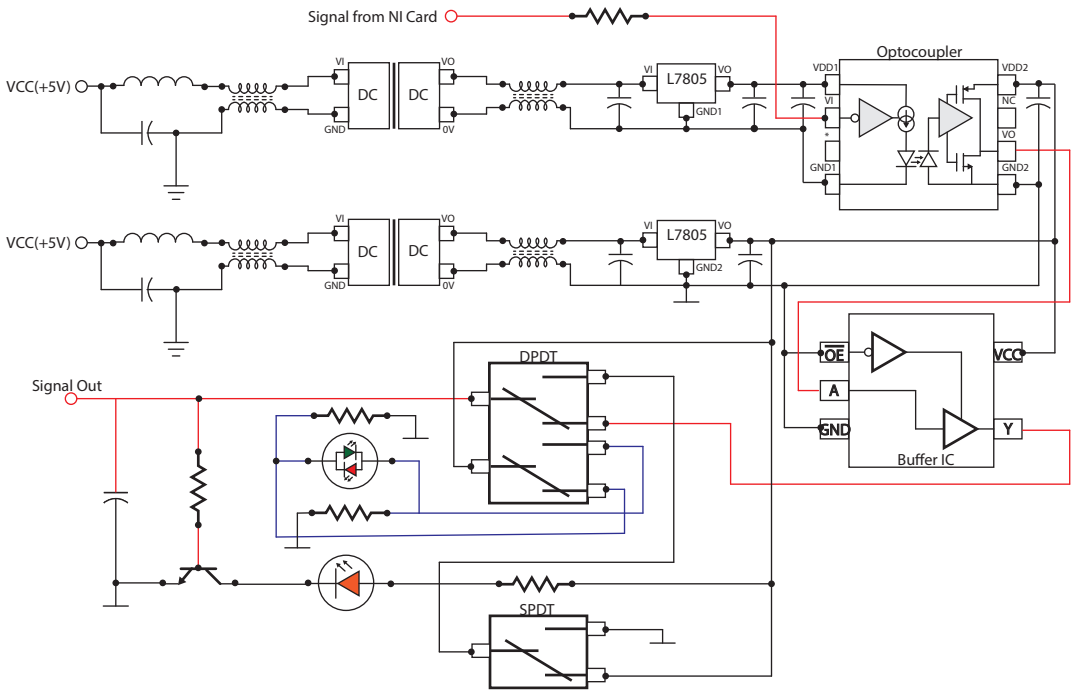

Figure 2-2: **Schematic of newly designed digital control instrumentation circuit for single channel.** This is a simplified schematic for single control output. In this new design eight duplicates of all the parts shown are built in a single "switch board".

buffering circuits. For this, we use mainly two types of instrumentation amplifier (INA): either INA117 or INA111. INA117 has a large common-mode input range of ±200V and a protected input voltage of ±500V which is necessary to control the output current of high-power power supply units. However, INA117 has a relatively large output voltage noise of, for example, 550 nV/$\sqrt{\text{Hz}}$ at 10 kHz. On the other hand, INA1111 has a small common-mode rejection voltage of ±10 V but low output voltage noise, for example, 10 nV/$\sqrt{\text{Hz}}$ at 10 kHz which is even lower than the low-noise system developed using high-precision DACs and floating power supplies. A circuit diagram and the printed board layout for buffering analog signals using INA111 are provided in Chapter A.1.

2.2 Coils and magnetic field

The ability to control the magnetic field in the main vacuum chamber where most of the science happens is essential for cooling and trapping atoms and molecules. For example, to prepare an ultracold Na/Li mixture in the lowest Zeeman energy states (in the $|F, m_F\rangle$ basis, where F is the total angular momentum and m_F is the projection of F on the magnetic quantization axis, these states correspond to $|1, 1\rangle$ for Na, and $|1/2, 1/2\rangle$ for Li) for the magnetic association of NaLi Feshbach molecules [1], we produce an ultracold mixture of ^{23}Na and ^{6}Li in their upper-stretched hyperfine states ($|2, 2\rangle$ for Na and $|3/2, 3/2\rangle$ for Li) using evaporative and sympathetic cooling in an Ioffe–Pritchard magnetic trap [57] at a bias field of $\sim$ 2 G. The mixture is later transferred to the lowest Zeeman states using a Landau–Zener (LZ) magnetic field sweep in an optical trap (see Chapter 2.3.3 for details). The magnetic trap requires two sets of four cloverleaf coils that create radial gradient fields in the x and z directions, and curvature coils that produce a parabolic field curvature in the y direction. Since the curvature coils also produce a substantial bias field along

[1] Ultracold mixture of ^{23}Na and ^{6}Li in their lowest Zeeman states ($|1, 1\rangle$ for Na and $|1/2, 1/2\rangle$ for Li) is required for the formation of NaLi Feshbach molecules. Our previous work on NaLi Feshbach molecules uses the 745.4 G d-wave Feshbach resonance between Na and Li in the lowest Zeeman energy states, which has a width of 10 mG [56].

Power supply unit	Connected coils	Bias field direction
Curvature	curvature & antibias	(+)
Bias	curvature	(+)
y-comp	compensation	(+)
y-trap-bias	compensation	(-)
spin-flip	compensation	(-)
Feshbach	antibias	(-)
MOK	MOK coil	(+)

Table 2.1: Magnetic field coils and power supply units.

y, a single power supply unit("Curvature") is connected to the curvature coils and the antibias coils, which can produce a relatively homogeneous bias field in the $-y$ direction (see Table 2.1 for details).

In addition, to study magnetically tunable scattering resonances, one should also be able to stabilize magnetic fields at high fields. For example, the formation of NaLi Feshbach molecules requires active stabilization of magnetic fields up to $\sim$ 800 G, with field noise less than 1 part in 10^5 and the experiments described in chapters 3 and 4 require active stabilization of magnetic fields up to $\sim$ 1500 G. For producing a high magnetic bias field, we use antibias coils powered by the "Feshbach" power supply unit.

2.2.1 Curvature cancellation

Although antibias coils are meant to produce a homogeneous bias field, they can create significant curvature fields (forming a saddle point) when the magnetic bias field by these coils is high. Unfortunately, there is a mismatch between the position of the saddle point of the field by antibias coils and the center of the Ioffe-Pritchard trap, where the atoms are trapped for evaporative and sympathetic cooling. Therefore, at a high bias field, atoms and molecules can feel a large gradient field if they are placed at the center of the Ioffe-Pritchard trap. The displacement is estimated to be about 2.5 mm in the x direction and a few hundred μm in the y direction. This estimation was done by monitoring the acceleration of atoms near the magnetic trap center which is driven by the curvature fields. To prevent atoms and molecules from

feeling a large gradient field, after evaporative and sympathetic cooling of the atoms in the magnetic trap, we had been applying an additional gradient field in the x direction using a compensation coil (x-compensation) that shifts the magnetic trap center to near the saddle point. This leads to heating and poor transfer efficiency of the atoms from the shifted magnetic trap to an optical trap[2]. One approach to solving this problem is to cancel the curvature created by the antibias coils. When the magnetic curvature is canceled out, atoms or molecules will not see a huge magnetic field gradient, even though they are not positioned at the saddle point.

The goal is to have the curvature created by the current through the antibias coils canceled out by that of the current through the curvature coils as shown in figure 2-3. The radius of antibias coils is larger than the spacing between sets of coils on the left and right sides. However, the spacing is larger than the radius for the curvature coils. Therefore, the signs of the curvature created by these two sets of coils are opposite to each other when the currents flow in the same direction. For this purpose, an additional power supply was connected anti-parallel to the "Bias" power supply unit. A rough condition to cancel out the curvature was found by maintaining the bias field near 745 G and monitoring Na atoms in the state $|2, 2\rangle$ (low-field seeker) and Li atoms in the state $|1/2, 1/2\rangle$ (high-field seeker) simultaneously. When the 210 amps pass through the antibias coils and the 22 amps pass through the curvature coils, the magnetic bias field is near 745 G while the curvature field in the y direction (axial direction) is close to zero. However, this condition did not allow us to eliminate inhomogeneity in the radial direction (xz plane) because the saddle point created by the curvature coils is also displaced by a few μm in the radial direction from that created by the antibias coils.

[2]In principle, this should not affect the transfer efficiency. However, since the displacement is significant, the shifted magnetic trap is no longer an approximate harmonic trap but can have multiple local minima.

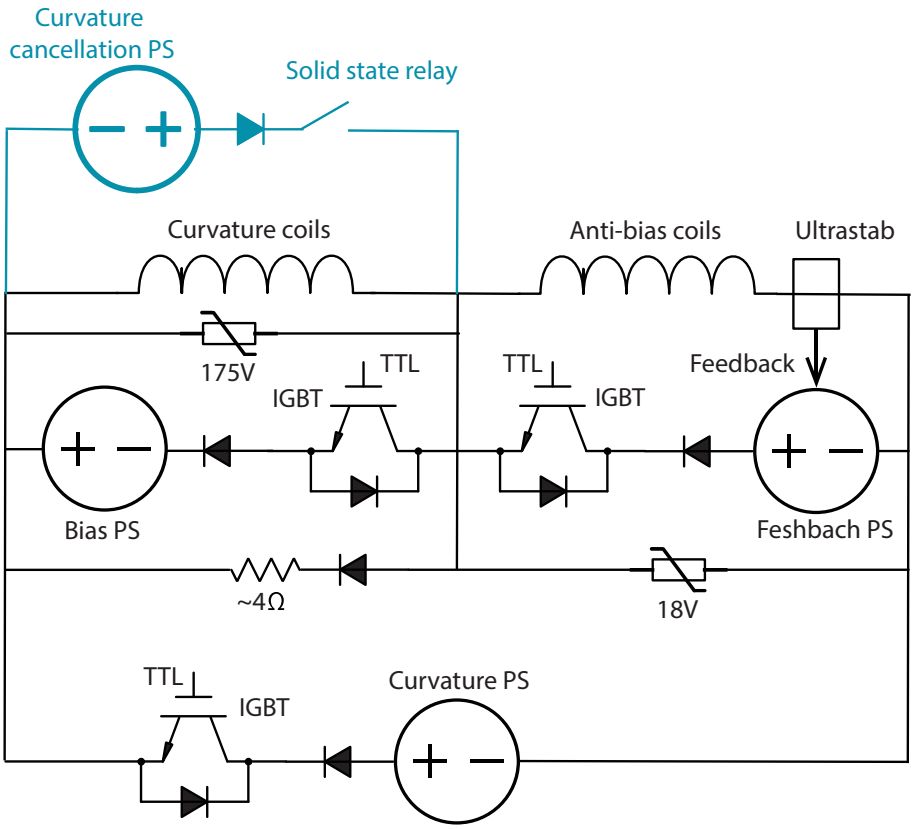

Figure 2-3: Circuit diagram of curvature field cancellation.

2.3 Laser systems

2.3.1 STIRAP lasers

The formation of NaLi molecules in the triplet ro-vibrational ground state ($v = 0, N = 0$) from the Feshbach state ($v = 10, N = 2, m_N = -2$) is carried out using the technique called the stimulated Raman adiabatic passage (STIRAP). This technique uses two laser pulses designed to keep the molecules in a coherent dark state that is decoupled from the intermediate excited state. For the molecular potentials of NaLi, we decided to use 833 nm (upleg) and 819 nm (downleg) laser frequencies to couple the NaLi Feshbach and ground states via the $v^* = 11$ excited vibrational state in the $c^3\Sigma^+$ potential, which are chosen to have strong downleg Rabi coupling with a compromised upleg coupling strength. Figure 2-4 is an energy level diagram showing the STIRAP transitions. The relatively strong downleg transition requires only a few 100 μW power and we use a home-built 818 nm external cavity diode laser (ECDL)[3] while the weak upleg transition requires higher power and we use an injection lock setup with a high power laser diode[4] seeded by a home-built 833 nm ECDL.

The two STIRAP lasers are locked to a commercial optical cavity made of ultra-low expansion (ULE) glass with a linewidth of 15 kHz. This cavity allowed for locking lasers over a range of 810-880 nm to relative linewidths of < 1 kHz. However, we observe that STIRAP transfer from the Feshbach state to the ground state efficiency drops significantly for STIRAP pulses longer than 50 μs. This is probably due to the upleg laser, which has much higher power than the downleg laser, acting on the downleg path (transition between $v = 0, N = 0, m_N = 0$ and $v^* = 11, N = 1, m_N = -1$). The strong upleg laser can induce AC Stark shift of the ground state on the order of 10 kHz, leading to large two-photon detuning[5].

[3] We use the ECDL design developed by the Steck group at the University of Oregon for the STIRAP ECDLs

[4] We use a laser diode mount and a 650 mW 830 nm single mode laser diode from Thorlabs (model: LD830-SE650) for the injection lock.

[5] Problem of two-photon detuning due to AC stark shift becomes much more serious for free-to-bound STIRAP described in Chapter 6.

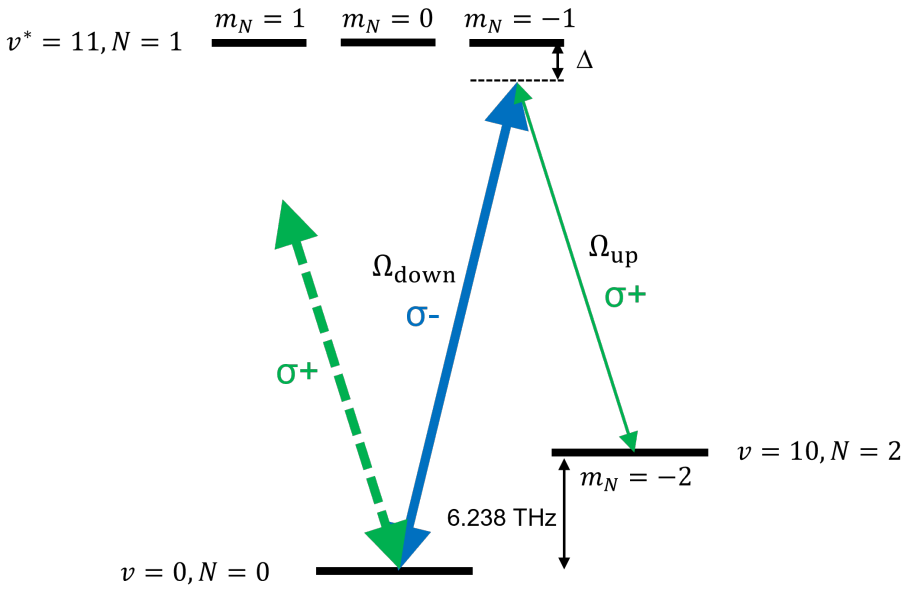

Figure 2-4: **STIRAP lasers.**

2.3.2 Imaging & cleaning

To reliably detect molecules and atoms, we need resonant laser beams for atoms at high bias field (745 G). Initially, imaging systems for Na in state $|F = 1, m_F = 1\rangle$ (upper-stretched state $|F = 2, m_F = 2\rangle$) and Li in state $|F = 1/2, m_F = 1/2\rangle$ (upper-stretched state $|F = 3/2, m_F = 3/2\rangle$) were built by past members of the BEC3 team to image atoms near 745 G (at low magnetic field near 0 G). In order to study collisions between atoms and molecules, imaging/cleaning laser systems for Na in state $|F = 2, m_F = 1\rangle$ and $|F = 2, m_F = 2\rangle$ at high field[6] were implemented later by setting up a double-pass acousto optical modulator (AOM) for each from the Na state $|F = 1, m_F = 1\rangle$ high field imaging beam. In addition, an imaging beam for Na in the lower-stretched state $|F = 2, m_F = -2\rangle$ was implemented to study collisions in the lower-stretched NaLi + Na mixture in the quartet potential. After the magneto optical trap (MOT) stage, the Na slower beam is frequency shifted by a -70 MHz

[6]Although we colloquially call 745 G as "the high field", it is not truly the high-field regime for Na in the ground state. m_J is not a good quantum number, and the state $|F = 1, m_F = 1\rangle$ does not have a well-defined quantum number $m_J = -1/2$ but also has a small fraction of $m_J = 1/2$ component. Therefore, the Na D_2 transition from the ground state $|F = 1, m_F = 1\rangle$ to the excited state $|F' = 0, m_{F'} = 0\rangle$ using $\sigma-$ polarized light is not a closed cycling transition, but the excited state can decay to state $|F = 2, m_F = 1\rangle$ as well.

single-pass AOM and sent to the imaging path for state $|F = 2, m_F = -2\rangle$ imaging at high field.

2.3.3 Optical trapping

The Na/Li mixture is transferred from a magnetic trap to the combination of two coaxial optical traps: a 1,064 nm optical dipole trap (ODT) (30 μm waist, 10 W power) and a 1,596 nm 1D optical lattice (50 μm waist, 2 W power). After 0.4 s of forced evaporation in the 1,064 nm optical dipole trap, the trap is switched off and the science is carried out in the 1,596 nm 1D lattice. The use of 1,596 nm light for the trap improves the lifetime of the NaLi molecules by suppressing spontaneous photon scattering compared to the more common 1064 nm trap. Later, instead of using a combination of the two coaxial optical traps, the mixture is transferred to a 1,550 nm 1D optical lattice (30 μm, 10 W power) and forced evaporated in the lattice. The 1D lattice provides strong axial confinement to overcome the anti-trapping produced by magnetic curvature even without shifting the magnetic trap or canceling out the curvature created by antibias coils[7].

[7]We realized that we do not need to shift the position of the magnetic trap center with a compensation coil in order to well-confine the atoms and molecules only when we performed the third experiment described in this thesis i.e., magnetic trapping and cooling of NaLi molecules.

Chapter 3

Spectrum of Feshbach resonances in NaLi+Na collision

Collisional resonances that are electromagnetically tunable have become an established tool for modifying interactions between ultracold atoms and have been the key for many applications, from magnetic association of loosely bound molecules to quantum simulations [58, 59]. For ultracold molecular systems, tunable collisional resonances are a powerful measure for understanding interaction potentials, probe collision complexes, and control chemical reactions [60].

In the case of cold collisions between alkali-metal atoms, the number of resonant states remains typically small, and the resonances are usually tractable. However, in the case of cold collisions involving molecules, due to strong and anisotropic interactions, ro-vibrational excited states can also contribute to resonant states, and therefore resonances themselves may not be well separated and are difficult to identify. Due to the large density of states of molecular systems [37, 39] it has been a challenge to perform rigorous scattering calculations and different methods enabling efficient scattering calculations have become an active field [61, 62]. Despite these efforts, due to the extreme sensitivity of the low-temperature observables to details of potential energy surfaces, [63, 64] there has been very little success in predicting Feshbach resonances in molecular collisions.

Rather than performing exact quantum calculations, using simple statistical short-

range models while treating the physics of long-range scattering within multichannel quantum defect theory is one feasible alternative approach that has been pursued for the description of molecular resonances [37–39,65]. However, the validity of statistical short-range models is controversial and, therefore, detailed experimental and further theoretical studies are needed.

Here we use a combined experimental and theoretical quantum chemistry approach, which, for the first time, sheds some light onto the nature of deeply bound complexes and the bottom-line mechanism of atom-molecule Feshbach resonances. There are two approaches to understanding and characterizing resonances in collisions involving ultracold molecules. Resonances supported by long-range states of the collision complex may be trackable, since the quantum numbers of the separated atoms and molecules are approximately preserved. For example, resonant states in collisions involving Feshbach molecules [66–69] and in collisions between ground state NaK and K [70, 71] were successfully analyzed in this way. In contrast, resonances supported by collision complexes in which different quantum numbers are mixed due to a strong anisotropic electronic interaction, as in the case for NaLi + Na [33], it is more difficult to understand the nature of the bound complexes. In these terms, patterns of resonances can provide information on the interaction potential and resonant states. In either case involving tightly bound molecules, the underlying coupling mechanism has not yet been characterized.

We report the map of Feshbach resonances in collisions between triplet ro-vibrational ground-state NaLi and Na, both prepared in the maximally spin-stretched state. NaLi + Na in the quartet potential is the lightest bialkali+atom system that has been realized and is chemically stable. Collisions of $^{23}Na^{6}Li(a^{3}\Sigma^{+})$ with Na are generally chemically reactive ($^{23}Na^{6}Li(a^{3}\Sigma^{+}) + Na \rightarrow Na_2(X^{1}\Sigma_g^{+}) + Li + heat$). However, the chemical reaction in the fully spin-polarized atom–molecule system is strongly suppressed due to the conservation of the total spin [29,33], and stable long-lived states can be supported. The system is suitable for modeling molecular scattering resonances because of the relatively small density of states and number of electrons, and therefore more accurate quantum calculations are feasible compared to other heavier

molecular systems.

3.1 Experimental protocol and results

Our experiments use triplet ground-state ^{23}Na^{6}Li ($a^3\Sigma^+$) molecule and Na atom mixtures in the spin-polarized quartet potential, which are chemically stable. The Hamiltonian that includes hyperfine coupling and Zeeman energy for triplet ground-state ^{23}Na^{6}Li is given as

$$\begin{aligned} H &= H_{\mathrm{HF}} + H_{\mathrm{Zeeman}} \\ &= a_1 \vec{S}\cdot\vec{I}_{\mathrm{Na}} + a_2 \vec{S}\cdot\vec{I}_{\mathrm{Li}} + \frac{\mu_B}{\hbar}(g_s\vec{S} + g_{I_{\mathrm{Na}}}\vec{I}_{\mathrm{Na}} + g_{I_{\mathrm{Li}}}\vec{I}_{\mathrm{Li}})\cdot\vec{B} \end{aligned} \tag{3.1}$$

where $a_1 = 433.2(1)$ MHz and $a_2 = 74.6(1)$ MHz [13]. There are 36 states in the ground rotational state manifold ($N = 0$). The states converge to 8 hyperfine thresholds in the zero-field limit due to the conservation of the total angular momentum $F = |\vec{F}| = |\vec{S} + \vec{I}_{\mathrm{Na}} + \vec{I}_{\mathrm{Li}}|$, where $S = |\vec{S}| = 1$ is the total electron spin of NaLi ($a^3\Sigma^+$) and $I_{\mathrm{Na}} = 3/2$ and $I_{\mathrm{Li}} = 1$ are the nuclear spins of Na and Li. The hyperfine splitting due to the Na nucleus is significantly larger than that due to the Li nucleus, so $F_1 = |\vec{S}+\vec{I}_{\mathrm{Na}}| = 1/2, 3/2$, and $5/2$ is an approximately good quantum number that characterizes the largest-scale hyperfine splittings in the zero-field limit. The energy level diagram of NaLi in the triplet ground state ($a^3\Sigma^+, v = 0, N = 0$) at zero bias field is shown in Fig. 3-1.

There are a total of two possible states in the spin-polarized quartet potential, the "upper stretched state" where all nuclear and electron spins are aligned to the bias magnetic field direction ($|F, M_F\rangle_{\mathrm{NaLi}} + |F, M_F\rangle_{\mathrm{Na}} = |7/2, 7/2\rangle_{\mathrm{NaLi}} + |2, 2\rangle_{\mathrm{Na}}$) and the "lower stretched state", where all nuclear and electron spins are anti-aligned to the field direction ($|7/2, -7/2\rangle_{\mathrm{NaLi}} + |2, -2\rangle_{\mathrm{NaLi}}$). Here, F is the total spin (electron and nuclear) and M_F is the B- field projection of F. The molecular and atom mixture in the "upper stretched hyperfine state" with typical numbers of $\sim 3\times10^4$ and $\sim 3\times10^5$ respectively is produced in a 1,596-nm one-dimensional optical lattice following the method described in ref. [33, 72]. The mixture of "lower stretched state" is produced

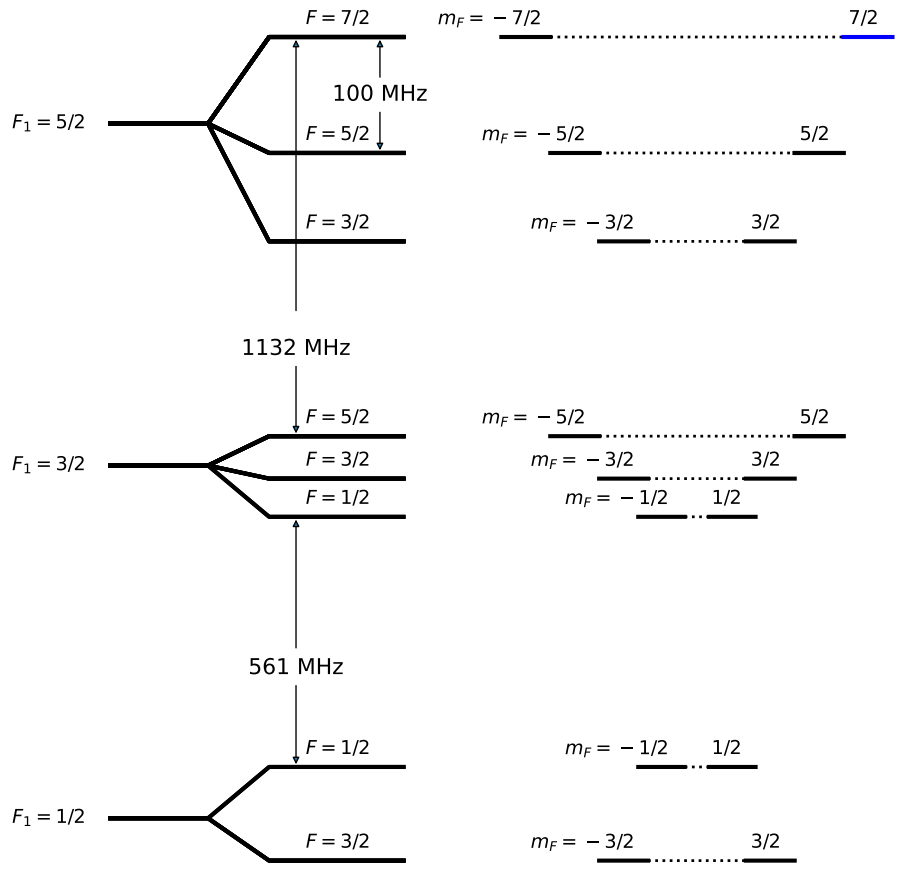

Figure 3-1: **Rovibrational ground state energy level diagram of NaLi in the triplet potential ($a^3\Sigma^+$) at zero bias field.** Quantum number $F = |\vec{F}| = |\vec{S} + \vec{I}_{\mathrm{Na}} + \vec{I}_{\mathrm{Li}}|$ is the total angular momentum, where $S = |\vec{S}| = 1$ is the total electron spin of NaLi and $I_{\mathrm{Na}} = 3/2$ and $I_{\mathrm{Li}} = 1$ are the nuclear spins of Na and Li. In the zero field limit, $F_1 = |\vec{S} + \vec{I}_{\mathrm{Na}}| = 1/2, 3/2$, and $5/2$ is an approximately good quantum number that characterizes the largest-scale hyperfine splittings as the hyperfine splitting due to the Na nucleus is significantly larger than that due to the Li nucleus. Molecules are formed in the low field seeking spin-polarized hyperfine state ($|F_1 = 5/2, F = 7/2, m_F = 7/2\rangle$) and is indicated in blue.

by coherent transfer from the sample of “upper stretched state" using a magnetic field sweep in the presence of radio frequency waves at a low bias field [73]. For this process, the bias field is dropped from 745 G where “upper stretched state" is prepared to a low field near 8 G in 15 ms. After the state preparation, the bias field is ramped to a target value in 15 ms. We determined the collisional lifetimes of the atom-molecule mixtures by holding the sample for a variable time at the target magnetic field.

The loss of NaLi molecules with Na atoms is measured as a function of the bias field for both spin-polarized states. The number of molecules left after the bias field is swept down by 12.6 G in each target field for 200 ms and normalized by that without the field sweep is shown in Fig. 3-2 from near zero to 1420 G in steps of 8.76 G. A fine scan that is at least a factor of 10 finer is performed in the fields where a noticeable loss is found from the coarse scan in Fig. 3-2. We identified 8 resonances in the upper stretched state and 17 resonances in the lower stretched state indicated with red vertical lines in Fig. 3-2.

The approximate spectral information of each resonance is estimated by fitting the observed loss features from a finer search to a simple Lorentzian function with a slope (the slope is to consider the overall change in the background loss and the effect of nearby other resonances). An example of a resonant loss feature near 884 G from a finer scan and a Lorentzian fit is shown in Fig. 3-3(a). The result of the fit is summarized in Table 3.1. The resonances are labeled with numbers in order of increasing resonance position in Gauss for two different initial collision channels, respectively. For three resonances 4,5 and 6 in the upper stretched state, the loss rates are mapped as a function of the bias field for a more accurate estimation of the resonance position and width, as shown in Fig. 3-3(b). For these three resonances, the center and width obtained by a Lorentzian fit to the loss rates instead of the loss feature are summarized in Table 3.1. We confirmed that the approximate widths from observed loss features can be broader due to saturation compared to the more accurate widths from the loss rate measurements with resonance 5 in the upper stretched state

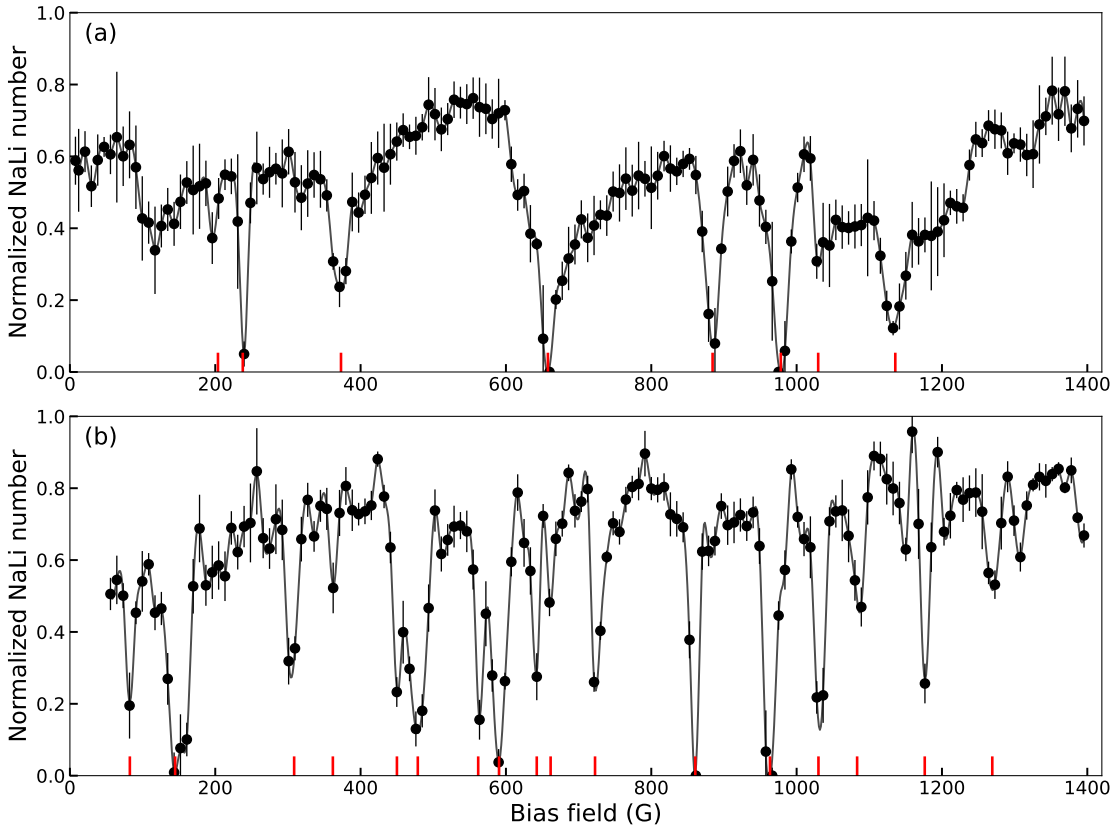

Figure 3-2: **Collisional loss spectrum of NaLi molecules with Na atoms as a function of magnetic field a. in upper stretched hyperfine states and b. in lower stretched hyperfine states.** Y-axis is the number of NaLi left after sweeping down the bias field by 13 G at each field for 200 ms, normalized by the number of NaLi without the field sweep. Each data point represents three to six measurements with and without the sweep respectively. The number of Na atoms in each pancake for each measurement was around 115, and the number of NaLi molecules without the field sweep was about 35. We observed total of 25 resonances: 8 in the upper spin-polarized mixture and 17 in the lower spin-polarized mixture. Red vertical lines indicate the position of Feshbach resonances. The errorbar represents one standard deviation of the mean. Grey lines are interpolated data with a piecewise cubic polynomial to guide the eye.

Collision channel : $\|\mathbf{7/2}, \mathbf{7/2}\rangle_{\mathrm{NaLi}} + \|\mathbf{2}, \mathbf{2}\rangle_{\mathrm{Na}}$			
	B_0 (G)	ΔB (G)	β ($\mathrm{cm^3 s^{-1}}$)
1	203.7(2)	5.3(7)	$1.5(6) \times 10^{-11}$
2	237.9(1)	6.3(4)	$7.1(1) \times 10^{-11}$
3	372.0(7)	20(3)	$2.3(5) \times 10^{-11}$
4	657.8(3)	5.2(8)	$1.0(1) \times 10^{-10}$
5	884.3(3)	10(2)	$6(1) \times 10^{-11}$
6	978.2(2)	4.9(3)	$7.4(5) \times 10^{-10}$
7	1029.7(3)	10(2)	$1.5(3) \times 10^{-11}$
8	1135.2(8)	15(3)	$3.0(5) \times 10^{-11}$

Collision channel : $\|\mathbf{7/2}, \mathbf{-7/2}\rangle_{\mathrm{NaLi}} + \|\mathbf{2}, \mathbf{-2}\rangle_{\mathrm{Na}}$			
	B_0 (G)	ΔB (G)	β ($\mathrm{cm^3 s^{-1}}$)
1	82.5(1)	1.3(2)	$1.0(3) \times 10^{-10}$
2	145(1)	18(4)	$5.3(9) \times 10^{-11}$
3	309(1)	13(4)	$1.9(4) \times 10^{-11}$
4	361.82(5)	1.0(2)	$4.5(8) \times 10^{-11}$
5	449.8(2)	3.1(5)	$6(2) \times 10^{-11}$
6	478(3)	35(13)	$3.4(6) \times 10^{-11}$
7	561.8(2)	2.4(6)	$8(2) \times 10^{-11}$
8	590.7(2)	9(1)	$8(2) \times 10^{-11}$
9	642.3(5)	3(2)	$2.9(4) \times 10^{-11}$
10	661.5(2)	3.9(9)	$2.4(5) \times 10^{-11}$
11	722.5(1)	2.7(3)	$8(4) \times 10^{-11}$
12	860.8(2)	2.1(6)	$2.4(6) \times 10^{-10}$
13	963.3(2)	6(1)	$2(1) \times 10^{-10}$
14	1030.1(2)	3.3(8)	$9(3) \times 10^{-11}$
15	1083.3(3)	4(1)	$5(1) \times 10^{-11}$
16	1176.3(3)	3.2(9)	$8(2) \times 10^{-11}$
17	1269.2(1)	2.6(3)	$3.3(5) \times 10^{-11}$

Table 3.1: **The Feshbach resonance position, width and peak loss rate constant.** Resonance positions and widths are obtained by Lorentzian fit to loss features, except for resonances 4 to 6 for the incoming collision channel $|7/2, 7/2\rangle_{\mathrm{NaLi}} + |2, 2\rangle_{\mathrm{Na}}$. The center and width are obtained by Lorentzian fit to the field-dependent loss rates instead for these three resonances.

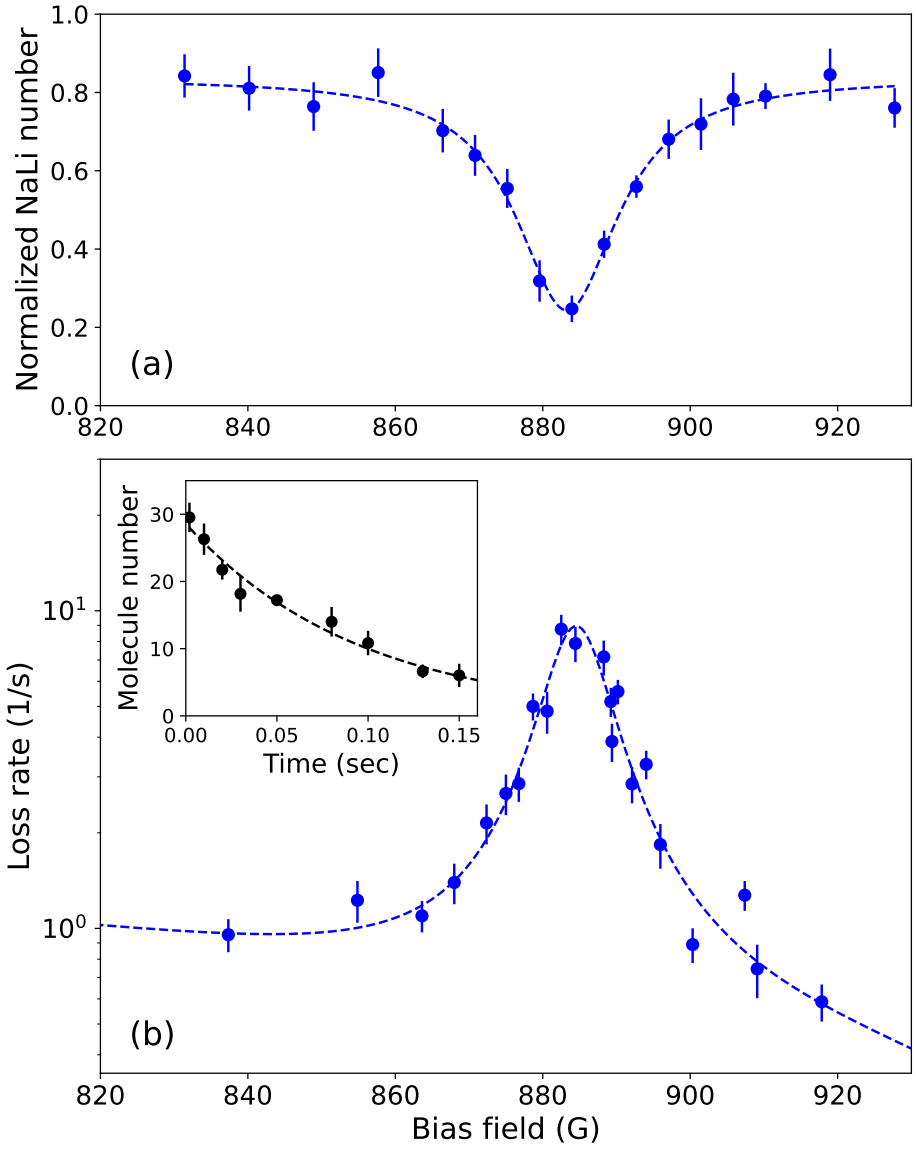

Figure 3-3: **Feshbach resonance in NaLi + Na upper stretched state near 884 G.** a. NaLi number as a function of bias field where the NaLi + Na mixture are held for 100 ms normalized to the number without the hold. b. Loss rate of NaLi molecules with about 100 Na atoms in each pancake as a function of bias field. The dashed blue lines are the fits to a simple Lorentzian function with a slope. The inset is the molecule number per pancake as a function of hold time near the center of the resonance ($\sim$ 884.3 G).

near 884 G. The width obtained from a Lorentzian fit to the loss feature of resonance 5 is 17(1) G, which is broader (about 50 %) compared to that from the loss rate measurement, which is 10(2) G.

The decay curves are taken as a function of the hold time near the center of loss features as in the inset of Fig. 3-3(b) for the peak loss rate constants β and are summarized in the last column of Table 3.1. Sodium densities are calibrated by comparing the measured decay rates with the decay rate of the mixture in a non-stretched spin state which is predicted to occur with the s-wave universal rate. This method was validated in ref. [33] by confirming that the measured loss rate in $|7/2, 7/2\rangle_{\mathrm{NaLi}} + |1, -1\rangle_{\mathrm{Na}}$ collision is, within the uncertainty, the s-wave universal rate, which is well known for our system [74].

The upper and lower stretched Na + NaLi loss rate constants away from resonances at low field near 0.5 G are $7.5(2.2) \times 10^{-12}\mathrm{cm}^3\mathrm{s}^{-1}$ and $6.7(2.0) \times 10^{-12}\mathrm{cm}^3\mathrm{s}^{-1}$, respectively, and at high field near 540 G are $4.5(1.4) \times 10^{-12}\mathrm{cm}^3\mathrm{s}^{-1}$ and $3.5(1.0) \times 10^{-12}\mathrm{cm}^3\mathrm{s}^{-1}$, respectively. These background loss rates are more than an order of magnitude smaller than the universal loss rate constant for Na + NaLi s-wave collisions, which is $1.7 \times 10^{-10}\mathrm{cm}^3\mathrm{s}^{-1}$. The loss rate constants of the two spin-polarized mixtures match both at low-field and high-field within the uncertainty. For both states, the background loss rates are lower at the higher magnetic field.

3.2 Analysis

One would expect the upper stretched state to have more possible decay channels due to its higher energy. However, we have observed similar rates of background loss and Feshbach enhanced losses for both states, and even more resonances for the lower stretched state. This implies that Zeeman energies do not play a major role and that dipolar relaxation is not a dominant decay mechanism for the collisional complex. Instead, the decay is probably dominated by short-range chemical reactions or inelastic loss, which are expected to be similar for both spin-stretched initial states.

In the range up to 1500 G, we observed 8 resonances in the upper stretched state

and 17 in the lower stretched state. This observation provides the density of stable atom-molecule bound states in our system. The linewidths of the resonances range from about 1 G to about 30 G and the spacing between resonances is on the order of 100 G. If the linewidths are interpreted as due to the finite lifetime of the resonant state, this implies atom-molecule complexes with lifetimes in the range of 10 to 350 ns. One possible interpretation of the spacing between resonances is the rotational structure of the intermediate complex. The spacing between resonances of the order of 100 G corresponds to single spin-flip energy differences of 280 MHz and a rotational constant with a moment of inertia for a complex of size around 30 a_0. Note that the rotationally excited states of the NaLi triplet molecules $N = 1$ are at 9.25 GHz and $N = 2$ are at 27.75 GHz [13] corresponding to a double spinflip energy at 1650 G and 5000 G, respectively.

We quantify the resonance statistics of 17 resonances from Na+NaLi collisions in the lower stretched state provided in Table 3.1 using the Brody parameter η, which is a standard measure of chaos. For non-chaotic systems, in which resonances have no correlations, the distribution of nearest-neighbor spacings is given by the Poisson distribution, $P_{\mathrm{P}}(s) = e^{-s}$. On the other hand, for chaotic systems, which emerge when the mean spacing between bound states is comparable to the coupling strength, the repulsion between energy levels occurs. In this regime, the distribution of nearest-neighbor spacings is given by a Wigner-Dyson distribution, $P_{\mathrm{WD}}(s) = \frac{\pi}{2} s e^{-\frac{\pi}{4}s^2}$ [75, 76]. The two distributions are smoothly interpolated through the Brody parameter η as $P_{\mathrm{B}}(s) = A s^{\eta} e^{-\frac{A}{\eta+1}\cdot s^{\eta+1}}$, known as the Brody distribution, where $A = (\eta+1)\cdot\Gamma\left(\frac{\eta+2}{\eta+1}\right)^{\eta+1}$ [77, 78]. Here, $\eta = 1$ and $\eta = 0$ lead to the Wigner-Dyson and Poisson distribution, respectively. The cumulative probability function of the Brody distribution is given as

$$F_B(s) = (\eta+1)\cdot[1 - e^{-\alpha s^{\eta+1}}]. \tag{3.2}$$

Fig. 3-4 shows the cumulative probability of resonance spacing of the 17 resonances from Na+NaLi collisions in the lower stretched state. The best fit of the data to Eq. 3.2 gives $\eta = 1.1(1)$, which shows the statistical signature of quantum chaos.

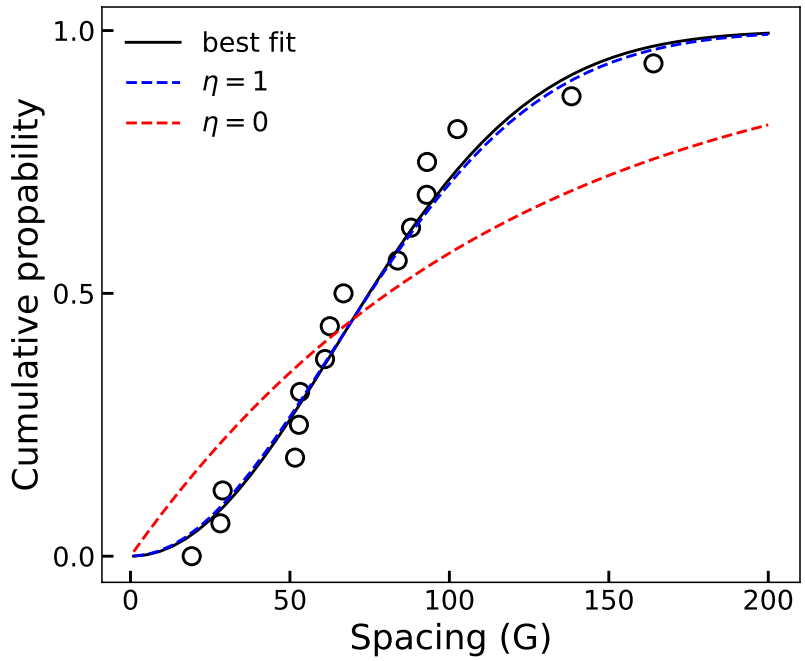

Figure 3-4: Cumulative probability of resonance spacing from Na+NaLi collisions in the lower stretched state. The black line is the best fit to the cumulative probability function of the Brody distribution given as Eq. 3.2 and the blue (red) dashed line is the cumulative distribution with $\eta = 1$ ($\eta = 0$).

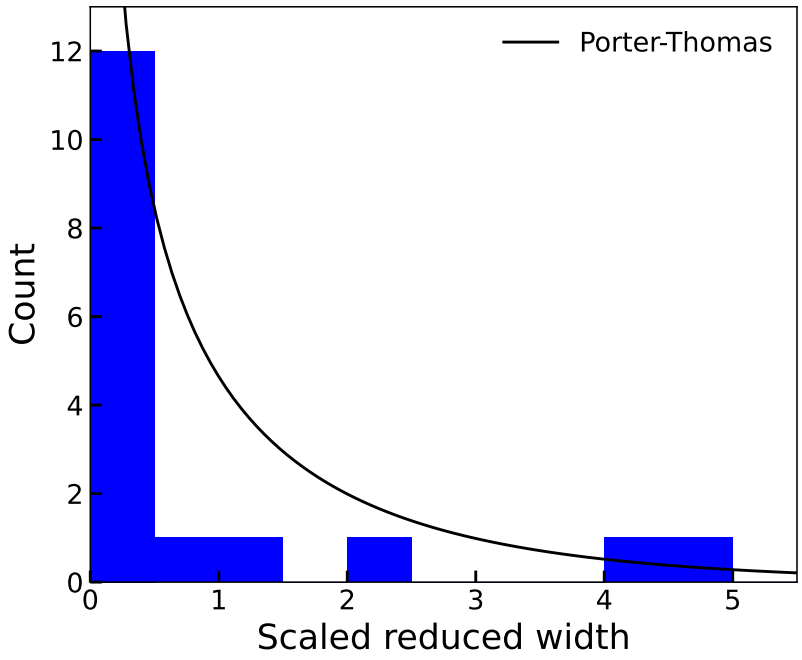

Figure 3-5: Distribution of scaled reduced widths for scattering resonances in the lower stretched state Na+NaLi mixture which are listed in Table 3.1. The Poter-Thomas distribution of scaled reduced widths is in black line.

However, statistical conclusions from only 17 resonances are speculative. On the basis of our quantum-scattering calculations (see Chapter B.1), the Wigner-Dyson statistics are not expected because each resonance can be assigned by M_S, J, M_J quantum numbers. (Resonances with different values for these quantum numbers do not see one another.) In addition, it is difficult to conclude that the broad trend of the distribution of resonance widths follows the Porter-Thomas distribution of resonance widths, $P_{\mathrm{PT}}(\bar{\gamma}) = \bar{\gamma}^{-1/2} e^{-\bar{\gamma}/2}$, which is also a statistical character of quantum chaos. Here, $\bar{\gamma}$ is the normalized velocity width divided by the mean value of all normalized widths [79]. Fig. 3-5 shows the histogram of the scaled reduced resonance width distribution and the Porter-Thomas distribution. Due to the small statistical sample, it is difficult to compare the broad trend of the distribution with the Porter-Thomas distribution.

Here, we have focused on analyzing the spectrum of Feshbach resonances solely based on the experimental observations. However, there are some open questions that

are not answered with immediate interpretations, and some of the interpretations may need further study for justification. First, the mechanism of coupling between the initial scattering channel and the loss channels or resonant closed channels that leads to back ground loss or resonances is not explained. Hypothetically, spin-flip transitions can be induced by intramolecular spin-spin, spin-rotation, atom-molecule magnetic dipole-dipole interactions, and others. What are the dominant interactions that are responsible for the resonances and the background loss, and the detailed mechanism, is still an open question. Second, there is insufficient information to explain the qualitative difference between the upper stretched states and the lower stretched states. One may expect the observed difference in the number of resonances between two spin-stretched initial states to result from the difference in the density of states because resonant coupling can probe the chemical structure of the complex, and the number of resonances is closely related to the density of states. However, only after further investigation can we make a decisive statement on the qualitative difference between the two states. Lastly, the nature of the collisional complex is inconclusive. The validity of the simple interpretation of the spacing between resonances as the rotational energy splitting of the complex, which leads to a complex size of around 30 a_0 is debateable. In addition, the analysis does not provide any other information on the nature of the complex. For example, one may ask what the good quantum numbers are of these collisional complexes. To unravel these open questions, we use a combined experimental and theoretical quantum chemistry approach. The details of quantum calculation are presented in Chapter B.1.

3.3 Interpretation

In this section, we will summarize the key points understood by the combined experimental and theoretical quantum chemistry approach rather than going through the details of the quantum calculations. Even state-of-the-art quantum chemistry calculations cannot predict the position of resonances because of the uncertainty in the interaction potentials. However, they can provide a deep understanding of the

relevant states and their couplings.

Background loss. The inelastic losses observed in Na + NaLi collisions are due to transitions to lower lying states — these are the singlet states of Na_2 or NaLi, and in the case of the upper stretched state, also lower Zeeman states. Similar losses observed for the upper and lower stretched states imply that Zeeman relaxation is not dominant. The loss is therefore due to transitions from the quartet to the doublet potential which occur at close range. If the input state already has a doublet component (e.g. by using Na in a different hyperfine state), the loss rate is much faster since the reaction can occur directly in the doublet potential and does not need a spinflip process, which is weak.

Feshbach resonance. Feshbach resonances increase the wavefunction at close range by coupling the open channel to closed channels. Our simulations show that the closed channels are 3-body complexes in the quartet state with rotational excitation, either of NaLi (quantum number N), or rotation of Na around NaLi (quantum number L). Doublet states have only a minor role. These complexes have a typical size of $20-40$ a_0. The input channel has $N = 0, L = 0$. The input state and the complex state involve different M_S, which is necessary for a magnetic Feshbach resonance. Molecular eigenstates in different Zeeman levels can be coupled by a strong anisotropic electronic interaction since the different molecular Zeeman states have different rotational state decompositions due to mainly spin-spin coupling and also spin-rotation coupling. As a result, the complexes have mechanical rotation $J = 2$. Note that spin-spin coupling depends on the orientation of the molecular axis and, therefore, provides tensorial coupling between the spin and the mechanical angular momentum. The enhanced loss near Feshbach resonances is either due to enhanced loss via the open channel or by a short lifetime of the admixed closed channel. At least for the strong resonances, it is the former.

Number of resonances. Our simulations can explain why the number of observed resonances is smaller for the upper stretched state. Simulations with decay to lower Zeeman states removed show a similar number of resonances. This implies that the difference in the number of resonances is not due to a different density of states

but is due to the rapid decay of some of the intermediate complexes which broaden the resonances and makes them unobservable. Those complexes decay to lower-lying Zeeman states via spin-spin coupling.

Chapter 4

Degeneracy-induced magnetic resonance in NaLi+NaLi collision

One of the powerful methods used in cold atoms is Feshbach resonances, which can happen when a molecular bound state in the closed channel approaches the threshold of the scattering state in the open channel. They act as fingerprints of molecular interaction potentials because of their high sensitivity to the shape of the molecular potential energy surface and shed light on expanding our understanding of collision dynamics.

However, there have been only a few discoveries of magnetically tunable Feshbach resonances in a molecular system. Exploration of Efimov physics was carried out by observation of Feshbach resonances in collisions of loosely bound Cs_2 and NaRb Feshbach molecules [66–69, 80]. There are two atom-molecule systems in which magenetically tuneable Feshbach resonances are observed. Scattering resonances in K+NaK collision identified an intermediate complex as a loosely bound state between the molecule and the atom [71] and in Na + NaLi collision probed three-body tightly bound states [33]. Feshbach resonances in collisions between two ground-state molecules have not yet been identified before.

Here we report the observation of a pronounced, isolated Feshbach resonance in collisions between fermionic NaLi molecules in their ro-vibronic ground state. The magnetically tunable resonance is extremely narrow ($\sim$ 25 mG) and enhances the

loss rate by more than two orders of magnitude, providing strong evidence for a stable and long-lived collision complex. The existence of long-lived complexes in a molecular system of high reactivity, such as NaLi, is unexpected and has strong implications for controlling ultracold chemistry via scattering resonances. The long-lived state revealed by our experiments is coherently excited, whereas so far, all other observations of collisional complexes are compatible with an incoherent population described by rate equations.

The observed resonance is special in two regards: In simple models, resonantly enhanced losses are only possible if the background loss rate is much smaller than the so-called universal limit. A loss rate near the universal limit implies almost complete inelastic loss at short-range and should suppress any long-lived resonant state. However, we observe loss rates close to the universal limit outside the narrow resonance. Second, the NaLi + NaLi Feshbach resonance is observed at a finite magnetic field where two open channels become degenerate, and it is possibly a new type of Feshbach resonance with a mechanism different from the Feshbach resonances observed in ultracold atomic systems. This mechanism is unique to molecule-molecule collisions, as the required single-molecule degeneracies cannot be realized in atomic systems at practicable field strengths. On the contrary, two-molecule degeneracies used to engineer shielding interactions in ultracold KRb + KRb and CaF + CaF collisions, are commonly found in molecular collisions. Our results suggest that the new type of degeneracy-induced magnetic resonance could be ubiquitous in ultracold molecular physics, offering an exquisite new mechanism for tuning intermolecular interactions with external electromagnetic fields. We present simple models which explain the observed behavior.

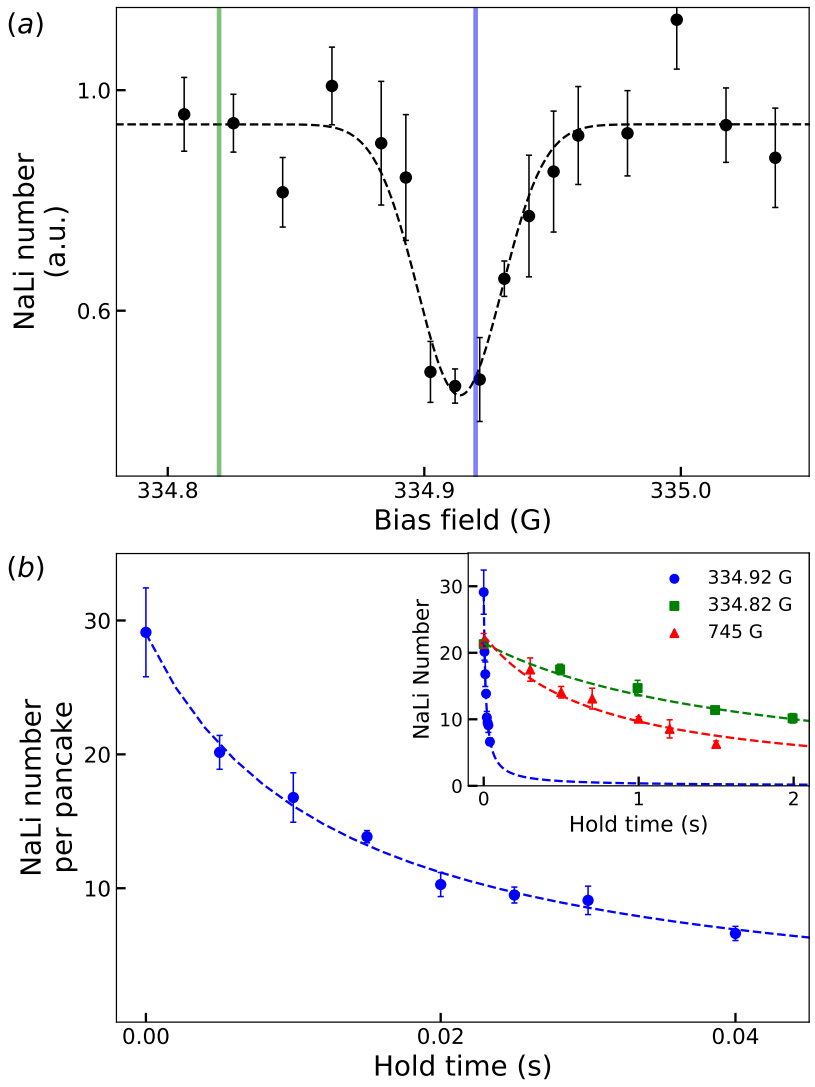

Figure 4-1: **a. Resonant molecular loss as a function of magnetic field.** The remaining molecule number after holding for 30ms at a target field is plotted near 334.9 G. Molecule numbers are normalized by the molecule number without the 30 ms hold. Each data point represents three to six measurements with and without 30 ms hold respectively, and the error bars are 1 standard deviation. The black dashed line is a Gaussian fit. The blue (green) vertical line indicates the field where the molecular decay curve in blue (green) is obtained in Fig. 4-1(b). **b. Molecular decay curves at 334.92 G resonance and away from the resonance.** The main plot shows the molecular decay curve near the center of the resonance within 50 ms. The upper right subplot shows decay curves away from the resonance at 334.82 G in green squares and at 745 G in red triangles and also near the resonance at 334.92 G with blue circles from 0 to 2 s. Dashed lines are fits to a simple model for two-body loss using mean square regression.

4.1 Measurement & Experimental Result

4.1.1 Experimental sequence

We prepare ground-state $^{23}Na^{6}Li$ ($a^3\Sigma^+$) molecules in their lower stretched hyperfine state, where all nuclear and electron spins are anti-aligned to the bias field direction. For the state preparation, we first produce triplet ground state molecules in the upper stretched hyperfine state, where all spins are aligned along the bias field, via magnetic association followed by stimulated Raman adiabatic passage (STIRAP) near 745 G in a 1 dimensional (1D) 1596 nm optical lattice [13, 33, 72]. The bias field is dropped from 745 G to a low field near 8G in 15ms for coherent microwave state transfer from the upper stretched state ($|F, m_F\rangle = |7/2, 7/2\rangle$) to the lower stretched state ($|F, m_F\rangle = |7/2, -7/2\rangle$). After the state preparation, field is ramped to a target value in 15ms. The search for scattering resonances is done for the bias field range of 40.5 G $< B <$ 1401.6 G. After waiting for a certain time for the molecules to collide at a target field, we return the field to $\sim$ 8 G for reverse state transfer ($|7/2, -7/2\rangle \rightarrow |7/2, 7/2\rangle$) for detection. We used absorption imaging of lithium atoms dissociated from molecules to measure the number and temperature of molecules, and thus the field was brought to 745 G. An extra time of 15 ms $<$ t $<$ 30 ms after each magnetic field ramp was sufficient for the bias field to settle within the range of the magnetic field inhomogeneity across the molecular sample.

Within more than 1000 G range in bias field, only one Feshbach resonance is observed as shown in Figure 4-1(a). While the number of molecules decreases by about 40% in 600 ms at most bias field values, more than half of the molecules are lost after 30 ms hold near 334.914(10) G (Fig.4-1(b)). In order to verify that the enhanced loss is due to a resonance in collisions between two fermionic NaLi molecules in the same hyperfine state, we investigate three aspects: the effect of impurities, the density dependence and temperature dependence on molecular decay rates. We confirm that the loss enhancement is not due to impurities by examining the decay curves at the resonance. About 30 molecules per lattice site decreases down to about 7 molecules in 40 ms as shown in Figure 4-1(b) and are depleted to the level

that is barely detectable in less than a hundred milliseconds. A little fraction of contamination of the molecular sample that may exist can only cause depletion of the sample up to the contamination level mainly through s-wave collisions. This confirms that the loss enhancement comes from two identical fermionic molecules and not from other unwanted states.

4.1.2 Model for molecular decay & density calibration

Exploration of the other two aspects: density dependence and temperature dependence on molecular decay rate requires careful modeling of molecular decay and density calibration. We model the two-body loss with a differential equation that takes into account the time dependence of temperature: [23]

$$\dot{n}(t) = -\beta(T(t))n^2(t) - \frac{3}{2}n(t)\frac{\dot{T}(t)}{T(t)}, \tag{4.1}$$

where β is the two-body loss rate constant, n is the mean density, and T is the temperature of the molecules. Anti-evaporation causes an increase in temperature of up to 50% within a molecular decay time near 334.9 G. We fit the measured temperatures to a linear function of time, $T(t) = Ht + T_o$, where H is the heating rate and T_o is the initial temperature. Both away from and near the resonance, the loss rate coefficient has a temperature dependence that can be expressed as $\beta = \beta_0(T(t)/T_0)$, where β_0 is the initial loss rate coefficient when the temperature is T_0. To determine the rate coefficient from equation Eq. (4.1) requires accurate knowledge of the molecular density. The mean molecular density can be expressed with the effective number of particles, N^{eff} and the mean volume, V_{eff}, of molecules for a single pancake, as $n = N^{\text{eff}}/V_{\text{eff}}$.

We obtained the effective particle numbers for a single pancake from the measured number of molecules, N^{tot}, and the distribution of the numbers over the pancakes. The observed axial profile of NaLi follows a Gaussian form with width σ=450(60)μm, so we assume a Gaussian distribution of the number of particles per pancake. As the average weighted over a Gaussian, the effective particle number per pancake is

N^{eff}=$N^{\text{tot}} \cdot a/(2\sqrt{\pi} \cdot \sigma)$, where the lattice constant is a=$\lambda/2$ and λ=1596 nm.

The trap volume of each pancake, V_{eff}, is determined from the measured molecule temperature and trap frequencies. For a purely harmonic trap, one obtains $V_{\text{eff}}^{(0)} = \bar{\omega}^{-3}(4\pi k_B T/m)^{3/2}$ where the geometric mean of the NaLi trap frequencies is $\bar{\omega}$=$(\omega_x\omega_y\omega_z)^{1/3}$. However, there are two corrections which we determine separately: (1) the confinement in each pancake is moderately anharmonic, and (2) the system is in the crossover regime between quasi-2D and 3D, $k_B T \sim \hbar\omega_z$.

First, the anharmonicity of the trapping potential leads to a modified mean volume $V_{\text{eff}}^{(1)}$

$$1/V_{\text{eff}}^{(1)} = \frac{\int dV \mathrm{e}^{-2\beta U(r,z)}}{[\int dV \mathrm{e}^{-\beta U(r,z)}]^2} \tag{4.2}$$

where $U(r,z)$ is the potential of a single lattice site. We use the same trap model validated in ref. [33] to determine $U(r,z)$ and integration limits. With typical conditions for molecular loss measurements, the mean volume $V_{\text{eff}}^{(1)}$ is larger than $V_{\text{eff}}^{(0)}$ by less than 25%. However, some measurements at lower density required weaker optical traps for which the anharmonicity correction is larger and had to be taken into account for proper density calibration.

Second, the tight confinement in the lattice direction makes the classical thermal distribution for harmonic trapping in the pancakes invalid for low molecular temperatures. We estimate the corrected volume as

$$1/V_{\text{eff}}^{(2)} = \frac{\int dV (\sum_{i=0}^{\infty} \rho(r)|\phi_i(z)|^2 \mathrm{e}^{\beta(-i-\frac{1}{2})\hbar\omega_z})^2}{[\int dV \sum_{i=0}^{\infty} \rho(r)|\phi_i(z)|^2 \mathrm{e}^{\beta(-i-\frac{1}{2})\hbar\omega_z}]^2} \tag{4.3}$$

where r is the radial coordinate, z is the axial coordinate along the beam direction, $\beta = (k_B T)^{-1}$, $\phi_i(z)$ is the i^{th} eigenstate of the axial harmonic oscillator and $\rho(r)$ is the classical thermal distribution in the radial direction, which is a Gaussian function. The black line in Figure 4-2 is the result of Eq. 4.3 using the typically radial trap frequency $(f_x, f_y) = (450, 640)$ Hz as a function of the ratio of thermal energy to axial zero-point energy. The red dashed line is $1/V_{\text{eff}}^{(0)}$ and the blue dashed line is the inverse of the quasi-2D volume $1/V_{\text{eff}}^{(2D)}$, assuming that all atoms in the 0^{th} eigenstate

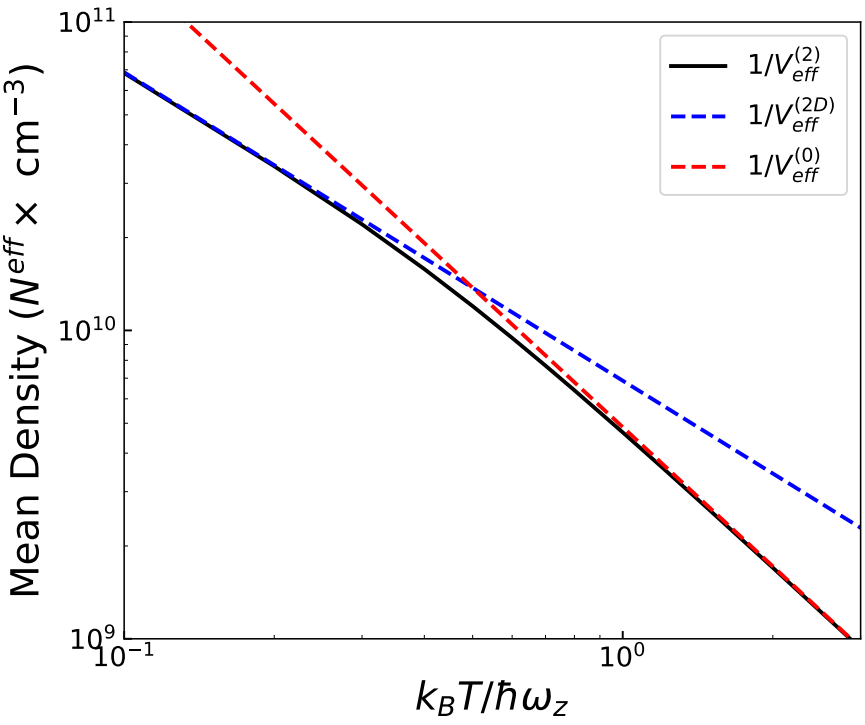

Figure 4-2: **Mean density estimation in the 3D to quasi-2D crossover regime as a function of the ratio of the thermal energy to axial zero-point energy.** Black line is the result of Eq. 4.3, red dashed line is the estimated $1/V_{\text{eff}}^{(0)}$ and blue dashed line is the inverse of the quasi-2D volume where it is assumed that all atoms are in the 0^{th} eigenstate of the axial harmonic oscillator, ϕ_0. Calculation is with the typically radial trap frequency $(f_x, f_y) = (450, 640)$ Hz.

of the axial harmonic oscillator, ϕ_0:

$$1/V_{\text{eff}}^{(2D)} = \frac{\int dV[\rho(r)|\phi_0(z)|^2]^2}{[\int dV \rho(r)|\phi_i(z)|^2]^2}. \tag{4.4}$$

For all the experimental conditions which is indicated with gray shaded area in Fig. 4-3, $V_{\text{eff}}^{(0)}$ differs from the more accurate $V_{\text{eff}}^{(2)}$ by less than 20% [1]. Since it is unclear how this correction might interact with the larger correction from $V_{\text{eff}}^{(1)}$, we include $V_{\text{eff}}^{(2)}$ only as an enlargement in the uncertainty.

[1] Difference between $V_{\text{eff}}^{(2D)}$ and $V_{\text{eff}}^{(2)}$ is much larger than that of $V_{\text{eff}}^{(0)}$ and $V_{\text{eff}}^{(2)}$. This implies that the system is closer to 3D than quasi-2D in terms of molecular density

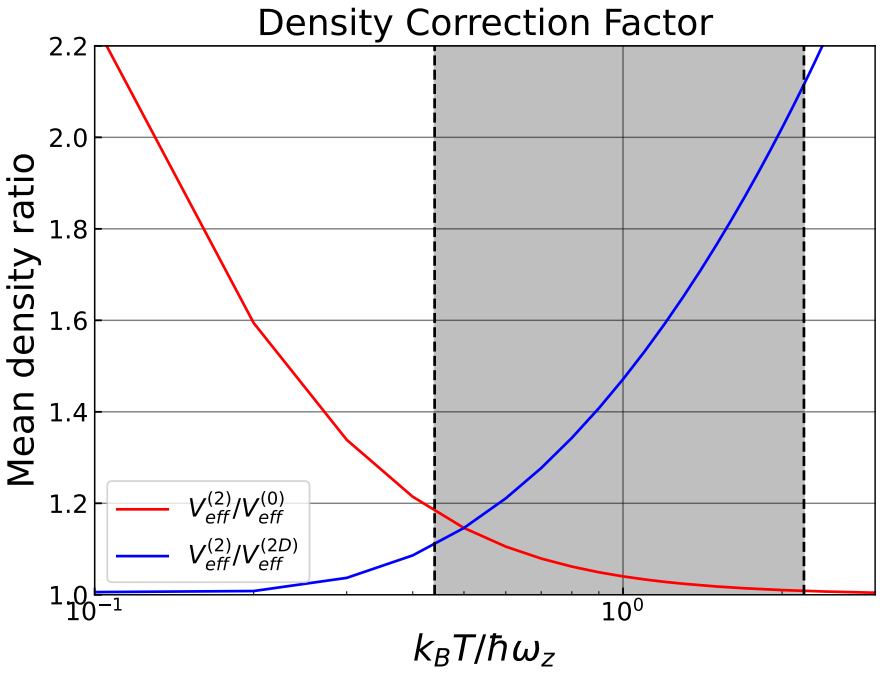

Figure 4-3: **Density correction factor.** Gray shaded area indicates the conditions in which the experiments were carried out. Ratio of $V_{\text{eff}}^{(2)}$ to $V_{\text{eff}}^{(0)}$ is in red and ratio of $V_{\text{eff}}^{(2)}$ to $V_{\text{eff}}^{(2D)}$ is in blue.

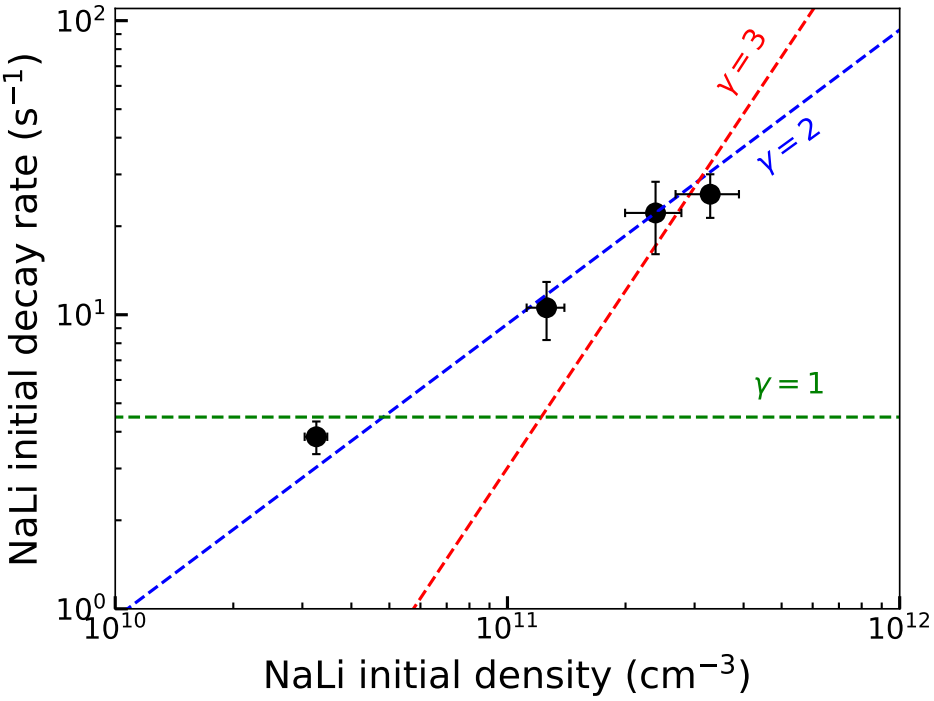

Figure 4-4: **Density dependency of molecular decay rate at** 334.92 **G.** The initial decay rates are plotted as a function of initial molecule mean density. The green, blue and red dashed lines are the fit results for $\gamma = 1$, 2 and 3 in $R_o = An_o^{(\gamma-1)}$ with $\chi^2_{red} = 13.50$, 1.43 and 20.42 respectively.

4.1.3 Density and temperature dependence on molecular decay rates

To understand the loss mechanism, the molecular decay rate is measured as a function of initial density and modeled with an equation $R_o = An_o^{(\gamma-1)}$ as shown in Figure 4-4. R_o is an initial decay rate, n_o is an initial molecular density, γ is a parameter determined by the number of particles involved in collision loss and $A = \beta N_o$ where N_o is an initial number of molecules. In general, the loss rate constant β is temperature dependent, and to treat A as a constant we controlled the initial temperatures of the molecules to be the same within 15 %. $\gamma = 1.82(9)$ gives the best fit, confirming that the resonant loss is due to two-body collisions. Molecule densities are estimated from the lattice trap frequencies and molecular temperature, as explained in Chapter 4.1.2.

We map the temperature dependence of the molecular decay rate constant and

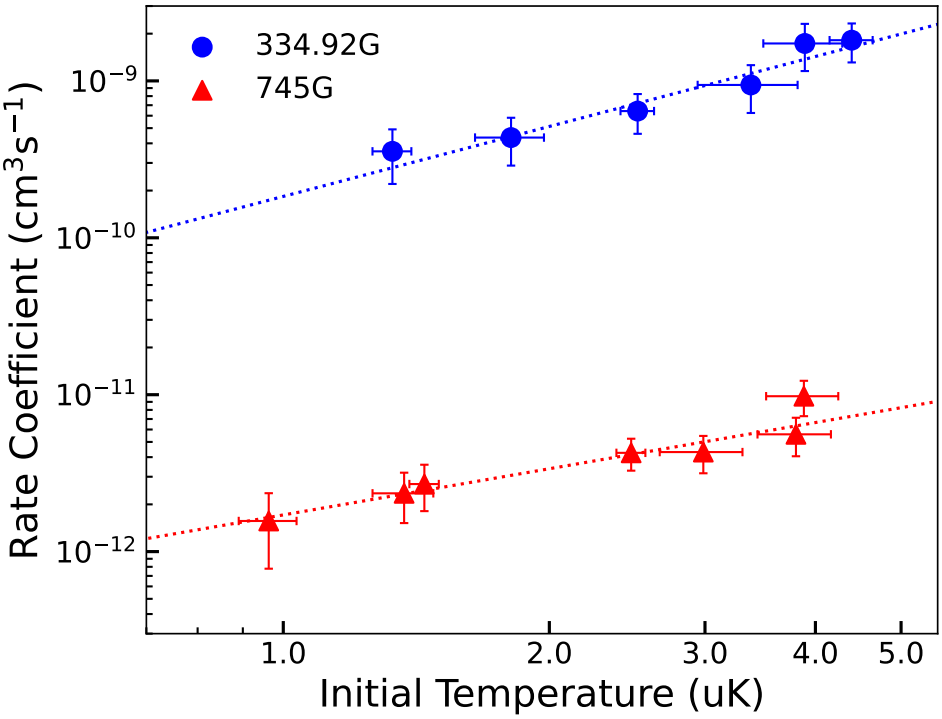

Figure 4-5: **Threshold laws of molecule-molecule collisions.** Initial rate coefficients are plotted as a function of initial temperature of NaLi molecules. Blue data points are measurements near the center of the resonance and red data points are measurements away from resonance near 745 G. Dotted lines are the fits to the polynomial function $\beta = CT^l$.

compare it with the Wigner threshold law [81]. We generate molecular gases at different temperatures by varying the initial temperature of the Na and Li atomic mixture. The initial temperature of the molecule ranging from 0.74(8) uK to 3.88(36) uK and from 1.33(7)uK to 4.40(25) uK is achieved away (745G) and at resonance (334.92 G), respectively. We model the temperature scaling with the polynomial function $\beta = CT^l$ and obtain $C = 1.8(7) \times 10^{-10}\ cm^3/(sK)$ and $l = 1.5(4)$ near the resonance in blue dotted line and $C = 1.7(5) \times 10^{-10}\ cm^3/(sK)$ and $l = 0.98(27)$ as shown in Fig. 4-5. This p-wave Wigner threshold law [81] like behavior implies that the loss is caused by collisions between two identical fermions[2].

4.1.4 Loss rate constant

We map out the measured loss rates as a function of the magnetic bias field. Natural comparisons for the observed decay rates are the unitary limit and the universal loss rate. As the 1D optical lattice creates a trapping potential tightly confined in the axial direction, our experiments are done in the crossover between 2D and 3D physics. The p-wave unitarity limit in a three dimensional trap, $\beta_{3D}^{unit.}=6\frac{\hbar}{\mu}\lambda_{dB}$, where λ_{dB} is the de Broglie wavelength given as $\lambda_{dB}=\sqrt{2\pi\hbar^2/k_B\mu T}$ and μ is the reduced mass which is half of the NaLi molecule mass, $\mu = m_{\mathrm{NaLi}}/2$ [3]. The unitarity limit in a quasi-2D trap, $\beta_{2D}^{unit.}=4\frac{\hbar}{\mu}(\sqrt{\pi}l_0)$. $\beta_{2D}^{unit.}$ scales linearly to the oscillator length in the tightly confined direction, $l_0 = (\hbar/m_{\mathrm{NaLi}}\omega_z)^{1/2}$, instead of the de Broglie wavelength, λ_{dB} (see Chapter C.1 for details). Here, ω_z is the trap angular frequency in the tightly confined direction. We use an approximate value of NaLi-NaLi long-range dispersion coefficient ($C_6 = 5879$ a.u) obtained by summing all C_6 coefficients between two constituent atoms [83]. The universal loss rate constant for p-wave (s-wave) collisions

[2]The system is in the quasi-2D to 3D crossover regime, and therefore, the Wigner threshold law in both quasi-2D and 3D regime had to be derived for proper comparison with the experimental result. We confirm in C.1 that $\beta \propto T$ in both regimes.

[3]Inelastic loss rate constant is given by $\beta_{3D}^{unit.} = g\sigma\frac{\pi\hbar}{mu}\left\langle\frac{1}{k_{rel}}\right\rangle$ in ref. [82] where $\left\langle\frac{1}{k_{rel}}\right\rangle$ is thermally averaged $\frac{1}{k_{rel}} = \frac{\hbar}{\mu}\frac{1}{v_{rel}}$, $g = 2$ for indistinguishable particles, and the degeneracy factor $\sigma = 3$ for p-wave collision. The thermal averaging of the inverse of relative velocity $\left\langle\frac{1}{v_{rel}}\right\rangle = \sqrt{\frac{2\mu}{\pi k_B T}}$, and therefore, $\beta_{3D}^{unit.}=6\frac{\hbar}{\mu}\lambda_{dB}$, where λ_{dB} is the de Broglie wavelength given as $\lambda_{dB}=\sqrt{2\pi\hbar^2/k_B\mu T}$.

is $\beta_{l=1}^{univ}/T = 1.2 \times 10^{-12}\ cm^3/s \cdot \mu\text{K}$ ($\beta_{l=0}^{univ} = 1.85 \times 10^{-10}\ cm^3/s$).

The rate constant, β, increases by more than two orders of magnitude as the bias field approaches 334.918(5) G from near p-wave universal value to above s-wave universal value. Loss rate coefficients are plotted as a function of magnetic field and fitted to a Lorentzian function for two temperatures, 1.8 μK and 4.2 μK, in Fig.4-6. The loss rate constant contrast is $\sim$ 155 for 1.8 μK and $\sim$ 230 for 4.2 μK. The rate constants at the peak are far below the 3D unitarity limits but approach near the 2D unitary limits. The width of the resonance is as narrow as or narrower than the inhomogeneity of the magnetic field across a molecular sample, $\sim$ 25 mG, given the fact that the Lorentian widths from the fits for both 1.8 μK and 4.2 μK are also $\sim$ 25 mG. The result of 4.2 μK shows an overall higher loss rate constant compared to that of 1.8 μK as expected from the p-wave threshold law at the resonance, $\beta \propto T$, mentioned earlier.

4.2 Analysis

We will now develop a model that addresses our major experimental findings. The universal limit assumes that the loss rate is given by all the flux which has not been quantum reflected, i.e. it has tunneled through the centrifugal barrier located at $\sim 2.2R_{\text{vdw}}$ with the van der Waals (vdW) length $R_{\text{vdw}} = \frac{1}{2}\left(\frac{2\mu C_6}{\hbar^2}\right)^{1/4} \approx 66a_0$. Rates higher than the universal limit observed here are only possible (1) if losses occur at *long-range* (outside the p wave barrier) as depicted in Figure 4-7, or if substantial back reflection from *short-range* (behind the centrifugal barrier) destructively interferes with quantum reflection.

A single narrow resonance between two NaLi molecules in their lower stretched hyperfine state is located at a magnetic field where there are multiple other hyperfine states that are energetically close by. We first rule out the possibility (1) by showing that these states are not directly coupled strongly to the initial scattering state at *long-range*. We then focus on the second possibility (2). Nearly degenerate states may have indirect coupling mediated by a bound state of an intermediate collision

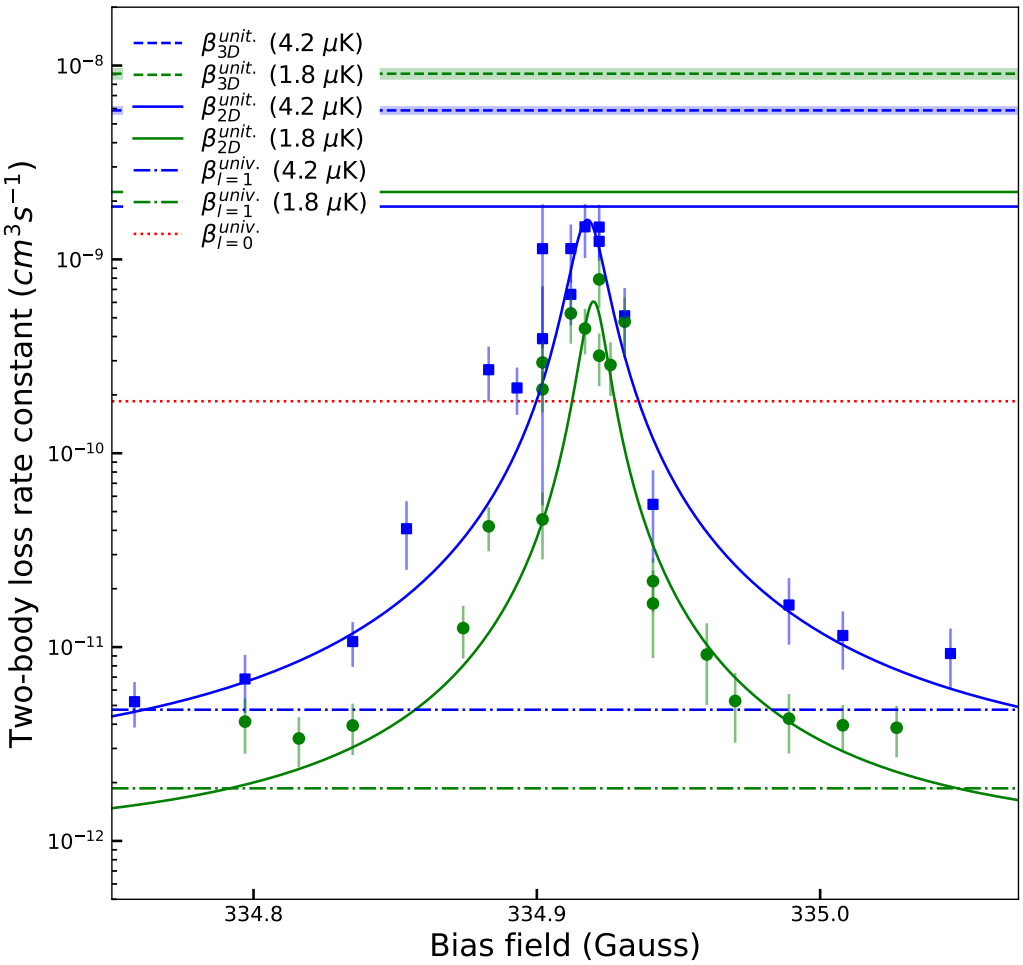

Figure 4-6: **Enhanced two-body loss rate coefficient of molecules.** Initial two-body loss rate coefficients which are indicated with blue squares and green circles, are plotted as a function of the bias field. Data points are obtained using a simple two-body loss model for initial temperatures $\sim$ 4.2 uK (blue squares) and $\sim$ 1.8 uK (green circles). Solid lines are Lorentzian fits to the data points. The dotted red line is the s-wave universal value and dash-dot lines are p-wave universal values for T = 4.2 uK (blue) and T = 1.8 uK (green). Dashed horizontal lines are the 3D unitarity limits and solid horizontal lines are the 2D unitarity limits.

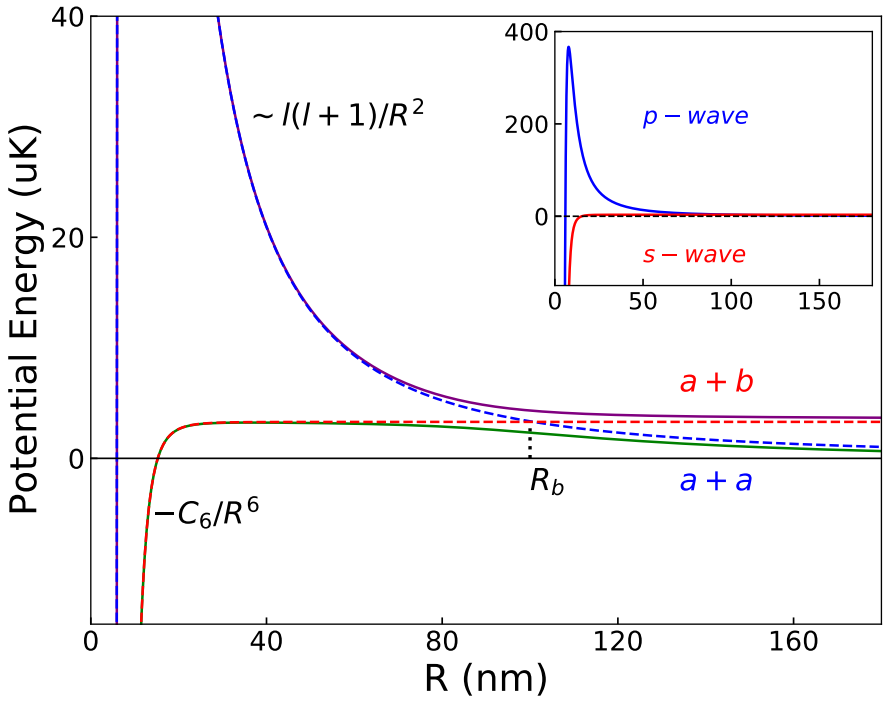

Figure 4-7: **Long-range coupling.** a+a is the initial collision channel where a is the lower stretched state. a+b is another collision channel coupled to a+a at *long-range* $R_b = 100$ nm where b is a near-degenerate hyperfine state.

complex. Our analysis shows that such long-range coupling is too weak to play a role in the observed molecular resonance (see chapter 4.2.1 for details). This suggests that the intermediate bound state does not suffer from short/close range loss and the resonance arises in an open channel.

4.2.1 Hyperfine structure of NaLi

There are a total of 9 hyperfine states crossing the lower stretched state at bias fields between 320 G and 340 G. There are three states that cross at fields within a few hundred mG of the resonance. Due to the uncertainty of the hyperfine constants, the uncertainty of their energies relative to the stretched state is ±400 kHz, and therefore each of them is a possible candidate to cross the stretched state at or near the observed Feshbach resonance at 334.92 G.

The state indicated with an red "a" in Figure 4-9 is the lower stretched state

$|F = 7/2, m_F = -7/2\rangle$. The three states close in energy near the resonance are indicated as b_1, b_2 and b_3 in Figure 4-9. The most likely candidate to couple to the stretched state is the state $b_1 = |F = 5/2, m_F = -3/2\rangle$ since its nuclear spin character overlaps with the stretched state by 50%, whereas for the other two states, non-zero nuclear spin overlap less than 0.1% may arise from small intra-molecular spin-spin (-551 MHz) and spin-rotation (14.5 MHz) couplings. More explicitly, The Zeeman states can be expanded in the fully uncoupled basis set

$$|N, m_N, S, m_S, I_{Na}, m_{I_{Na}}, I_{Li}, m_{I_{Li}}\rangle \tag{4.5}$$

where $|N, m_N\rangle$ are the eigenstates of the rotational angular momentum $\vec{N}$ and of its projection on the B-field axis, $|S, m_S\rangle$ are those of the electron spin angular momentum, and $|I, m_{I_i}\rangle$ are the eigenstates of the nuclear spin angular momenta of Na and Li ($i = Na, Li$). The leading terms in the expansion of the Zeeman states involved in the avoided crossings near $B = 334.92$ G are, neglecting small ($\lesssim 1\%$) contributions from the $N = 2$ rotationally excited states,

$$\begin{aligned}
|a\rangle &= |F_1 = 5/2, F = 7/2, m_F = -\frac{7}{2}\rangle = |0, 0, -1, -1, -\frac{3}{2}\rangle\,, \\
|b_1\rangle &= |F_1 = 3/2, F = 5/2, m_F = -\frac{3}{2}\rangle \\
&\approx 0.71\,|0, 0, 1, -1, -\frac{3}{2}\rangle - 0.57\,|0, 0, 0, -1, -\frac{1}{2}\rangle - 0.40\,|0, 0, -1, -1, \frac{1}{2}\rangle\,, \\
|b_2\rangle &= |F_1 = 3/2, F = 5/2, m_F = -\frac{1}{2}\rangle \\
&\approx 0.76\,|0, 0, 0, -1, \frac{1}{2}\rangle - 0.55\,|0, 0, 1, -1, -\frac{1}{2}\rangle + 0.31\,|0, 0, -1, -1, \frac{3}{2}\rangle\,, \\
|b_3\rangle &= |F_1 = 3/2, F = 5/2, m_F = -\frac{1}{2}\rangle \\
&\approx 0.91\,|0, 0, 0, -1, \frac{3}{2}\rangle - 0.38\,|0, 0, 1, -1, \frac{1}{2}\rangle\,.
\end{aligned} \tag{4.6}$$

Additionally, the difference in m_F to the lower stretched state, is the smallest for state b_1 which is 2 [4].

Spin flip processes can, in principle, happen at *long-range* outside the p-wave

[4] State b_1 lies $\sim$ 100 kHz above the lower stretched state at 334.92 G in figure 4-9. Given the uncertainty of the hyperfine constants, this value can be as high as 480 kHz or as low as -300 kHz

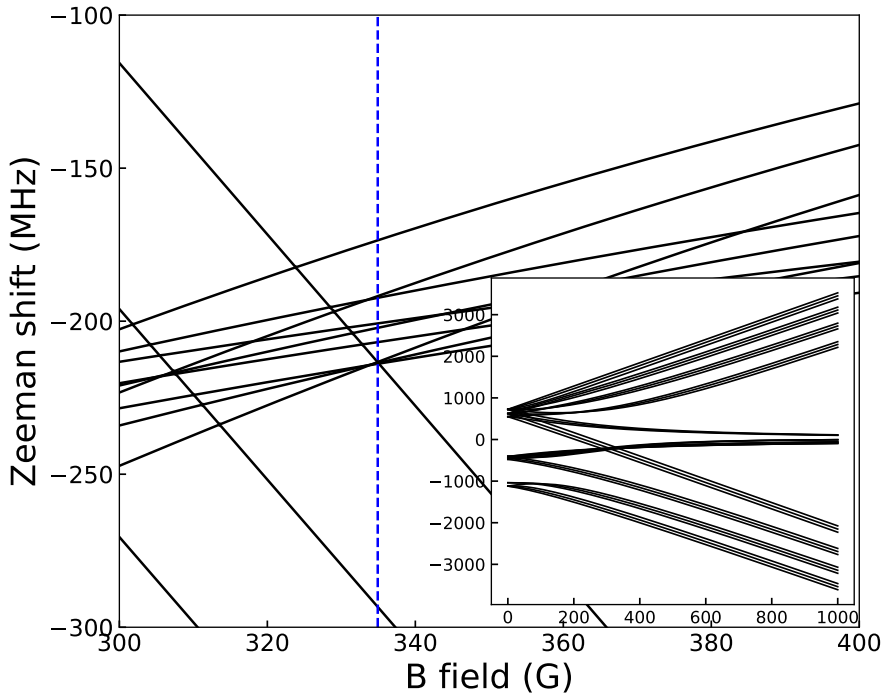

Figure 4-8: **Hyperfine structure of NaLi($a\Sigma^+$) in an external magnetic field.** The blue dashed vertical line indicates the position of the Feshbach resonance ($\sim$ 334.92 G). The subplot show the Zeeman shifts from 0 to 1000 G whereas the main plot is zoomed into where there are 9 near degenerate states.

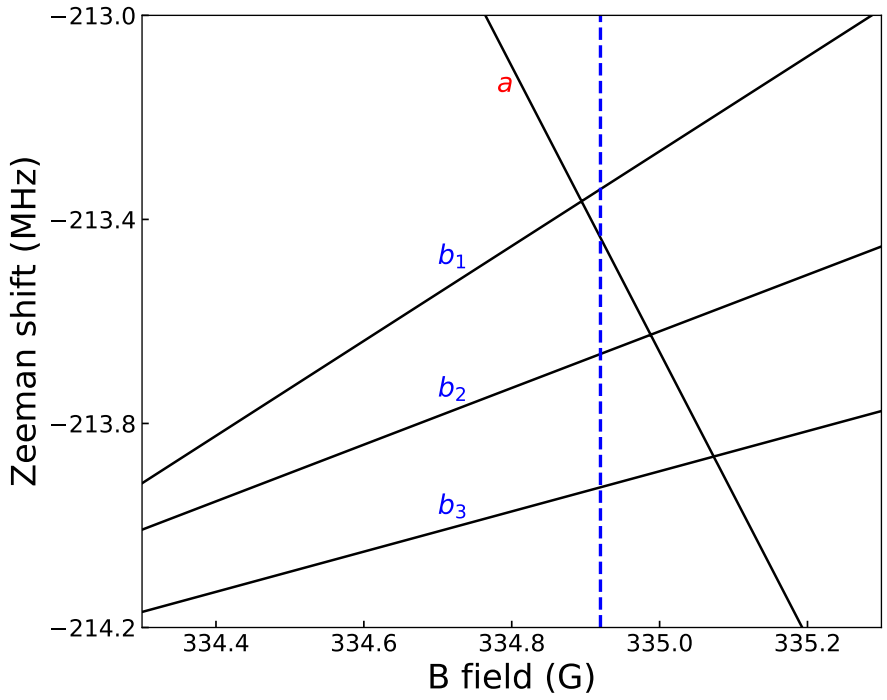

Figure 4-9: **Hyperfine structure of NaLi($a\Sigma^+$) in an external magnetic field.** a in red is the lower stretched hyperfine state of NaLi molecules. b_1, b_2 and b_3 in blue are other hyperfine states that are energetically close to state a near 334.92 G.

barrier due to the dipole-dipole interaction. However, due to the selection rules of the magnetic dipolar interaction ($|\Delta m_S| = 1$), a single spin flip cannot provide coupling between the near-degenerate hyperfine states of interest $|a\rangle$ and $|b_1\rangle$, which correspond to $m_S = 1$ and $m_S = -1$, respectively. Therefore, only weak higher order spinflips[5] or spin-rotation couplings exist. A loss rate constant higher than 10^{-10} cm^{3}s^{-1} requires a coupling strength on the order of 100 kHz at *long-range* (~ 100 nm)[6]. However, the strongest higher-order process has a coupling strength around 0.05 kHz. We therefore assume that we have a p-wave resonance enabled by high reflectivity at close range.

4.2.2 Three-state model of p-wave resonant scattering

To explain the observed Feshbach resonance, it is necessary to assume the presence of a *short-range* loss mechanism. A minimal model for such a mechanism involves a bound state (state 3) coupled to the open channels. The simplest model for the Feshbach resonance near state degeneracies that involves enhanced loss contains two open channels $|1\rangle$ and $|2\rangle$ coupled to a stable bound state, channel $|3\rangle$, where $|1\rangle$ is the incident scattering channel and $|2\rangle$ is the loss channel where particles are in a different internal state from $|1\rangle$ as depicted in Figure 4-10(a) [84]. This is analogous to an incident light coupled in at one side and coupled out at the other side of a single mode cavity. The transmission through a cavity as illustrated in Figure 4-10(b) is expressed in a simple form with the mirror coupling strengths $\bar{\gamma}_i$ as:

$$T = I\frac{\bar{\gamma}_1\bar{\gamma}_2}{(\omega_o - \omega)^2 + [(\bar{\gamma}_1 + \bar{\gamma}_2)/2]^2}. \tag{4.7}$$

Here, $\bar{\gamma}_i = -2\ln r_i/\tau_{RT}$ where r_i is the reflection coefficients of two mirrors, M_1 and M_2 and τ_{RT} is the round-trip time of the flux travelling in the cavity [7]. ω_0 is the

[5] At the position of the p-wave barrier ($R_b = 100$ nm), the interaction between two spins with magnetic moments $2\mu_0$, where μ_0 is the Bohr magneton, is $V^{mDD} = 0.052$ kHz. Higher order spinflip must involve an intermediate state $|k\rangle$, which is off-resonant by its Zeeman energy $\Delta_{ak} \simeq 1\mu_0 \times 300$ G $\simeq 400$ MHz. This further reduces the magnetic dipolar coupling between the open channels by the factor $(V^{mDD}/\Delta_{ak})^{-1} = 7.7 \times 10^6$ to much less than 1 mHz.

[6] The peak of the barrier is at $24^{1/4} \cdot R_{\rm vdw} \approx 7.8$ nm where the van der Waals length $R_{\rm vdw} = \frac{1}{2}\left(\frac{2\mu C_6}{\hbar^2}\right)^{1/4}$, and the outer turning point R_b is at 100 nm at 3.35 μK temperature.

[7] Transmission of flux through a Fabry–Pérot cavity with two mirrors, M_1 and M_2, normally has the Airy distribution expressed in terms of the incoming light flux, I, mirror reflec-

angular frequency of the cavity mode, ω is the angular frequency of the light, and I is the incoming flux[8].

Assuming that the input mode is either (nearly) resonant ($\omega - \omega_0 \ll \bar{\gamma}_1$) or far-off resonant ($\omega - \omega_0 \gg \bar{\gamma}_1$) with the Fabry-Perot cavity, tuning the coupling term $\bar{\gamma}_2$ now leads to a pronounced resonance-type feature in the Fabry-Perot transmission. For small $\bar{\gamma}_2$, transmission is proportional to $\bar{\gamma}_2$. However, for large $\bar{\gamma}_2$, the quality factor of the resonance is reduced, there is less and less built up of light inside the resonator, and the transmission decreases with $\bar{\gamma}_2$. For resonant coupling, the maximum transmission is at 100% ($T = I$) when $\bar{\gamma}_2 = \bar{\gamma}_1$ while for off-resonant coupling, the maximum transmission is at the reduced value by a factor of $\bar{\gamma}_1/(\omega - \omega_0)$ when $\bar{\gamma}_2 = 2(\omega - \omega_0)$ as shown in Figure 4-11(a). For on (or off) resonant coupling, the full width at half maximum (FWHM) of the transmission spectrum as a function of $\bar{\gamma}_2$ is expressed as FWHM $= 4\sqrt{2}\bar{\gamma}_1$ (of $2\sqrt{\omega - \omega_0}$), and the transmission line is narrower or sharper for smaller $\bar{\gamma}_1$ (or $\omega - \omega_0$) as shown in Figure 4-11(a) and (b).

We suggest that this mechanism is responsible for the observed resonance. For this, we assume the existence of a coupling between the incoming channel and a long-lived collision complex with energies that do not tune relative to one another with the magnetic field. This may seem to call for a remarkable coincidence, but molecule-molecule collisions are predicted to have a high density of resonances. The decay strengths of the channel $|3\rangle$ to the open channels γ_i, where $i = 1, 2$, are represented by the mirror coupling strengths $\bar{\gamma}_i$. The incoming scattering flux and collision loss of molecules are represented by the incoming flux of light and the transmission through the second mirror in the optical filter picture, respectively.

The transmission of a Fabry–Pérot exhibits the analytical result of the inelastic loss rate extended from the p-wave interaction model in Ref. [86] by Prof. Timur

tion and transmission coefficients, r_i and t_i, and single-pass phase shift that light exhibits, ϕ as $T = I\frac{t_1^2 t_2^2}{(1-r_1 r_2)^2 + 4 r_1 r_2 \sin^2\phi}$. This Airy distribution is well approximated to a Lorentzian spectral line shape near a resonance ($\omega \sim \omega_o$) for highly reflective cavities ($r_1^2 r_2^2 < 0.1$) as Eq.4.7 [85].

[8]The process is fully analogous to an harmonic oscillator with resonance ω_0 and damping rate $\bar{\gamma}_2$ driven at frequency ω via a frictional input coupling $\bar{\gamma}_1$. The ratio of the power dissipated via γ_2 to quarter of the nominal drive power (drive power at zero amplitude of the harmonic oscillator) is exactly given by Eq. 4.7. (see appendix)

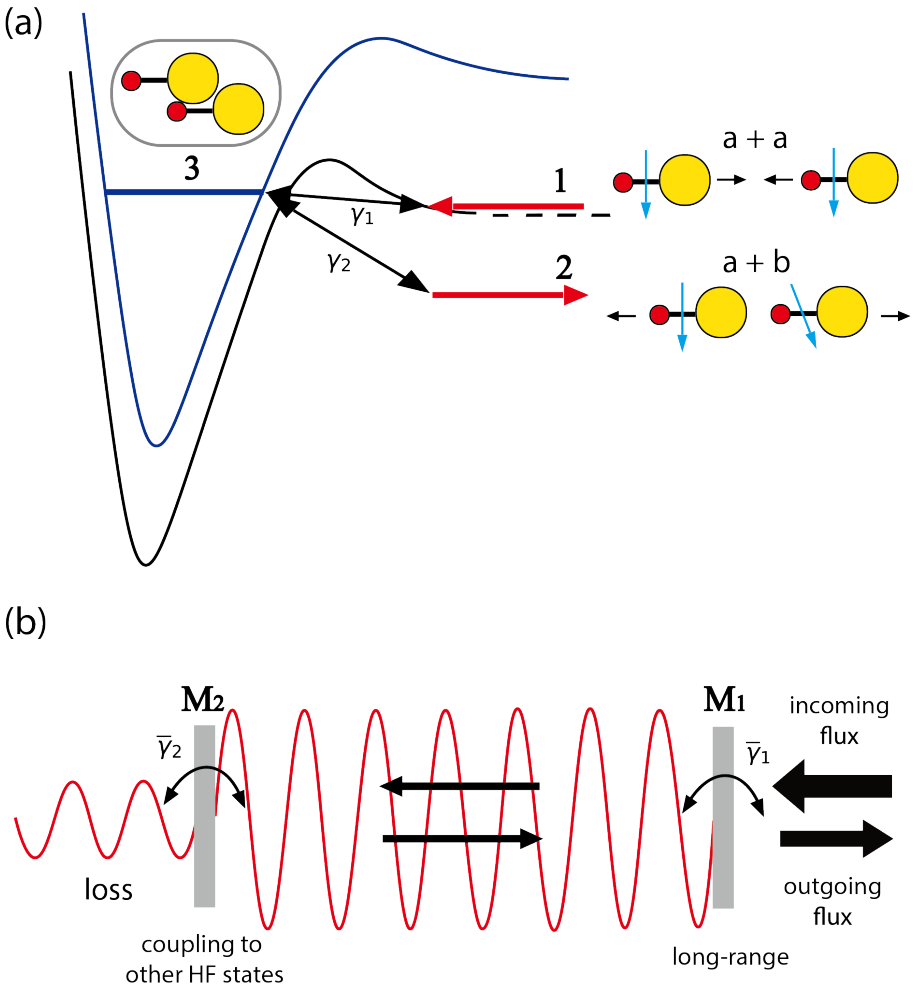

Figure 4-10: **a. Schematic of the resonance model with two open channels and a p-wave bound state trapped behind a centrifugal barrier.** Channel $|1\rangle$ and $|2\rangle$ are the open channels that are coupled to a closed channel $|3\rangle$, Channel $|1\rangle$ corresponds to the initial scattering channel where two NaLi molecules are in the lower stretched hyperfine state. Channel $|2\rangle$ corresponds to another open channel where molecules are in a different hyperfine state and energetically close to the incident scattering state. **b. Schematic of a Fabry–Pérot cavity.** Two mirrors M_1 and M_2 couple light into and out of the Fabry–Pérot resonator created by these mirrors with coupling strengths $\bar{\gamma}_i$. When the spacing between the mirrors is tuned to form a cavity mode that is resonant to the incoming light, transmission loss is enhanced by constructive interference of the light amplitude inside the cavity.

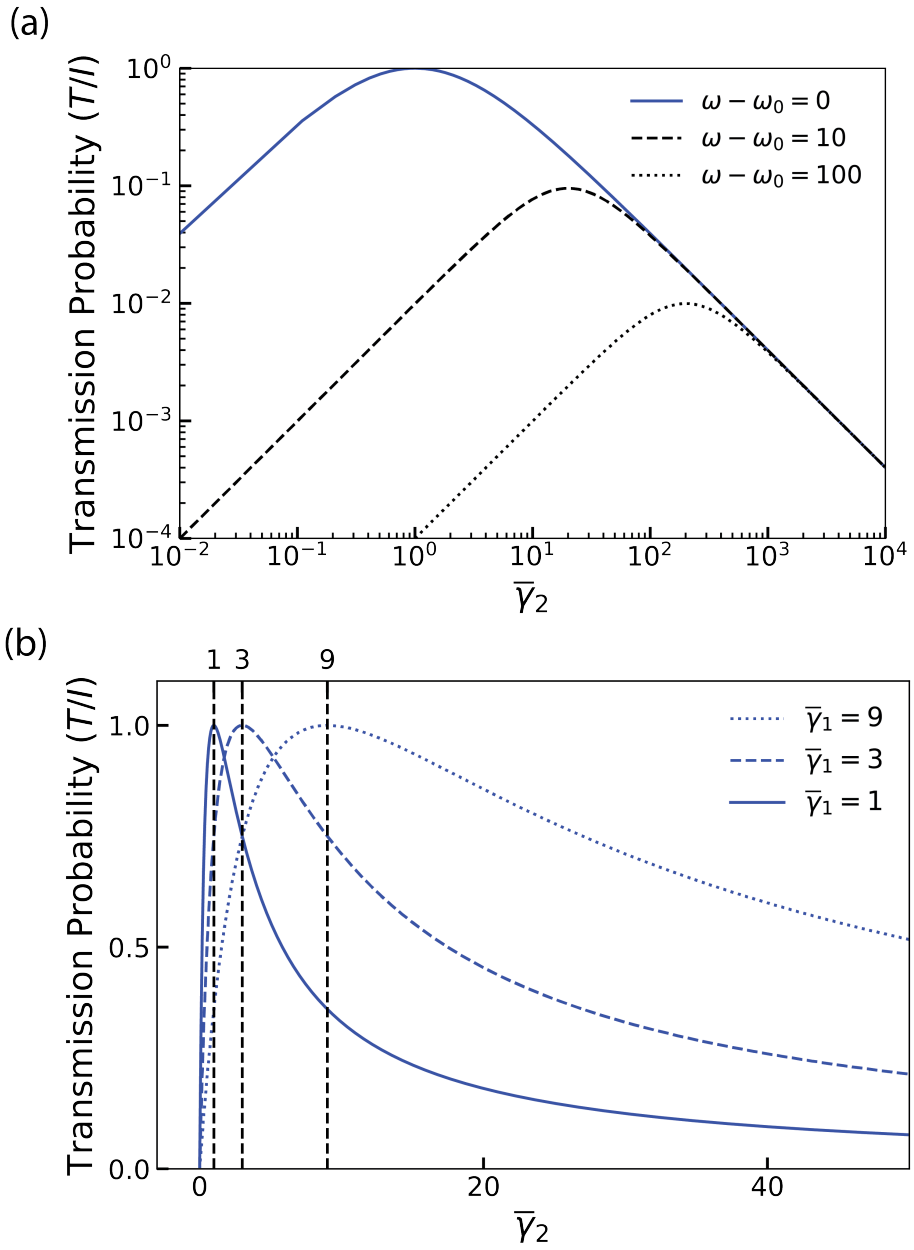

Figure 4-11: **a. Transmission probability of a cavity for different detunings,** $\omega - \omega_0$**.** For given coupling strengths of the first mirror, $\bar{\gamma}_1 = 1$ (in arbitrary units), transmission probability reaches unity for resonant coupling (blue) while maximizes to $\gamma_1/(\omega - \omega_0)$ for far off-resonant coupling (black). **b. Transmission probability of a resonant cavity for different first mirror coupling,** $\bar{\gamma}_1$**.** For given coupling strengths of the first mirror, $\bar{\gamma}_1$=1, 3 or 9, transmission probability reaches unity when $\bar{\gamma}_2 = \bar{\gamma}_1$ at a resonance. The line width of the transmission probability as a function of $\bar{\gamma}_2$ is narrower for smaller $\bar{\gamma}_1$.

Tscherbul, to whom we are grateful. The details of the derivation of the inelastic loss rate are included in Chap. C.4. The decay strengths from channel $|3\rangle$ to $|1\rangle$ ($|2\rangle$) are proportional to $\gamma_1 \propto \lambda_1 k^3$ ($\gamma_2 \propto \lambda_2 k'^3$) where λ_1 (λ_2) is the open-closed channel coupling and k (k') is the open channel wavevector. k^3 scaling of the decay strength comes from the threshold behavior of p-wave inelastic collision rate ($\propto k^2$) and the density of states of an open channel ($\propto k$). Using this scaling, we obtain the inelastic loss rate:

$$g_2 \propto \frac{k^{-1}\gamma_1\gamma_2}{(E-E_0)^2 + [(\gamma_1+\gamma_2)/2]^2} \tag{4.8}$$

where E is the incident energy and E_0 is the resonant energy. The numerator scales with k^2 instead of k^3, which is different in structure from equation (4.7)[9]. For particle collisions, the initial channel is in a single wavevector, so we see threshold p-wave scaling (k^2) for the input coupling. Inelastic decay from the closed channel proceeds into a continuum of states, which adds the third power of k for the density of states in that continuum. The experimentally observed k^2 dependence of the loss rate constant implies that the γ_1 never dominates the other terms in the denominator of g_2.

The model presented so far can explain a resonant enhancement of the loss as a function of the magnetic field. However, unlike in the case of spin-protected NaLi+Na [33] or non-reactive NaK+K Feshbach resonances [71] where the background loss rates were observed to be far below the universal values, NaLi+NaLi collision is reactive and the loss rate is saturated to near p-wave universal value ($y \sim 1$) at the background. Despite the fact, the loss rate is enhanced from the background by more than two orders of magnitude at the resonance. This peculiar enhanced loss feature was unexpected based on existing simple models for reactive collisions in molecular system. Collision of ultracold molecules is often described with the quantum-defect model used in Ref. [35] where quantum-defect parameter $y = (1-\sqrt{R})/(1+\sqrt{R})$ is directly related to the probability of incoming scattering flux being reflected back at short range R. This single-channel model was extended to describe the Feshbach resonance in collision between the NaLi molecule and Na atom and it was shown

[9] In the appendix, Eq. 4.8 is derived using a T matrix formalism.

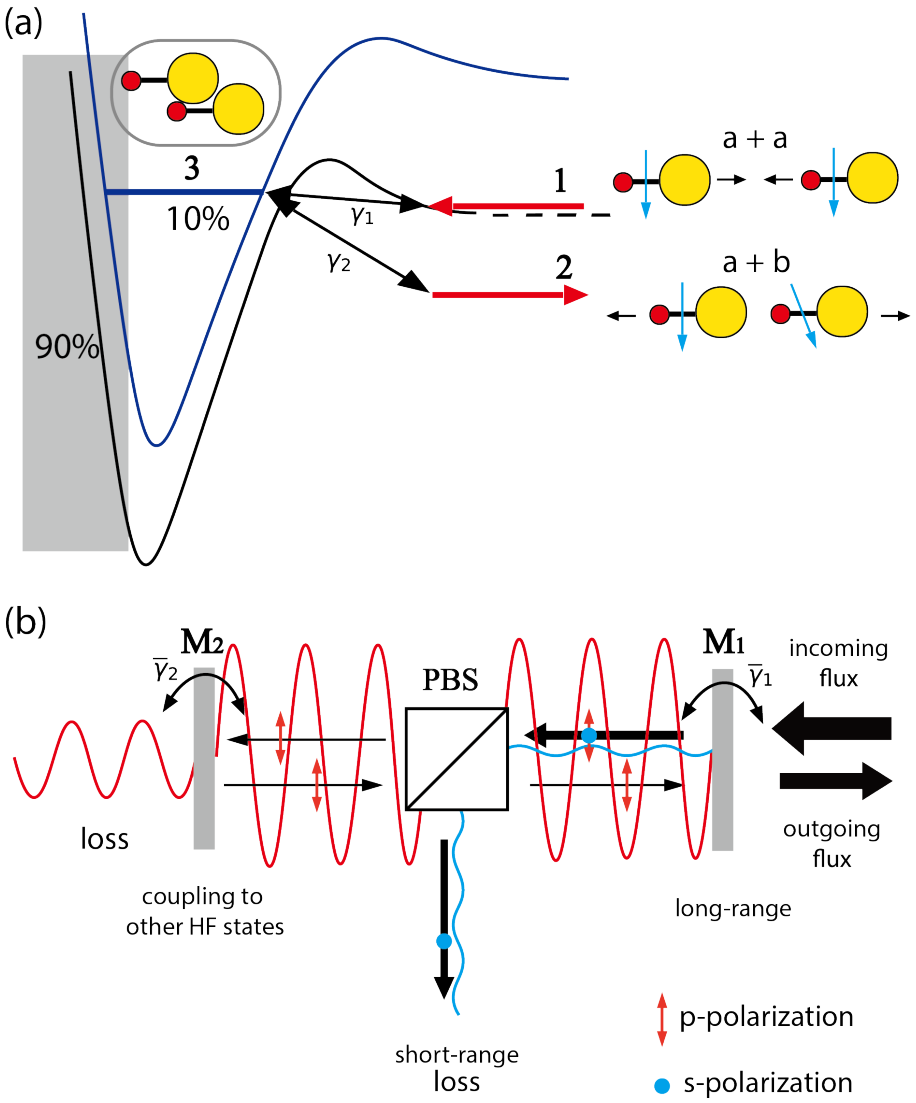

Figure 4-12: **a. Schematic of the resonance model with more than one orthogonal collisional path.** The incoming flux is split into two or more (orthogonal) components, one part (10%) has the resonant behavior, whereas the other part (90%) has non-resonant universal loss. **b. Schematic of a Fabry–Pérot cavity with a polarizing beam splitter (PBS).** Two mirrors form a resonator where p-polarization component of light amplitude is enhanced near a resonance. There are two paths for light to travel that are decoupled by a PBS. s-polarization component is reflected by the PBS and rejected.

that the scattering loss rate that is suppressed below the universal value by a factor of y can be enhanced by a Feshbach resonance at most above the universal value by $1/y$ [33]. With the extended single channel model, this large enhancement which requires $y \ll 1$ cannot be explained for NaLi+NaLi collisions which are reactive (2NaLi$\rightarrow$$Na_2$+$Li_2$+heat) and have $y \sim 1$.

One possible explanation is that the incoming flux is split into two or more (orthogonal) components, one part has the resonant behavior described above, whereas the other part has non-resonant universal loss (i.e. full transmission at short range) as depicted in Fig.4-12(a). For example, if one tenth of the scattering flux is coupled to the resonance, but its loss is enhanced by a factor of 1000, the total loss can be 100 times the universal limit. Outside the resonance, the majority of the flux (here assumed to be 90 %) provides the background loss near the universal rate. At resonance, the enhancement of the collision loss rate is inversely proportional to γ_2, which can be easily obtained from the Fabry–Pérot picture. With sufficiently weak open-closed channel couplings, large enhancement in collision loss is allowed despite close to unity loss of scattering flux that reaches short/close range.

This model can be pictured with a polarizing beam splitter(PBS) placed inside a Fabry–Pérot cavity as illustrated in Figure 4-12(b). As an extension of a simple cavity picture described earlier, the mirror M_1 represents quantum reflection by the long-range vdW potential, and M_2 represents the reflection of a stable bound state by coupling to another near degenerate hyperfine state. There are two optical paths which are decoupled at the PBS by the light polarization. Light that enters through the outer mirror M_1 has fraction, κ_p, of p-polarization which represents the long-lived bound state and passes through the PBS traveling toward mirror M_2. The other fraction, κ_s, corresponding to s-polarization represents short-lived states and is reflected at the PBS resulting in complete rejection. This perfect removal of the flux represents short/close range loss with unity probability ($y = 1$). The total loss of incoming flux is composed of the transmission of p-polarization through M_2 and the rejection of the s-polarization. Transmission through M_2, T_p is given as equation (4.7) with an extra factor κ_p and loss or s-polarization is given as $T_s = I\kappa_s\bar{\gamma}_1\tau_{RT}/2$.

When $\kappa_s \gg \kappa_p$ off-resonant transmission is dominated by the complete rejection of the s-polarization component of light, which is analogous to the molecular collision loss at the background being close to the universal value.

4.3 Discussion

The simplest model for an atom-like p-wave Feshbach resonance in the NaLi+NaLi collision assumes two resonances at a certain magnetic field. It is unusual to have three states that are near degenerate by coincidence, and one may suggest two possibilities: the existence of many stable bound states or a resonant bound state having the same magnetic moment as the initial state. The presence of dense stable bound states that may couple to the incident channel allows having Feshbach resonances all through while scanning the magnetic field. Similarly, if the magnetic moment and the energy of a stable bound state match that of the initial state, the Feshbach resonance is insensitive to magnetic field change, and the system will always be on resonance. For these cases, the energy difference between two hyperfine states is tuned by changing the magnetic field, while always being at a Feshbach resonance. The coupling of a bound state to a degenerate loss channel is tuned by an external magnetic field and allows the Feshbach resonance to be visible.

4.3.1 Collision complex lifetime

One may estimate the collision complex lifetime to be ~ 28.6 μs from the width of the scattering loss feature assuming that magnetic field scan sweeps through a p-wave Feshbach resonance like previously observed Feshbach resonances [10]. However, according to our model, the observed width may not reflect the width of the long-lived state but would depend instead on the ratio of coupling strengths for the two open channels. A more reliable estimate uses the classical round-trip time for a zero-energy particle in the combined centrifugal and van der Waals (vdW) potential,

[10] Difference in magnetic moment between the initial state and the bound state is assumed to be 1 Bohr magneton for this estimate.

which is equal to $\hbar/E_{\mathrm{vdW}}$. The vdW energy, $E_{\mathrm{vdW}} = \frac{\hbar^2}{2\mu}\frac{1}{R_{\mathrm{vdw}}^2}$ is determined by the vdW length $R_{\mathrm{vdw}} = \frac{1}{2}\left(\frac{2\mu C_6}{\hbar^2}\right)^{1/4} \approx 66a_0$, where μ is the reduced mass of two NaLi molecules and C_6 is the NaLi-NaLi long-range dispersion coefficient.

We consider the threshold limit with the molecule-molecule potential in Eq. 4.9 and a hard wall at an intermolecular distance $R = 0$.

$$V(R) = -\frac{C_6}{R^6} + \frac{l(l+1)\hbar^2}{2\mu R^2} \tag{4.9}$$

Classically, the round-trip time of a particle in this potential between two turning points, the inner turning point $R = R_i = 0$ and the outer turning point $R = R_o = (C_6\mu/\hbar^2)^{1/4}$, is given as:

$$\begin{aligned}
t_{RT} &= 2\int_0^{\bar{R}} \frac{1}{v} dR = 2\int_0^{\bar{R}} \frac{1}{\sqrt{\frac{2}{\mu}}\sqrt{\frac{C_6}{R^6} - \frac{\hbar^2}{\mu R^2}}} dR \\
&= 2\sqrt{\frac{\mu}{2C_6}} \int_0^1 \frac{\bar{R}^4}{\sqrt{\frac{1}{X^6} - \frac{1}{X^2}}} dX \\
&= \sqrt{2}\frac{\mu^{3/2} C_6^{1/2}}{\hbar^2} \int_0^1 \frac{1}{\sqrt{\frac{1}{X^6} - \frac{1}{X^2}}} dX \\
&= \sqrt{2}\frac{\mu^{3/2} C_6^{1/2}}{\hbar^2} \int_0^1 \frac{X^3}{\sqrt{1 - X^4}} dX \\
&= \sqrt{2}\frac{\mu^{3/2} C_6^{1/2}}{\hbar^2} \frac{1}{4} \int_0^1 \frac{1}{\sqrt{Y}} dY \\
&= \frac{\mu^{3/2} C_6^{1/2}}{2^{1/2}\hbar^2} = \frac{\hbar}{E_{\mathrm{vdw}}}.
\end{aligned} \tag{4.10}$$

Here, for the integrand on the first line of Eq. 4.10, substitute $X = R/\bar{R}$ and, for the integrand on the fourth line of the equation, substitute $Y = 1 - X^4$. For collisions between two identical NaLi molecules, this classical round trip time t_{RT} is approximately 5.67 ns.

The lifetime of the collision complex is finite due to losses resulting from coupling to other channels (nonzero mirror transmissions in the cavity model). The decay of a radiation mode of a cavity can be expressed as $I(t) = I_0 e^{-t/t_C}$. For reflectivity R, the

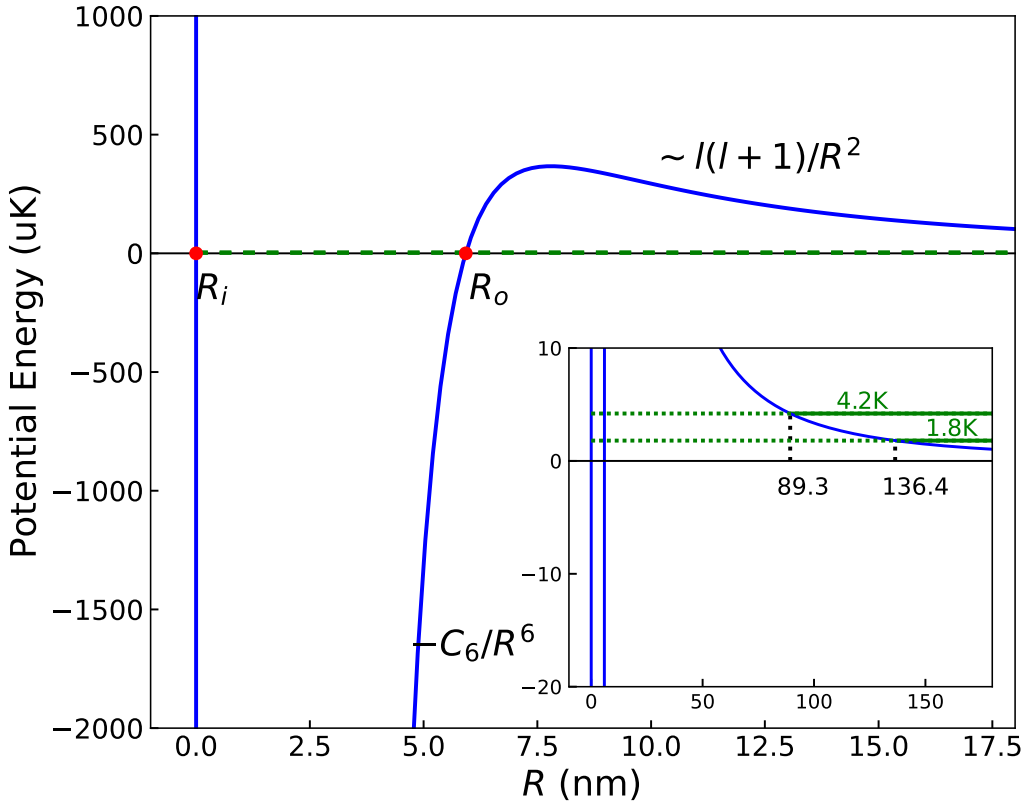

Figure 4-13: **Intermolecular potential of the NaLi ($a^3\Sigma^+$) molecules.** The p-wave centrifugal barrier is also shown. The upper and lower bounds on the experimental collision energies (4.2 μK and 1.8 μK) are marked by green horizontal lines. The outer turning points for these collision energies are R_b = 89.3 and 136.4 nm, respectively.

time to make N reflections is $t = Nt_{RT}$ where t_{RT} is the round trip time. After N reflections, the radiation intensity is $I_0 e^{-Nt_{RT}/t_C} = I_0 R^N$ which gives for the lifetime $t_c = \frac{t_{RT}}{ln(1/R)} \approx t_{RT}/(1-R)$. Therefore, the photon lifetime in a cavity is the round-trip time times the resonant enhancement divided by 4 [11]. Using this analogy and the observed loss enhancement factor of 230, we obtain an estimate for the lifetime of the complex of 320 ns.

We consider this to be a low estimate. Even if the p-wave resonance is at resonance, due to thermal broadening, the maximum loss enhancement is reduced by a factor $\hbar\gamma_1/k_B T \approx 0.1$ which implies a 10-fold longer lifetime (see chapter 4.3.2 for details). In addition, if we assume that the loss enhancement is possibly not 230, but 2300 for 10% of the incident flux (model with polarization beam splitter), then the lifetime would be another factor of ten higher and could be tens of microseconds.

4.3.2 Estimation of coupling strength γ_1

The coupling between channel 1 and channel 3, γ_1, can be estimated from the reflection coefficient for quantum reflection and the round trip time behind the p-wave barrier. For this, we use the optical cavity analogy, where the first mirror coupling is $\bar{\gamma}_1 = -4 \ln r_1/\tau_{RT}$. With the classical round trip time $t_{RT} \sim 5.67$ ns and p-wave quantum transmission T_p [12], one can estimate $\gamma_1 \approx -\ln(1-T_p)/t_{RT} \approx 2T_p/t_{RT} \approx 2\bar{a}_1\bar{a}^2k^3/\tau_{RT}$, where $\bar{a} = 4\pi R_{\mathrm{vdW}}/\Gamma(\frac{1}{4})^2$, $\bar{a}_1 = \bar{a}\Gamma(\frac{1}{4})^6$ and k is the collision wavevector. γ_1 is calculated as a function of the collision energy, as shown in Fig.4-14(a). We can confirm that γ_1 is much smaller than the thermal energy for our experimental conditions ($T \simeq 4.2$ μK) as shown in Fig.4-14(b).

[11] Quantum-defect parameter $0 \leq y \leq 1$ is related to the probability of irreversible loss of incoming scattering flux from the entrance channel due to chemical reaction or inelastic loss at short range. Based on the single-channel Fabry-Perot model introduced in chapter 1.2.2, $t_2 = 2\sqrt{y}/(1+y)$ where t_2 represents the short-range reflectivity of the scattering flux and the factor $1/y$ is the maximum enhancement possible above the universal limit with the tuneable round trip phase of the cavity. This relation leads to $t_2^2 = 1 - R = 4y/(1+y)^2 \approx 4y$ for $y \ll 1$.

[12] The short-range transition matrix T reduces to the quantum transmission coefficient t_1 at threshold [87] and the universal loss rate coefficient is directly related to the transition matrix as $K = 2g\frac{\pi\hbar}{\mu k}|T|^2$. By comparing this relation with the known universal loss rate coefficient [88], we obtain the probability of quantum transmission for p wave collision, $T_p \approx 2\bar{a}_1\bar{a}^2k^3$.

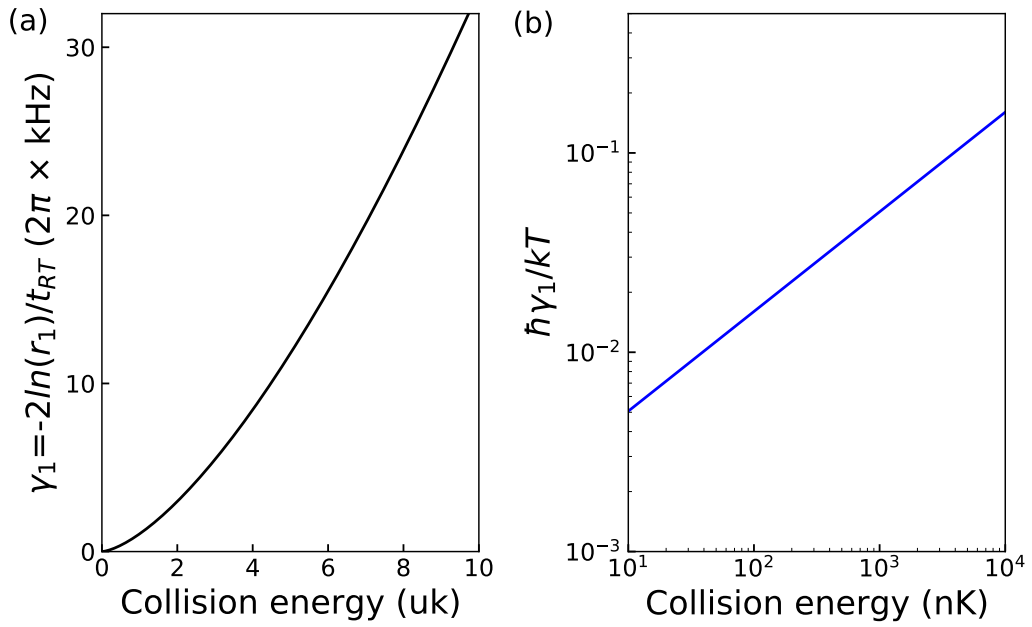

Figure 4-14: **The coupling between the incident open channel $|1\rangle$ with the p-wave bound state γ_1 as a function of collision energy.** a. γ_1 estimated by taking the classical round trip frequency $1/\tau_{RT}$ times minus the log of quantum reflection probability $|r_1|^2$ is plotted as a function of collision energy. b. The ratio between the estimated $\hbar\gamma_1$ and the thermal energy is plotted as a function of the collision energy.

4.3.3 Conclusion

The most surprising aspect of our results is the existence of a long-lived collision complex in NaLi+NaLi collisions, which allows barrier-free chemical reactions in all channels [29]. A long-lived complex is necessary for the existence of a high-Q resonance, such as we observed, independently of any detailed model. Magnetically tuneable resonances between two ground state molecules have yet to be discovered in other systems, although it has been uncovered that long-lived four-body collision complexes can form in other molecular systems including Rb_2Cs_2 [50] and K_2Rb_2 [40]. These other observations are most likely related to "sticky" collisions [37–39, 89] connected with a high density of states. These complexes are formed incoherently and lead to a loss rate at the universal rate. In contrast, an enhancement above the universal rate (as observed here) is only possible when the flux reflected at short range destructively interferes with the quantum reflected flux and, therefore, requires full phase coherence.

There exists a challenge of answering the question why Feshbach resonances are unseen in other systems. Feshbach resonances may be too dense, or intermediate collision complexes may undergo a fast loss from higher-body collision or photo-induced processes in other systems. In these cases, Feshbach resonances are almost impossible to detect, as they are unresolved or broadened, although they exist. So far, the Feshbach resonance in NaLi+NaLi collisions is unique. It is created by a long-lived collision complex which does not go through fast collision loss or photo-induced loss and it is detected by the coupling of the complex to a nearly degenerate hyperfine state.

Chapter 5

Magnetic trapping and cooling of molecules

Trapping ultracold molecules in conservative traps is essential for applications—such as quantum state-controlled chemistry, quantum simulations, and quantum information processing. These applications require high densities or phase-space densities. We report magnetic trapping of NaLi molecules in the triplet ground state at high density ($\approx 10^{11}$ cm^{-3}) and ultralow temperature (≈ 1 μK). Magnetic trapping at these densities allows studies on both atom-molecule and molecule-molecule collisions in the ultracold regime in the absence of trapping light, which has often lead to undesired photo-chemistry. We measure the inelastic loss rates in a single spin sample and spin-mixtures of fermionic NaLi as well as spin-stretched NaLi+Na mixtures. We demonstrate sympathetic cooling of NaLi molecules in the magnetic trap by radio frequency evaporation of co-trapped Na atoms and observe an increase in the molecules' phase-space density by a factor of ≈ 16.

5.1 Introduction

Ultracold molecules offer new opportunities for quantum state controlled chemistry [1, 2], for quantum simulations [3–5], and for quantum information processing [6–9]. For more than two decades, various methods were developed with the goal to trap

molecular samples at densities high enough to study molecular collisions. Using buffer gas cooling [90–93] or Stark or magnetic deceleration [94–96], molecules were trapped in magnetic traps in the temperature range of tens or hundreds of millikelvin. In only one case (O_2) were densities high enough (estimated at $\approx 10^{10}$ cm^{-3}) to observe molecular collisions [97]. Dipolar molecules can be trapped with electric forces. Collisions between CH_3F molecules were observed in an electrostatic trap at densities of 10^7 cm^{-3} [98], and elastic collisions of OH were observed in an electromagnetic trap at temperatures around 60 mK [99], though none of these studies reached the ultracold temperature regime. Ultracold laser-cooled molecules (in the 50 - 100 μK range) were transferred into magnetic traps at densities $\lesssim 10^6$ cm^{-3} [20,100], too low for the observation of intermolecular collisions.

Optical traps have the advantages of trapping non-magnetic molecules and providing tight confinement, which has allowed the study of collisions involving molecules created by ultracold assembly or direct laser cooling. For example, collisional resonances have been observed in atom-molecule mixtures [33,70,71] and between molecules [73] in optical traps. The disadvantage of optical traps is the small trapping volume and the presence of intense laser light, which can induce photochemistry. This has become a major concern recently after many experiments have found fast collisional losses even for non-reactive molecules, possibly due to "sticky collisions" connected with long-lived complexes [37–39,89,101]. Recent experiments to test these proposals suggest that optical traps can cause short lifetimes of molecules and are not truly conservative [40,50,102–104] emphasizing the need for "laser-free" trapping.

Here, we report magnetic trapping of triplet NaLi molecules in the rovibrational ground state with high density ($\approx 10^{11}$ cm^{-3}) and ultracold temperature ($\approx 1\mu$K). The typical density is a factor of 10^5 higher compared to previous experiments with magnetically trapped ultracold molecular gases. Inelastic losses are detected in single-component and in spin-mixtures of a fermionic NaLi molecular gas.

Another major long-standing goal has been magnetic trapping of molecules together with atoms for sympathetic cooling of molecules to achieve higher molecular densities or phase-space densities [105,106]. Magnetic co-trapping of NH and N [107],

and more recently of CaF and Rb [108] and O_2 with Li atoms [109] has been achieved. However, so far only inelastic collisions were observed [107,108], with atomic densities far too low for sympathetic cooling.

Here we demonstrate sympathetic cooling of molecules in a magnetic trap. We use a spin-stretched NaLi+Na mixture, which had been studied in ref. [72] and observe an increase in the phase-space density (PSD) of the molecular gas by more than an order of magnitude after radio frequency (RF) evaporation of Na atoms.

5.2 Experimental methods

The experiments are carried out with NaLi molecules in the triplet ground state ($a^3\Sigma^+$, $v = 0$, $N = 0$) created by means of ultracold assembly of Na and Li atoms in the lowest-energy Zeeman states following the procedure described in ref. [33,72,73]. The procedure has been improved so that the Na/Li mixture is transferred directly from the initial magnetic trap into a 1550 nm 1D optical lattice without the use of extra optical traps (previous configurations required a 1064 nm optical dipole trap and a 1596 nm 1D optical lattice). After 0.4 seconds of forced evaporation of the atom mixture, 10^5 molecules at 1.8 μK temperature are formed in the maximally stretched low-field seeking hyperfine state ($|F_1 = 5/2, F = 7/2, m_F = 7/2\rangle$) using Feshbach association and STIRAP transfer to the triplet ground state. Here, F is the total angular momentum including electron and nuclear spins, m_F is the F projection to the quantization axis, and F_1 is a good quantum number in the zero-field limit combining the electron spin and the Na nuclear spin [13].

After ramping down the bias field from ~ 745 G, where the association of molecules occurs, to a low magnetic bias field in 20 ms, molecules are transferred from the optical lattice to an Ioffe-Pritchard magnetic trap with a bias field of 0.56 G in 100 ms. The molecules are trapped for various hold times and transferred back to the optical lattice in 100 ms for detection at high field (~ 745 G). The number of molecules is counted by absorption imaging of the Li atoms from the recaptured and dissociated molecules. The experimental sequence is illustrated in Figure 5-1. The transfer efficiency of

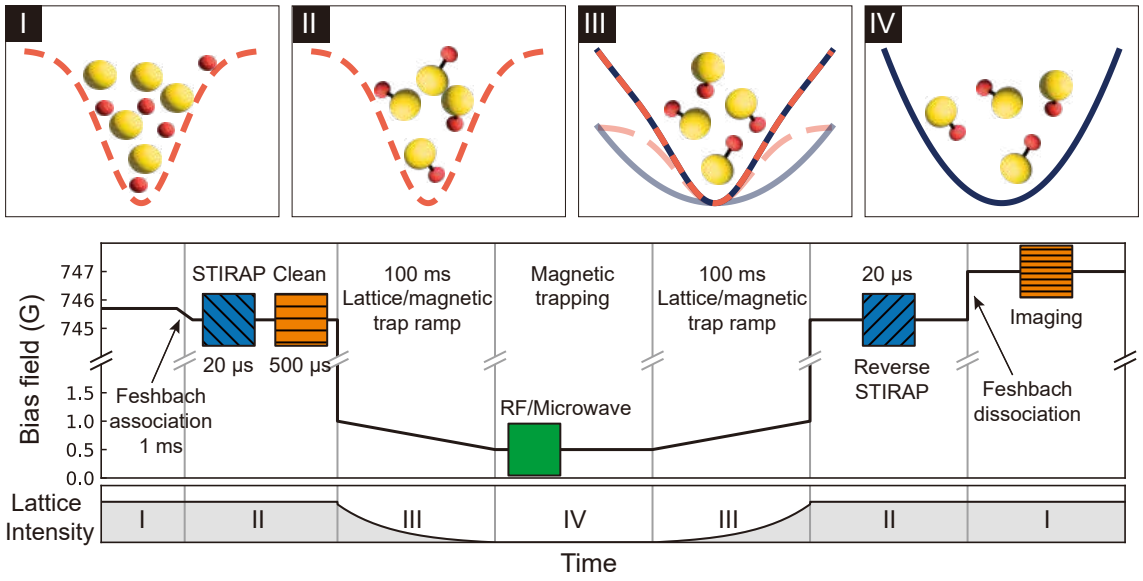

Figure 5-1: Top figures are the illustration of particles confined in different traps. I. Na/Li mixture is confined in a 1D lattice potential (indicated with orange dashed line). II. NaLi molecules are trapped in the same 1D lattice. III. NaLi molecules are trapped in a hybrid trap created by a 1D lattice and a magnetic trap (indicated with black line). IV. Molecules are purely confined by a magnetic trap. The middle plot is the experimental sequence to produce and isolate NaLi molecules (time axis is not to scale). Molecules are formed via Feshbach formation and STIRAP in a 1D lattice, and the free atoms are removed using resonant light pulses at high field. After the magnetic bias field is dropped to low field, the lattice is ramped down and the magnetic trap is turned on in 100 ms. In the magnetic trap RF or microwave is applied to the molecules for thermometry or preparation of molecular spin mixtures. For detection, molecules are transferred back to the 1D lattice, the molecule formation process is reversed, and the dissociated free atoms are imaged. The bottom row is the lattice intensity as a function of time along with particle and trap type indicated using index I-IV.

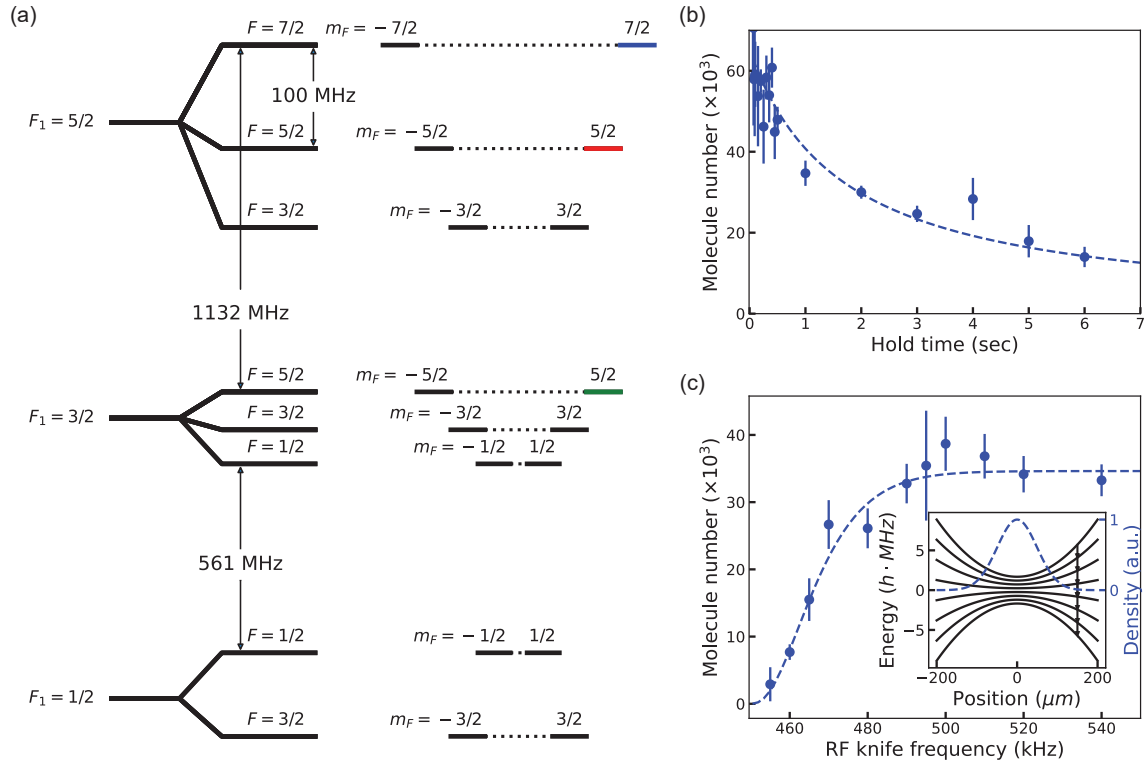

Figure 5-2: (a) Rovibrational ground state energy level diagram of NaLi molecules in the triplet potential ($a^3\Sigma^+$) at zero bias field. Molecules are initially formed in the low field seeking spin-polarized hyperfine state ($|F_1 = 5/2, F = 7/2, m_F = 7/2\rangle$) indicated in blue. States in red and green are the other hyperfine states used for creating molecular spin-mixtures. (b) Number decay of low field seeking spin-polarized NaLi molecules ($|F_1 = 5/2, F = 7/2, m_F = 7/2\rangle$) in a magnetic trap. (c) The number of molecules left in the magnetic trap as a function of the RF-knife frequency. The dashed line is a fitting function for a temperature of 1.06 μK. The inset is the m_F energy levels of NaLi in $|F_1 = 5/2, F = 7/2\rangle$ near the center of a magnetic trap (in black lines). Exemplary density profile of molecules in the top hyperfine state is in blue dashed line.

molecules from the optical trap to the magnetic trap is close to 100 % whereas the recapture efficiency back to the optical trap is only about 50 % due to a smaller optical trap volume.

We investigate mainly three types of inelastic collisions: p-wave collisions in single spin component molecular gas, s-wave collisions in molecular spin-mixutures, and low-reactivity atom-molecule collisions i.e. NaLi+Na in the low field seeking spin-stretched states. For this, molecules in the hyperfine state $|F_1 = 5/2, F = 7/2, m_F = 7/2\rangle$ are held by the magnetic trap in the single spin state, or together with molecules in another hyperfine state or Na atoms in the upper spin-stretched state ($|F = 2, m_F = 2\rangle$). The energy level diagram of NaLi molecules in the triplet ground state is shown in Fig. 5-2(a). We focus on the number decay of NaLi in state $|F_1 = 5/2, F = 7/2, m_F = 7/2\rangle$ in the magnetic trap.

5.2.1 Decay models

The differential equations that describe the decay of molecules in the upper stretched state in the presence of another type of particle i are given as:

$$\dot{N}_{\mathrm{NaLi}} = -(K_i/V_{\mathrm{ov}})N_i N_{\mathrm{NaLi}} - (\beta_0/V_{\mathrm{eff,NaLi}})N_{\mathrm{NaLi}}^2 \tag{5.1}$$

$$\dot{N}_i = -(K_i/V_{\mathrm{ov}})N_{\mathrm{NaLi}} N_i - (\beta_i/V_{\mathrm{eff},i})N_i^2, \tag{5.2}$$

where N_{NaLi} represents the number of NaLi in the upper stretched state and N_i represents the number of particles of type i that are magnetically trapped with the molecules. Here, V_{ov} is the volume of the regime where the i-type particles overlap with the upper stretched molecules, $V_{\mathrm{eff},i}$ is the mean volume filled with i particles, β_0 (β_i) is the two-body molecular (particle i) loss rate coefficient, and K_i is the loss rate coefficient for the collisions of i +NaLi pairs.

We solve the given differential equations for three different conditions: $N_i = 0$, $N_i \approx N_{\mathrm{NaLi}}$, and $N_i \gg N_{\mathrm{NaLi}}$. The two-body loss in the single spin component ($|F_1 = \frac{5}{2}, F = \frac{7}{2}, m_F = \frac{7}{2}\rangle$) molecular gas, i.e. $N_i = 0$, is described by the second term

of Eq. 5.1 only. The analytical solution is given as $N_{\mathrm{NaLi}}(t) = N_0 \frac{1}{1+\beta_0 N_0 t/V_{\mathrm{eff}}}$ [1], where N_0 is the initial NaLi number.

For collisions in two-component mixtures that we study experimentally, the decay of the NaLi number is well described by Eq. (5.1) and (5.2) with the second terms approximated to zero since $\beta_0, \beta_i \ll K_i$. With this approximation, the analytic solution becomes[2]:

$$N_{\mathrm{NaLi}}(t) = \frac{D}{Ce^{D\Gamma t} - 1} \tag{5.3}$$

$$N_i(t) = -\frac{D}{\frac{1}{C}e^{-D\Gamma t} - 1} \tag{5.4}$$

where $\Gamma = K_i N_i(0)/V_{\mathrm{ov}}$ is the loss rate, $C = N_i(0)/N_{\mathrm{NaLi}}(0)$, and $D = N_i(0) - N_{\mathrm{NaLi}}(0)$. In a regime where $N_i(0) \gg N_{\mathrm{NaLi}}(0)$ in a two-component mixture, $N_i(t)$ can be approximated to $N_i(0)$ throughout and Eq. 5.3 is reduced to a simple exponential decay, $N_{\mathrm{NaLi}}(t) = N_0 e^{-K_i t/V_{\mathrm{ov}}}$. In the experiment, the Na atom number was more than a factor of 10 larger than the NaLi molecule number, so the decay of NaLi is well described by the exponential function.

Now we discuss the volumes V_{eff} and V_{ov} in Eqs. (5.1) and (5.2). Assuming a harmonic trap, one obtains:

$$\begin{aligned} V_{\mathrm{eff},i} &= \bar{\omega}_i^{-3}(4\pi k_B T_i/m_i)^{3/2} \\ V_{\mathrm{ov}} &= \frac{N_i N_{\mathrm{NaLi}}}{\int dV\, n_i n_{\mathrm{NaLi}}} \\ &= \bar{\omega}_{\mathrm{Na}}^{-3}\left[\left(\frac{2\pi k_B T_i}{m_i}\right)\left(\frac{\mu_{\mathrm{Na}}}{\mu_i} + \frac{\mu_{\mathrm{Na}}}{\mu_2}\frac{T_{\mathrm{NaLi}}}{T_i}\right)\right]^{\frac{3}{2}}, \end{aligned}$$

where the geometric mean of the sodium trap angular frequencies, $\bar{\omega}_{\mathrm{Na}} = (\omega_x\omega_y\omega_z)^{1/3}$

[1] In order to account for the additional loss while and after the transfer back to an optical trap, the $\alpha\tau$ term should be added to $\beta_0 N_0 t$. α is the ratio of decay rate in the optical trap to that in the magnetic trap and τ is the time molecules spend in the optical trap. Although the optical trap is tighter than the magnetic trap, since only 50% of the molecules are transferred back to the optical trap, α is typically not much greater than 1. In addition, τ is short (effectively $\approx$ 50 ms under maximum trap depth). Therefore, this additional loss term can be neglected under the experimental conditions.

[2] The $\alpha\tau$ term should be added on top of $D\Gamma t$ in Eq. 5.1 in order to account for the additional loss while and after the transfer back to an optical trap. Similarly, this additional loss term can be neglected under the experimental conditions.

$= 2\pi\times(282\cdot282\cdot14.8)^{1/3}$ Hz $\approx 2\pi \times 106$ Hz. Here, n_i is the density, T_i is the temperature, m_i is the mass and μ_i is the magnetic moment of an i particle. The geometric mean of the trap angular frequencies for NaLi in the upper stretched state, $\bar{\omega}_{\rm NaLi}$=$\bar{\omega}_{\rm Na}\cdot(m_{\rm Na}/m_{\rm NaLi})\cdot(\mu_{\rm NaLi}/\mu_{\rm Na})$, where the mass ratio, $m_{\rm NaLi}/m_{\rm Na} \approx 29/23$ and the magnetic moment ratio, $\mu_{\rm NaLi}/\mu_{\rm Na} \approx 2$.

5.2.2 Thermometry

We determine the temperature of a NaLi gas in the magnetic trap from its density profile. To find this, we let NaLi molecules in the $|F_1 = 5/2, F = 7/2, m_F = 7/2\rangle$ hyperfine state undergo radio frequency (RF) induced spin-flips in a magnetic trap that has a trap bottom of 0.56 G. RF is swept from some high value (> 600 kHz) to a lower value f in 600 ms [3]. This RF can induce 7 simultaneous transitions, by one quanta of m_F each, from state $|F_1 = 5/2, F = 7/2, m_F = 7/2\rangle$ to $|F_1 = 5/2, F = 7/2, m_F = -7/2\rangle$, allowing the molecules to escape from the trap. The number of molecules left in the magnetic trap is determined by the final RF value (RF-knife frequency). The maximum possible energy of the molecules is $A = \frac{7}{2}h(f - f_0)$ where f is the RF-knife frequnecy and f_0 is the transition frequency from $|F_1 = 5/2, F = 7/2, m_F = 7/2\rangle$ to $|F_1 = 5/2, F = 7/2, m_F = 5/2\rangle$ at the bottom of the magnetic trap.

Near the center, the magnetic field of the Ioffe-Pritchard magnetic trap varies quadratically with the distance from the origin. The states of the particles are enumerated by a set of quantum numbers $[n_x, n_y, n_z]$ in a general three-dimensional harmonic trap potential $V(x, y, z) = \frac{1}{2}m(\omega_x^2x^2 + \omega_y^2y^2 + \omega_z^2z^2)$ and the energy of a particular state is given by $\epsilon = \hbar(n_x\omega_x + n_y\omega_y + n_z\omega_z) + \epsilon_0$, where $\epsilon_0 = \frac{1}{2}\hbar(\omega_x + \omega_y + \omega_z)$ is the zero-point energy in this harmonic trap. For $\epsilon \gg \epsilon_0$, the number of states with energy between ϵ and $\epsilon + d\epsilon$ is estimated as $g(\epsilon)d\epsilon$, with $g(\epsilon) = \frac{\epsilon^2}{2\hbar^3\bar{\omega}^3}$ where $\bar{\omega} = (\omega_x \cdot \omega_y \cdot \omega_z)^{1/3}$ is the geometric mean of the trap angular frequencies. Therefore,

[3] The thermometry is carried out when there are only NaLi molecules in the upper-stretched state, and s-wave collisions are impossible. Therefore, 600 ms is far too short for molecules to thermalize during the RF sweep.

the particle number with energy between 0 and A is

$$N(A) = N_{\text{tot}} \frac{\int_0^A g(\epsilon) e^{-\beta\epsilon} d\epsilon}{\int_0^\infty g(\epsilon) e^{-\beta\epsilon} d\epsilon} \tag{5.5}$$

$$= \frac{N_{\text{tot}}}{2} \left[e^{-\beta A} \{ -\beta A \cdot (\beta A + 2) - 2 \} + 2 \right] \tag{5.6}$$

where $\beta = (k_B T)^{-1}$ is the Boltzmann factor. Fitting the data in Fig. 5-2(c), which is the NaLi number as a function of the RF-knife frequency f, to Eq. 5.6 provides the estimate for the molecule temperature of 1.06 ± 0.18 μK.

For the temperature estimation of NaLi in the other hyperfine state either state $|F_1 = 5/2, F = 5/2, m_F = 5/2\rangle$ or state $|F_1 = 3/2, F = 5/2, m_F = 5/2\rangle$ of a molecular spin mixture, we assume that the average total kinetic energy and the average total potential energy are equal in the harmonic trap by the virial theorem. After molecules are transferred from the upper-stretched state to the other hyperfine state, the average potential energy of NaLi is reduced by the magnetic moment ratio $\mu_{\text{NaLi}^*}/\mu_{\text{NaLi}}$ momentarily, while the kinetic energy remains the same. Here, NaLi represents the upper stretched state and NaLi* indicates the other hyperfine state. The average potential and kinetic energy redistribute to be equal. With this simple model, the temperature is estimated as $T_{\text{NaLi}^*} \approx T_{\text{NaLi}}(\mu_{\text{NaLi}^*}/\mu_{\text{NaLi}} + 1)/2$. The Na temperature is measured directly from the time-of-flight (TOF) absorption imaging out of the magnetic trap at low field.

5.3 Results

5.3.1 p-wave collisions between molecules

We first observe p-wave inelastic collisions of NaLi in the upper spin-stretched state. The number of molecules in the magnetic trap decays by more than 50% starting from 6×10^4 in a few seconds, as shown in Fig. 5-2(b), while the typical vacuum lifetime is greater than 20 seconds. The molecular temperature is 1.06 ± 0.18 μK, which is measured by applying an RF-knife of various frequencies as shown in Fig. 5-2(c).

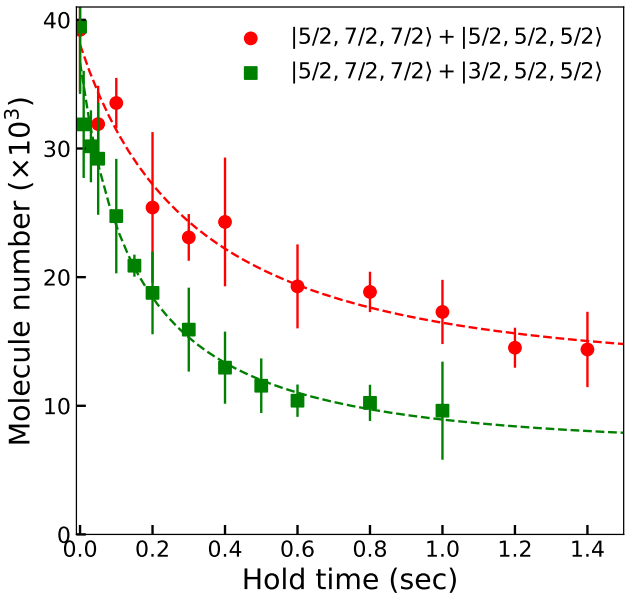

Figure 5-3: Number decay of low field seeking spin-polarized NaLi molecules ($|F_1 = 5/2, F = 7/2, m_F = 7/2\rangle$) when magnetically trapped together with molecules in state $|F_1 = 5/2, F = 5/2, m_F = 5/2\rangle$ (in red circles) and with molecules in state $|F_1 = 3/2, F = 5/2, m_F = 5/2\rangle$ (in green squares).

The initial density is 1.7×10^{11} cm^{-3}—a factor of 10^5 greater than the experiments carried out in ref. [20, 100]. The loss rate coefficient is calculated as $(3.6 \pm 1.4) \times 10^{-12}$ (cm^3/s)($\mathrm{T_{NaLi}}/\mu$K) from the best fit to a two-body loss model described above. Within the uncertainty, this value is consistent with the value reported in ref. [33], which was measured near 980 G.

5.3.2 *s*-wave collisions between molecules

Next, we observe *s*-wave inelastic collisions by creating a spin-mixture of molecules in two different hyperfine states. A transition from $|F_1 = 5/2, F = 7/2, m_F = 7/2\rangle$ to $|F_1 = 5/2, F = 5/2, m_F = 5/2\rangle$ is driven by 100 MHz RF until the molecules form a near 50/50 spin mixture in the magnetic trap. Similarly, the mixture of $|5/2, 7/2, 7/2\rangle$ and $|3/2, 5/2, 5/2\rangle$ is prepared with a 1133 MHz microwave drive. Due to magnetic field inhomogeneity, the superposition of the two spin states decoheres within $T_2 \approx \frac{h}{\Delta\mu \cdot \delta B} \lesssim 500\mu$s, where $\Delta\mu$ is the magnetic moment difference between the two hyperfine states, and $\delta B \approx 10$ mG is the magnetic field inhomogeneity, during

and after an approximate $\pi/2$ pulse. The loss rate coefficients are calculated to be $(3.6 \pm 1.5) \times 10^{-11}$ cm^3/s and $(1.1 \pm 0.4) \times 10^{-10}$ cm^3/s respectively by fitting the data in Fig. 5-3 to a loss model described in the Methods section. These values are significantly lower than the s-wave universal value estimated using the approximate NaLi-NaLi long-range dispersion coefficient ($K_{l=0}^{univ} = 1.85 \times 10^{-10}$ cm^3/s).

5.3.3 Collisions between NaLi and Na

For atom-molecule collisions, we load together about 4×10^5 Na atoms and about 4×10^4 NaLi in the upper stretched hyperfine states into the magnetic trap. The temperature of the atoms is $\approx 2\mu$K from the TOF imaging. Since the Na number is much greater than the NaLi number we fit the molecule decay in Fig. 5-4(a) to a simple exponential decay curve. The measured loss rate constant $\beta = (6.3 \pm 1.4) \times 10^{-12}$cm^3/s is about a factor of 30 lower than the universal value (1.72×10^{-10}cm^3/s) which is well known for this system [74].

5.3.4 Sympathetic cooling of NaLi with Na

With the low-reactivity atom-molecule mixture, we demonstrate sympathetic cooling of molecules in the magnetic trap. Here, via RF controlled evaporation, we have independent control over the molecule and atom trap depths. It is possible to cool spin-polarized NaLi using collisions with Na, also spin-polarized in the same direction as NaLi, because NaLi has a favorable ratio of elastic to inelastic collisions γ with Na. At high field, it was measured to be $\gamma \approx 300$ [72]. After loading the atom-molecule mixture into the magnetic trap, we slowly evaporate Na atoms out of the trap with a microwave sweep. We perform a microwave sweep to remove all Na from the magnetic trap in 1 second, which is chosen to be similar to the lifetime of NaLi with Na and longer than the thermalization time among Na ($\sim$ 670 ms) and between Na and NaLi ($\sim$ 90 ms) (see Chap.5.3.5 for details).

We compare the temperature of NaLi after the Na evaporation to that of NaLi from an identical mixture loaded to the magnetic trap but with sudden removal of Na using

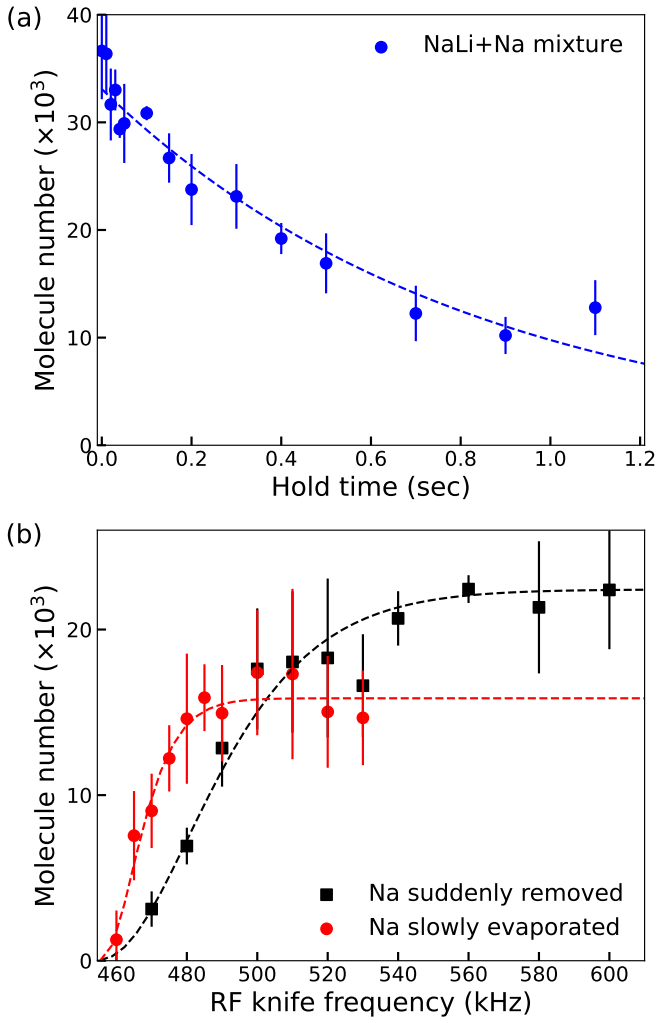

Figure 5-4: (a) Molecule number as a function of hold time in a magnetic trap when trapped together with Na. The atom-molecule mixture is in the low-field seeking spin-stretched state. Na number is about 4×10^5 and the temperature is $\approx 2\mu$K. (b) Molecule number as a function of RF-knife frequency. Data in red circles is with slow evaporation of Na and data in black squares is with Na suddenly removed after loading into a magnetic trap. The density profile obtained from the red (black) data implies a temperature of 0.8(1) μK (2.3(3) μK). The fits in dashed lines use a fit function described in Chap.5.2.2.

a resonant light pulse after the loading. The two temperatures are estimated by the RF-knife frequency scan described earlier (Fig.5-4(b)). Evaporation of Na leads to a temperature of NaLi molecules of 0.8(1) μK, substantially lower than the temperature without the evaporation (2.3(3) μK), while the molecule number is decreased by 30%. This corresponds to an increase in PSD of the molecular gas by a factor of ≈ 16.

5.3.5 Inelastic collision and thermalization rates

To investigate the limiting factor for sympathetic cooling, we compare the three relevant time scales in a Na+NaLi mixture: the inelastic collision and thermalization rates between Na and NaLi, and the thermalization rate among Na atoms. The experiment was done with about 33×10^3 NaLi and 420×10^3 Na at a temperature of $\approx 2\mu$K in a magnetic trap. The initial densities of Na and NaLi are 1.25×10^{11} cm^{-3} and 3.3×10^{10} cm^{-3}, respectively. The initial inelastic collision rate is experimentally measured to be $\Gamma_{\mathrm{inel}} \approx 1.2$ s^{-1} as shown in Fig. 5-4(a).

Next, we estimate the thermalization rate between Na and NaLi. In a mass-imbalanced system, the factor $3/\xi$ quantifies the approximate average number of collisions per particle required for thermalization, where $\xi = 4m_{\mathrm{Na}}m_{\mathrm{NaLi}}/(m_{\mathrm{Na}} + m_{\mathrm{NaLi}})^2 \approx 0.987$ [72,110]. Thus, the relation between the thermalization rate and the elastic scattering rate is given by $\Gamma_{\mathrm{th}} \approx \Gamma_{\mathrm{el}}/(3/\xi)$. In our system, where the particle number is largely imbalanced, we can write the thermalization rate as

$$\Gamma_{\mathrm{th}} \approx \frac{(N_{\mathrm{Na}}/V_{\mathrm{ov}})\sigma_{\mathrm{el}}v_{\mathrm{rel}}}{3/\xi}, \tag{5.7}$$

where $N_{\mathrm{Na}}/V_{\mathrm{ov}}$ is the average density of Na atoms seen by NaLi molecules, σ_{el} is the elastic scattering cross-section and the relative velocity $v_{\mathrm{rel}} = \sqrt{\frac{8k_B}{\pi}\left(\frac{T_{\mathrm{Na}}}{m_{\mathrm{Na}}} + \frac{T_{\mathrm{NaLi}}}{m_{\mathrm{NaLi}}}\right)}$. The s-wave elastic scattering cross-section between Na and NaLi is given by $\sigma_{\mathrm{el}} \approx 4\pi a^2$, where a is the scattering length. Using an approximate value for the scattering length $a = 263(66)a_0$, where a_0 is the Bohr radius [72], the thermalization rate is estimated to be ≈ 11 s^{-1} .

Similarly, the thermalization rate among Na is given as $\tilde{\Gamma}_{\mathrm{th}} = \frac{(N_{\mathrm{Na}}/V_{\mathrm{eff,Na}})\tilde{\sigma}_{\mathrm{el}}\tilde{v}_{\mathrm{rel}}}{3} \approx$

1.5 s^{-1}, where the s-wave elastic scattering cross-section between Na atoms $\tilde{\sigma}_{\rm el} \approx 8\pi\tilde{a}^2$, where the scattering length between Na atoms $\tilde{a} = 85(3)a_0$ [111]. The relative velocity $\tilde{v}_{\rm rel} = \sqrt{\frac{16k_B}{\pi}\frac{T_{\rm Na}}{m_{\rm Na}}}$. We see that $\Gamma_{\rm inel} \sim \tilde{\Gamma}_{\rm th} \ll \Gamma_{\rm th}$, and the sympathetic cooling of NaLi is limited by the slow Na thermalization rate.

5.4 Summary

In summary, we have shown magnetic trapping of molecules with a factor of 10^5 higher density compared to ultracold molecules previously studied in a magnetic trap. We have measured the inelastic collision rates for two selected molecular spin mixtures and a spin-stretched Na+NaLi mixture that serve as prototypes for future studies on state-dependent molecule-molecule and atom-molecule collisions in the magnetic trap. Quantitative analysis of molecular collisions in the magnetic trap is much simpler than in optical traps, because the magnetic trap is well-approximated by a harmonic potential whose trap frequencies are determined by molecule magnetic moments, which are typically well known. In contrast, optical traps can be highly anharmonic near the top of the trap, and ratios of trap frequencies (unless directly measured) can be difficult to determine because of the unknown molecular ac polarizability.

Our collisional studies show that NaLi molecules with various collision partners have loss rates far below the universal limit. Although all collision systems are reactive, the absorption probability at close range is much smaller than one. This is well understood for the collisions in the spin-stretched Na+NaLi mixture [29,33] where the quartet potential in the input channel is non-reactive, and inelastic collisions are only possible via spiflips. However, this explanation does not apply to the s-wave molecule-molecule collisions studied here. Also, a molecule-molecule Feshbach resonance has been observed for a strongly reactive input potential [73]. These observations suggest that collisional resonances and collisional complexes should occur more generally, and motivate more systematic studies of collisions involving NaLi and collision partners in various hyperfine states, and also for other molecules [112]. We also demonstrated sympathetic cooling of NaLi by RF evaporation of Na atoms, increasing the PSD of

the molecules by a factor of ≈ 16. This can be further optimized, but is eventually limited by the slow Na thermalization rate, which is significantly slower than the rate of elastic collisions between Na and NaLi. Using a second trap for Na that enhances the thermalization rate should allow cooling into the quantum-degenerate regime.

Chapter 6

Free to bound Raman transfer

Progress toward ultracold molecular system has been made with various species by either synthesis of preliminarily cooled atoms or direct cooling of molecules chemically produced. One of the most successful recipes for achieving ground state molecules (without direct laser cooling of molecules) has two combined steps. The first step is the magnetic association of cold atoms into weakly bound molecules near a Feshbach resonance. The second step is the efficient formation of ground-state ultracold molecules via the stimulated Raman adiabatic passage (STIRAP). Although this recipe allowed the production of cold molecules as low as tens of nano Kelvin, it also has some drawbacks. It requires a Feshbach resonance to be at an experimentally accessible bias field and to be strong compared to any decoherence rate for an efficient magnetic association. The Na + Li mixture has very narrow ($\sim$mG) resonances only at high fields ($>$700 G), compared to other diatomic alkali metal mixtures, and using these resonances for molecule formation is technically challenging. However, we have relied on one of these resonances at 745G to generate ground-state molecules. Even with a low magnetic association efficiency of about 5%, having a large initial atomic mixture number allowed a competitive number of ground-state molecules, typically 5×10^4.

All-optical creation of molecules in which the magnetic association step near a Feshbach resonance is eliminated can broaden the horizon of ultracold molecules to a larger pool and simplify some of the experimental complication. There have been

efforts toward all-optical creation of molecules. However, there are only a couple of different molecules that have been successfully formed in their ground state. Recent experiments on Sr_2 molecule formation have shown the all-optical creation of an ultracold gas of alkaline-earth metal dimers in their absolute ground state [113, 114]. In addition, all optical creation of RbCs molecules using photoassociation (PA) was demonstrated using spontaneous emission [115–119].

In the following subsections, three different approaches to the all-optical formation of NaLi molecules in the ground state of the $a^3\Sigma^+$ potential are discussed in a chain of thought that gradually develops on top of a simplified model. Therefore, the full picture is revealed only at the end of the chapter. The work described in this chapter heavily utilizes *ab initio* calculations of the NaLi triplet potentials ($a^3\Sigma^+$, $c^3\Sigma^+$, and $b^3\Pi$) provided to us by Prof. Olivier Dulieu, to whom we are grateful. The table of *ab initio* potential values for the lowest three triplet potentials of NaLi is provided in Appendix C of ref. [120].

Here, we model the NaLi free-to-bound Raman transitions as an effective three-level system. The most complete knowledge of the system is contained in the state vector $|\psi\rangle = c_i|i\rangle + c_e|e\rangle + c_f|f\rangle$, which is a superposition of three orthogonal state vectors: the initial state $|i\rangle$, the intermediate excited state $|e\rangle$ and the final state $|f\rangle$. Here, we do simple modeling and numerical calculation of the Schrodinger equation that describes our system (effective three-level system with additional loss terms and energy shifts) given by:

$$\begin{aligned}\frac{d}{dt}\begin{bmatrix} c_i \\ c_e \\ c_f \end{bmatrix} = i\begin{bmatrix} 0 & \frac{\Omega_{down}(t)}{2} & 0 \\ \frac{\Omega_{down}(t)}{2} & \Delta - \frac{\Omega_{down}^2+\Omega_{up}^2}{4\Delta} & \frac{\Omega_{up}(t)}{2} \\ 0 & \frac{\Omega_{up}(t)}{2} & \delta \end{bmatrix}\begin{bmatrix} c_i \\ c_e \\ c_f \end{bmatrix} \\ -\frac{1}{2}\begin{bmatrix} R_A & 0 & 0 \\ 0 & \Gamma_M + R_M & 0 \\ 0 & 0 & R_C \end{bmatrix}\begin{bmatrix} c_i \\ c_e \\ c_f \end{bmatrix}\end{aligned} \tag{6.1}$$

where the two Rabi frequencies are Ω_{up} and Ω_{down} and Δ and δ are single- and two-

photon detunings set by the laser frequencies, respectively. We can define the effective detunings $\bar{\Delta} \equiv \Delta + \Delta'$ and $\bar{\delta} \equiv \delta + \delta'$ where Δ' and δ' are detunings caused by the Raman beams acting on other nearby atomic or molecular transitions, and creating light shifts. The term in blue compensates the AC Stark shifts caused by two Rabi couplings in an isolated three-level system. Γ_M is the linewidth of the intermediate excited state. The terms in red and orange are additional decay terms that arise specifically in our system. R_A and R_M are decay rates of the initial atomic state and the final molecular state by photon scattering. R_C is the atom-molecule collision loss rate. We first focus on optimizing the Raman transition with only atomic and molecular photon scattering (R_A, R_M) setting Δ' and $\bar{\delta}$ to zero and with complete Stark shift compensation (with term in blue). We then further explore the effects of collisional loss and light shifts.

6.1 Double Raman transfer via Feshbach molecule state

The most staightforward approach to forming a ground state molecule is to replace the well-established method of forming Feshbach molecules, magnetic association near a Feshbach resonance, with a two-photon Raman transfer from the ultracold atomic mixture to molecules in the Feshbach state $(v = 10, N = 2)$. Stable ground-state molecules are eventually created from optically created Feshbach molecules by the standard STIRAP sequence. The Feshbach state $v = 10, N = 2$ has a binding energy of 5.85 GHz, which can be bridged with an electro-optic modulator (EOM) from the energy of free atoms. This allows using a single laser source with an EOM driven with 5.86 GHz radiofrequency (RF) to achieve a two-photon π pulse. There are a few advantages to this method. First of all, by having an EOM in addition to a single laser source, it is easier to achieve a much longer coherence time between two Raman beams compared to having two independent lasers locked to a stable reference cavity. Second, only one additional laser is required to create Feshbach molecules, and

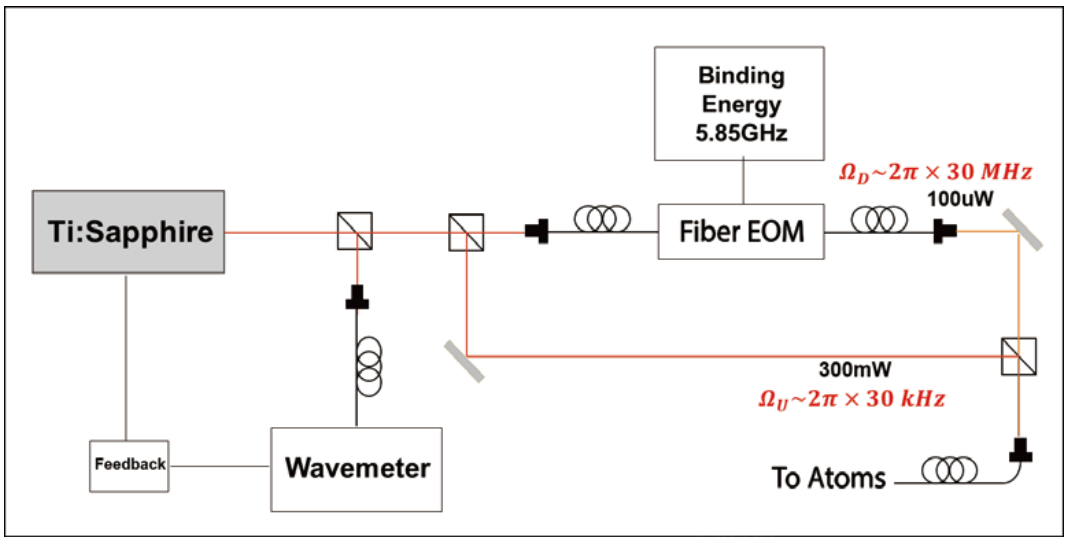

Figure 6-1: Ti:Sapphire laser setup for Raman transfer from free atoms to the Feshbach state.

the existing STIRAP lasers can be used to form the ground-state molecules from the Feshbach molecule. Lastly, it can be checked whether the first step (optical formation of Feshbach molecules) was successful by imaging atoms that are dissociated from a Feshbach molecule near the ~ 745 G Feshbach resonance.

However, this approach has limitations. The Frank-Condon factors (FCF) of two paths: a. FCF between free atomic states and the intermediate excited molecular state (upleg path), and b. FCF between the Feshbach state and the intermediate excited molecular state (downleg path) differ by more than two orders of magnitude, and the binding energy of the Feshbach state is only 5.85 GHz; the Raman beam that bridges the atomic state to one of the excited molecular bound states (upleg) also acts strongly on the other path (downleg path), causing significant off-resonant Rayleigh scattering of Feshbach molecules. Additionally, this also causes large AC stark shifts of the molecular bound states leading to fast decoherence during the Raman transition. We will ignore the effect of AC stark shifts for now, since in principle, it can be compensated with additional laser beams. However, it turns out to be one of the most critical aspects in evaluating the approach.

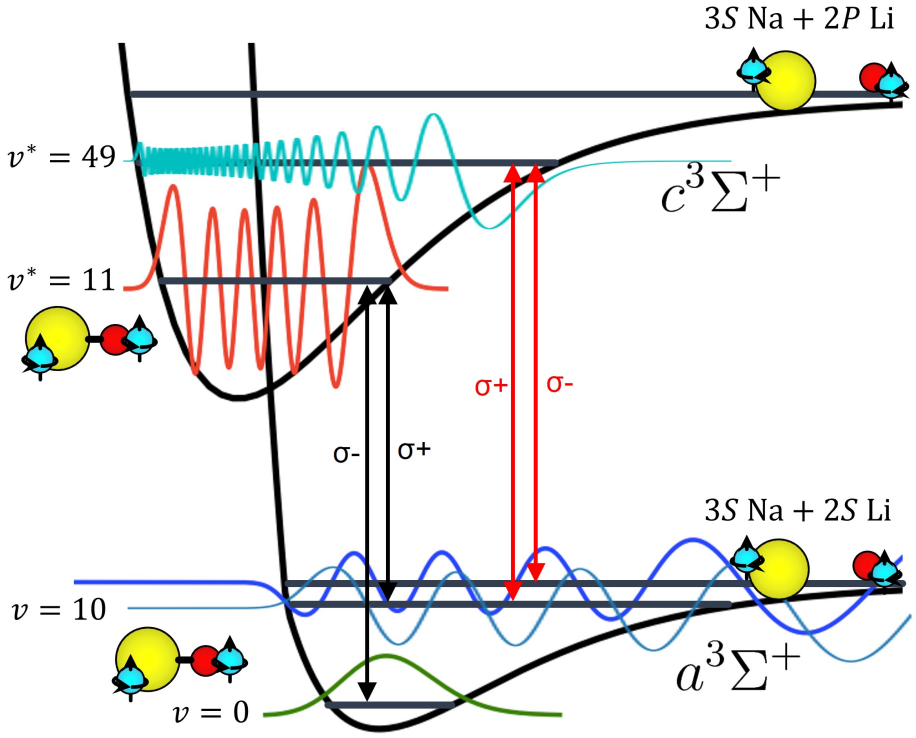

Figure 6-2: **Four photon transfer of sodium and lithium atoms to the rovibrational ground state of NaLi molecules in the $a^3\Sigma^+$ potential via Feshbach molecule state.** Free sodium and lithium atoms are transferred to the Feshbach state $(v = 10, N = 2)$ in the $a^3\Sigma^+$ potential by two photon Raman transfer mediated by an excited molecular state $(v^* = 49)$ in the $c^3\Sigma^+$ potential. Feshbach molecules are eventually transfered to the rovibrational ground state of NaLi molecules in the $a^3\Sigma^+$ potential either using two photon Raman pulse or STIRAP mediated by $v^* = 11$. The two red arrows indicate the first two photon couplings and the two black arrows indicate the second two photon couplings.

6.1.1 Coupling strengths of Raman beams

A newer model of Ti:Sapphire laser from M-Squared Laser spanning 670-725 nm range[1] can be used for Raman transfer of free atoms to the Feshbach state. With the current continuum-to-bound Raman experimental setup using the Ti:Sapphire laser and a fiber EOM from EOSpace (PM-0S5-10-PFU-PFU-670), we are able to get up to 300 mW for Upleg and 100 uW for Downleg, respectively. Assuming a beam waist of 50 μ m, which is comparable to the size of 1596 nm lattice and a 1064 nm dipole trap, the intensities of the two Raman beams are given as:

$$\begin{aligned} I_{up} &= \frac{300\text{mW}}{\pi(50\times10^{-4}\text{cm})^2} = 3.82\times10^{6}\ \text{mW}\cdot\text{cm}^{-2} = 3.82\times10^{3}\ \text{W}\cdot\text{cm}^{-2} \\ I_{down} &= \frac{100\text{uW}}{\pi(50\times10^{-3}\text{cm})^2} = 1.27\times10^{3}\ \text{mW}\cdot\text{cm}^{-2} = 1.27\ \text{W}\cdot\text{cm}^{-2} \end{aligned} \tag{6.2}$$

The Rabi coupling strength between the free atomic state and $v^* = 49$ by the upleg beam of intensity I_{up} is estimated to be $\Omega_{up} \approx 2\pi \times 31.1$kHz for the atomic density of $n = 5\times10^{12}$ cm^{-3} for both sodium and lithium atomic clouds. Given the Franck-Condon factor[2] difference between the upleg and the downleg as shown in Fig.6-3, the Rabi frequency of the downleg (Ω_{down}) is roughly 1000 times higher than the Rabi frequency of the upleg for individual excited vibrational states when v^* is smaller than 50.

6.1.2 Li 2S to 2P transition strengths

States in the $c^3\Sigma^+$ potential have electronic states dissociating into Na($3s$)+Li($2p$), and therefore, free-to-bound upleg and downleg pulses can cause near-resonant light scattering by Li D_1 and D_2 transitions leading to atomic loss [3]. This effect can be large for highly excited vibrational states as an intermediate excited state, and it is dominated by the upleg pulse, since its intensity is normally a few orders of magnitude

[1] A newer model of Ti:Sapphire laser from M-Squared Laser spanning 670-725 nm range was originally used for finding photoassociation (PA) lines of high vibrational states of $c^3\Sigma^+$ NaLi.

[2] Fanck-Condon factors are calculated from *ab initio* potentials.

[3] Na D_1 and D_2 transitions are far off-resonant to upleg and downleg optical frequencies (tens of THz or more), and the caused loss is negligible compared to the loss caused by Li transitions.

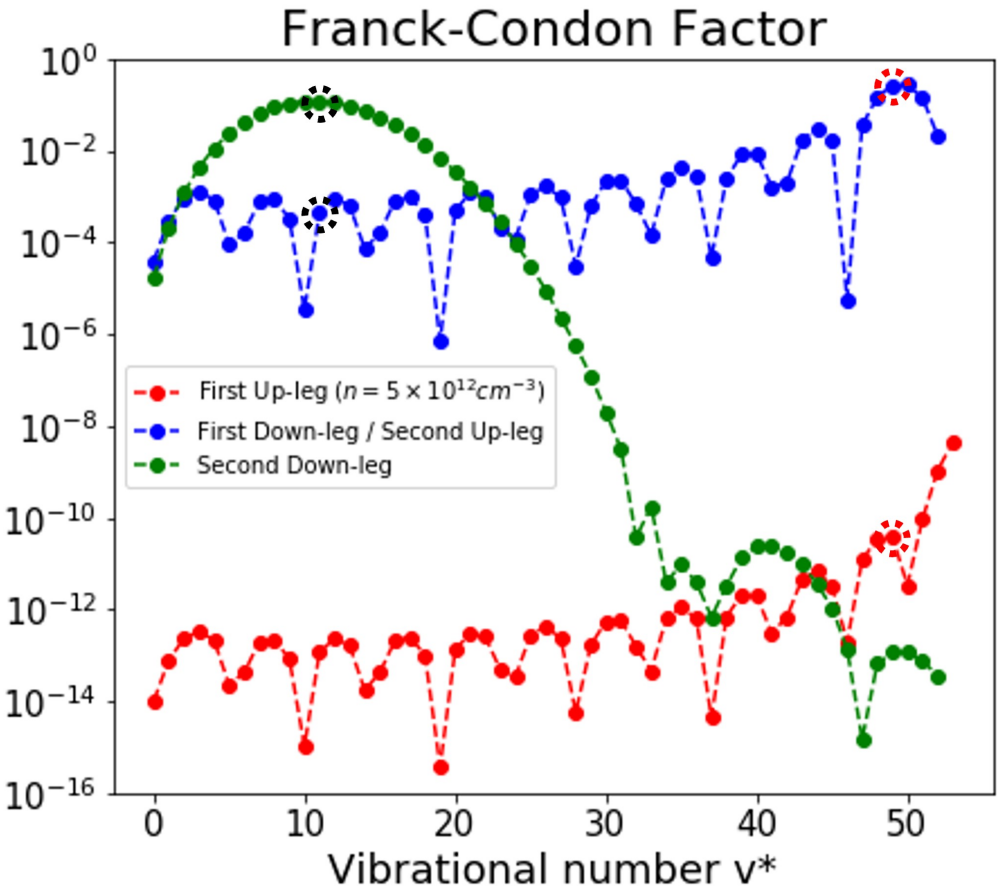

Figure 6-3: **Franck-Condon factors (FCF) calculated from *ab initio* potentials.** Free-to-bound (v^*) FCFs are indicated in red, Feshbach state ($v = 10, N = 2$) to excited state FCFs are indicated in blue and the ground state to excited state FCFs are indicated in green. The red dashed circles are identifying the two FCFs relevant to the first two photon transfer: free-to-bound (atoms to $v^* = 49$) FCF and $v^* = 49$ to $v = 10$ FCF. The black dashed circles are identifying the two FCFs relevant to the second two photon transfer: FCF between $v = 10$ and $v^* = 11$, and FCF between $v^* = 11$ and $v = 0$.

larger than that of the downleg pulse as estimated in Eq. 6.2.

Here, we first quantify the strengths of these atomic transitions driven by the upleg pulse. In a two-level system with a coherent drive by near-resonant light, the optical Rabi frequency is given by $\Omega = \langle b| \hat{\mu} \cdot \mathbf{E} |a\rangle / \hbar = \mu_{ba} E_0 / \hbar$ where μ_{ba} is the electric-dipole transition matrix element for states a and b, and E_0 is the electric field strength of the incident optical field. We can write this as $\Omega = 4.37 \mu_{ba} \sqrt{I}$ with Ω in unit of $2\pi \times$MHz, μ_{ba} in Debye, and I, the light intensity, in mW/mm^2. However, for a full description, we need to consider all the hyperfine states. The interaction between the internal states of the atom and an external, near-resonant optical field is quantified through the electric dipole transition matrix elements. These matrix elements describe how the internal states of the atom couple to each other via an electric dipole ($\vec{\mu} \cdot \vec{E}$) interaction with the near-resonant field. If we start in a hyperfine state represented by $|(JI)Fm_F\rangle$ and couple to a state $|(J'I')F'm_{F'}\rangle$, then the matrix element for this transition is given by $\langle (J'I')F'm_{F'}| \hat{\mu} |(JI)Fm_F\rangle$, where $\hat{\mu}$ is the electric dipole operator. We can use the Wigner-Echart Theorem to represent this matrix element in terms of a m-independent reduced matrix element $\langle J'| |\hat{\mu}(1)| |J\rangle$, *Wigner 3-J* and *6-J* symbols as:

$$\begin{aligned} \langle (J'I')F'm_{F'}| \hat{\mu} |(JI)Fm_F\rangle = \delta_{I'I} (-1)^{F'+F+J'+I-m_F+1} \sqrt{(2F'+1)(2F+1)} \\ \times \begin{pmatrix} J' & 1 & J \\ -m_{F'} & q & m_F \end{pmatrix} \begin{Bmatrix} J' & I & F' \\ F & 1 & J \end{Bmatrix} \langle J'| |\hat{\mu}(1)| |J\rangle \end{aligned} \tag{6.3}$$

where $\hat{\mu}(1,q)$ is an irreducible spherical tensor operator for the electric dipole operator with $q = -1, 0, 1$ for electric dipole radiation with polarization σ^-, π and σ^+, respectively.

For example, let us consider a free-to-bound Raman transition from Na and Li atoms with their electron spins aligned to the bias field direction in the ground levels, $|S_{\mathrm{Na}} = 1/2, m_{S_{\mathrm{Na}}} = 1/2, S_{\mathrm{Li}} = 1/2, m_{S_{\mathrm{Li}}} = 1/2\rangle$, to the NaLi Feshbach state ($|v = 10, N = 2, m_N = -2, S = 1, m_S = 1\rangle$) in the $a^3\Sigma^+$ potential via an intermediate excited state ($|v^* = 49, N = 1, m_N = -1, S = 1, m_s = 1\rangle$) in the NaLi $c^3\Sigma^+$ po-

tential. This process requires that the upleg pulse be polarized $\sigma-$ and the downleg pulse be polarized $\sigma+$, as illustrated in Fig. 6-2. With the Upleg intensity mentioned above which is $I_{up} = 3.82 \times 10^4$ mW $\cdot$ mm^{-2}, optical Rabi frequency, for example, of Li D_1 transition from the ground upper stretched hyperfine state $|J = 1/2, F = 3/2, m_F = 3/2\rangle$ to the excited state $|J' = 1/2, F' = 3/2, m_{F'} = 1/2\rangle$ is $\Omega = 4.37 \times (-\frac{\sqrt{2}}{3}) \times (-8.433 \text{ Debye}) \times \sqrt{\text{I}} \approx 3.4$ GHz [4].

The photon scattering rate of a two-level atomic system $R_{scatt} = \Gamma\rho_{bb}$ where ρ_{bb} is the fraction of the population in the excited state b and Γ is the linewidth of state b. Using the solution of *optical Bloch equations* that describes the excitation of a two-level atom by radiation, the scattering rate is expressed as $R_{scatt} = \frac{\Gamma}{2}\frac{\Omega^2/2}{\Delta^2+\Omega^2/2+\Gamma^2/2}$ which is approximated to $\frac{\Omega^2}{4\Delta^2}\Gamma$ when detuning Δ is much greater than the Rabi frequency Ω and the linewidth Γ. Therefore, the total atomic scattering rate R_A, considering all near-resonant hyperfine states, is perturbatively given by:

$$R_A = \sum_{F',m_{F'}} \left| \frac{\langle (J'I')F'm_{F'}| \hat{\mu} \cdot \mathbf{E} |(JI)Fm_F\rangle}{2\Delta_{F',m_{F'}}} \right|^2 \Gamma_{F',m_{F'}} \tag{6.4}$$

where $\Gamma_{F',m_{F'}}$ is the natural linewidth $\Delta_{F',m_{F'}}$ is the photon detuning of an excited state $|F', m_{F'}\rangle$. From Eq.6.3 and Eq.6.4, the photon scattering rate by Li D_1 line is about 381 Hz and by D_2 line is about 177 Hz leading to total scattering rate of about 558 Hz [5].

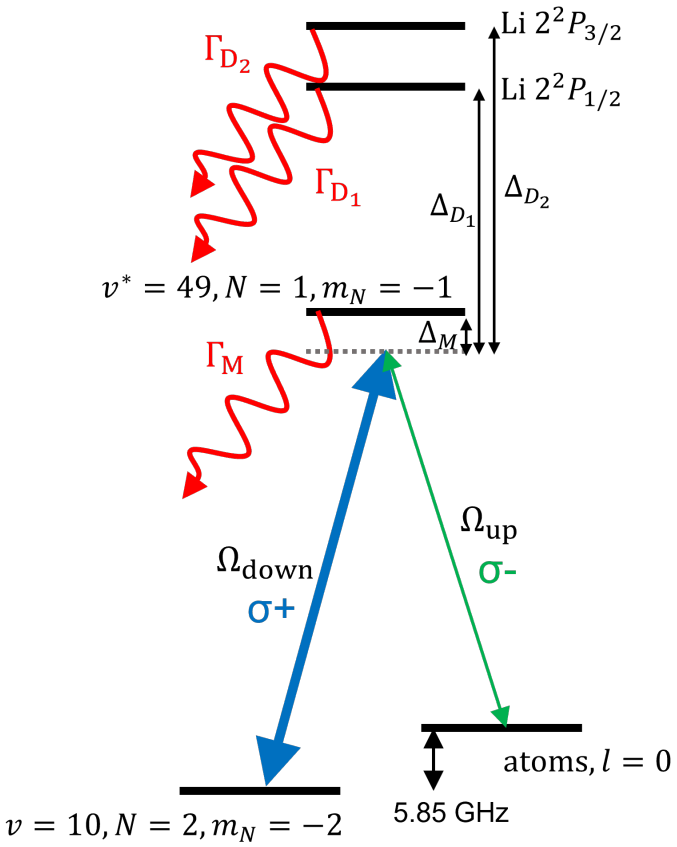

Figure 6-4: **Atomic and molecular photon scattering losses.** High intensity upleg pulse with $\sigma-$ polarization in green can drive Li D_1 and D_2 transitions leading to photon scattering. Strong downleg Rabi coupling Ω_{down} causes photon scattering through the molecular transition ($v = 10 \rightarrow v^* = 49$).

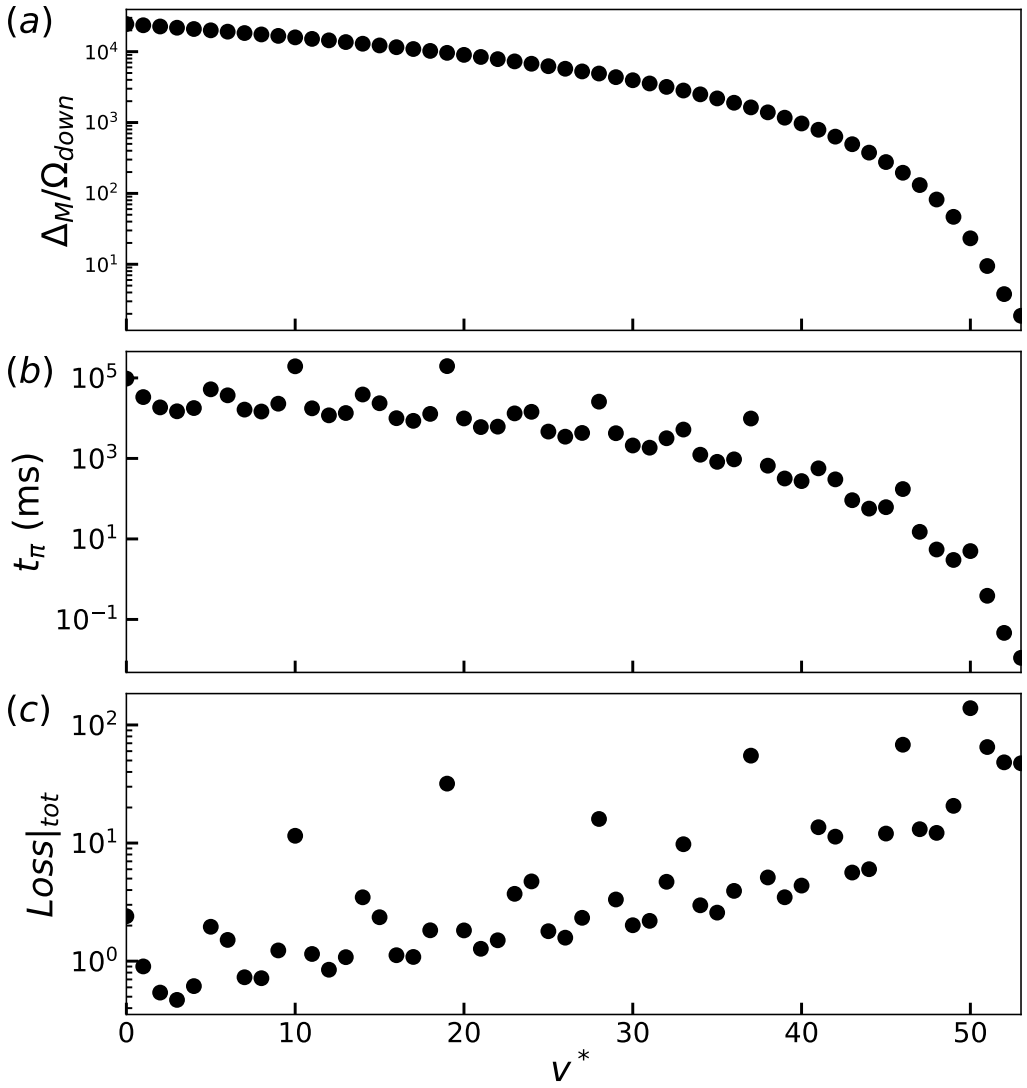

Figure 6-5: **Results of a simplified loss model for free-to bound Raman transition.** (a) Optimum ratio of the single photon detuning to the downleg Rabi frequency ($\frac{\Delta_M}{\Omega_{down}} = \sqrt{\frac{\Gamma_M}{\Gamma_A}}\frac{\Delta_A}{\Omega_A}$) as a function of excited vibrational state v^* picked as an intermediate state. (b) Raman π pulse duration in ms obtained with the optimum ratio in (a). (c) Minimum total photon scattering loss given by Eq. 6.6 as a function of excited vibrational state v^*.

6.1.3 Molecular and atomic losses

Near-full-contrast Raman transitions require a single Rabi cycle time to be shorter than the laser coherence time ($\sim$ 1 ms). For this, it is necessary to have Ω_{down} much greater than Ω_{up} in order to provide a sufficient two-photon rabi frequency $\Omega_{eff} = \Omega_{up}\Omega_{down}/\Delta$ with weak upleg. However, in this case ,$\Omega_{down} \gg \Omega_{up}$, photon scattering loss of the molecule population by the downleg pulse can be significant as well in addition to the atomic losses by the Li D_1 and D_2 transitions as mentioned in the previous section. The goal of this section is to find the condition of minimum photon scattering loss created by these two effects illustrated in Fig. 6-4.

Molecular and atomic photon scatting losses in half the Rabi cycle $t = t_\pi = \frac{4\pi\Delta_M}{\Omega_{up}\Omega_{down}}$ [6] are given by:

$$\begin{aligned} \text{Loss}|_{\text{M}} &= \frac{\Omega_{down}^2}{4\Delta_M^2} \cdot \Gamma_M \cdot t \xrightarrow{t=t_R} \frac{\pi \cdot \Gamma_M \cdot x}{\sqrt{\overline{FC}}} \\ \text{Loss}|_{\text{A}} &= \frac{\Omega_A^2}{4\Delta_A^2} \cdot \Gamma_A \cdot t \xrightarrow{t=t_R} \frac{\pi \cdot \Gamma_A}{\sqrt{\overline{FC}} \cdot \Delta_A^2 \cdot x} \end{aligned} \tag{6.5}$$

where the relative FCF, $\overline{FC}$ is defined by $\Omega_{up}^2 = \overline{FC} \cdot \Omega_A^2$, Γ_M is the linewidth of the molecular excited state ($\sim$ 9 MHz) and $x = \frac{\Omega_{down}}{\Omega_A \cdot \Delta_M}$. Here, Ω_A is the effective atomic Rabi frequency[7] and Δ_M is the single photon detuning of the two-photon Raman transition. We regard scattering of a single photon as a loss, since we want to stay below the recoil temperature. To minimize the total loss $\text{Loss}|_{\text{tot}} = \text{Loss}|_{\text{M}} + \text{Loss}|_{\text{A}}$,

[4] D_1 line reduced matrix element $\langle J' = 1/2| \, |\hat{\mu}(1)| \, |J = 1/2\rangle = -8.433$ Debye and D_2 line reduced matrix element $\langle J' = e/2| \, |\hat{\mu}(1)| \, |J = 1/2\rangle = 11.925$ Debye [121].

[5] The estimate assumed the upleg frequency is resonant to the free to $v^* = 49$ transition. ($\Delta_{D_1} \approx$ 258 GHz and $\Delta_{D_2} \approx$ 268 GHz) Since the excited-state hyperfine splittings are much smaller than the photon detunings in this case, the effective Rabi frequency of D_1 transitions Ω_{D_1} and that of D_2 transitions Ω_{D_2} can be approximated to the sum of all relevant individual Rabi frequencies. Therefore, $\Omega_{D_1} \approx \left|\Omega_{1/2,3/2,1/2}\right| + \left|\Omega_{1/2,1/2,1/2}\right| = \left[\left|-\frac{\sqrt{2}}{3}\right| + \left|\frac{1}{3}\right|\right] \times \left|4.37 \times (-8.433 \text{ Debye}) \times \sqrt{\text{I}}\right| \approx$ 4.158 GHz and $\Omega_{D_2} \approx \left|\Omega_{3/2,5/2,1/2}\right| + \left|\Omega_{3/2,3/2,1/2}\right| + \left|\Omega_{3/2,1/2,1/2}\right| = \left[\left|-\frac{1}{6\sqrt{2}}\right| + \left|-\frac{1}{3}\sqrt{\frac{2}{5}}\right| + \left|\frac{1}{2\sqrt{10}}\right|\right] \times$ $\left|4.37 \times (11.925 \text{ Debye}) \times \sqrt{\text{I}}\right| \approx 2.940$ GHz . The three numbers as subscripts of Ω s indicate the J', F' and $m_{F'}$ quantum numbers in order

[6] The duration of a π pulse t_π is defined by $t_\pi \cdot \Omega_{eff} = \pi$ where two photon Rabi frequency $\Omega_{eff} = \frac{\Omega_{up}\Omega_{down}}{4\Delta}$.

[7] Since $\Delta_{D_1} \approx \Delta_{D_2} = \Delta_A$ ($\Delta_{D_1}, \Delta_{D_2} \gg |\Delta_{D_1} - \Delta_{D_2}|$) and $\Gamma_{D_1} \approx \Gamma_{D_2}$, we can define the effective atomic Rabi frequency Ω_A by $\Omega_A^2 = \sum_{F',m_{F'}} |\langle (J'I')F'm_{F'}| \, \hat{\mu} \, |(JI)Fm_F\rangle|^2$.

we take the derivative of $\text{Loss}|_{\text{tot}}$ with respect to x to find the optimal value of x. We come to the conclusion that in this model, the optimal value x does not depend on the FCF if the pulse duration is fixed to half the Rabi cycle and $x = \frac{\Omega_D}{\Omega_A \cdot \Delta_M} = \sqrt{\frac{\Gamma_A}{\Gamma_M}} \frac{1}{\Delta_A}$ gives the minimum total loss. From this relation, we can find the optimal ratio between the molecular single-photon detuning Δ_M and the downleg Rabi frequency Ω_{down} as $\frac{\Delta_M}{\Omega_{down}} = \sqrt{\frac{\Gamma_M}{\Gamma_A}} \frac{\Delta_A}{\Omega_A}$. The optimal ratio is plotted as a function of v^* in Fig. 6-5(a). For a given excited molecular state, the minimum scattering loss achieved by the optimum value x is given as:

$$\text{Loss}|_{\text{tot}} = \frac{2\pi}{\Delta_{\text{A}}} \sqrt{\frac{\Gamma_{\text{A}} \Gamma_{\text{M}}}{\overline{\text{FC}}}}. \tag{6.6}$$

Therefore, using a lower lying exit state that has a larger Δ_A than that of $v^* = 49$ for a Raman transfer has a smaller scattering loss, as plotted in Fig. 6-5(c). However, the maximum upleg and downleg Rabi frequencies that we can achieve become smaller with low v^* molecular states, and t_{pi} starts to become much larger than 1 ms (Fig. 6-5(b)). If we do not have a limited laser coherence time, using, for example, $v^* = 44$ as an intermediate excited state is a better choice. Figures 6-6 and Figure 6-7 are numerical calculations of the Schrödinder equation describing the three-level system with an extra decay term that accounts for the atomic photon scattering using an intermediate state $v^* = 49$ and $v^* = 44$ respectively. With $v^* = 49$, the maximum population transfer efficiency to the Feshbach state is ~ 1.2 % at around 0.25 ms, while with $v^* = 44$, the maximum population transfer efficiency to the Feshbach state is ~ 11.5 % at around 15 ms, which is much longer than the laser coherence time ($\sim$ 1 ms). In case the Raman pulse duration is limited to 1 ms, the transfer efficiency reaches only ~ 0.3 %, which is worse than what we can achieve with $v^* = 49$.

So far, we have been optimizing a rather simplified process: Raman transition in a three-level system with an additional atomic loss term. However, unlike alkali atoms, molecules have many vibrational and rotational states, which may interfere with the simplified process. For example, there are more than 100 rovibrational states within the $v^* = 49$ branch. Despite the upleg free-to-bound Rabi frequency being only about

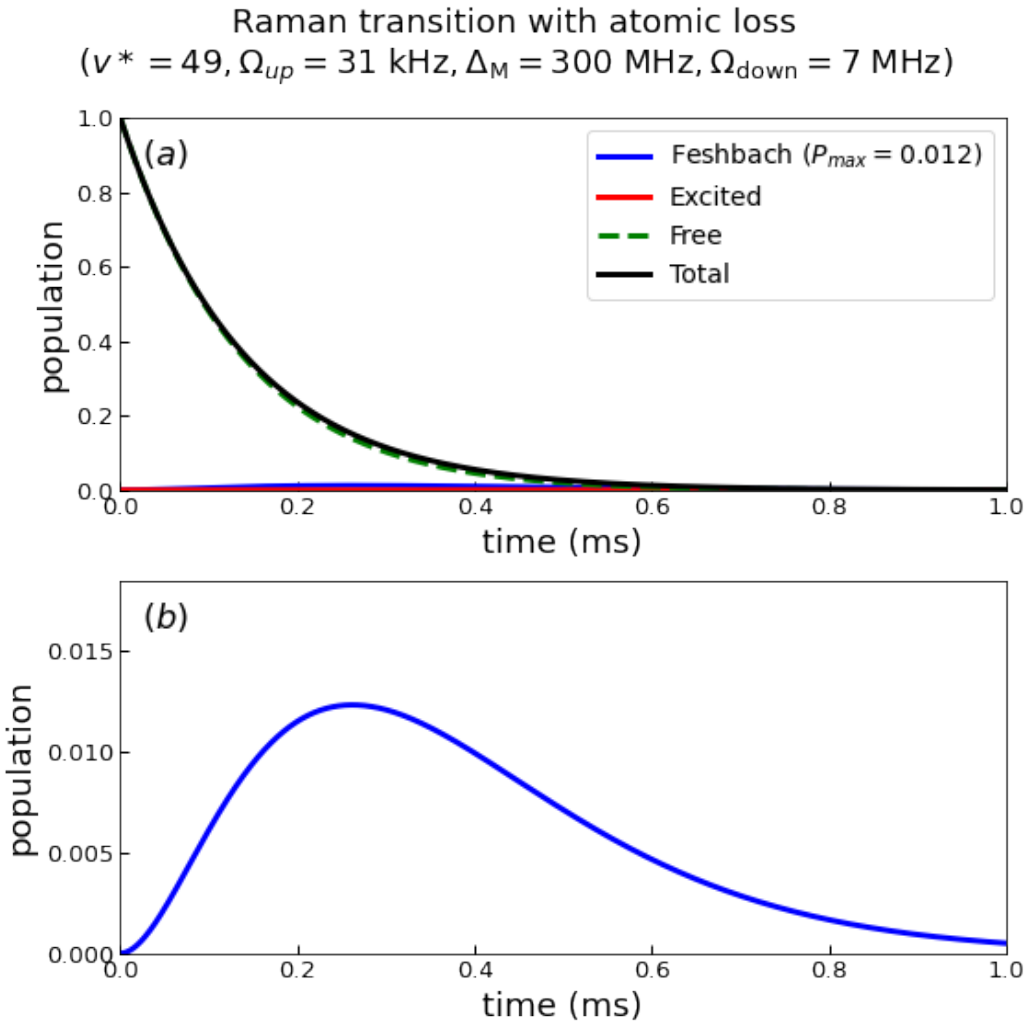

Figure 6-6: **Numerical calculation of free-to bound Raman transition to the Feshbach state via $v^* = 49$ with atomic photon scattering.** (a) Time evolution of the populations in the final Feshbach state (in blue), intermediate excited state (in red), initial free atomic state (in dashed green) and the total population (in black) are plotted. The total population decreases over time because of atomic loss term from Li D_1 and D_2 transitions is included in the calculation. Optimum ratio of the single photon detuning to the downleg Rabi frequency is chosen in the numerical calculation. (b) Transferred population to the Feshbach state is plotted as a function of pulse duration. The transfer is maximized to ~ 1.2 % at around 0.25 ms.

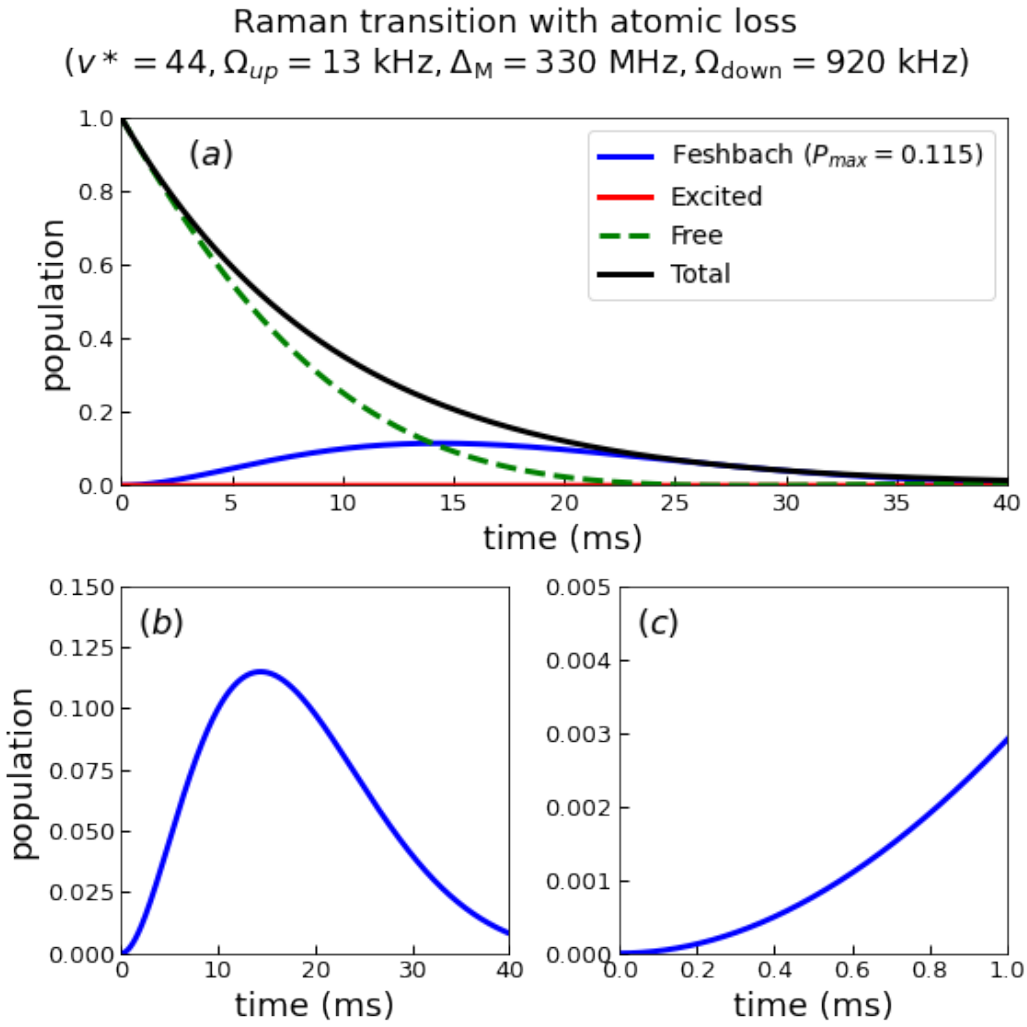

Figure 6-7: **Numerical calculation of free-to bound Raman transition to the Feshbach state via $v^* = 44$ with atomic photon scattering.** (a) Time evolution of the populations in the final Feshbach state (in blue), intermediate excited state (in red), initial free atomic state (in dashed green) and the total population (in black) are plotted. The total population decreases over time because of atomic loss term from Li D_1 and D_2 transitions is included in the calculation. Optimum ratio of the single photon detuning to the downleg Rabi frequency is chosen in the numerical calculation. (b) Transferred population to the Feshbach state iS plotted as a function of pulse duration up to 40 ms. The transfer is maximized to $\sim$ 11.5 % at around 15 ms. (c) The transfer to the Feshbach state only reaches to $\sim$ 0.3 % if the pulse duration is limited to 1 ms.

30 kHz at most, the upleg can act strongly on the downleg path driving transitions between the Feshbach state to some of these other rovibronic states (e.g. $v^* = 49$, $N = 3$, $m_N = -3$)[8]. Additionally, even small fraction of upleg polarization impurity ($\sigma+$ component) can cause fast molecular scattering through the Feshbach state to $N = 3$, $m_N = -1$ states in the $c^3\Sigma^+$ potential. Figure 6-8 is an illustration of the upleg beam acting on the downleg path through nearby excited rovibronic states in the $c^3\Sigma^+$ potential. For example, the upleg beam of 3.82×10^4 mW/mm^2 intensity leads to a molecular scattering rate of more than 20 kHz with $\Delta_M \approx 1.45$ GHz [9]. The photon scattering rate of about 22 kHz is caused by the molecular transition between the Feshbach state and $v^* = 49, N = 3, m_N = -3$ and scattering rate of more than 1 kHz can be caused by only 1% impurity of the upleg beam polarization ($\sigma+$) through the Feshbach state to the $v^* = 49, N = 1, m_N = -1$ transition. Using a highly excited vibrational state v^* as an intermediate state tends to have a higher additional molecular scattering loss by the upleg acting on the downleg path, since the higher v^* has a smaller rotational constant B (see Table 6.1) and, therefore, the optical frequency of the upleg is closer to these molecular transition frequencies. Even without considering molecular photon scattering losses by the upleg beam acting on the downleg path, population transfer efficiency was less than 2 % (see Figs. 6-6 and 6-7). The inclusion of additional molecular decay in the numerical calculation further reduces the transfer efficiency.

6.1.4 Effects of atomic densities and collisional loss

One way of reducing the loss by atomic and molecular light scattering to obtain a non-negligible population transfer from the free atomic state to the Feshbach state is to shorten the Rabi cycle time or in other words, increase the two-photon Rabi frequency ($\Omega_{eff} = \Omega_{up} \times \frac{\Omega_{down}}{4\Delta_M}$). We saw previously that simply increasing Ω_{down}/ rather increases molecular loss by strong Ω_{down} and there is an optimum value for

[8]The rotational selection rules for $\Sigma \leftrightarrow \Sigma$ potential transitions are $\Delta N = 1$, hence from a $N = 2$ Feshbach state it is possible to access $N = 1, 3$ excited states.

[9]With downleg intensity given in Eq. 6.2 and $v^* = 49$, optimum single photon detuning $\Delta_M = \sqrt{\frac{\Gamma_M}{\Gamma_A}\frac{\Delta_A}{\Omega_A}} \times \Omega_{down} \approx 1.45$ GHz.

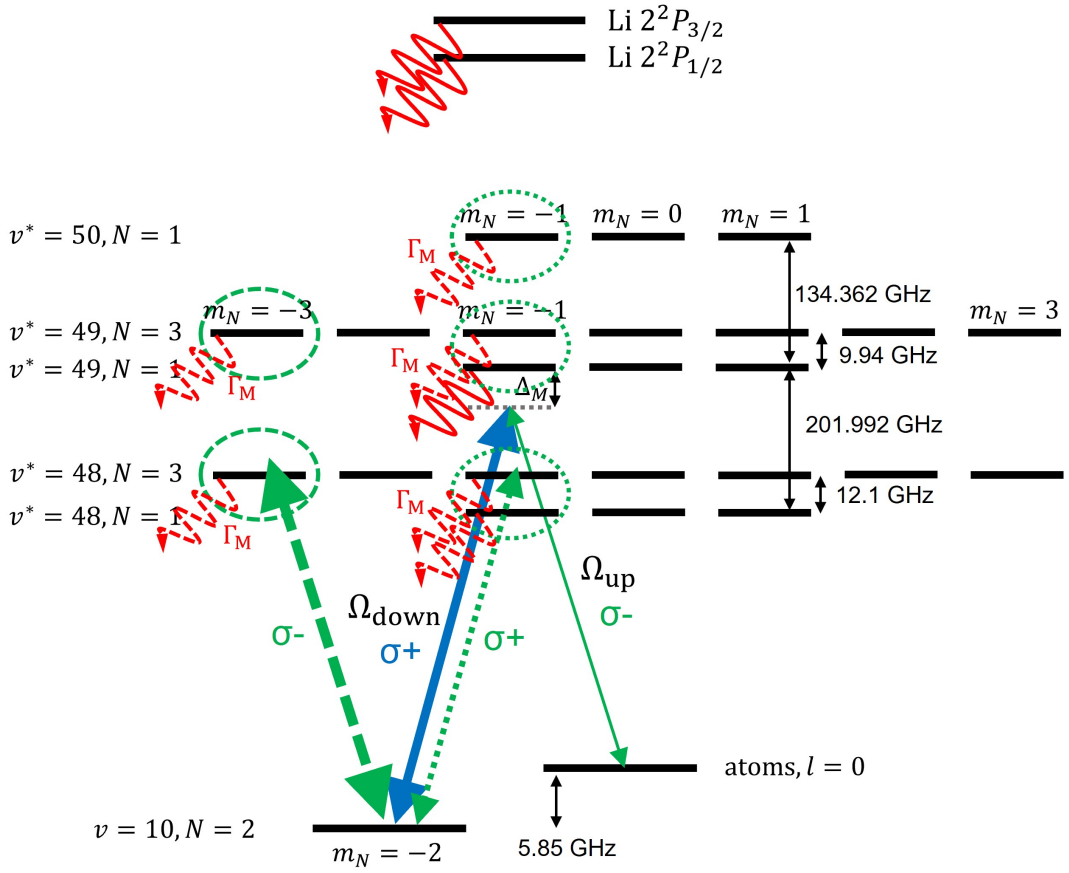

Figure 6-8: **Molecular photon scattering losses by the upleg beam driving transitions to nearby excited states in the $c^3\Sigma^+$ potential from the Feshbach state.** High intensity upleg pulse with $\sigma-$ polarization indicated with a dashed green arrow can drive transitions from the Feshbach state $(v = 10, N = 2, m_N = -2)$ to vibrational states with $N = 3, m_N = -3$ in the $c^3\Sigma^+$ potential (green dashed circles). Small fraction of $\sigma-$ polarization component due to polarization impurity of the upleg can drive transitions from the Feshbach state $(v = 10, N = 2, m_N = -2)$ to excited states in the $c^3\Sigma^+$ potential with $N = 1, m_N = -1$ or $N = 3, m_N = -1$ (green dotted circles). These transitions lead to molecular photon scattering losses indicated with red dashed wiggles in addition to those caused by the strong downleg Rabi frequency.

v^*	B constant (GHz)	v^*	B constant (GHz)
0	8.83	26	5.51
1	8.71	27	5.36
2	8.59	28	5.20
3	8.48	29	5.02
4	8.36	30	4.86
5	8.24	31	4.67
6	8.12	32	4.51
7	8.00	33	4.32
8	7.88	34	4.14
9	7.76	35	3.96
10	7.64	36	3.77
11	7.52	37	3.57
12	7.40	38	3.38
13	7.27	39	3.16
14	7.15	40	2.96
15	7.02	41	2.75
16	6.89	42	2.53
17	6.76	43	2.31
18	6.63	44	2.10
19	6.50	45	1.88
20	6.38	46	1.65
21	6.24	47	1.42
22	6.08	48	1.21
23	5.93	49	0.994
24	5.79	50	0.905
25	5.66		

Table 6.1: **Rotational constants of excited vibrational states ($c^3\Sigma^+$, v^*).** The rotational constants are calculated from the $c^3\Sigma^+$ *ab initio* potential.

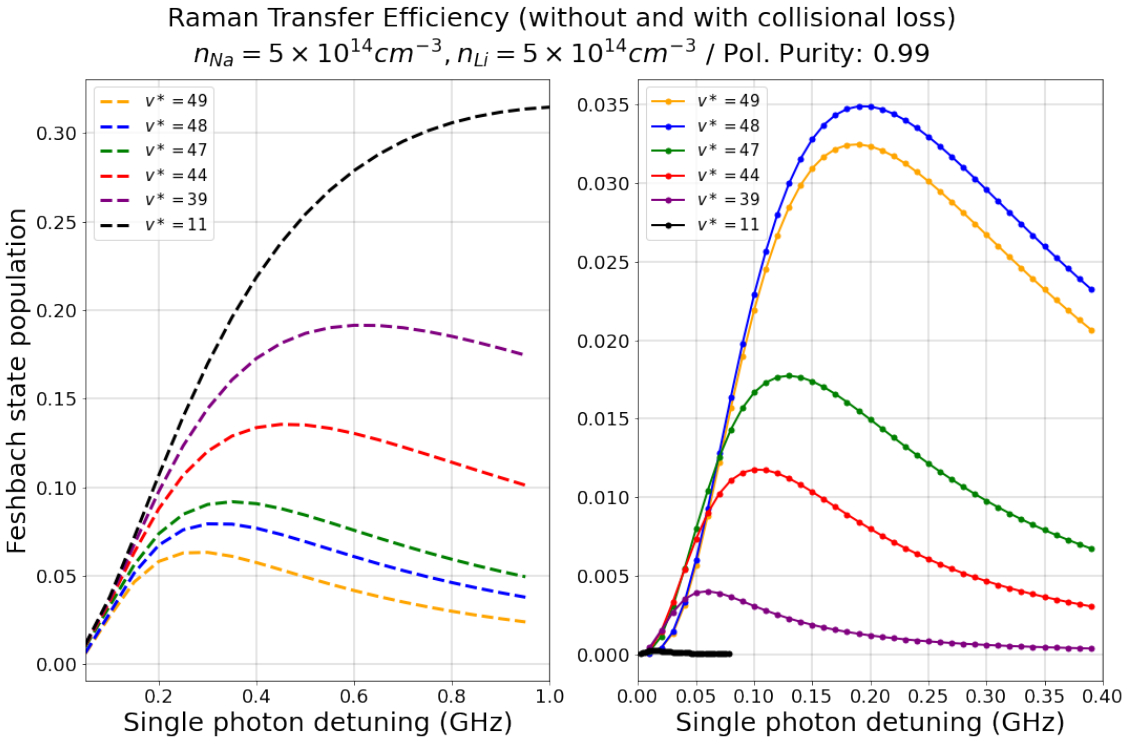

Figure 6-9: **Raman transfer with atomic and molecular decay as a function of Δ_M via different v^*.** The plots are the numerical calculation of free to Feshbach state Raman transfer with additional atomic and molecular decay driven by the upleg pulse. The left (right) plot is the result without (with) a molecule-atom collisional loss term. The calculation is done assuming upleg beam polarization purity of 99% and atomic densities of 5×10^{14} cm^{-3}. The upleg beam power is set to 300 mW and the downleg beam power is set to 100 μW with beam waists of 50 μm.

Ω_{down}/Δ_M for minimum total loss. Therefore, it is necessary to increase Ω_{up} to actually benefit from larger Ω_{eff}. Since FCF is proportional to the larger density among the two atomic clouds (Na and Li) [10], this can be achieved by preparing atomic clouds with higher densities.

However, Feshbach molecules are chemically reactive with Na atoms or Li atoms, and it is natural to assume that the molecule+atom collisional loss rates are close

[10]Photoassociation (PA) rate equation is given by $\dot{n}_{Na} = \dot{n}_{Li} = -\bar{K} I n_{Na} n_{Li}$ where I is the PA laser intensity and $\bar{K}$ is the intensity normalized PA rate coefficient. By defining $D \equiv n_{Li}(0) - n_{Na}(0) = n_{Li}(t) - n_{Na}(t)$, the rate equation is expressed as $\dot{n}_{Li} = -\bar{K} I n_{Li}(n_{Li} + D)$. The solution of the differential equation is given by $n_{Na}(t) = \frac{D}{[n_{Li}(0)/n_{Na}(0)]e^{D\bar{K}It} - 1}$ and $n_{Li}(t) = \frac{-D}{[n_{Na}(0)/n_{Li}(0)]e^{-D\bar{K}It} - 1}$. *i)* If $n_{Na}(0) = n_{Li} = n(0)$, $\frac{n(t)}{n(0)} = \frac{1}{1+n(0)\bar{K}It} \approx 1 - n(0)\bar{K}It$ and therefore FCF is proportional to $n(0)$ of the relation $n(0)\bar{K}I = \Omega_{PA}^2/\Gamma_{PA}$. *ii)* If $n_{Na}(0) \gg n_{Li}$, $\frac{n_{Li}(t)}{n_{Li}(0)} \approx e^{-n_{Na}(0)\bar{K}It} \approx 1 - n_{Na}(0)\bar{K}It$ and therefore FCF is proportional to $n_{Na}(0)$.

to the universal values [11]. Universal loss rate constants are $K_{\mathrm{NaLi-Na}} \approx 1.53 \times 10^{-10}$ s^{-1}cm^3 with Na atoms and $K_{\mathrm{NaLi-Li}} \approx 3.425 \times 10^{-10}$ s^{-1}cm^3 with Li atoms. Figure 6-9 is the result of numerical calculations of the Raman transition with atomic and molecular decay as a function of Δ_M through different excited states v^* with stronger Ω_{up} achieved by denser atomic clouds (5×10^{14} cm^{-3}). The left graph is the result without including the molecular loss from molecule + atom collisions and the right graph includes the collisional losses of molecules by Na and Li atoms. The calculation is done assuming a polarization purity of the upleg beam of 99% and atomic densities of 5×10^{14} cm^{-3}. The upleg beam power is set to 300 mW and the downleg beam power is set to 100 μW with beam waists of 50 μm. With denser atomic clouds, much higher population transfer can be achieved especially with low v^* (for example, more than 30% via $v^* = 11$) if collisional losses do not exist, as you can see in the left plot. Once, collisional losses are taken into account, as transfer with low lying v^* tends to have a longer t_π, experiences a longer time for collisional loss as well, and therefore, stronger suppression of population transfer, as shown in the right graph. Therefore, higher densities may not be always helpful because of the universal rate limited collisional loss of NaLi with surrounded atoms [12], and only a few percent transfer is achieved with $n_{Na} = n_{Li} = 5 \times 10^{14}$ at most with $v^* = 48$. It is important to optimize both the atomic densities and v^* to maximize the number of Feshbach molecules.

In summarity, atomic scattering is suppressed by increasing the detuning from the atomic resonance, e.g. going to smaller v^*. However, this increases molecular scattering and gives an optimum detuning. Density can speed up the molecule formation, but then runs into the limit of collisional loss. For the optimum choice, all three loss

[11] It is experimentally confirmed by us that NaLi Feshbach molecule+atom (with Na state $|F = 2, m_F = 2\rangle$ and $|F = 1, m_F = 1\rangle$, and Li state $|F = 1/2, m_F = 1/2\rangle$) collision rates are s-wave universal rate limited. However, ground-state molecules in their stretched state live long with Na atoms also in their stretched state (when they are aligned) unlike Feshbach molecules. (The collisional loss rate constant is about 2 orders of magnitude smaller than the universal value.)

[12] We will see later that, indeed, $n = 5 \times 10^{14}$ gives more transfer than $n = 5 \times 10^{15}$. The loss with Li atoms is about twice larger than with Na atoms, and preparing the Li density 10 times lower while keeping the Na density high may lead to a higher transfer efficiency. However, this will require loading 10 times less Li atoms, and the transferred molecule number will be less since a 10 time lower Li number does not increase the transfer efficiency by more than a factor of 10.

processes contribute about equally.

6.2 Direct transfer to the ro-vibrational ground state

The second approach is to perform a single Raman transfer from an ultracold gas of atoms directly to the molecular ro-vibrational ground state. This approach allows for a single Raman transfer to create ground-state molecules, and hence, the experimental complexity can be reduced. The FCF of the ground state $v = 0$ to an excited state v^* transition becomes comparable to or even smaller than that of the free to v^* transition for a high v^* as in Fig. 6-3, and it is natural to choose a rather lower lying v^* as an intermediate excited state for the Raman transition. As an example, Figure 6-10 illustrates a free-to-ground direct Raman transition via an intermediate excited state $v^* = 26$, $N = 1$, $m_N = -1$ using $\sigma-$ polarization for both upleg and downleg beams. As in the Raman transition from free to the Feshbach state, high intensity upleg can act on the downleg path causing light scattering. The binding energy of the ground state (6.2381 THz) is large compared to that of the Feshbach state (5.85 GHz), and therefore, the rate of this molecular light scattering can be tuned to much smaller value than we saw in the free-to-Feshbach state Raman transfer. Upleg frequency can be tuned to have relatively large detuning from the ground state to excited molecular state transition lines. However, achieving a sufficiently high two-photon Rabi frequency can be extremely challenging because of even smaller FCFs.

Direct Raman transfer from free to the $v = 0$ ground-state molecules can be divided into mainly two different situations: Either i) $\Omega_{down} \gg \Omega_{up}$ or ii) $\Omega_{down} \lesssim \Omega_{up}$ unlike the free-to-Feshbach state transfer where Ω_{down} was always greater than Ω_{up}. For case i) $\Omega_{down} \gg \Omega_{up}$, which is achieved with an intermediate state $0 \leq v^* \leq 31$ when the maximum upleg power is set to 300 mW and the downleg power to 10 mW, the molecular photon scattering by the strong downleg cannot be neglected, while the atomic photon scattering by the upleg is relatively small, since the upleg frequency is far detuned from the Li D_1 and D_2 lines. Close-to-perfect Raman transfer to the ground state could be possible using one of the excited states deep in the excited $c^3\Sigma^+$

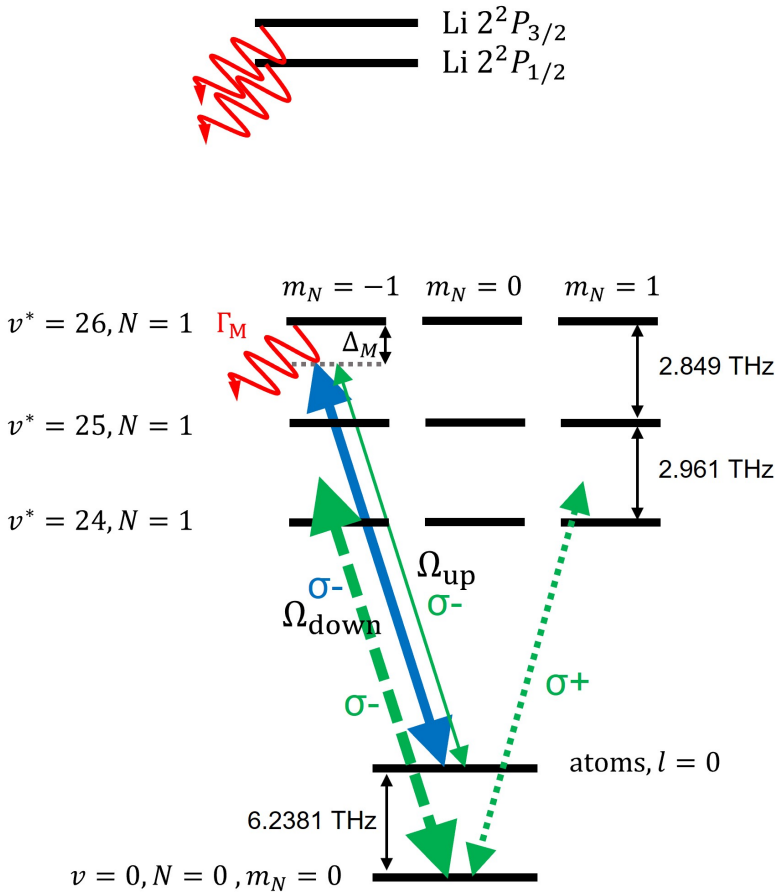

Figure 6-10: **Illustration of a Raman transition from free atoms to the rovibrational ground state of NaLi** $a^3\Sigma^+$**.** $v^* = 26$, $N = 1$, $m_N = -1$ in the $c^3\Sigma^+$ potential is chosen as an intermediate excited state as an example. $\sigma-$ polarization for both upleg (green arrow) and downleg (blue arrow) beams are used. High intensity upleg pulse with $\sigma-$ polarization indicated with a dashed green arrow can drive transitions from the ground state $(v = 0, N = 0, m_N = 0)$ to vibrational states with $N = 1, m_N = -1$ in the $c^3\Sigma^+$ potential. Small fraction of $\sigma+$ due to polarization impurity of the upleg can drive transitions from the ground state to excited states in the $c^3\Sigma^+$ potential with $N = 1, m_N = 1$.

potential if laser coherence time was not limited and collisional losses were negligible. Eliminating collisional loss could possibly be achieved by having only one Na and Li atom per each 3D optical lattice site or optical tweezer. However, as the optical frequency difference between the upleg and downleg is several THz, one cannot use a single laser source for both pulses, and the coherence time of these beams are expected to be not much smaller than 1 ms. Here, we will assume that the laser coherence time is only 50 μs [13]. Under these conditions, the maximum transfer occurs when $\text{Loss}|_{\text{tot}} \approx \text{Loss}|_{\text{M}} \approx \frac{\Omega_{\text{down}}^2}{4\Delta_{\text{M}}^2} \cdot \Gamma_{\text{M}} \cdot \text{t}_\pi$ is minimized. If we set the π pulse duration $t_\pi = \frac{4\pi\Delta_M}{\Omega_{up}\Omega_{down}}$ to be at most the coherence time t_C, we find that $\text{Loss}|_{\text{tot}} \approx \frac{4\pi}{\Omega_{\text{up}}^2 \cdot \text{t}_\text{C}} \cdot \Gamma_{\text{M}}$, and therefore, less loss for larger upleg FCF. On the other hand, for case ii) $\Omega_{down} \lesssim \Omega_{up}$, which is achieved with an intermediate state $32 \leq v^* \leq 52$, the molecular loss by the downleg pulse becomes significantly smaller than the atomic loss if far detuned ($|\Delta_M| > \Gamma_M$). Similarly, the total loss is expressed as $\text{Loss}|_{\text{tot}} \approx \text{Loss}|_{\text{A}} = \frac{\Omega_{\text{A}}^2}{4\Delta_{\text{A}}^2} \cdot \Gamma_{\text{A}} \cdot \text{t}_\text{C}$, and therefore the loss is smaller for lower v^*. However, we are more limited by small two-photon Rabi coupling strength, and unable to be in the far detuned limit. Therefore, the total loss $\text{Loss}|_{\text{tot}} \approx \text{Loss}|_{\text{M}} = \frac{\Omega_{\text{up}}^2 + \Omega_{\text{down}}}{4\Delta_{\text{M}}^2} \cdot \Gamma_{\text{M}} \cdot \text{t}_\text{C} \approx 4\pi^2 \left(\frac{1}{\Omega_{\text{up}}^2} + \frac{1}{\Omega_{\text{down}}^2}\right) \cdot \Gamma_{\text{M}}$, and less loss through v^* with smaller $\left(\frac{1}{\Omega_{up}^2} + \frac{1}{\Omega_{down}^2}\right)$. A strong correlation between the maximum transferred population to the ground state and the FCFs can be seen in Fig. 6-11. Assuming 30 μm beam waists for upleg and downleg beams instead of 50 μm allows at least a factor of few higher transfer efficiency for transitions with relatively small upleg FCF as it allows further transfer within 50 μs. However, as will be discussed later in the chapter, this will create larger inhomogeneity, causing larger two-photon detuning during the Raman transition.

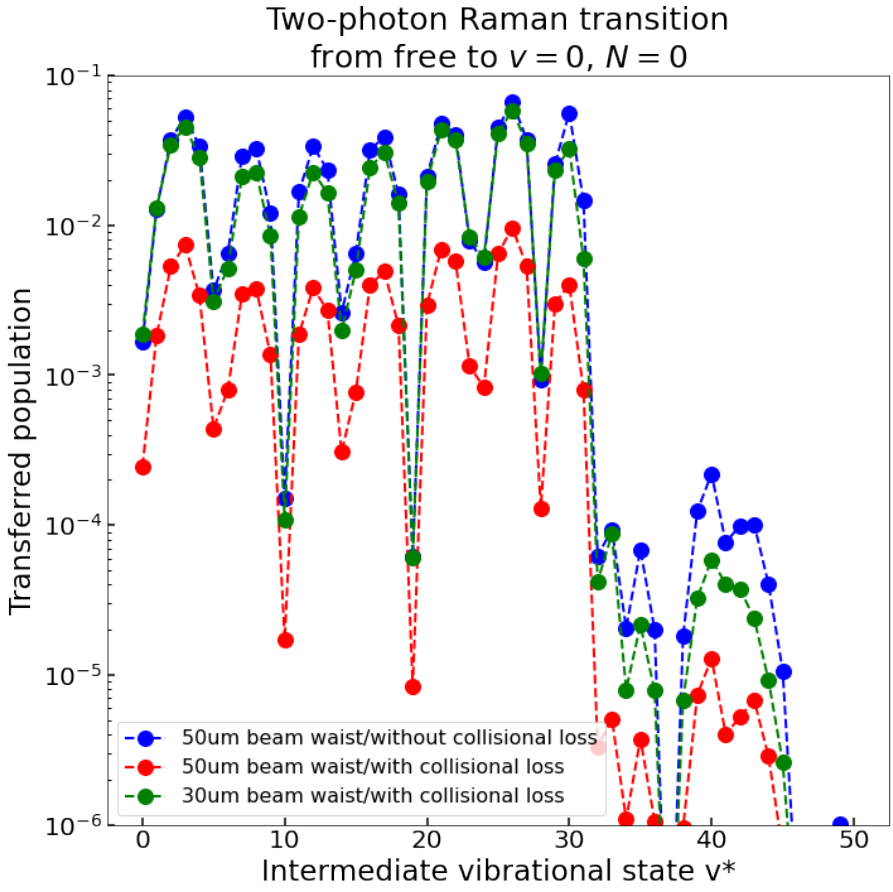

Figure 6-11: **Maximum transfer to the ground state of NaLi $a^3\Sigma^+$ potential as a function of intermediate excited vibrational state v^*.** Transfer efficiency to the ground state was numerically calculated for atomic densities of $n_{Na} = n_{Li} = 5 \times 10^{14}\text{cm}^{-3}$ with the upleg power of 300 mW and downleg power of 10 mW. Molecule+atom collisional loss is ignored only in the blue plot. Blue and red plots are the results with the upleg and downleg beam waists of 50 μm and the green plot is the result with 30 μm. Polarization purity of the two Raman beams are assumed to be 95 % and the pulse duration is limited to 50 μs.

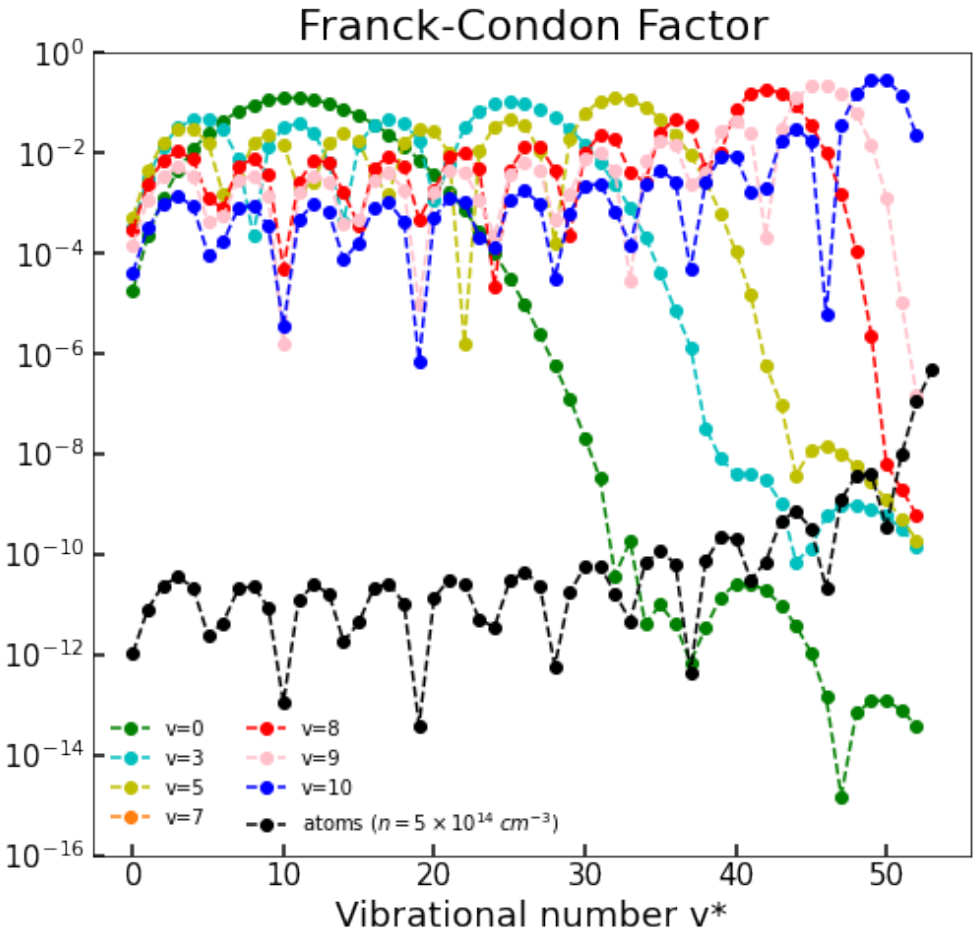

Figure 6-12: **Franck-Condon factors between vibrational states in $a^3\Sigma^+$ and $c^3\Sigma^+$ potentials.** They are calculated from *ab initio* potentials. Free-to-bound (v^*) FCFs of $n = 5 \times 10^{14}$ cm^{-1} are indicated in black.

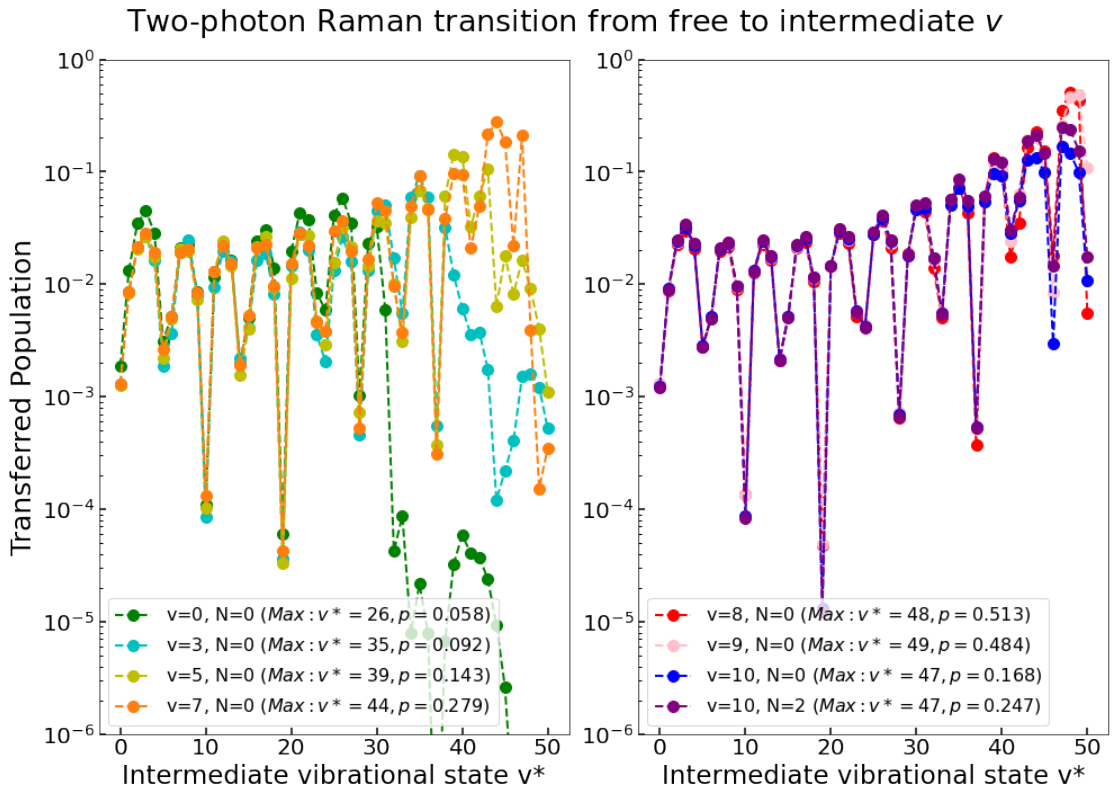

Figure 6-13: **Maximum transfer to the ground state of NaLi $a^3\Sigma^+$ potential as a function of intermediate excited vibrational state v^*.** Transfer efficiency to the ground state was numerically calculated for atomic densities of $n_{Na} = n_{Li} = 5 \times 10^{14}\text{cm}^{-3}$ with the upleg power of 300 mw and downleg power of 10 mW except for $v = 10$. The blue and purple data are with the downleg power of 100 μW. Beam waist, polarization purity and pulse duration of the two Raman beams are assumed to be 30 μm, 95 % and at most 50 μs respectively except for $v = 10$. Pulse duration to $v = 10$ is limited to 1 ms.

6.3 Free to intermediate vibrational state v

The goal of this section is to optimize the free-to-bound transition by exploring Raman transitions from free to an intermediately bound vibrational state in the $a^3\Sigma^+$ potential. As mentioned in the previous sections, for Raman transition from free to Feshbach state (a high-lying vibrational state in $a^3\Sigma^+$ potential), high atomic and molecular photon scattering by the upleg acting on the downleg path is the main limiting factor while for transfer to the ground state $v = 0$, $N = 0$ (a low-lying vibrational state), molecular photon scattering by weak upleg Rabi frequency is the main limiting factor. Collisional loss is a common factor in both cases.

Choosing a vibrational state v with a large binding energy can decouple the downleg and upleg paths by creating a large frequency difference of the two Raman beams. However, low-lying vibrational states v tend to have a small FCF with a highly excited vibrational state v^* in the $c^3\Sigma^+$ potential and therefore require the use of low-lying v^* that has a small Frank-Condon factor (FCF) with the atomic scattering wavefunction. The calculation of FCF between different v and v^* is plotted in Fig.6-12.

Transfer efficiency to a bound state v from free atoms including atomic and molecular photon scattering loss and collsional loss is numerically calculated and plotted in Fig.6-13. The duration of the Raman pulse is restricted to at most 50 μs for $v < 10$ and 1 ms for the final state $v = 10$. Atomic densities are assumed to be $n_{Na} = n_{Li} = 5 \times 10^{14}\text{cm}^{-3}$, the upleg and downleg power are set to 300 mW and 10 mW except for $v = 10$. The blue and purple data for $v = 10$ in Fig.6-13 are with a downleg power of 100 μW. The beam waist, polarization purity and pulse duration of the two Raman beams are assumed to be 30 μm, 95 % and at most 50 μs, respectively, except for $v = 10$. The transfer efficiency to the $v = 8$ state reaches more than 50 % through $v^* = 48$, which is greater than what can be achieved by transfer to the

[13]In principle, one can achieve longer coherence time by using cavity lock to a stabilized cavity. However, we initially thought our STIRAP lasers for coherent transfer of NaLi in the Feshbach state to the ground state is in the order of 50 μs from the fact that the transfer efficiency drops for longer STIRAP pulses. However, we later noticed that this is possibly due to AC Stark shifts in the order of 10 kHz causing large two-photo detunings. Although we assumed that the coherence time of two Raman beams for free-to-bound transfer is only 50μs, this is probably one of the worse we can achieve

Feshbach state, which is $\sim 25\%$ or to the ground state, which is $\sim 6\%$.

6.4 Comparison of three all-optical methods

We have explored three approaches: four-photon Raman transfer via Feshbach state, direct two-photon transfer to the rovibrational ground state, and four-photon transfer via intermediate vibrational state. The first approach is the most obvious approach, and therefore the first approach we considered, which is simply replacing a Feshbach resonance with a Raman transition. This approach allows using a single laser source for both Raman beams, and having long coherence time (~ 1 ms or more). However, the large photon scattering rate prevents one from taking advantage of this long coherence time. The second approach, direct transfer to the ground state, is the most simple among the three. Photon scattering is relatively small, due to the large binding energy of the ground state. However, the transfer efficiency is mainly limited by weak Rabi coupling strength or short two-photon coherence time. The analysis of the last approach is to find the middle ground of the first two approaches. The transfer to state $v = 8, N = 0$ gave the best performance, and here we only focus on this particular state among different paths of the third approach. Figure 6-14 is the result of the three approaches for different atomic densities. Transfer efficiency increases for higher densities until collisional loss becomes significant. For example, for transfer to $v = 0$, $N = 0$, the transfer efficiency is rather lower when $n = 5 \times 10^{15}$ cm^{-3} than when $n = 5 \times 10^{14}$ cm^{-3}. Table 6.2 shows the list of limiting factors for efficient Raman transfer, comparing the three approaches for different atomic densities.

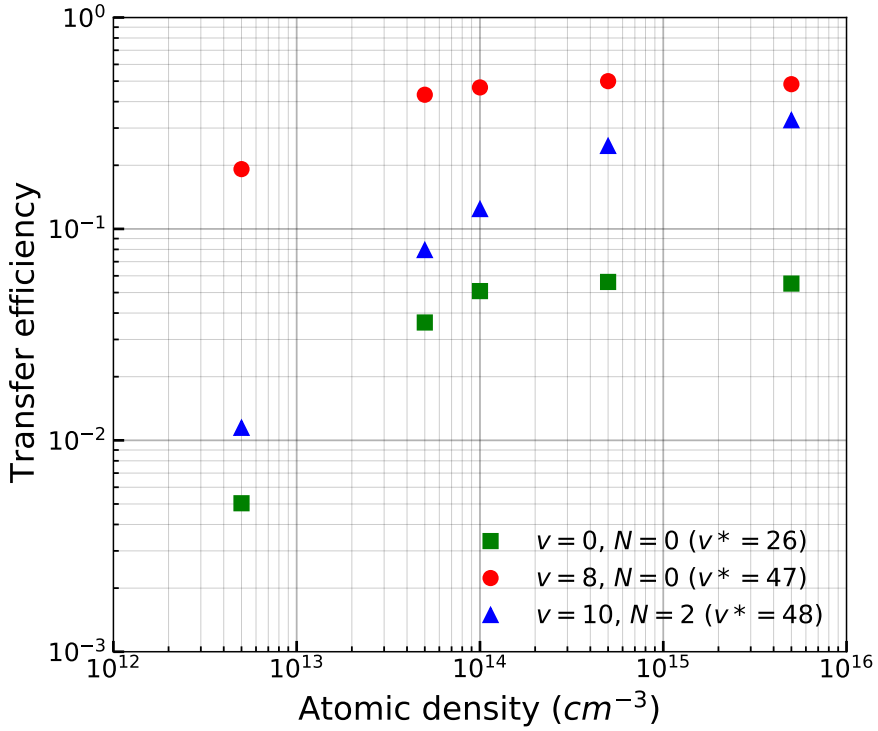

Figure 6-14: **Maximum transfer to a vibration state v in NaLi $a^3\Sigma^+$ potential as a function of atomic density.** Transfer efficiency to three different bound states are numerically calculated for different atomic densities with the upleg power of 300 mW and downleg power of 10 mW except for $v = 10$. $v = 10$, $N = 2$ is with the downleg power of 100 μW. Beam waist, polarization purity and pulse duration of the two Raman beams are assumed to be 30 μm, 95 % and at most 50 μs respectively except for $v = 10$. Pulse duration to $v = 10$ is limited to 1 ms.

Density (cm^{-3})	$v = 0,\ N = 0$ (via $v^* = 26$)	$v = 8,\ N = 0$ (via $v^* = 48$)	$v = 10,\ N = 2$ (via $v^* = 47$)
5×10^{14}	5.613 %, 16.844us **Weak Rabi Coupling** **Collisional Loss** $\gg$ Atomic Scattering, Molecular Rayleigh Scattering	49.991 %, 2.510 us **Weak Rabi Coupling** **Collisional Loss** $>$ Atomic Scattering, Molecular Rayleigh Scattering	24.686%, 2.712us **Molecular Rayleigh Scattering** **Weak Rabi Coupling** **Collisional Loss** $\gg$ Atomic Scattering
1×10^{14}	5.081%, 50us **Weak Rabi Coupling** $>$ Collisional Loss $\gg$ Atomic Scattering, Molecular Rayleigh Scattering	46.688 %, 11.001 us **Weak Rabi Coupling** **Collisional Loss** $>$ Atomic Scattering, Molecular Rayleigh Scattering	12.414 %, 6.484us **Molecular Rayleigh Scattering** **Weak Rabi Coupling** $>$ Collisional Loss $\gg$ Atomic Scattering
5×10^{13}	3.609 %, 50 us **Weak Rabi Coupling** $\gg$ Collisional Loss $\gg$ Atomic Scattering Molecular Rayleigh Scattering	43.122 %, 19.000 us **Weak Rabi Coupling** $>$ Collisional Loss $>$ Atomic Scattering $>$ Molecular Rayleigh Scattering	7.943 %, 8.101 us **Molecular Rayleigh Scattering** **Weak Rabi Coupling** $\gg$ Collisional loss $\gg$ Atomic Scattering
5×10^{12}	0.504%, 50us **Weak Rabi Coupling** $\gg$ Collisional Loss Atomic Scattering, Molecular Rayleigh Scattering	19.180%, 50us **Weak Rabi Coupling** $>$ Atomic Scattering $\gg$ Collisional loss, Molecular Rayleigh Scattering	1.146%, 14.341us **Weak Rabi Coupling** **Molecular Rayleigh Scattering** $\gg$ Atomic Scattering Collisional Loss

Table 6.2: **Limiting factors of free-to-bound Raman transition.** Three different cases, transfer to the ground state, intermediate vibrational state $v = 8$ and Feshbach state, are analyzed for four different atomic densities. The analysis is performed with a Raman beam waist of 30 um and a upleg power of 300 mW. The downleg power (maximum pulse duration) is 10 mW (50 us) for free to $v = 0$ and $v = 8$ transitions and 100 μW (1 ms) for free to $v = 10$ transitions. The maximum transfer efficiencies and the time it takes to reach that value are colored blue. The strongest contributions on limiting the transfer are in bold text.

6.4.1 AC stark shifts

So far, all calculations have been done with perfect compensation of AC Stark shifts driven by the two Raman beams. Although there are ways to experimentally compensate for these light shifts [113], it can be challenging to completely cancel them out, and single-photon and two-photon detunings may vary during a Raman transfer. Therefore, it is important to analyze the size of light shifts caused by the Raman beams and the effects on free-to-bound transfer efficiencies. AC stark shifts can be broken down mainly into two parts: AC Stark shifts on the downleg path and on the upleg path. Here, we define the AC Stark shift on the downleg (upleg) path as a change in the energy difference between the intermediate excited state, e, and the final state (initial state), f (i), as illustrated in Figure 6-15. There are three leading terms of the AC Stark shift on the downleg (up) path: The light shift of state e and f (i) driven by the downleg (upleg) coupling between these two states, the light shift of state e by the upleg (downleg) coupling between state e and i (f), and the light shift of state f (i) by the upleg (downleg) coupling between state f (i) and nearby excited states, e'_js. However, the light shift of state i by the downleg is relatively small among these terms, and the two AC Stark shifts are approximated as:

AC Stark shift on the downleg path

$$\approx \frac{(\Omega_{down}^{f,e})^2}{2\Delta_M} + \frac{(\Omega_{up}^{i,e})^2}{4\Delta_M} + \sum_j \left[\frac{(\Omega_{down}^{f,e'_j})^2}{4\Delta_M} + \frac{(\Omega_{up}^{f,e'_j})^2}{4(E_B + \Delta_M)} \right] \tag{6.7}$$

AC Stark shift on the upleg path

$$\approx \frac{(\Omega_{down}^{f,e})^2}{4\Delta_M} + \frac{(\Omega_{up}^{i,e})^2}{2\Delta_M} \tag{6.8}$$

where, $\Omega_x^{y,z}$ is the coupling strength between state y and z by a Raman beam x, Δ_M is the single-photon detuning, and E_B is the binding energy of the final state f. The common factors in Eq. 6.7 and 6.8 serve as changes in single-photon detuning during

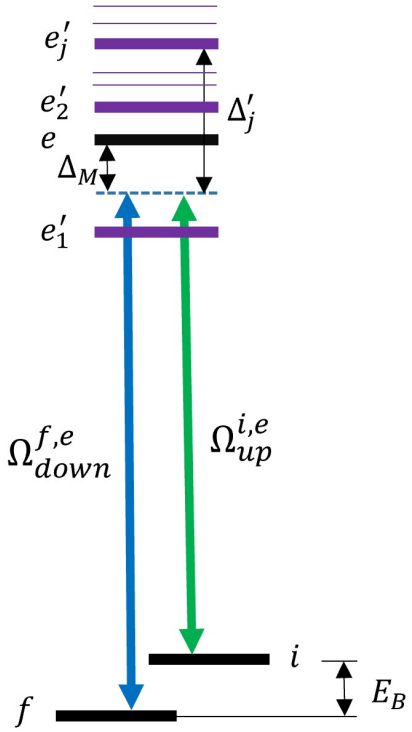

Figure 6-15: **Illustration of a lambda type two-photon transition with multiple excited states near an intermediate excited state.** Initial state i is coupled to an excited state e by a upleg beam with coupling strength of $\Omega^{i,e}_{up}$. Final state f is coupled to an excited state e by a downleg beam with coupling strength of $\Omega^{f,e}_{down}$. There may be non-zero coupling between state i or f and other excited states e'_js with coupling strength of Ω_x^{y,e'_j} where $x = up, down$ and $y = i, f$. Δ_M is the single-photon detuning, Δ'_j is the upleg (downleg) detuning from transition i (f) to e'_j, and E_B is the binding energy of the final state, f.

a Raman transition, and the effective single-photon detuning is given by:

$$\bar{\Delta}_M \approx \Delta_M + \frac{(\Omega_{down}^{f,e})^2}{4\Delta_M} + \frac{(\Omega_{up}^{i,e})^2}{2\Delta_M}. \tag{6.9}$$

On the other hand, the difference between Eq. 6.7 and 6.8 serve as the change in two-photon detuning, and if the system is on two-photon resonance in the limit of weak light coupling, the effective two-photon detuning is given by:

$$\begin{aligned} \bar{\delta}_M &\approx \delta_M + \frac{(\Omega_{down}^{f,e})^2}{4\Delta_M} - \frac{(\Omega_{up}^{i,e})^2}{2\Delta_M} + \sum_j \left[\frac{(\Omega_{down}^{f,e'_j})^2}{4\Delta_M} + \frac{(\Omega_{up}^{f,e'_j})^2}{4(E_B + \Delta_M)} \right] \\ &= \delta_M + \bar{\delta}_{down} + \bar{\delta}_{up} \end{aligned} \tag{6.10}$$

where $\bar{\delta}_{down}$ and $\bar{\delta}_{up}$ are defined as:

$$\begin{aligned} \bar{\delta}_{down} &\equiv \frac{(\Omega_{down}^{f,e})^2}{4\Delta_M} + \sum_j \frac{(\Omega_{down}^{f,e'_j})^2}{4\Delta_M} \\ \bar{\delta}_{up} &\equiv -\frac{(\Omega_{up}^{i,e})^2}{2\Delta_M} + \sum_j \frac{(\Omega_{up}^{f,e'_j})^2}{4(E_B + \Delta_M)}. \end{aligned} \tag{6.11}$$

The effective single-photon and two-photon detunings are calculated for three different free-to-bound transitions: transfer to $v = 0, N = 0$ via $v^* = 26$, transfer to $v = 8, N = 0$ via $v^* = 47$ and transfer to $v = 10, N = 2$ via $v^* = 48$. The results are in Table 6.3. AC Stark shift by the upleg acting on the downleg path plays a major role in creating two-photon detuning. To what extent AC stark shifts should be compensated in order to maintain the transfer efficiencies obtained from complete compensations can be estimated by comparing the calculated shifts with the Raman pulse duration. In other words, effective two-photon detuning must be much less than the inverse of the Raman pulse duration to prevent a significant decrease in transfer. For this, both Raman beams and additional laser beams that may be used for light shift compensation must be intensity, polarization, and frequency stabilized to meet this condition. Laser intensity fluctuations and light shift compensation fluctuation are required to be much less than 2.5 %, 0.9 % and 0.15 % for transfer to state $v = 0$,

$N = 0$, state $v = 8$, $N = 0$, and $v = 10$, $N = 2$, respectively.

Meeting the estimated laser requirements can be already demanding even though we only considered nearby excited molecular states in NaLi $c^3\Sigma$ potential. Including also the states in the NaLi $1^3\Pi$ potential is important for an accurate analysis. As the AC Stark shift by the upleg acting on the downleg path takes a dominant part of the two-photon detuning, we now focus only on $\bar{\delta}_{up}$. The calculations of $\bar{\delta}_{up}$ by $c^3\Sigma^+$ and $b^3\Pi^+$ are listed in Table 6.4. $\bar{\delta}_{up}$ by $c^3\Sigma^+$ and $b^3\Pi^+$ are comparable in size and add up to create even larger two-photon detuning. Therefore, laser intensity fluctuations and light shift compensation fluctuation are rather required to be much less than 1.5 %, 0.39 % and 0.08 % for transfer to state $v = 0$, $N = 0$, state $v = 8$, $N = 0$, and $v = 10$, $N = 2$ respectively. For example, if the two Raman beams have a Gaussian profile with a beam waist of 30 μ m and the atomic clouds are in an isotropic harmonic trap leading to density of 10^{14} cm^{-3} and 4 μm cloud size, without any light shift compensation, the free-to-bound transfer efficiencies become 0.1 %, 0.4 %, and 0.05 % instead of 5.1 %, 46.7 %, and 12.4 % as listed in Table 6.3 and 6.4.

An intermediate excited state, which allows the upleg wavelength to be at a 'magic wavelength' (causes a significantly smaller AC Stark shift), is worth exploring at this point. The calculations of $\bar{\delta}$ taking into account the potentials $c^3\Sigma^+$ and $b^3\Pi$ are given in Fig. 6-16. For example, when transferring free atoms to the $v = 0$, $N = 0$ state, choosing an excited intermediate state $v^* = 3$ or $v^* = 12$, which requires a upleg wavelength of $\sim$ 930.822 nm, gives a smaller AC Stark shift compared to choosing $v^* = 26$. $\bar{\delta}$ is approximately 0.25 MHz and 0.6 MHz respectively, and without any light shift compensation, under the same condition explained above, the free-to-bound transfer efficiency is 1.8 % and 0.7 % instead of 5%, and 3.2% respectively. These are higher than 0.1 %, which we can achieve with $v^* = 26$.

Final State	Downleg Power	$\bar{\Delta}_M - \Delta_M$	$\bar{\delta}_{down}$	$\bar{\delta}_{up}$	Transfer Efficiency (Time t_R)	Laser Requirements
$v = 0$ $N = 0$ (v^*=26)	10 mW (100 μW)	$\sim$ 100 kHz ($\sim$ 10 kHz)	$\sim$ 100 kHz ($\sim$ 10 kHz)	$\sim$ -800 kHz	5.1 % (50 μs)	$\delta I \ll 2.5\%$ (6.238 THz) 724.315 nm, 713.561 nm a.Do not need second Raman transition b. Need an extra laser for the Downleg and a way to lock it
$v = 8$ $N = 0$ (v^*=48)	10 mW (100 μW)	$\sim$ 300 kHz ($\sim$ 30 kHz)	$\sim$ 500 kHz ($\sim$ 50 kHz)	$\sim$ -12 MHz	46.7 % (11 μs)	$\delta I \ll 0.9\%$ (232.9 GHz) 671.684 nm, 671.334 nm a.Can use current STIRAP lasers for the second Raman transfer b.Need an extra laser for the Downleg and a way to lock it
$v = 10$ $N = 2$ (v^*=47)	100 μW (10 μW)	$\sim$ 1.5 MHz ($\sim$ 1 MHz)	$\sim$ 1.5 MHz ($\sim$ 1 MHz)	$\sim$ 100 MHz	12.4 % (6.5 μs)	$\delta I \ll 0.15\%$ (5.85 GHz) 672.108 nm, 672.099 nm a.We have all the lasers that we need for two step Raman transfer

Table 6.3: **AC Stark shifts and laser requirements.** Calculation is done with atomic densities of 1×10^{14} cm^{-3}, upleg power of 300 mW, Raman beam waists of 30 μm, and a maximum pulse duration of 50 μs. The laser intensity fluctuation δI should be much less than the ratio of $1/t_R$ to $\bar{\delta}$ to maintain the transfer efficiencies calculated with perfect light shift compensation.

In conclusion, all-optical transfer from free atoms to the NaLi rovibrational ground state of the $a^3\Sigma^+$ potential is not straightforward. A simple replacement of the well-established method of creating loosely bound Feshbach molecules with a two-photon Raman transition will lead to a transfer efficiency of less than 0.1%. However, careful selection of a Raman transition path (use of 'magic wavelength') or using additional lasers for light shift compensation may achieve a few percent or higher transfer efficiency to the ground state.

Final State	Upleg Power (Downleg Power)	$\bar{\delta}_{up}$ ($c^3\Sigma^+$)	$\bar{\delta}_{up}$ ($b^3\Pi$)	Transfer Efficiency (Time)	Laser Requirements
$v = 0$ $N = 0$ (v^*=26)	300 mW (10 mW)	$\sim$ -800 kHz	$\sim$ -500 kHz	5.1 % (50 μs)	$\delta I \ll 1.5\%$ 724.315 nm, 713.561 nm (6.238 THz)
$v = 8$ $N = 0$ (v^*=48)	300 mW (10 mW)	$\sim$ -12 MHz	$\sim$ -11 MHz	46.7 % (11 μs)	$\delta I \ll 0.39\%$ 671.684 nm, 671.334 nm (232.9 GHz)
$v = 10$ $N = 2$ (v^*=47)	300 mW (100 μW)	$\sim$ 100 MHz	$\sim$ 85 MHz	12.4 % (6.5 μs)	$\delta I \ll 0.08\%$ 672.108 nm, 672.099 nm (5.85 GHz)

Table 6.4: **AC Stark shifts and laser requirements including NaLi $b^3\Pi$ potential.** Calculation is with atomic densities of 1×10^{14} cm^{-3}, Raman beam waists of 30 μm, and maximum pulse duration of 50 μs.

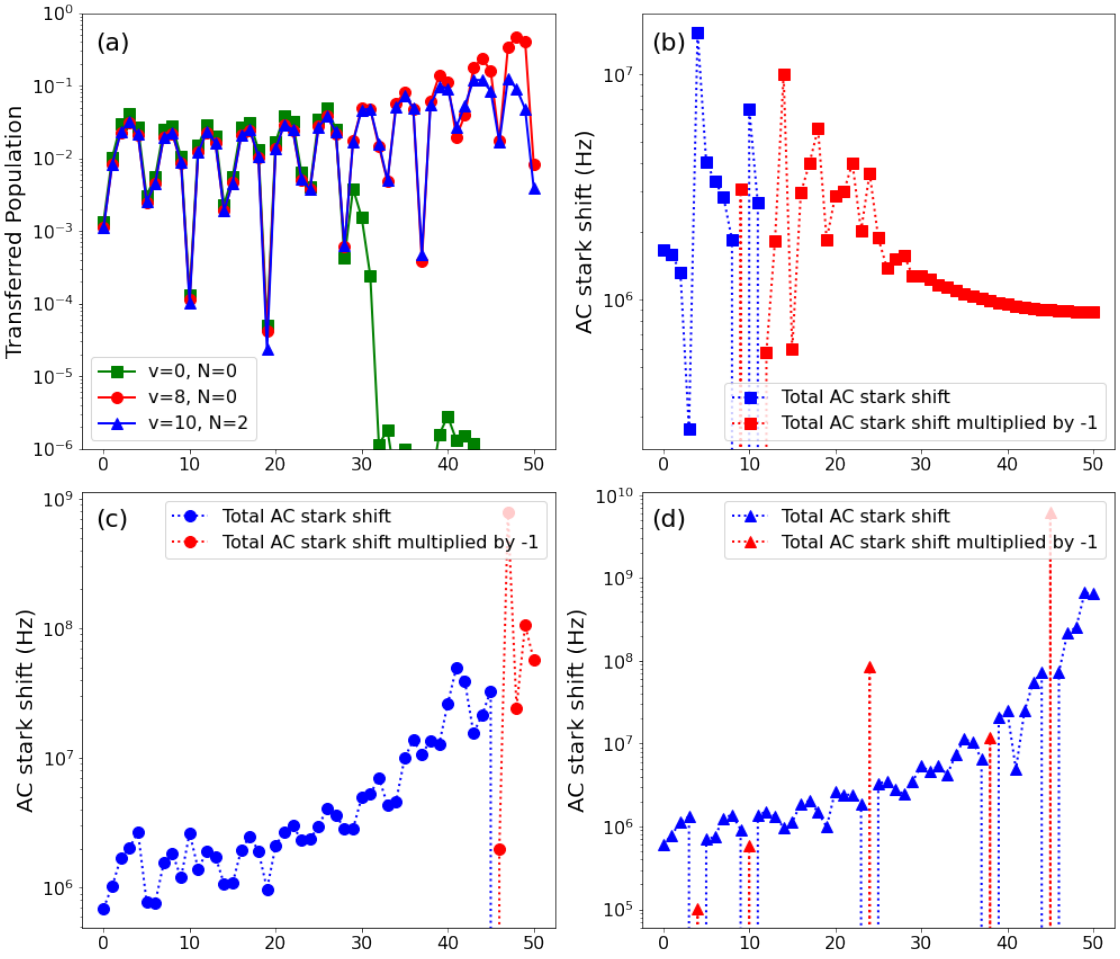

Figure 6-16: **Free-to-bound transfer efficiencies and two-photon detuning from both $c^3\Sigma^+$ and $b^3\Pi$ potentials.** (a) Numerically calculated transfer efficiencies from free atoms to a bound state via different intermediate excited state v^* are plotted for three different final bound states. (b),(c) and (d) are total effective two-photon detuning $\bar{\delta}$ including all the states in $c^3\Sigma^+$ and $b^3\Pi$ potentials. Data in square, circle, and triangle correspond to transfer to state $v = 0$, $N = 0$, state $v = 8$, $N = 0$, and state $v = 10$, $N = 2$ respectively.

Chapter 7

Summary and Outlook

7.1 Summary

This thesis described collision studies on $^{23}Na^{6}Li$ molecules in the triplet ground state. It explained a spectroscopic investigation of Feshbach resonances in two possible spin-polarized $^{23}Na^{6}Li+^{23}Na$ collisions from near 0 to 1400 G magnetic bias field using combined experimental and theoretical quantum chemistry approach. By focusing on analysis of the Feshbach spectrum solely on the basis of the experimental observations, we could rule out some of the possible coupling mechanism for the resonances, and estimate the number, lifetime, and size of stable NaLi-Na complexes. Together with coupled-channel calculations, although they cannot predict the position of resonances, for the first time, questions on the dominant interactions that are responsible for the resonances and the background loss, the qualitative difference between the two spin-stretched states, and the nature of the complex could be answered.

It also described the first observation of a Feshbach resonance between rovibrational ground-state molecules at ultracold temperatures. This discovery was made by careful search through a magnetic bias-field range of 1500 G with triplet NaLi molecules in the lower-stretched hyperfine state. The resonance rises from a background loss at the universal limit, which is not compatible with the most commonly studied models of ultracold collisions. The more than hundred-fold enhancement of loss observed implies the existence of a remarkably long-lived collision complex in a

system with barrier-free reactions in all channels [29] and requires full phase coherence for the flux reflected at short range destructively interferes with the quantum reflected flux. This result is surprising and raises many questions for future work.

In addition to the exploration of magnetically tuneable scattering resonances, ^{23}Na^{6}Li molecules in the triplet potential are suitable for magnetic trapping. With an improved experimental setup that allows magnetic trapping of ^{23}Na^{6}Li molecules, quantitative studies on various collisions in the magnetic trap was demonstrated by quantum state control of molecules and atoms. The molecular density is a factor of 10^5 higher than that of other magnetically trapped ultracold molecules [20, 100], and the temperature is $\approx 1\mu K$. This enabled observation of both atom-molecule and molecule-molecule collisions in the ultracold regime and sympathetic cooling of ^{23}Na^{6}Li by evaporative cooling of ^{23}Na in the magnetic trap.

This new method allows studies of molecular collisions in a photon-free environment. Experiments probing photo-induced loss for ultracold molecular systems in optical traps have been reported using chopped optical dipole traps or repulsive box potentials made with blue-detuned light. However, even for the longest dark times and the lowest intensities, photo-induces loss could not be completely suppressed, and loss rates consistent with universal loss were observed [50, 103, 104]. For magnetically trapped molecules, photo-induced losses can be studied with arbitrarily small light intensities.

Lastly, this thesis described numerical and theoretical work on finding a condition for all-optical creation of molecules using Raman transitions from ^{23}Na and ^{6}Li atoms to ^{23}Na^{6}Li molecules. The well-established method for creating ultracold bialkali molecules is by ultracold assembly which requires a Feshbach resonance to be at an experimentally accessible bias field and magnetic field stabilization within the width of the Feshbach resonance for an efficient magnetic association. All-optical creation of molecules is expected to broaden the choice of ultracold molecules to a larger pool and eliminate going to high magnetic fields. However, we discovered that all-optical transfer from free atoms to the NaLi rovibrational ground state of the $a^3\Sigma^+$ potential is not straightforward. Simple replacement of the well-established method of creating

loosely bound Feshbach molecules with a two-photon Raman transition will lead to a transfer efficiency of less than 0.1%. With careful selection of a Raman transition path (use of 'magic wavelength') or using additional lasers for light shift compensation, we expect to achieve transfer efficiency comparable to that of the scheme with the Feshbach resonance.

7.2 Outlook

7.2.1 Mysteries of non-universal reactive collisions

For chemically stable collisions, one would expect loss rates below the universal limit and for highly reactive collisions, loss rates at the universal limit. Many experiments found loss rate constants at or close to the universal value predicted for reactive collisions even for non-reactive molecules. It has been proposed that this is possibly due to "sticky collisions" connected with long-lived complexes [37–39, 89, 101] and intense trap light, which can induce photo-chemistry. Recent experiments [40,50,102] showed that optical traps can cause short lifetimes of molecules and are not truly conservative, but others [103,104] showed inconclusive results, and the reason for fast loss in non-reactive systems still remain as an open question.

In addition, we have now observed several types of highly reactive collisions where loss rates do not match the universal limit. Our collision studies in a magnetic trap show that NaLi molecules with various collision partners have loss rates that deviate from the universal limit although they are all reactive. First, p-wave loss rate between NaLi molecules in the upper-stretched state was measured to be a factor of 2 higher than the universal limit in a 1,596 nm 1D lattice [33] although molecules in the lower-stretched state decay at the universal limit [73] as expected. This was initially thought to be originating from an error in the trap volume estimation of the 1D optical lattice or additional loss due to the trapping light or magnetic force at high field. However, we observed the same factor of 2 in a light-free magnetic trap with low bias field near the trap bottom. Second, s-wave collisions in NaLi spin mixtures and

NaLi+Na mixture have loss rates much lower than the universal limit. Although all collision systems are reactive, the absorption probability at close range is much lower than one. This is well understood for the collisions in the spin-stretched Na+NaLi mixture [29, 33] where the quartet potential in the input channel is non-reactive, and inelastic collisions are only possible via spiflips. However, this explanation does not apply to the *s*-wave molecule-molecule collisions. This is a new open question that is not explained with existing models. In addition, a Feshbach resonance has been observed between molecules in a strongly reactive input potential [73]. These observations suggest that collisional resonances and collisional complexes should occur more generally and motivate more systematic studies of collisions involving NaLi and collision partners in various hyperfine states, and also for other molecules [112].

7.2.2 Towards a deeply degenerate gas of NaLi

Sympathetic cooling of NaLi by evaporation of Na atoms has been demonstrated in this work and also in [34]. In particular, this thesis described the microwave evaporation of Na in a magnetic trap to cool NaLi molecules. This increased the phase space density of the molecules by a factor of ≈ 16. This can be further improved but is eventually limited by the slow Na thermalization rate, which is significantly slower than the rate of elastic collisions between Na and NaLi. Using a second trap for Na that enhances the thermalization rate should allow cooling into the quantum-degenerate regime.

Another approach toward a deeply degenerate gas of NaLi is to have somewhat lossy evaporation, but compensate for this by increasing the numbers of trapped atoms and molecules. In Chapter 6, we explored the possibility of all-optical formation of NaLi in the triplet ground state. Although this method cannot increase the atom-to-molecule conversion efficiency but can only do a similar job, it allows complete elimination of optical trapping. Combining the magnetic trapping that we saw in Chapter 5 and all-optical formation of molecules can be a new direction to achieve a higher number of molecules, since multiple transfer steps from one trap to another that cause significant loss of atoms or molecules can also be eliminated.

7.2.3 Creation of stable qubits with rotational states

The work of this thesis mainly focused on molecular collisions and quantum chemistry. However, ultracold molecules are also recognized as a new platform for quantum computing and quantum information processing. Qubit coherence times are critical to the performance of any robust quantum computing platform. With state-of-the-art technology, the most stable rotational qubits that have been reported have a coherence time of 100 ms [122]. Even with careful tuning of the angle between the optical trap polarization and the applied magnetic field to a 'magic' angle that greatly reduces the differential polarizability, the dominant decoherence mechanism was still the differential polarizability between two qubit states. With minor technical upgrades to our apparatus, stable microwave-induced dipoles or rotational state qubits can be achieved. In the light-free magnetic trap, we expect to produce dipoles with a coherence time that is even longer than the record long coherence time.

For example, rotational qubits $\frac{1}{\sqrt{2}}$ ($|N=0, m_N=0, m_S=1, m_{I_{\mathrm{Na}}}=3/2, m_{I_{\mathrm{Li}}}=1\rangle$ + $|N=1, m_N=1, m_S=1, m_{I_{\mathrm{Na}}}=3/2, m_{I_{\mathrm{Li}}}=1\rangle$) with collision energy of 1 μK are estimated to have a coherence time of $\sim$ 1.2 second in a magnetic trap [1]. However, the dominant decoherence mechanism of rotational qubits for NaLi in the triplet state is the mixing between different electron spin states due to the intramolecular spin-spin coupling[2]. This leads to a coherence time of $\approx$ 200 ms ($t_c \approx \frac{h}{\Delta\mu \times \Delta B \times 10^{-4}} \approx$ 200 ms) which is, without careful adjustment for suppressed differential polarizability, still longer than the longest previously observed coherence time.

[1] NaLi has rotational g-factor $g_r \approx 0.06$ based on simple analysis provided in [123] which divides the nuclear and electron contributions to g_r and provides how they scale with mass. Using this estimate value for g_r, coherence time of a superposition state $h/(g_r \times \mu_N \times \Delta B) \approx 1.2$ s (where the magnetic field inhomogeneity, ΔB, is approximately 20 mG in this case.)

[2] spin-rotation coupling contribution is relatively small. Approximatetely, the $N = 0$ upper-stretched state, $|N=0, m_N=0, m_S=1, m_{I_{\mathrm{Na}}}=3/2, m_{I_{\mathrm{Li}}}=1\rangle$, is mixed with the state $|N=2, m_N=2, m_S=-1, m_{I_{\mathrm{Na}}}=3/2, m_{I_{\mathrm{Li}}}=1\rangle$ by 0.02%. $N = 1$ upper-stretched state, $|N=1, m_N=1, m_S=1, m_{I_{\mathrm{Na}}}=3/2, m_{I_{\mathrm{Li}}}=1\rangle$ is mixed with state $|N=3, m_N=3, m_S=-1, m_{I_{\mathrm{Na}}}=3/2, m_{I_{\mathrm{Li}}}=1\rangle$ by 0.01%.

Appendix A

A.1 Circuit designs

Part	Value	MFG
C(IN)	22×10^{-6} F	FK11X7R1C226M
C(IN_OC)	10^{-7} F	SR205E104MAR
C(OUT_OC)	10^{-7} F	SR205E104MAR
CH(IN_L)	CHOKE	PE-1812ACC101STS
CH(IN_R)	CHOKE	PE-1812ACC101STS
CH(OUT_L)	CHOKE	PE-1812ACC101STS
CH(OUT_R)	CHOKE	PE-1812ACC101STS
DC-DC(IN)	5V - 9V Converter	PDS1-S5-S9-S
DC-DC(OUT)	5V - 9V Converter	PDS1-S5-S9-S
F(SIG)	2K	FMP100JR-52-2K2
L(IN)	3.3×10^{-7} F	AR205F334K4R
L(OUT)	3.3×10^{-7} F	AR205F334K4R
LPF	15×10^{-9} F	RCER72A153K0DBH03A
L_IN	680×10^{-6} H	DC630R-684K
OUT	SMA Connector	5-1814832-1
R(BI_B)	1 kΩ	FMP100JR-52-1K
R(BI_F)	1 kΩ	FMP100JR-52-1K
R(IN)	10^{-7} F	SR205E104MAR

Table A.1 continued from previous page

Part	Value	MFG
R(OUT)	10^{-7} F	SR205E104MAR
R(S)	2 kΩ	FMP100JR-52-2K2
R(TRAN)	2 kΩ	FMP100JR-52-2K2
R0	470 Ω	FMP100JR-52-470R
T1	2N3904	2N3904BU
U$1	OPTOCOUPLER	FOD0720
U$2	ICBUFFER	SN74AHCT1G125DCKR
U$5	SIGNAL_JUMPER	1729089
VCC	SMA Connector	5-1814832-1
VREG(IN)	5V VOLTAGEREG	L7805CV
VREG(OUT)	5V VOLTAGEREG	L7805CV

Table A.1: **Parts of a PCB design for digital control instrumentation.**

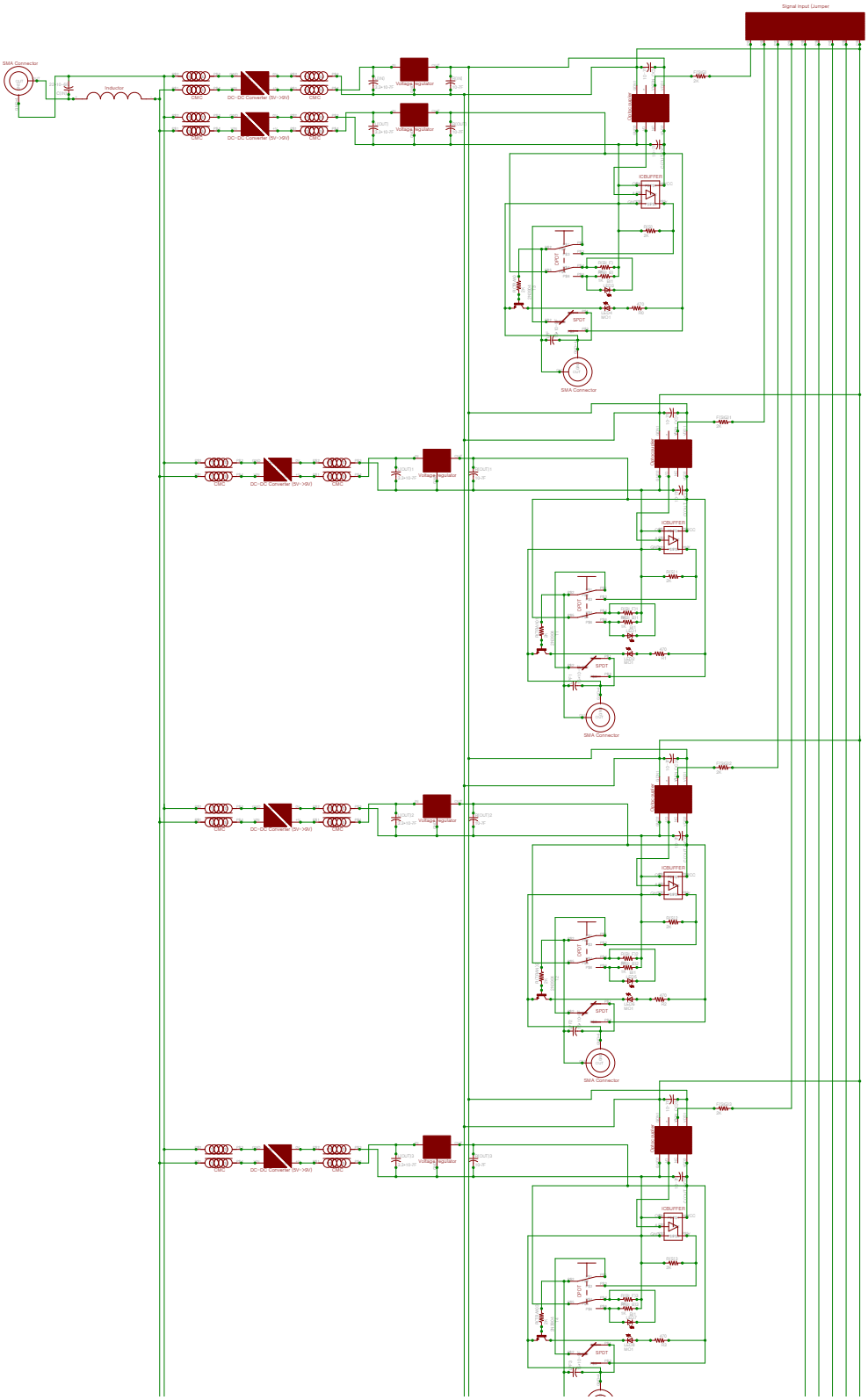
Signal Input (Jumper
SMA Connector
Inductor
DC-DC Converter (5V->3V)
Voltage Regulator
ICBUFFER
SPDT
SMA Connector

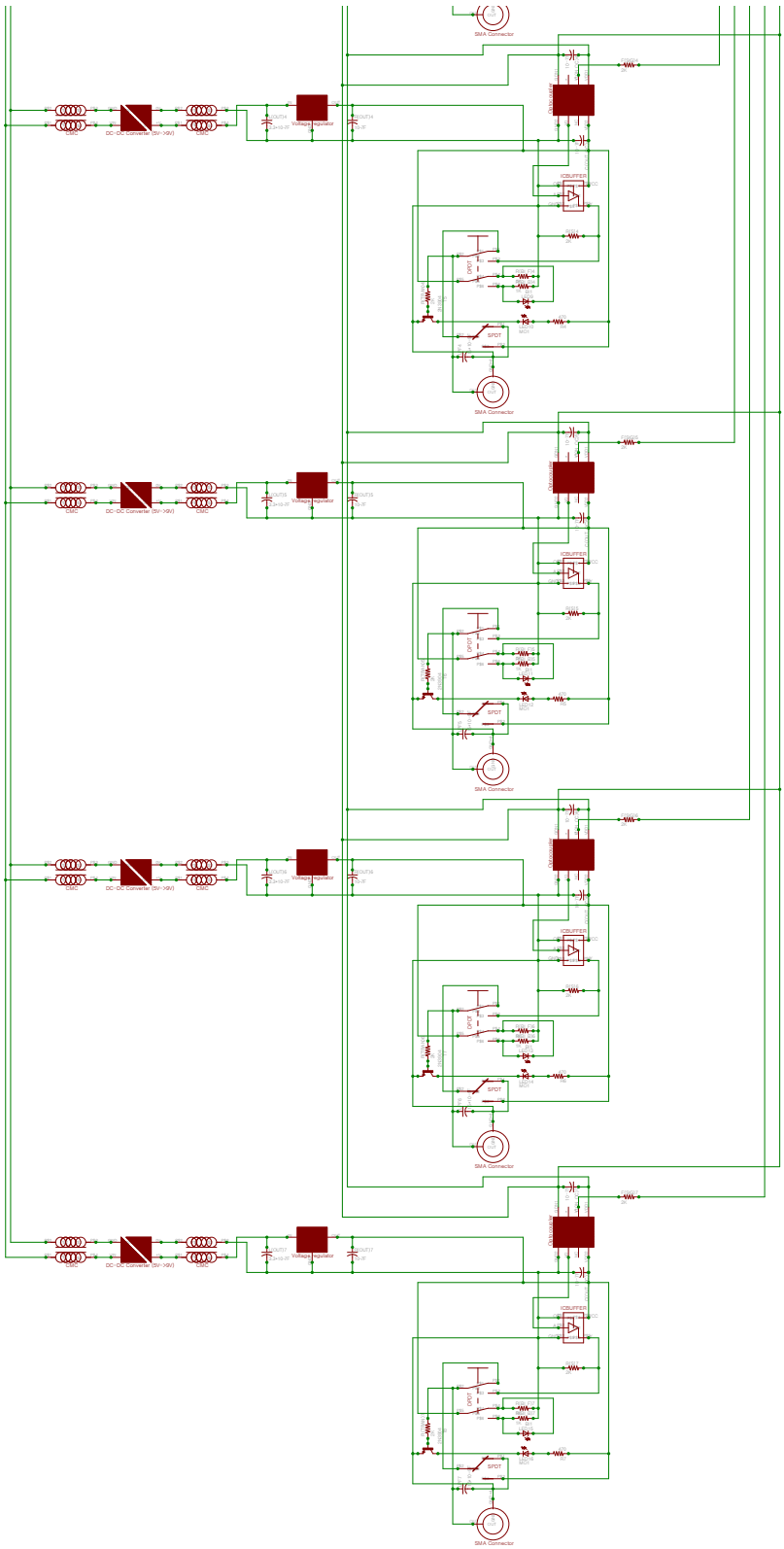

Figure A-1: **Schematic of a PCB design for digital control instrumentation.**

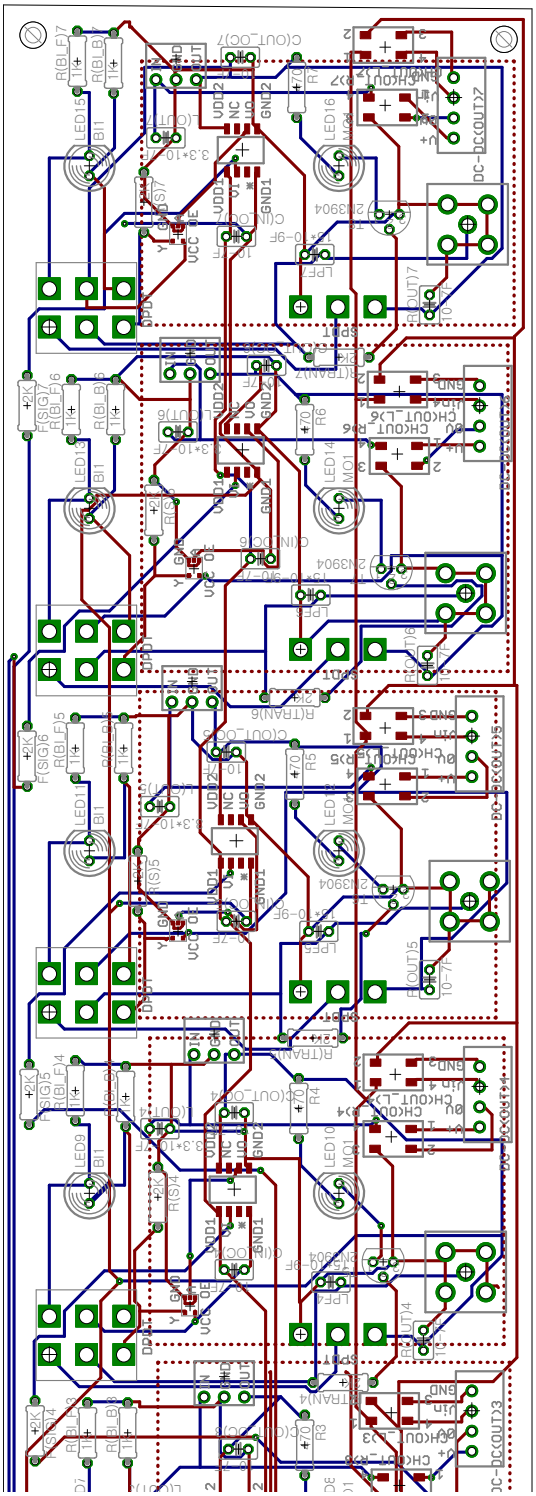

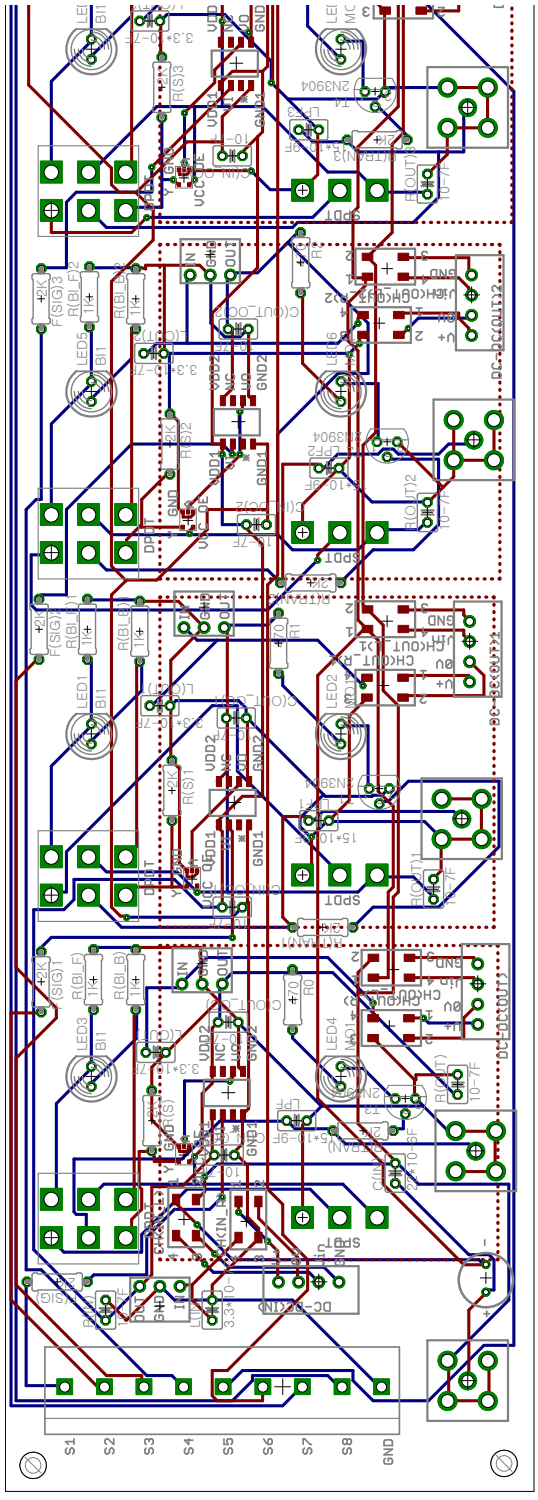

Figure A-2: **Board of a PCB design for digital control instrumentation.**

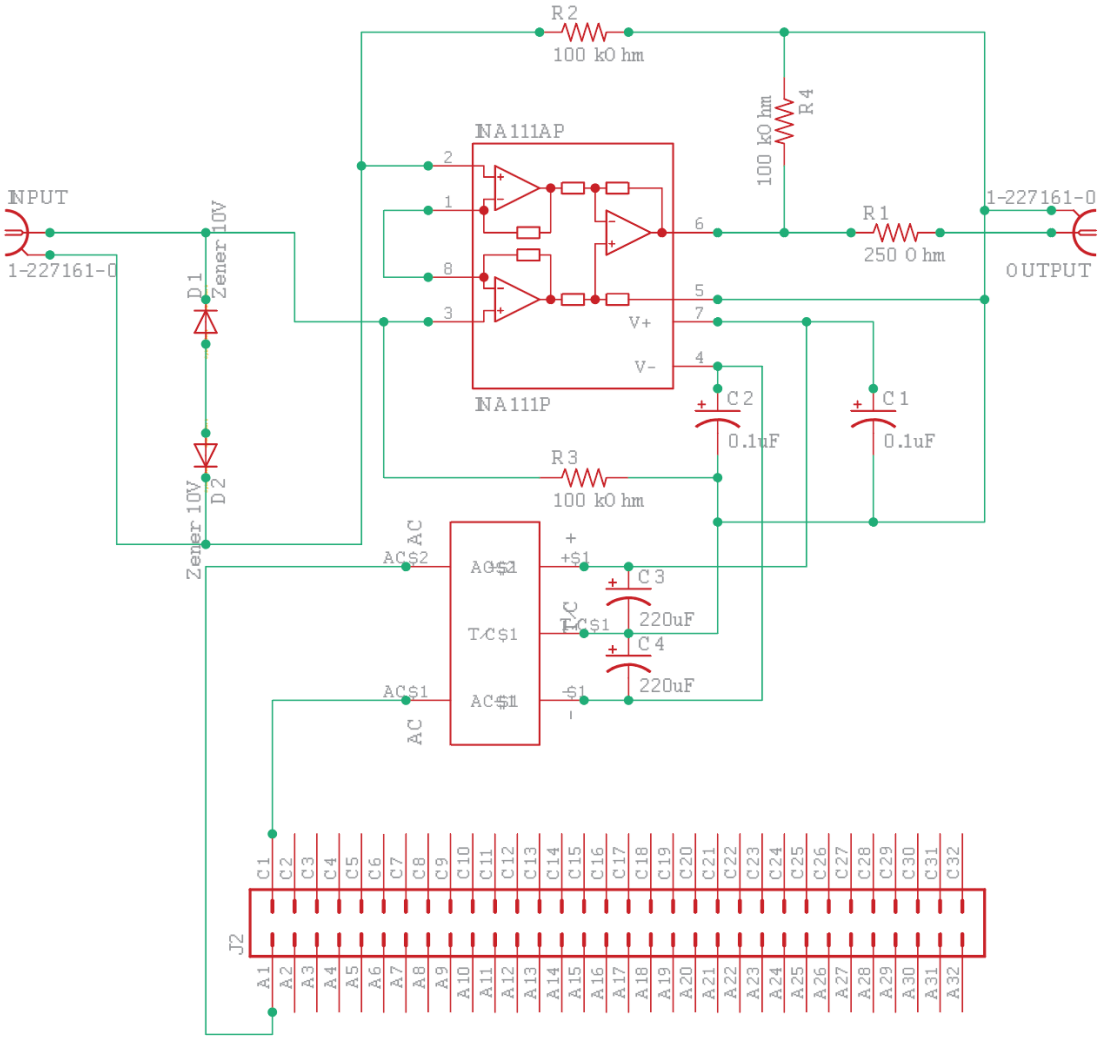

Figure A-3: **Schematic of PCB design for analog signal buffer.**

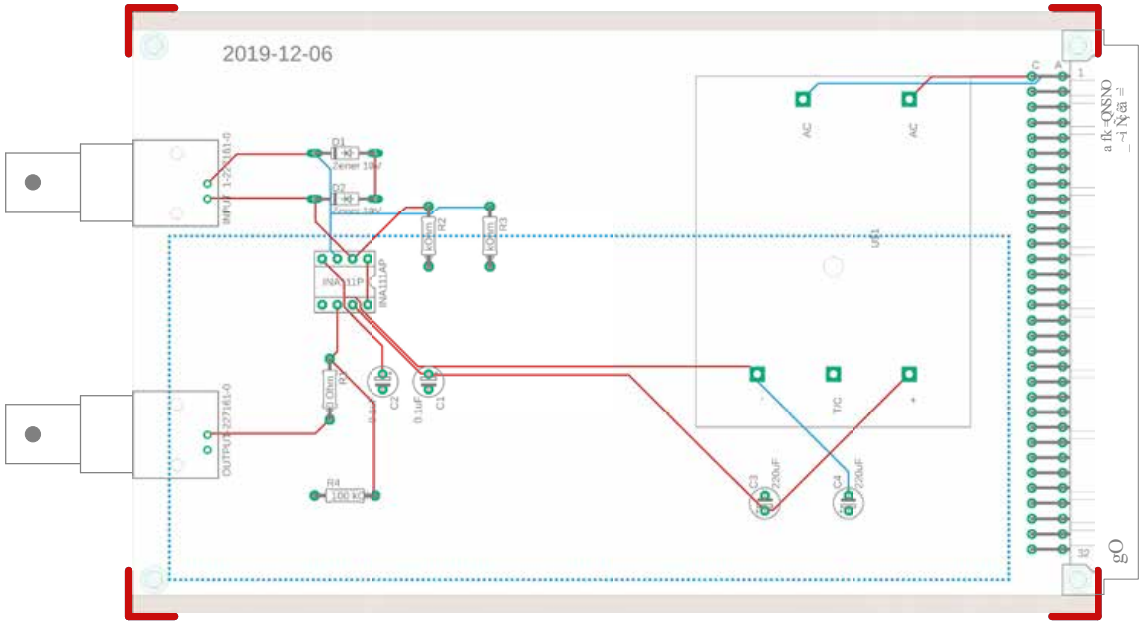

Figure A-4: **Board of PCB design for analog signal buffer.**

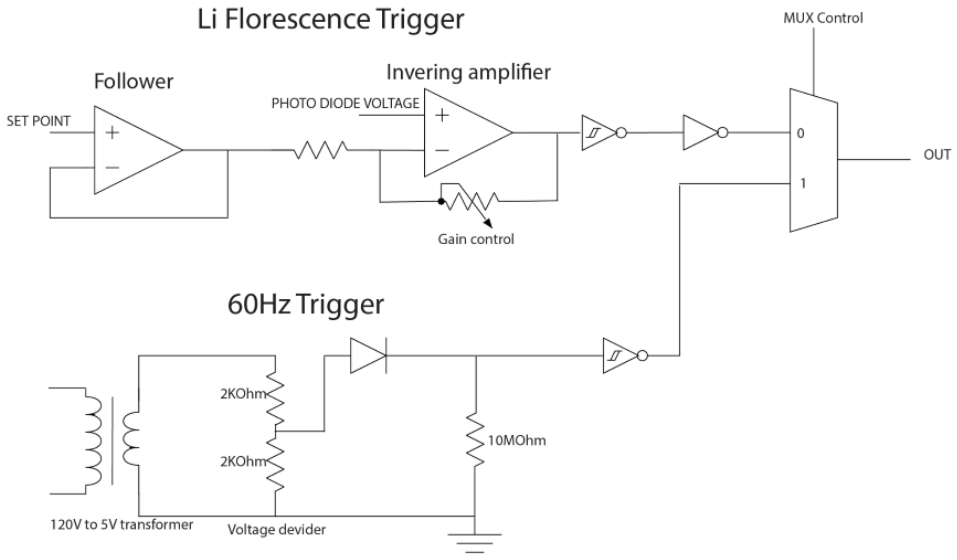

Figure A-5: **Circuit diagram of Li MOT fluorescence trigger and 60Hz trigger.**

Appendix B

B.1 Coupled-channels calculations

This section describes quantum mechanical coupled-channel calculations for Na-NaLi scattering which were carried out by Tijs Karman. The calculations include the electronic interactions, the Zeeman interaction with the magnetic field, the magnetic dipole-dipole interaction, and the spin-rotation and spin-spin couplings. The electronic interaction is partitioned into two-body interactions that are taken from experiment [25, 124, 125], and a non-additive three-body interaction that is calculated with state-of-the-art coupled-cluster calculations that are described in a forthcoming paper [126]. We assume that the molecular bond length is fixed at the equilibrium position of the triplet potential, which naively cannot explain the chemical reactions that form singlet NaLi or Na_2 molecules at the low-spin potential. In our coupled-channel calculations, we model these by imposing an absorbing boundary condition at $R = 4.5\ a_0$, which can be reached on the low-spin potential, but not on the high-spin potential, which is highly repulsive at these short distances.

For simplicity we start by ignoring hyperfine and vibrational degrees of freedom. The scattering wavefunction is expanded in the basis of fully coupled channel functions of the form

$$|(NL)J(s_{\mathrm{mol}}, s_{\mathrm{atom}})S; \mathcal{J}\mathcal{M}\rangle = \sum_{M_J, M_S} \langle JM_J SM_S|\mathcal{J}\mathcal{M}\rangle \times |(NL)JM_J\rangle\, |(s_{\mathrm{mol}}\ s_{\mathrm{atom}})SM_S\rangle \quad \text{(B.1)}$$

where $\langle JM_J SM_S|\mathcal{J}\mathcal{M}\rangle$ is a Clebsh-Gordan coefficient. The quantum number N represents the rotational angular momentum of the NaLi molecule, and L the angular momentum associated with the end-over-end rotation, which are Clebsch-Gordan coupled to a total mechanical angular momentum J with the B-field project M_J. Similarly, $s_{\text{mol}} = 0$ or 1 denotes the NaLi molecular electronic spin and $s_{\text{atom}} = {}^1/_2$ is the atomic electronic spin, and S the total electronic spin with B-field projection M_S. In the coupled basis, J and S are subsequently coupled to a total angular momentum $\mathcal{J}$ and a magnetic field projection $\mathcal{M} = M_J + M_S$. $\mathcal{M}$ is strictly conserved, whereas, for a large enough magnetic field, M_S becomes a good quantum number and therefore $M_J = \mathcal{M} - M_S$ is also a good quantum number. Due to the large singlet-triplet splitting in the NaLi molecule, $s_{\text{mol}} = 0$ or 1 is also a good quantum number. For a separated atom and molecule, $m_{s_{\text{mol}}}$ and $m_{s_{\text{atom}}}$ would separately become good quantum numbers, but at chemically relevant distances the exchange splitting between the doublet and quartet interaction potentials is dominant, so that $S = 1/2$ and $3/2$ are good quantum numbers. Hence, we can effectively consider each $|S\ M_S\rangle$ state separately, with only perturbatively weak couplings between them. For each of these spin channels, there are strong and anisotropic interactions that couple different N and L channels but conserve J and M_J. The initial channel corresponds to s-wave collisions in the spin-stretched ground state, $|(00)00\rangle\,|3/2\ 3/2\rangle$.

First, we consider the sensitivity of the scattering rates to the interaction potential shown in Figure B-1(a). Here, we scale by a factor $1 + \lambda$ the non-additive three-body part of the interaction potential, that is, the part that is computed *ab initio* and is uncertain up to an estimated 10 %. By modifying the potential by only 0.1 % we find that the resonances start to shift so that realistically their positions are completely undetermined, and when the scaling reaches several percent we tune across magnetic field-independent resonances, indicating that the background scattering length is undetermined. Next, shown in Figure B-1(b), we again scale the three-body interaction but now only for the low-spin doublet potential, leaving the high-spin quartet potential unchanged. In this case, we find that several of the resonances are now completely independent of the scaling of the low-spin potential up to $\lambda = 0.1$, indicating that are

these resonances are supported by the high-spin potential, *i.e.*, the resonance states have well defined $S = {}^3/_2$.

This can be understood as no stable resonance states are supported by the chemically reactive low-spin potential.

The analysis above indicates that the *ab initio* prediction of resonance positions is beyond the capability of state-of-the-art calculations. Although the coupled-channels calculations cannot predict the positions of the resonances, we can still use these calculations as a "numerical experiment" to investigate the nature of the resonance states, the coupling mechanisms, and the observed differences between the two spin-stretched states.

We perform coupled-channels scattering calculations with the interactions scaled by $1 + \lambda$ and analyze the *typical* behavior observed for different λ between -0.1 and $+0.1$. Representative magnetic field scans can be seen in Fig. B-2. We observe approximately 10 resonances for the high-field seeking bottom spin-stretched state and only around 5 resonances in the low-field seeking top spin-stretched state, respectively. This is in qualitative agreement with the experiment which observes 17 and 8 resonances, respectively. In the companion paper we show that based on the density of states we would expect to see approximately 10 resonances for either spin-stretched state [126]. We furthermore show that including molecular vibrations would increase the density of state by approximately 50 %, which can partially explain the lower number of observed resonances compared to experiment. We show that including hyperfine interactions increases the density of resonances somewhat. With these effects in mind, one could almost claim quantitative agreement with experiment regarding the density of resonances, although again it is not possible to *ab initio* predict their positions.

One may expect that the high-field seeking state supports more magnetically tunable resonances because the other Zeeman states correspond to closed channels – and hence can support Feshbach resonances – even in the rotational ground state, whereas closed channels for the low-field seeking state occur only for excited rotational states. We investigate this in our coupled-channels calculations by artificially excluding the

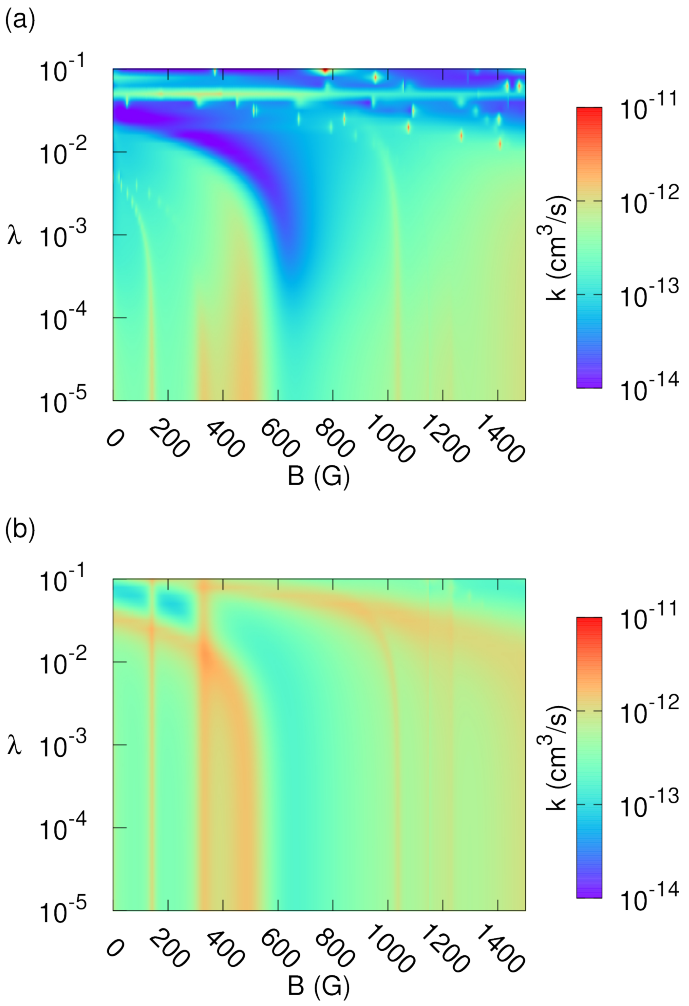

Figure B-1: Loss rates as a function of B-field and scaling of the spin-independent three-body interaction by a factor $1+\lambda$ for $N_{\max} = 20$. This shows scalings within the uncertainty of at least several percents, the background loss and resonance positions are undetermined. Several B-independent resonances are observed, where the λ-scaling tunes the initial spin-stretched potential such that it supports a resonance, i.e., a bound state near zero energy. Hence, prediction of resonance positions requires knowledge of the interaction potentials to an accuracy that cannot realistically be achieved by *ab initio* calculations.

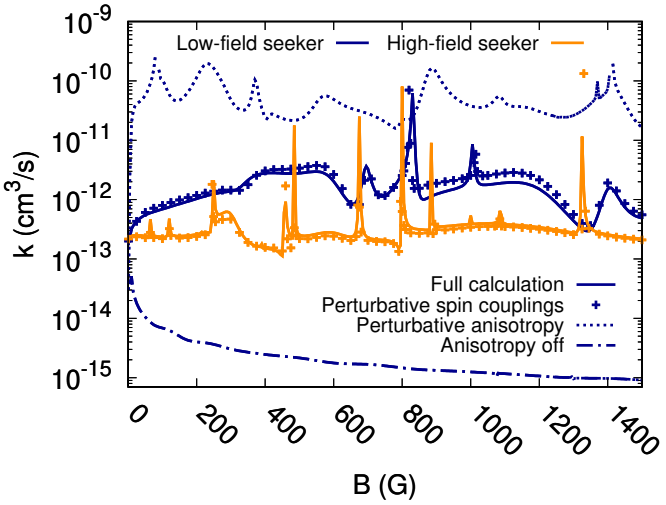

Figure B-2: Representative magnetic field scans. Results for the low and high-field seeking states in orange and blue solid lines. The high-field seeking state typically shows around 10 resonances below 1500 G, whereas the low-field seeker shows around half as many resonances. This qualitative difference between the two states is also observed experimentally. We investigate whether the anisotropy of the electronic interaction and the spin-spin and spin-rotation coupling act perturbatively, by scaling down these couplings by a factor of two and scaling the resulting cross section up by a factor four. Agreement with the full calculation indicates the spin-spin and spin-rotation coupling act perturbatively, whereas the interaction anisotropy does not. The coupling mechanism however does involve the anisotropy as turning this off entirely produces a much smaller cross section dominated by the magnetic dipole-dipole interaction (dash-dotted line). When both anisotropy and dipole-dipole are turned off, the calculated cross section is zero.

non-initial Zeeman states in the rotational ground state, see Fig. B-3. Somewhat surprisingly we find that *excluding* channels from the calculation does not reduce the number of resonances for the high-field seeking state, but rather increases the observed number of resonances for the low-field seeker, where the excluded channels correspond to asymptotically open channels. In the presence of these open channels some of the resonances decay rapidly such that they are not resolved, leading to a lower number of observable resonances, explaining the observed qualitative difference between the low and high-field seeking states.

Finally, we investigate numerically the coupling mechanism that gives rise to the observed resonances. As argued above, each resonance state can essentially be assigned a molecular and a total electron spin quantum number $s_{\mathrm{mol}} = 1$ and $S = {}^3/_2$,

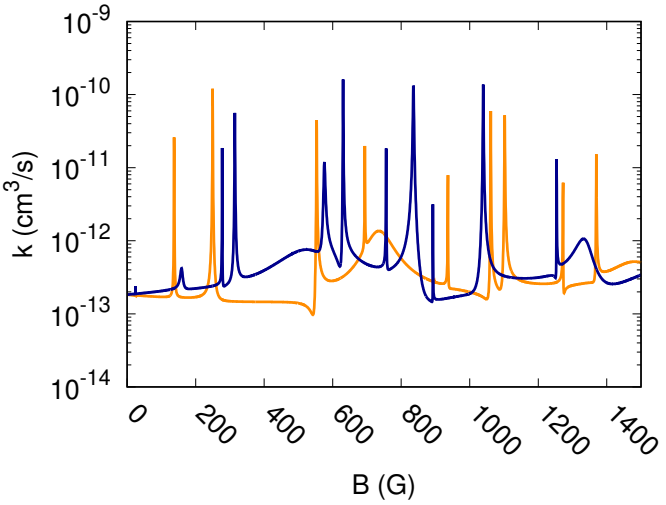

Figure B-3: Representative magnetic field scans. Qualitative differences in the typical number of resonances for the low and high-field seeker disappear when we *exclude* from the calculation channels corresponding to non-initial Zeeman states in the rotational ground state. Excluding these channels does not reduce the number of resonances for the high-field seeker, but rather increases the typical number of resonances for the low-field seeker. In this case, asymptotically open channels are removed from the calculation, which otherwise would lead to fast decay that renders some of the resonances unresolved.

as only the non-reactive quartet spin state supports stable resonance states. The resonance is magnetically tunable only if the Zeeman state M_S is changes. To couple states with $\Delta M_S \neq 0$ a spin-dependent coupling must be involved, such as the spin-rotation and spin-spin coupling. From the tensor rank of these couplings we can determine they couple states with the selection rules, $J = 0 \rightarrow 1$ and $|\Delta M_S| \leq 1$, and $J = 0 \rightarrow 2$ and $|\Delta M_S| \leq 2$, respectively. Since J is approximately a good quantum number, both mechanisms give rise to distinct and independent resonances. Since the density of states of the collision complex scales with $2J + 1$ and the differential magnetic moment is higher for larger $|\Delta M_S|$ transitions, we conclude that most – aproximately 75 % – of the resonances are due to spin-spin coupling. Spin-spin coupling does not occur for $^2\Sigma$ molecules, and hence is a somewhat unique coupling mechanism for NaLi($^3\Sigma$). To confirm that the role of the spin-dependent interactions in the coupling mechanism we have performed coupled-channels calculations where we reduced these couplings by a factor two. The resulting cross section multiplied

by four is shown as the crosses in Fig. B-2. The agreement with the full calculation indicates scaling with the square of the coupling strength that is expected for perturbatively weak spin-dependent couplings. This confirms we can fully assign the resonances approximately good quantum numbers $s_{\rm mol} = 1$, $S = {}^3/_2$, each resonance also has definite M_S constrained by $\Delta M_S \leq 1$ and ≤ 2 selection rules, and $J = 1$ or 2, for spin-rotation and spin-spin coupling, respectively, whereas the N and L quantum numbers are strongly mixed due to the anisotropic interaction at short range.

The coupling mechanism involving the spin-rotation and spin-spin coupling also requires an anisotropic interaction potential. The physical picture is that the anisotropic interaction with the atom can reorient the molecule, and because the spin is coupled to the molecular axis by spin-rotation and spin-spin coupling, this can lead to Zeeman transitions. To confirm this picture we have performed calculations that exclude interaction anisotropy, shown as the dash-dotted line in Fig. B-2. The resulting cross section is smaller and results from long-range Zeeman relaxation by the magnetic dipole-dipole coupling. If both the magnetic dipole-dipole interaction and the interaction anisotropy are switched off, the cross section in our model vanishes. The role of the interaction anisotropy is non-perturbative, however, as can be seen from comparison between the solid and dotted line in Fig. B-2, which compares the cross section from the full calculation to four times the cross section obtained with the interaction anisotropy halved. The crucial and non-perturbative role of the anisotropic electronic interaction implies that the spectrum of resonances cannot be described by a simplified model that accounts only for the isotropic long-range R^{-6} interaction, contrary to previous observations of ultracold atom-molecule resonances [71].

We make a direct comparison to the scattering calculations with the density of states computed quantum mechanically using the same channel basis as used in the scattering calculations in a forthcoming paper [126]. The total number of states from the quasiclassical estimate is close to the number of resonances from the scattering calculations, but not in perfect agreement with it, because of the light masses and relatively weak interactions in the spin-stretched state. We see most of the 3-body states are between 20 and 40 a_0 which is in agreement with the complex size estimated

from the simple interpretation of the spacing between resonances as rotational energy splitting of the collision complex.

Appendix C

C.1 Quasi-2D threshold law for p-wave collision

Two particles confined axially in an external harmonic trap can be described by the stationary Schrödinger equation [127]:

$$\left[-\frac{\hbar}{2\mu} + U(\boldsymbol{r}) + V_{tr}(\boldsymbol{r})\right]\Psi(\boldsymbol{r}) = E\Psi(\boldsymbol{r}). \tag{C.1}$$

Here, $V_{tr}(\boldsymbol{r}) = \frac{1}{2}\mu\omega^2 z^2$, $U(\boldsymbol{r})$ is the interparticle interation and μ is the reduced mass. The energy in quasi-2D consists of harmonic oscillator energy and the 2D kinetic energy given by $\frac{\hbar^2 k^2}{2\mu} = E = \frac{1}{2}\hbar\omega + \frac{\hbar^2 q^2}{2\mu}$ where q is the wavenumber in the 2D plane. Provided that the van der Waals (vdW) length scale is much smaller than the oscillator length $\bar{a} \ll l_o$, where $\bar{a} = \frac{2\pi}{\Gamma(\frac{1}{4})^2}\left(\frac{2\mu C_6}{\hbar^2}\right)^{1/4}$ and $l_o = \sqrt{\hbar/(\mu\omega)}$, so that the trapping potential can be regarded as constant in the interaction range, the scattering process can be described by the s or p-wave pseudopotential using the 3D scattering length or the scattering volume as:

$$\begin{aligned} U_s(\boldsymbol{r}) &= \frac{2\pi\hbar^2 a_s^{3D}}{\mu}\delta(\boldsymbol{r})\frac{\partial}{\partial r}r \\ U_p(\boldsymbol{r}) &= \frac{\pi\hbar^2 V_p^{3D}(k)}{\mu}\vec{\nabla}\delta(\boldsymbol{r})\frac{\partial^3}{\partial r^3}r^3\vec{\nabla} \end{aligned} \tag{C.2}$$

Here, μ is the reduced mass, C_6 is the vdW long-range dispersion coefficient, and the scattering length and volume are defined with the 3D phase shift η_l by $a_l^{3D}(k) = -\tan\eta_l/k$ and $V_l^{3D}(k) - \tan\eta_l/k^3$ respectively. The relation between the 2D and 3D scattering length for p-wave collision is derived to be:

$$
\begin{aligned}
|a_p^{2D}|^2 &= \left(\frac{3\sqrt{\pi}}{2l_o}\right)^2 \left(\frac{q^2}{k^2}\right)^2 |l_p|^2 |a_p^{3D}|^2 \\
\beta_p^{2D} &= \left(\frac{3\sqrt{\pi}}{2l_o}\right) \left(\frac{q^2}{k^2}\right) |l_p|^2 \beta_p^{3D}
\end{aligned}
\tag{C.3}
$$

where $l_p = (1 - a_p^{3D} \times W(0)/(\sqrt{\pi} l_o^3 k^2))^{-1}$ and $W(0) \approx 0.328$ [1] from the solution of the Schrödinger equation C.1 to connect the 2D and 3D scattering lengths given in ref. [127].

Reactive scattering rate constant in quasi-2D is given as $K_{2D}^{ls} = g\frac{4\hbar}{\mu}\beta^{2D} f_{2D}$ where $f_{2D} = (1 + |a^{2D}|^2 + 2\beta^{2D})^{-1}$ [127]. From the relation between the loss rate constant and the scattering lengths given by Eq.C.3, the quasi-2D loss rate constant for p-wave collision can be expressed with 3D scattering parameters as:

$$
\begin{aligned}
K_{2D}^{ls} &= g\frac{4\hbar}{\mu} \cdot \beta_p^{2D} \cdot f_{2D} \\
&= g\frac{4\hbar}{\mu} \cdot \left[\left(\frac{3\sqrt{\pi}}{2l_o}\right) \left(\frac{q^2}{k^2}\right) |l_p|^2 \beta_p^{3D}\right] \cdot f_{2D} \\
&= g\frac{4\hbar}{\mu} \cdot \left(\frac{3\sqrt{\pi}}{2l_o}\right) \left(\frac{q^2}{k^2}\right) \left[2\bar{a}_1 (k\bar{a})^2 \frac{(s-1)ys - (s-2)y}{(ys)^2 + (s-2)^2}\right] \cdot |l_p|^2 f_{2D} \\
&= g\frac{4\hbar}{\mu} \cdot \left(\frac{3\sqrt{\pi}}{2l_o}\right) q^2 \left[(2\bar{a}_1 \bar{a}^2) \frac{(s-1)ys - (s-2)y}{(ys)^2 + (s-2)^2}\right] \cdot |l_p|^2 f_{2D}
\end{aligned}
\tag{C.4}
$$

supported by 3D complex scattering length of p-wave collision expressed with two dimensionless quantum defect parameters s and y [88] as $a_p^{3D} = \alpha_p^{3D} - i\beta_p^{3D} = -2\bar{a}_1 (k\bar{a})^2 \frac{y + i(s-1)}{ys + i(s-2)}$, and thus $\beta_p^{3D} = 2\bar{a}_1 (k\bar{a})^2 \frac{(s-1)ys - (s-2)y}{(ys)^2 + (s-2)^2}$. Eq. C.4 implies that the 3D p-wave scattering rate is modified by the factor $|l_p|^2$ and q^2/k^2 with a wavenumber $\bar{k}_p = \frac{3\sqrt{\pi}}{2l_o}$ [2]. As 3D loss rate constant is proportional to temperature or k^2, this k^2 factor cancels out with $1/k^2$ of q^2/k^2 in the second line of Eq. C.4 leading to the relation $K_{2D}^{ls} \propto q^2 \cdot |l_p|^2 f_{2D}$, and recovering the linearly dependent loss rate on temperature.

[1] Scattering length for s-wave collision is given by $|a_s^{2D}|^2 = \left(\frac{\sqrt{\pi}}{l_o}\right)^2 |l_s|^2 |a_s^{3D}|^2$ and $\beta_s^{2D} = \left(\frac{\sqrt{\pi}}{l_o}\right) |l_s|^2 \beta_s^{3D}$ where, $l_s = (1 + a_s^{3D}/(\sqrt{\pi} l_o) \times ln(B\hbar\omega/\pi\epsilon))^{-1}$ and $B \approx 0.9049$ [27].

[2] s-wave scattering rate is modified by the factor $|l_s|^2$ with a wavenumber $\bar{k}_s = \frac{\sqrt{\pi}}{l_o}$ [27].

C.2 Long-range coupling

Here we show that the *long-range* coupling between the two hyperfine states $|a\rangle$ and $|b_1\rangle$ involved in the crossing shown in 4-9 is too weak to explain the observed loss rates. To explain the observed Feshbach resonance, it is, therefore, necessary to assume the presence of a *short-range* loss mechanism. A minimal model for such a mechanism involves a bound state (channel $|3\rangle$) coupled to the open channels ($|aa\rangle$ and $|ab_1\rangle$).

Long-range coupling would occur outside the centrifugal p-wave barrier of the input channel. The peak of the barrier is at $24^{1/4} \cdot R_{\rm vdw} \approx 7.8$ nm where the van der Waals length $R_{\rm vdw} = \frac{1}{2}\left(\frac{2\mu C_6}{\hbar^2}\right)^{1/4}$, and the inner turning point is at 100 nm at 3.35 μK temperature. In the Born approximation, for a potential of average strength V_0 in an effective volume $4\pi R_0^3/3$, the total low energy elastic scattering cross section $\sigma = 4\pi(\frac{2\mu V_0 R_0^3}{3\hbar^2})^2$ (identical to the solution for a spherical square well potential with radius R_0). Applying this relation to the observed nearly unitarity limited cross section of 2.95×10^{-11} cm^2 corresponding to the loss rate constant of 10^{-10} cm^{3}s^{-1} at 1 μK and using the position of the inner turning point to estimate $R_0 = 100$ nm, provides a coupling matrix element V_0 of 16 kHz. This is the required value for coupling outside the p-wave barrier to be compatible with the observed loss rates. For inelastic collisions with final wavevector k', the rate has an additional factor k'/k due to the density of states, but for large k', the matrix element will decrease with k', so our rough estimate for the required spatial coupling matrix element should also apply to inelastic collisions.

First, we show that magnetic dipolar interactions [128] which lead to spin exchange and dipolar relaxation and often limit the lifetime of magnetically trapped atoms, are very weak outside the barrier. At the position of the p-wave barrier ($R_b = 100$ nm), the interaction between two spins with magnetic moments $2\mu_0$, where μ_0 is the Bohr magneton, is $V^{mDD} = 0.052$ kHz, which is already small. However, due to the selection rules of the magnetic dipolar interaction ($|\Delta M_S| = 1$), a single spin flip cannot provide coupling between the near-degenerate hyperfine states of interest $|a\rangle$ and $|b_1\rangle$, which correspond to $M_S = 1$ and $M_S = -1$, respectively (see above).

Therefore, the coupling must involve an intermediate state $|k\rangle$, which is off-resonant by its Zeeman energy $\Delta_{ak} \simeq 1\mu_0 \times 300$ G $\simeq 400$ MHz. This further reduces the magnetic dipolar coupling between the open channels by the factor $(V^{mDD}/\Delta_{ak})^{-1} = 7.7 \times 10^6$ to much less than 1 mHz. We can thus rule out the magnetic dipolar interaction as a source of the observed loss.

Spin flips in collisions of $^3\Sigma$ molecules can also occur via coupling of the incident channels $|a\rangle$ and $|b_1\rangle$ to excited rotational states [129,130]. This mechanism is similar to that of magnetic dipolar relaxation discussed above, with the excited rotational states ($N \geq 1$) playing the role of the intermediate Zeeman states. A distinctive feature of this mechanism is that it is mediated by the anisotropy of the electrostatic interaction between $^3\Sigma$ molecules (which couples the $N = 0$ incident states to $N \geq 1$ closed-channel states of the same M_S) and the spin-rotation and spin-spin interactions in the $N \geq 1$ manifolds, which couple states of different M_S.

Below, we quantify this molecular spin relaxation mechanism by estimating the magnitude of the anisotropic coupling between the degenerate open channels $|a\rangle$ and $|b_1\rangle$ due to the excited rotational states at $R = 100$ nm. We find that the strongest coupling due to the electric dipole-dipole interaction is only 0.05 kHz, and is therefore too small to explain the observed loss rate.

C.2.1 Coupling matrix elements between degenerate open channels $|aa\rangle$ and $|ab_1\rangle$ due to rotationally excited states

Here, we estimate the matrix elements between the degenerate open channels $|aa\rangle$ and $|ab_1\rangle$ due to long-range interactions between NaLi($a^3\Sigma^+$) molecules. The interactions are described by the multipole expansion [131]

$$\hat{V}(\mathbf{R}, \mathbf{r}_A, \mathbf{r}_B) = (4\pi)^{3/2} \sum_{\lambda_A,\lambda_B,\lambda} V_{\lambda_A,\lambda_B,\lambda}(R, r_A, r_B) A_{\lambda_A,\lambda_B,\lambda}(\hat{R}, \hat{r}_A, \hat{r}_B) \tag{C.5}$$

where $A_{\lambda_A,\lambda_B,\lambda}(\hat{R}, \hat{r}_A, \hat{r}_B)$ are the angular functions, $V_{\lambda_A,\lambda_B,\lambda}(R, r_A, r_B)$ are the radial expansion coefficients [131], $\hat{R} = \mathbf{R}/R$, and $\hat{r}_i = \mathbf{r}_i/r_i$. To leading order, the expansion (C.5) contains the electric dipole-dipole, dipole-quadrupole, and quadrupole-

quadrupole interactions. We assume that the internuclear distances of NaLi molecules are fixed at their equilibrium values. The rigid rotor approximation is expected to be extremely accurate since the long-range NaLi-NaLi interactions at $R = R_b$ (see below) are thousands of times smaller than the spacing between the ground and the first excited vibrational states of NaLi ($\hbar\omega_{10} = 40.2$ cm^{-1} [132]). Since we are interested in long-range physics outside the p-wave barrier, we will also neglect the spin dependence of the NaLi-NaLi interaction, which is significant only at very close range ($R \leq 10\, a_0$).

The radial expansion coefficients in Eq. (C.5) are expressed in terms of the multipole moments $Q_{\lambda_i,0}$ of the interacting molecules ($i = A, B$)

$$\begin{aligned} V_{\lambda_A,\lambda_B,\lambda}(R, r_A, r_B) = & \frac{Q_{\lambda_A 0} Q_{\lambda_B 0}}{R^{\lambda+1}} \delta_{\lambda,\lambda_A+\lambda_B} \\ & \cdot \frac{(-1)^{\lambda_A}}{[(2\lambda_A+1)(2\lambda_B+1)(2\lambda+1)]^{1/2}} \\ & \cdot \left[\frac{(2\lambda_A+2\lambda_B+1)!}{(2\lambda_A)!(2\lambda_B)!}\right]^{1/2} \end{aligned} \tag{C.6}$$

The leading terms for two interacting neutral polar molecules such as NaLi are

$$\begin{aligned} V_{112}(R) &= -\frac{d^A d^B}{R^3}\sqrt{\frac{2}{3}} \text{ (dipole-dipole)}, \\ V_{123}(R) &= -\frac{d^A Q^B_{20}}{R^4} \text{ (dipole-quadrupole)}, \\ V_{224}(R) &= \frac{Q^A_{20} Q^B_{20}}{R^5}\sqrt{\frac{14}{5}} \text{ (quadrupole-quadrupole)}. \end{aligned} \tag{C.7}$$

where d^i and Q^i_{20} are the electric dipole and quadrupole moments of the i-th molecule. Note that the long-range interaction (C.5) is spin-independent, and hence can only couple the states of the same M_S, M_{I_1}, and M_{I_2}. We use the accurate *ab initio* value of the molecule-frame electric dipole moment $d_{\text{NaLi}} = 0.167$ D [132], and an approximate value of the electric quadrupole moment $\Theta_{\text{NaLi}} = 10$ a.u. based on the calculated values for Na_2 and Li_2 from Ref. [133]. Our estimates are not sensitive to the precise magnitude of Θ_{NaLi}, since the dominant contribution at $R = R_b$ is given by the electric dipole-dipole interaction.

Figure C-1 shows the radial dependence of the long range interactions between

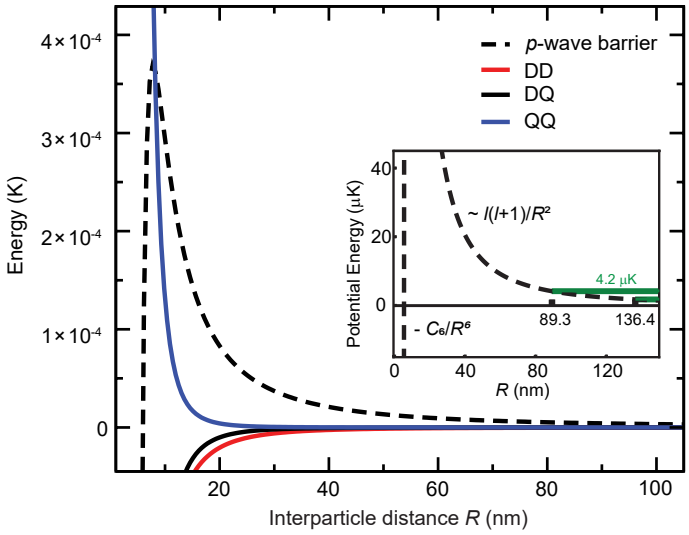

Figure C-1: Radial dependence of the dipole-dipole, dipole-quadrupole, and quadrupole-quadrupole interactions of NaLi ($a^3\Sigma^+$) molecules. The p-wave centrifugal barrier is also shown (dashed line). The upper and lower bounds on the experimental collision energies (4.2 μK and 1.8 μK) are marked by green horizontal lines. The turning points at the centrifugal barrier for these collision energies are $R_b = 89.3$ and 136.4 nm, respectively.

two NaLi molecules. While the dipole-dipole interaction dominates outside the p-wave barrier ($R \geq 100$ nm) both the dipole-quadrupole and quadrupole-quadrupole interactions grow in magnitude as R becomes shorter. At $R = 100$ nm, the magnitude of the electric dipole-dipole, dipole-quadrupole, quadrupole-quadrupole, and magnetic dipole-dipole interaction terms in Eq. (C.7) are (in kHz): $V_{DD} = -3.446$, $V_{DQ} = -0.339$, $V_{QQ} = 0.0273$, and $V_{mDD} = 0.0519$.

Equating the barrier energy plotted in Figure C-1 and the endpoints of the experimental range of collision energies (1.8−4.2 μK), we obtain the corresponding range of distances of closest approach of two NaLi molecules in the p-wave channel as $R_b = 89.3$−136.4 nm. For simplicity, we will use a value close to the middle of this interval, $R_b = 100$ nm $= 1890\ a_0$, to estimate the magnitude of all long-range coupling matrix elements.

Having parameterized the anisotropic long-range interaction between two NaLi molecules (C.7), we now proceed to evaluate its matrix elements between the degenerate open channels $|a\rangle$ and $|b_1\rangle$. The general matrix elements are given by:

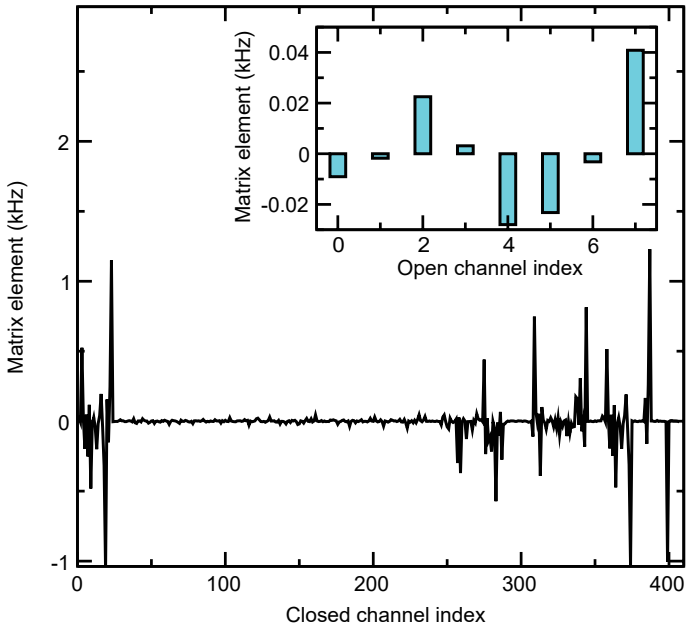

Figure C-2: Matrix elements of the NaLi-NaLi interaction at $R = 100$ nm as a function of the channel index labeling the basis states $|\gamma_A \gamma_B l m_l \eta\rangle$. The initial channel is $|aa, l = 1, m_l = 0\rangle$ and the total angular momentum projection $M_{\rm tot} = -7$. The channel index labels closed channels, in which one or both NaLi molecules are in their $N \geq 1$ excited rotational states. Only the matrix elements with the absolute magnitude exceeding 1 Hz are plotted. The magnetic field $B = 333$ G is tuned near the crossing between the $|a\rangle$ and $|b_1\rangle$ hyperfine-Zeeman levels. Inset: Histogram of direct coupling matrix elements between the incident channel and lower-lying open channels, where both NaLi molecules are in the ground $N = 0$ rotational states.

$$\langle \gamma_A \gamma_B l m_l \eta | \, \hat{V}(\mathbf{R}, \mathbf{r}_A, \mathbf{r}_B) \, | \gamma'_A \gamma'_B l' m'_l \eta' \rangle \tag{C.8}$$

where $\langle \gamma_A \gamma_B l m_l \eta |$ are the properly symmetrized basis states for two identical molecules ($\eta = -1$ for identical fermions), γ_A and γ_B refer to the internal hyperfine-Zeeman states of the molecules, l is the orbital angular momentum for the collision, and m_l is its projection on the space-fixed quantization axis defined by the external magnetic field [130]. The initial scattering state of interest corresponds to $\gamma_A = \gamma_B = a$, $l = 1$, $m_l = 0$, and $\eta = -1$.

The matrix elements are calculated by a straightforward extension of the procedure described in Ref. [130] to include the hyperfine structure of both NaLi molecules (see the Supplemental Material of Ref. [134] for more details about the basis functions). Using a minimal basis including three lowest rotational states of each of the NaLi molecules ($N = 0{-}2$) and two partial waves ($l = 1, 3$), leads to the total number of coupled channels $N_{\rm ch} = 9908$ for the total angular momentum projection $M_{\rm tot} = -7$. We note that this basis set is expected to produce converged results at $R = 100$ nm, where the largest anisotropic long-range coupling $|V_{DD}| = 3.446$ kHz is much smaller than the spacing between the $N = 0$ and $N = 1$ rotational levels ($2B_e = 8.4$ GHz).

Figure C-2 shows the matrix elements between the incident channel $|aa, l = 1, m_l = 0\rangle$ at $R = 100$ nm and all final channels. The largest of these matrix elements $V_{01} \simeq 1.5$ kHz is due to the long-range electric dipole-dipole coupling between the ground and excited ($N = 1$) rotational states. While these matrix elements do not directly couple the degenerate channels $|a\rangle$ and $|b_1\rangle$, they do contribute to indirect second-order couplings estimated below. There are also direct couplings between the incident channel and lower-lying relaxation channels (with single-molecule hyperfine-Zeeman state lower in energy that the incident state $|aa\rangle$), which occur between the $l = 1$ and $l = 3$ partial waves. These couplings are mediated by the intramolecular spin-spin interaction, which couples the different M_S components of the $N = 0$ and $N = 2$ rotational states [129]. As shown in the inset of Figure C-2, the largest of these direct couplings is about 0.04 kHz, which is too small to be responsible for the observed loss.

It remains to consider the second-oder couplings between two degenerate channels

$|a\rangle$ and $|b_1\rangle$ via rotationally excited states. These couplings are suppressed by the factor $(V_{01}/\Delta_{01})^{-1}$, where $\Delta_{01} = 2B_e$ is the energy of $N = 1$ rotational states relative to the ground rotational state. Using the values $\Delta_{01} = 8.4$ GHz and $V_{01} = 1.5$ kHz, we obtain $(V_{01}/\Delta_{01})^{-1} = 5.6 \times 10^6$, and thus the second-order couplings are smaller than 1 mHz, and can be neglected.

C.3 Harmonic oscillator model

Resonant dissipation energy in a driven harmonic oscillator via frictional input coupling with damping is fully analogous to the resonant transmission of flux through a Fabry-Perot cavity explained above. A harmonic oscillator with resonance ω_0 and damping rate γ_2 driven at frequency ω via a frictional input coupling γ_1 is described by the differential equation:

$$\frac{d^2q(t)}{dt^2} + \gamma_2\frac{dq(t)}{dt} + \gamma_1\frac{d}{dt}(q(t) - q_d(t)) + \omega_0^2 q(t) = 0. \tag{C.9}$$

Here, we assume the drive $q_d(t) = q_0 \sin\omega t$. By rearranging the terms, we obtain the more intuitive equation of driven harmonic oscillator with damping $\gamma = \gamma_1 + \gamma_2$

$$\frac{d^2q(t)}{dt^2} + \gamma\frac{dq(t)}{dt} + \omega_0^2 q(t) = \gamma_1\frac{d}{dt}q_d(t). \tag{C.10}$$

The complete solution of the Eq. C.10 is a superposition of the particular solution, $q_p(t)$ and the homogeneous solution, $q_h(t)$. However, if there is any damping at all in the system (that is, if $\gamma > 0$), then the homogeneous part of the solution goes to zero for large t, and we are left with only the particular solution. Therefore, the steady state solution is given as:

$$q(t) = q_p(t) = \frac{\gamma_1 q_d \omega}{(\omega^2 - \omega_0^2)^2 + (\gamma\omega)^2}\cos(\omega t - \phi) \tag{C.11}$$

where ϕ is defined by $\tan\phi = \gamma\omega/(\omega^2 - \omega_0^2)$. Rate of energy dissipated due to γ_2, $P_{out} = \gamma_2\dot{q}(t)^2$. Let us calculate the rate at which energy is being dissipated, which

should be equal to the rate at which work is being done. Starting with Eq. C.9 and multiplying both sides by $\dot{q}$, we obtain the equation $[\ddot{q}\dot{q} + \omega_0^2 q\dot{q}] + \gamma_2\dot{q}^2 = \gamma_1(\dot{q}_d - \dot{q})\dot{q}$ that shows that [Rate of change in kinetic and potential energy] + [Rate at which energy is being dissipated by γ_2] = [Power transferred to the system (P_{in})][3].

By substituting for $q(t)$ and $q_d(t)$ from any particular solution, we can prove that the average power transferred to the system $\langle P_{in}\rangle$ and the rate of energy dissipation by γ_2 $\langle P_{out}\rangle$ are

$$\begin{aligned}\langle P_{in}\rangle &= \langle \gamma_1(\dot{q}_d - \dot{q})\dot{q}_d\rangle \\ &= \left\langle \gamma_1 \left(q_0^2\omega^2\cos^2\omega t - \frac{\gamma_1 q_0^2\omega^3}{\sqrt{(\omega^2-\omega_0^2)^2+(\gamma\omega)^2}}\sin(\omega t-\phi)\cos\omega t\right)\right\rangle \\ &= \frac{1}{2}\gamma_1 q_0^2\omega^2\left(1 - \frac{\gamma_1\omega}{\sqrt{(\omega^2-\omega_0^2)^2+(\gamma\omega)^2}}\sin\phi\right).\end{aligned} \tag{C.12}$$

$$\begin{aligned}\langle P_{out}\rangle &= \left\langle \gamma_2\dot{q}^2\right\rangle \\ &= \left\langle \gamma_2 \frac{\gamma_1^2 q_0^2\omega^4}{(\omega^2-\omega_0^2)^2+(\gamma\omega)^2}\sin^2(\omega t-\phi)\right\rangle \\ &\approx \frac{1}{8}\frac{\gamma_1^2\gamma_2 q_0^2\omega^2}{(\omega-\omega_0)^2+(\gamma/2)^2}\end{aligned} \tag{C.13}$$

The last line of Eq. C.13 is obtained by taking the limit $\omega - \omega_0 \ll \gamma$. The ratio of the power dissipated via γ_2 to a quarter of the nominal drive power (drive power at zero amplitude of the harmonic oscillator) has the exact form as Eq. 4.7.

C.4 Three-state T-matrix model of p-wave resonant scattering near degeneracies

This section provides a microscopic derivation for Eq. 6.3 which was developed by our theory collaborator Prof. Timur Tscherbul using an extended nonperturbative T-matrix model of p-wave resonant scattering [86]. The model includes a single p-

[3]The rate at which work is done by the drive can be decomposed into two parts: rate of loss as friction in γ_1 and the power transferred to the system (P_{in}). That is, $\gamma_1(\dot{q}_d - \dot{q})\dot{q}_d = \gamma_1(\dot{q} - \dot{q}_d)^2 + \gamma_1(\dot{q}_d - \dot{q})\dot{q}$

wave bound state (or closed channel) $|3\rangle$ coupled to two open channels: the incident channel $|1\rangle$ and the outgoing inelastic channel $|2\rangle$ with threshold energies E_1 and E_2 ($E_1 > E_2$). The open channels are separated by the energy gap $\Delta > 0$ such that $E_1 = E_2 + \Delta$. The total energy of the two-molecule system before the collision is $E_1(k) = k^2/2\mu = k^2/m$, $\mu = m/2$ is the reduced mass of the two identical molecules of mass m, k is the wavevector in the incident open channel $|1\rangle$, and we have set $E_1 = 0$, so that $E_2 = -\Delta$. The incident scattering state in channel $|1\rangle$ is a plane wave $|\mathbf{k}\rangle$ with energy $E_1(k) = k^2/m$ multiplied by the internal state vector of the colliding molecules $|\alpha\rangle$.

By summing the diagrammatic expansion for the T-matrix, one obtains the following expression for the off-diagonal matrix elements between the open channels α and α' ($\alpha, \alpha' = 1, 2$) [86]

$$T_{\alpha,\alpha'} = \frac{C}{L^3} \frac{k k' F_\alpha(k) F_{\alpha'}(k')}{E - \delta - \Sigma_1 - \Sigma_2}, \tag{C.14}$$

where $E = k^2/m$ is the collision energy in the incident channel $|1\rangle$ and $\delta > 0$ is the energy of the bare p-wave bound state $|3\rangle$, L^3 is the quantization volume, and $C = \cos\theta$, where θ is the angle between the incoming and outgoing wavevectors [86]. The functions $F_\alpha(k)$ quantify the coupling between the open and closed channels as a function of the wavevector k, and $\Sigma_\alpha(E) = \frac{4\pi}{3}(2\pi)^{-3} \int q^4 dq \frac{|F_\alpha(q)|^2}{E - E_\alpha(q)}$ are the open-closed channel couplings in the energy space. These couplings are crucial as they determine the resonance width. They can be evaluated by regularizing the diverging terms, and then setting $F(q) \to F(0)$, which results in the following expression

$$\begin{aligned} \Sigma_\alpha(E) = \lambda_\alpha \frac{-i}{12\pi} m (m[E - E_\alpha(0)])^{3/2} \\ - \delta_0^{(\alpha)} - \eta_\alpha [E - E_\alpha(0)] \end{aligned} \tag{C.15}$$

where $\lambda_\alpha = |F_\alpha(0)|^2$ are the $q \to 0$ limits of the open-closed channel couplings, and the integrals

$$\delta_0^{(\alpha)} = (6\pi^2)^{-1} \int |F_\alpha(q)|^2 m q^2 dq \tag{C.16}$$

$$\eta_\alpha = (6\pi^2)^{-1} \int |F_\alpha(q)|^2 m dq \tag{C.17}$$

depend on the exact form of the coupling matrix elements between the open and closed channels. Note that (i) $E_1(0) = 0$ and $E_2(0) = -\Delta$ by definition, and (ii) the first term on the right-hand side of Eq. (C.15) is purely imaginary (since we assume $\Delta > 0$) and thus gives rise to resonance width

$$\begin{aligned}\gamma(E,\Delta) =& (\gamma_1 + \gamma_2) + \gamma_d \\ =& -2\mathrm{Im}(\Sigma_1 + \Sigma_2) + \gamma_d \\ =& \frac{m^{5/2}}{6\pi}(\lambda_1 E^{3/2} + \lambda_2(\Delta + E)^{3/2}) + \gamma_d\end{aligned} \tag{C.18}$$

where we have introduced the intrinsic width γ_d of the p-wave bound state due to the coupling to lower-lying inelastic channels other then $|1\rangle$ and $|2\rangle$ [see Figure C-3(a)]. While Ref. [86] assumes that Δ is much larger than all the other energy scales in the problem, we do not make such an assumption here. Indeed, in our model, the new Feshbach resonance occurs when $\Delta \to 0$.

Defining the resonance shift $\delta_0 = \delta_0^1 + \delta_0^2$ and neglecting the dimensionless terms η_α, which are expected to be very small compared to unity [86], we obtain from Eq. (C.14)

$$T_{\alpha,\alpha'} = \frac{C}{L^3} \frac{k k' F_\alpha(0) F_{\alpha'}(0)}{E - (\delta - \delta_0) + i\gamma(E,\Delta)/2}. \tag{C.19}$$

Here, we have also assumed that the bound-continuum coupling matrix elements $F(k)$ are well approximated by their zero-k values $F_\alpha(0)$, which is a good approximation in the limit $k \to 0$ (note, however, that this approximation starts to break down as kR_b approaches 1, where R_b is the "size" of the p-wave bound state, as shown below). The final wavevector in Eq. (C.19) $k' = \sqrt{m(\Delta + E)}$. We are interested in the two-body inelastic rate for the transition $|1\rangle \to |2\rangle$ at fixed collision energy

$$\begin{aligned} g_2(E,\Delta) &= |T_{1,2}|^2 \rho_2(k') \\ &\simeq \frac{1}{L^6} \frac{k^2 m (\Delta + E)^{3/2} \lambda_1 \lambda_2}{[E - (\delta - \delta_0)]^2 + [\frac{m^{5/2}}{6\pi}\{\lambda_1 E^{3/2} + \lambda_2(\Delta + E)^{3/2}\} + \gamma_d]^2/4} \end{aligned} \tag{C.20}$$

where $\rho_2(k') = (m/2)^{3/2}\sqrt{2(\Delta+E)}/2\pi^2$ is the density of states in the final channel $|2\rangle$ [135]. Eq. 6.3 is identical to Eq. (C.20) up to a constant overall scaling factor and with the intrinsic decay width of state $|3\rangle$ $\gamma_d = 0$. This provides a microscopic justification for the Fabry-Pérot model. In particular, the Fabry-Pérot decay rates may be expressed as $\gamma_1 = \frac{m^{5/2}}{6\pi}\lambda_1 E^{3/2}$ and $\gamma_2 = \frac{m^{5/2}}{6\pi}\lambda_2(\Delta+E)^{3/2}$, providing insight into their collision energy and Δ dependence.

We now discuss the main features of the expression for the two-body inelastic rate (C.20). To this end, consider the expression for the resonance width $\gamma(E,\Delta)$ in the denominator of Eq. (C.20) given by Eq.(C.18). In addition to the intrinsic width γ_d, the width contains contribution from (i) the coupling between the incident open channel $|1\rangle$ with the p-wave bound state $\gamma_1 \propto E^{3/2} \propto k^3$, and (ii) the coupling between open channels $|1\rangle$ and $|2\rangle$ through the bound state $\gamma_2 \propto (E+\Delta)^{3/2} \propto (k')^3$.

Equation (C.20) shows that the inelastic rate away from the resonance (when $E-(\delta-\delta_0) > \gamma_1+\gamma_2$) or for $\gamma_d > \gamma_1+\gamma_2$ exhibits the standard p-wave scaling $g_2 \propto k^2(k')^3$ [86]. This seems to apply to the experimental result, which does not see a change of temperature scaling at the resonance. This is expected to be the common situation, since $\Delta/E > 1$ in the experimentally relevant regime. The normal p-wave threshold scaling will be modified if the denominator of Eq. C.20 becomes energy-dependent, which requires the detuning $E-(\delta-\delta_0)$ and γ_d to be small compared to $\gamma_1+\gamma_2$. Under these (rather unlikely) conditions, the scaling changes to $g_2(E) \propto k^2(k')^3/[\lambda_1 k^3 + \lambda_2(k')^3]$.

C.4.1 Derivation of $F_\alpha(k)$ matrix elements

The p-wave bound state in channel $|3\rangle$ is described by the wavefunction $\langle \mathbf{R}|\psi_b\rangle = \psi_b(\mathbf{R})$ of the intermolecular separation vector $\mathbf{R}$. For a single p-wave bound state, the radial and angular variables separate to give $\psi_b(\mathbf{R}) = g_1 Y_{1m_\mathbf{u}}(\hat{R})$, where $m_\mathbf{u}$ is the projection of the bound state's angular momentum $l=1$ on a quantization axis $\mathbf{u}$. We assume that the bound state is coupled to both of the open channels $|\mathbf{k},\alpha\rangle$ ($\alpha = 1,2$) via the coupling matrix elements $\langle \mathbf{k},\alpha|\, V\, |3m_k\rangle$, where $\langle \mathbf{R}|\mathbf{k}\alpha\rangle = e^{ikz}\,|\alpha\rangle$ are the scattering states in the open channels α. Expanding the incoming plane wave

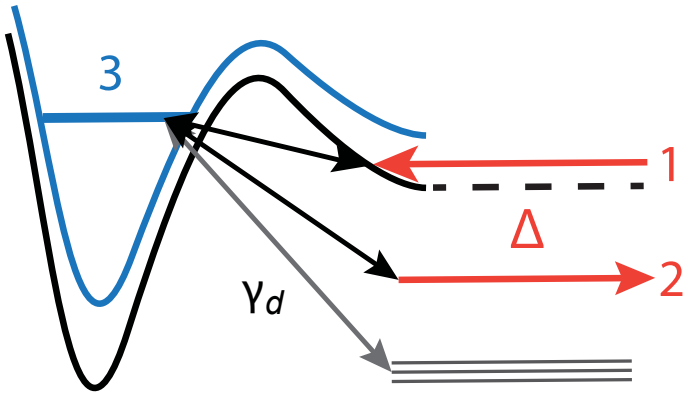

Figure C-3: a. Schematic of the resonance model with two open channels and a p-wave bound state trapped behind a centrifugal barrier.

in spherical waves, $e^{ikz} = \sum_l i^l \sqrt{4\pi(2l+1)} j_l(kR) Y_{l0}(\theta, \phi)$, we see that only the $l = 1$ component couples to the p-wave bound state due to the orthogonality of the spherical harmonics (and the assumption of isotropic bound-continuum coupling).

For practical purposes it is convenient to define the bound-continuum couplings in the k-space [86]

$$F_\alpha(k) = i\sqrt{12} \langle \alpha | \hat{V} | 3 \rangle \frac{1}{k} \int_0^\infty g_1^*(R) j_1(kR) R^2 dR \tag{C.21}$$

where $\langle \alpha | \hat{V} | 3 \rangle$ is a spin matrix element. The advantage og the $F_\alpha(k)$ matrix elements is that they have a well-defined $k \to 0$ limit. Expanding $j_1 kR \simeq kR/3 + O((kR)^5)$, we get

$$F_\alpha(0) = i\sqrt{12} \langle \alpha | \hat{V} | 3 \rangle \frac{1}{k} \int_0^\infty g_1^*(R) R^3 dR \tag{C.22}$$

The approximation $F(k) \simeq F(0)$ is used in the previous section and in Ref. [86] to simplify the expression for the T-matrix elements near threshold. To assess the quality of this approximation, we plot in Figure C-4 the coupling matrix element $F(k)$ as a function of the dimensionless parameter qR_b, where R_b gives the characteristic size of the p-wave bound state [$g_1(R) = R^2 e^{-R/R_b}$]. We observe that $F(k)$ starts to deviate from unity at $qR_b \geq 0.01$. Using $R_b = 100 a_0$, we see that $F(k) \simeq F(0)$ is a good approximation for the incident collision channel ($kR_b \simeq 0.1$ for $E = 10$ kHz). This is no longer the case when the open-closed splitting becomes large compared to

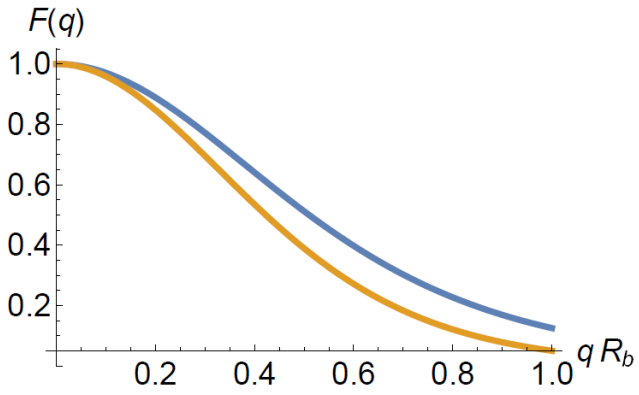

Figure C-4: Coupling matrix elements between the open and closed channels plotted as a function of the wavevector k for two sample bound-state wavefunctions: $g_l(R) = R^{l+1}e^{-R/R_b}$ with $l = 1$ (top curve) and $l = 2$ (bottom curve). THe couplings are normalized to unity at $k = 0$.

the collision energy ($\Delta/E \gg 1$). We observe from Fig.C-4 that while for $\Delta/E = 30$ ($k'R_b \simeq 0.1$) the approximation is still good, it becomes too crude when the energy release into the final channel exceeds the collision energy by a factor of ≥ 100. In this situation (which include the one considered in Ref. [86]), the exact k-dependent matrix element $F(k)$ should be used.

C.5 Analysis on the two-body inelastic rate expression

In this section we focus on what we can learn about p-wave resonance from the two-body inelastic rate for the transition $|1\rangle \rightarrow |2\rangle$ at fixed collision energy which is given as Eq. C.20 we simplify the form of the two-body inelastic rate as $g_2(E,\Delta) = G\frac{\gamma_1\gamma_2}{\Theta^2+(\gamma_1+\gamma_2+\gamma_d)^2}$ by redefining a few physical parameters with simplified notations given as

$$\begin{aligned} G &= \frac{24\pi}{L^6} m^{-1/2} E^{-1/2} \\ \gamma_1 &= \frac{m^{5/2}}{6\pi}\lambda_1 E^{3/2} \\ \gamma_2 &= \frac{m^{5/2}}{6\pi}\lambda_1 (\Delta + E)^{3/2} \\ \Theta &= 2[E - (\delta - \delta_0)]. \end{aligned} \tag{C.23}$$

We consider mainly the two cases: (i) sweeping through γ_2 or Δ to the optimum point, and (ii) sweeping through $\Theta = 0$ point for maximum inelastic loss. The inelastic rate which varies as a function of γ_2 has it's maximum value when $\gamma_2 = \gamma_2^M$. This optimum value γ_2^M is found by taking the partial derivative of g_2 with respect to γ_2 as

$$\begin{aligned} \left.\frac{\partial g_2}{\partial \gamma_2}\right|_{\gamma_2^M} &= G\gamma_1 \left[\frac{1}{\Theta^2 + (\gamma_1 + \gamma_2^M + \gamma_d)^2} - \frac{2\gamma_2^M}{\{\Theta^2 + (\gamma_1 + \gamma_2^M + \gamma_d)^2\}^2}\right] \\ &= 0 \\ &\rightarrow \gamma_2^M = \sqrt{(\gamma_1 + \gamma_d)^2 + \Theta^2} \end{aligned} \tag{C.24}$$

As γ_2 is tuned away from γ_2^M the inelastic rate g_2 decreases. The full width at half maximum (FWHM) of the loss feature as a function of γ_2 is found by finding the two values of γ_2^m in which $g_2(\gamma_2^m) = \frac{1}{2}g_2(\gamma_2^M)$. The two values are given as

$$\begin{aligned} \gamma_2^m &= 2\sqrt{(\gamma_1 + \gamma_d)^2 + \Theta^2} + (\gamma_1 + \gamma_d) \\ &\pm\sqrt{\left[2\sqrt{(\gamma_1 + \gamma_d)^2 + \Theta^2} + (\gamma_1 + \gamma_d)\right]^2 - (\Theta^2 + (\gamma_1 + \gamma_d)^2)} \end{aligned} \tag{C.25}$$

The FWHM is the difference between the two points given in Eq.(C.25). In certain limits, the FWHM can be simplified as

$$\begin{aligned}(FWHM) &= 2\sqrt{\left[2\sqrt{(\gamma_1+\gamma_d)^2+\Theta^2}+(\gamma_1+\gamma_d)\right]^2-(\Theta^2+(\gamma_1+\gamma_d)^2)} \\ &\xrightarrow{\Theta\gg\gamma_1+\gamma_d} 2\sqrt{3}\Theta = 4\sqrt{3}\left[E-(\delta-\delta_0)\right] \\ &\xrightarrow{\Theta\ll\gamma_1+\gamma_d} 4\sqrt{2}(\gamma_1+\gamma_d).\end{aligned} \tag{C.26}$$

In the limit in which the intermediate bound state is far away from the incident channel energetically compared to γ_1 and γ_d ($\Theta \ll \gamma_1+\gamma_d$), the maximum loss occurs when $\gamma_2 = \Theta$ and the width indicates the detuning of the intermediate bound state. In the limit in which the system is close to the Feshbach resonance $\Theta \sim 0$, the maximum loss occurs when $\gamma_2 = \gamma_1+\gamma_d$ and the width is proportional to $\gamma_1+\gamma_d$. From this analysis, it is difficult to know the absolute value of Θ or $\gamma_1+\gamma_d$ from the experimentally obtained width as we only know the FWHM in the unit of Δ and not in the unit of γ_2.

We now focus on what we can learn from the enhancement of the loss rate. We assume the incident scattering flux is divided into two parts: fraction κ_{short} that is coupled to states that undergo fast short-range loss and fraction $1-\kappa_{short} = \kappa_{long}$ that is stable and long-lived. The inelastic loss rate at the background is close to universal value as we also assume that $\kappa_{short} \gg \kappa_{long}$. The loss rate at the background $g_2 = G\cdot\kappa_{short}\cdot t^2$ where t^2 is the transmission probability of the incident flux at long-range. We define Γ such that $\gamma_1 = \kappa_{long}\Gamma$. Note that Γ is approximately proportional to t^2 in the limit of $t \sim 1$, $\gamma \approx \alpha t^2$. The factor α is unknown. The enhancement factor in the case of optimizing γ_2, is expressed as

$$\begin{aligned}C &\equiv \frac{g_2(\gamma_2^M)}{g_2^{background}} \\ &= \left[G\frac{\gamma_1\gamma_2^M}{\Theta^2+(\gamma_1+\gamma_2^M+\gamma_d)^2}\right]\left[G\cdot\kappa_{short}\cdot t^2\right]^{-1} \\ &= \frac{\kappa_{long}}{\kappa_{short}}\cdot\alpha\cdot\frac{\gamma_2}{\Theta^2+(\gamma_1+\gamma_2^M+\gamma_d)^2}\end{aligned} \tag{C.27}$$

where γ_2^M is the optimum value of γ_2 for maximum loss rate which was calculated in Eq.(C.24). It is necessary to know what α is in order to learn about γ_1 and γ_d from the experimentally observed enhancement factor, ~ 100. We come back to the same problem that we encountered from the analysis of FWHM. α is directly related to λ_1, and knowing the open-closed channel couplings λ_1 and λ_2 is necessary to estimate the lifetime of the collision complex.

The enhancement of total loss in a Fabry–Pérot with a PBS for a given mirror coupling strength $\bar{\gamma}_1$ as illustrated in Figure 4-12(b) can be analyzes in a similar manner. The loss has two components: transmission of p-polarized light through the second mirror, $T_p(\omega_0, \bar{\gamma}_2)$, which varies as a function of the cavity mode frequency and mirror coupling strength $\bar{\gamma}_2$ and reflection of s-polarized light at the PBS, T_s. We assume s-polarization component is much greater than p-polarization component of the coupled incoming flux after the mirror M_1 ($\kappa_s \gg \kappa_p$) and consider two situations. In the first situation, the spacing between two mirrors are fixed to create either a resonant or off resonant mode to the incoming light and $\bar{\gamma}_2$ is scanned. In the second situation both $\bar{\gamma}_1$ and $\bar{\gamma}_2$ are fixed but the Fabry–Pérot resonator mode is scanned across the mode of the incoming light. The enhancement factors of the two settings, C_1 and C_2, are given respectively as

$$\begin{aligned} C_1 &\equiv \frac{T_s + T_p(\omega_0 = \omega, \bar{\gamma}_2 = \bar{\gamma}_1)}{T_s + T_p(\omega_0 = \omega, \bar{\gamma}_2 \gg \bar{\gamma}_1 \text{ or } \bar{\gamma}_2 \ll \bar{\gamma}_1)} \approx \frac{\kappa_p}{\kappa_s} \cdot \frac{2}{\bar{\gamma}_2 \tau_{RT}} \\ C_2 &\equiv \frac{T_s + T_p(\omega_0 = \omega)}{T_s + T_p(\omega_0 = \omega + \Delta\omega)} \approx \frac{\kappa_p}{\kappa_s} \cdot \frac{8\bar{\gamma}_2}{(\bar{\gamma}_1 + \bar{\gamma}_2)^2 \tau_{RT}} \\ &\xrightarrow{\bar{\gamma}_1 = \bar{\gamma}_2} \frac{\kappa_p}{\kappa_s} \cdot \frac{2}{\bar{\gamma}_2 \tau_{RT}}. \end{aligned} \tag{C.28}$$

where $|\Delta\omega| \gg (\bar{\gamma}_1 + \bar{\gamma}_2)/2$. The enhancement factors are inversely proportional to the mirror coupling strength and even for small κ_p, large loss enhancement can be achieved with sufficiently weak mirror couplings.

Bibliography

[1] Roman V Krems. Cold controlled chemistry. *Physical Chemistry Chemical Physics*, 10(28):4079–4092, 2008.

[2] N Balakrishnan. Perspective: Ultracold molecules and the dawn of cold controlled chemistry. *The Journal of chemical physics*, 145(15):150901, 2016.

[3] Andrea Micheli, GK Brennen, and Peter Zoller. A toolbox for lattice-spin models with polar molecules. *Nature Physics*, 2(5):341–347, 2006.

[4] B Capogrosso-Sansone, C Trefzger, M Lewenstein, P Zoller, and G Pupillo. Quantum phases of cold polar molecules in 2d optical lattices. *Physical review letters*, 104(12):125301, 2010.

[5] Jacob A Blackmore, Luke Caldwell, Philip D Gregory, Elizabeth M Bridge, Rahul Sawant, Jesús Aldegunde, Jordi Mur-Petit, Dieter Jaksch, Jeremy M Hutson, BE Sauer, et al. Ultracold molecules for quantum simulation: rotational coherences in caf and rbcs. *Quantum Science and Technology*, 4(1):014010, 2018.

[6] Kang-Kuen Ni, Till Rosenband, and David D Grimes. Dipolar exchange quantum logic gate with polar molecules. *Chemical science*, 9(33):6830–6838, 2018.

[7] Felipe Herrera, Yudong Cao, Sabre Kais, and K Birgitta Whaley. Infrared-dressed entanglement of cold open-shell polar molecules for universal matchgate quantum computing. *New Journal of Physics*, 16(7):075001, 2014.

[8] Michael Hughes, Matthew D Frye, Rahul Sawant, Gaurav Bhole, Jonathan A Jones, Simon L Cornish, MR Tarbutt, Jeremy M Hutson, Dieter Jaksch, and Jordi Mur-Petit. Robust entangling gate for polar molecules using magnetic and microwave fields. *Physical Review A*, 101(6):062308, 2020.

[9] Rahul Sawant, Jacob A Blackmore, Philip D Gregory, Jordi Mur-Petit, Dieter Jaksch, Jesus Aldegunde, Jeremy M Hutson, MR Tarbutt, and Simon L Cornish. Ultracold polar molecules as qudits. *New Journal of Physics*, 22(1):013027, 2020.

[10] Edward S Shuman, John F Barry, and David DeMille. Laser cooling of a diatomic molecule. *Nature*, 467(7317):820–823, 2010.

[11] Loïc Anderegg, Benjamin L Augenbraun, Yicheng Bao, Sean Burchesky, Lawrence W Cheuk, Wolfgang Ketterle, and John M Doyle. Laser cooling of optically trapped molecules. *Nature Physics*, 14(9):890–893, 2018.

[12] Matthew T Hummon, Mark Yeo, Benjamin K Stuhl, Alejandra L Collopy, Yong Xia, and Jun Ye. 2D magneto-optical trapping of diatomic molecules. *Physical review letters*, 110(14):143001, 2013.

[13] Timur M. Rvachov, Hyungmok Son, Ariel T. Sommer, Sepehr Ebadi, Juliana J. Park, Martin W. Zwierlein, Wolfgang Ketterle, and Alan O. Jamison. Long-lived ultracold molecules with electric and magnetic dipole moments. *Phys. Rev. Lett.*, 119:143001, Oct 2017.

[14] K-K Ni, S Ospelkaus, MHG De Miranda, A Pe'Er, B Neyenhuis, JJ Zirbel, S Kotochigova, PS Julienne, DS Jin, and Jun Ye. A high phase-space-density gas of polar molecules. *science*, 322(5899):231–235, 2008.

[15] K Winkler, F Lang, G Thalhammer, P vd Straten, R Grimm, and J Hecker Denschlag. Coherent optical transfer of feshbach molecules to a lower vibrational state. *Physical review letters*, 98(4):043201, 2007.

[16] Johann G Danzl, Manfred J Mark, Elmar Haller, Mattias Gustavsson, Russell Hart, Jesus Aldegunde, Jeremy M Hutson, and Hanns-Christoph Nägerl. An ultracold high-density sample of rovibronic ground-state molecules in an optical lattice. *Nature Physics*, 6(4):265–270, 2010.

[17] Jee Woo Park, Sebastian A Will, and Martin W Zwierlein. Ultracold dipolar gas of fermionic $Na^{23}K^{40}$ molecules in their absolute ground state. *Physical review letters*, 114(20):205302, 2015.

[18] Johann G Danzl, Elmar Haller, Mattias Gustavsson, Manfred J Mark, Russell Hart, Nadia Bouloufa, Olivier Dulieu, Helmut Ritsch, and Hanns-Christoph Nägerl. Quantum gas of deeply bound ground state molecules. *Science*, 321(5892):1062–1066, 2008.

[19] S. P. Krzyzewski, T. G. Akin, J. Dizikes, Michael A. Morrison, and E. R. I. Abraham. Observation of deeply bound $^{85}Rb_2$ vibrational levels using feshbach optimized photoassociation. *Phys. Rev. A*, 92:062714, Dec 2015.

[20] DJ McCarron, MH Steinecker, Y Zhu, and D DeMille. Magnetic trapping of an ultracold gas of polar molecules. *Physical review letters*, 121(1):013202, 2018.

[21] Yewei Wu, Justin J Burau, Kameron Mehling, Jun Ye, and Shiqian Ding. High phase-space density of laser-cooled molecules in an optical lattice. *Physical review letters*, 127(26):263201, 2021.

[22] Lawrence W Cheuk, Loïc Anderegg, Benjamin L Augenbraun, Yicheng Bao, Sean Burchesky, Wolfgang Ketterle, and John M Doyle. λ-enhanced imaging of molecules in an optical trap. *Physical review letters*, 121(8):083201, 2018.

[23] Luigi De Marco, Giacomo Valtolina, Kyle Matsuda, William G Tobias, Jacob P Covey, and Jun Ye. A degenerate fermi gas of polar molecules. *Science*, 363(6429):853–856, 2019.

[24] Myoung-Sun Heo, Tout T Wang, Caleb A Christensen, Timur M Rvachov, Dylan A Cotta, Jae-Hoon Choi, Ye-Ryoung Lee, and Wolfgang Ketterle. Formation of ultracold fermionic NaLi feshbach molecules. *Physical Review A*, 86(2):021602, 2012.

[25] Timur M. Rvachov, Hyungmok Son, Juliana J. Park, Sepehr Ebadi, Martin W. Zwierlein, Wolfgang Ketterle, and Alan O. Jamison. Two-photon spectroscopy of the NaLi triplet ground state. *Phys. Chem. Chem. Phys.*, 20:4739–4745, 2018.

[26] Timur M. Rvachov, Hyungmok Son, Juliana J. Park, Pascal M. Notz, Tout T. Wang, Martin W. Zwierlein, Wolfgang Ketterle, and Alan O. Jamison. Photoassociation of ultracold NaLi. *Phys. Chem. Chem. Phys.*, 20:4746–4751, 2018.

[27] Hyungmok Son and Harvard University. Department of Physics. *Collisional Cooling and Magnetic Control of Reactions in Ultracold Spin-polarized $NaLi + Na$ Mixture*. Harvard University, Department of Physics, 2022.

[28] R Vexiau, D Borsalino, M Lepers, A Orbán, M Aymar, O Dulieu, and N Bouloufa-Maafa. Dynamic dipole polarizabilities of heteronuclear alkali dimers: optical response, trapping and control of ultracold molecules. *International Reviews in Physical Chemistry*, 36(4):709–750, 2017.

[29] Michał Tomza, Kirk W Madison, Robert Moszynski, and Roman V Krems. Chemical reactions of ultracold alkali-metal dimers in the lowest-energy $^3\Sigma$ state. *Physical Review A*, 88(5):050701, 2013.

[30] PS Żuchowski, M Kosicki, M Kodrycka, and P Soldán. van der waals coefficients for systems with ultracold polar alkali-metal molecules. *Physical Review A*, 87(2):022706, 2013.

[31] Piotr S Żuchowski and Jeremy M Hutson. Reactions of ultracold alkali-metal dimers. *Physical Review A*, 81(6):060703, 2010.

[32] T-S Ho, H Rabitz, and G Scoles. Reproducing kernel technique for extracting accurate potentials from spectral data: Potential curves of the two lowest states $x^1\Sigma_g^+$ and $a^3\Sigma_u^+$ of the sodium dimer. *The Journal of Chemical Physics*, 112(14):6218–6227, 2000.

[33] Hyungmok Son, Juliana J Park, Yu-Kun Lu, Alan O Jamison, Tijs Karman, and Wolfgang Ketterle. Control of reactive collisions by quantum interference. *Science*, 375(6584):1006–1010, 2022.

[34] Hyungmok Son, Juliana J Park, Wolfgang Ketterle, and Alan O Jamison. Collisional cooling of ultracold molecules. *Nature*, 580(7802):197–200, 2020.

[35] Zbigniew Idziaszek and Paul S. Julienne. Universal rate constants for reactive collisions of ultracold molecules. *Phys. Rev. Lett.*, 104:113202, Mar 2010.

[36] Svetlana Kotochigova. Dispersion interactions and reactive collisions of ultracold polar molecules. *New Journal of Physics*, 12(7):073041, 2010.

[37] Michael Mayle, Brandon P Ruzic, and John L Bohn. Statistical aspects of ultracold resonant scattering. *Physical Review A*, 85(6):062712, 2012.

[38] Michael Mayle, Goulven Quéméner, Brandon P Ruzic, and John L Bohn. Scattering of ultracold molecules in the highly resonant regime. *Physical Review A*, 87(1):012709, 2013.

[39] Arthur Christianen, Tijs Karman, and Gerrit C Groenenboom. Quasiclassical method for calculating the density of states of ultracold collision complexes. *Physical Review A*, 100(3):032708, 2019.

[40] Yu Liu, Ming-Guang Hu, Matthew A Nichols, David D Grimes, Tijs Karman, Hua Guo, and Kang-Kuen Ni. Photo-excitation of long-lived transient intermediates in ultracold reactions. *Nature Physics*, 16(11):1132–1136, 2020.

[41] S. Ospelkaus, K.-K. Ni, D. Wang, M. H. G. de Miranda, B. Neyenhuis, G. Quéméner, P. S. Julienne, J. L. Bohn, D. S. Jin, and J. Ye. Quantum-state controlled chemical reactions of ultracold potassium-rubidium molecules. *Science*, 327(5967):853–857, 2010.

[42] Xin Ye, Mingyang Guo, Maykel L. González-Martínez, Goulven Quéméner, and Dajun Wang. Collisions of ultracold $^{23}Na^{87}Rb$ molecules with controlled chemical reactivities. *Science Advances*, 4(1), 2018.

[43] Lawrence W. Cheuk, Loïc Anderegg, Yicheng Bao, Sean Burchesky, Scarlett S. Yu, Wolfgang Ketterle, Kang-Kuen Ni, and John M. Doyle. Observation of collisions between two ultracold ground-state caf molecules. *Phys. Rev. Lett.*, 125:043401, Jul 2020.

[44] Björn Drews, Markus Deiß, Krzysztof Jachymski, Zbigniew Idziaszek, and Johannes Hecker Denschlag. Inelastic collisions of ultracold triplet rb2 molecules in the rovibrational ground state. *Nature Communications*, 8(1):14854, Mar 2017.

[45] Gene Polovy, Erik Frieling, Denis Uhland, Julian Schmidt, and Kirk W. Madison. Quantum-state-dependent chemistry of ultracold $^6Li_2$ dimers. *Phys. Rev. A*, 102:013310, Jul 2020.

[46] N. Zahzam, T. Vogt, M. Mudrich, D. Comparat, and P. Pillet. Atom-molecule collisions in an optically trapped gas. *Phys. Rev. Lett.*, 96:023202, Jan 2006.

[47] Peter Staanum, Stephan D. Kraft, Jörg Lange, Roland Wester, and Matthias Weidemüller. Experimental investigation of ultracold atom-molecule collisions. *Phys. Rev. Lett.*, 96:023201, Jan 2006.

[48] J Deiglmayr, M Repp, A Grochola, O Dulieu, R Wester, and M Weidemüller. Dipolar effects and collisions in an ultracold gas of LiCs molecules. *Journal of Physics: Conference Series*, 264:012014, Jan 2011.

[49] Eric R. Hudson, Nathan B. Gilfoy, S. Kotochigova, Jeremy M. Sage, and D. DeMille. Inelastic collisions of ultracold heteronuclear molecules in an optical trap. *Phys. Rev. Lett.*, 100:203201, May 2008.

[50] Philip D Gregory, Jacob A Blackmore, Luke M Fernley, Sarah L Bromley, Jeremy M Hutson, Simon L Cornish, et al. Molecule–molecule and atom–molecule collisions with ultracold rbcs molecules. *New Journal of Physics*, 23(12):125004, 2021.

[51] Matthew A Nichols, Yi-Xiang Liu, Lingbang Zhu, Ming-Guang Hu, Yu Liu, and Kang-Kuen Ni. Detection of long-lived complexes in ultracold atom-molecule collisions. *arXiv preprint arXiv:2105.14960*, 2021.

[52] Matthew D Frye, Paul S Julienne, and Jeremy M Hutson. Cold atomic and molecular collisions: approaching the universal loss regime. *New Journal of Physics*, 17(4):045019, apr 2015.

[53] Jeremy M Hutson. Feshbach resonances in ultracold atomic and molecular collisions: threshold behaviour and suppression of poles in scattering lengths. *New Journal of Physics*, 9(5):152–152, may 2007.

[54] Jeremy M. Hutson, Musie Beyene, and Maykel Leonardo González-Martínez. Dramatic reductions in inelastic cross sections for ultracold collisions near feshbach resonances. *Phys. Rev. Lett.*, 103:163201, Oct 2009.

[55] William Lunden. *Development of a new Dy quantum gas experiment.* PhD thesis, Massachusetts Institute of Technology, 2020.

[56] T Schuster, R Scelle, A Trautmann, S Knoop, MK Oberthaler, MM Haverhals, MR Goosen, SJJMF Kokkelmans, and E Tiemann. Feshbach spectroscopy and scattering properties of ultracold Li + Na mixtures. *Physical Review A*, 85(4):042721, 2012.

[57] Erik W Streed, Ananth P Chikkatur, Todd L Gustavson, Micah Boyd, Yoshio Torii, Dominik Schneble, Gretchen K Campbell, David E Pritchard, and Wolfgang Ketterle. Large atom number bose-einstein condensate machines. *Review of Scientific Instruments*, 77(2):023106, 2006.

[58] Cheng Chin, Rudolf Grimm, Paul Julienne, and Eite Tiesinga. Feshbach resonances in ultracold gases. *Reviews of Modern Physics*, 82(2):1225, 2010.

[59] Immanuel Bloch, Jean Dalibard, and Sylvain Nascimbene. Quantum simulations with ultracold quantum gases. *Nature Physics*, 8(4):267–276, 2012.

[60] Bo Zhao and Jian-Wei Pan. Quantum control of reactions and collisions at ultralow temperatures. *Chemical Society Reviews*, 2022.

[61] Masato Morita and Timur V Tscherbul. Restricted basis set coupled-channel calculations on atom-molecule collisions in magnetic fields. *The Journal of Chemical Physics*, 150(7):074110, 2019.

[62] Suyesh Koyu, Rebekah Hermsmeier, and Timur V Tscherbul. Total angular momentum representation for state-to-state quantum scattering of cold molecules in a magnetic field. *The Journal of Chemical Physics*, 156(3):034112, 2022.

[63] Alisdair OG Wallis, Edward JJ Longdon, Piotr S Żuchowski, and Jeremy M Hutson. The prospects of sympathetic cooling of nh molecules with li atoms. *The European Physical Journal D*, 65(1):151–160, 2011.

[64] Masato Morita, Roman V Krems, and Timur V Tscherbul. Universal probability distributions of scattering observables in ultracold molecular collisions. *Physical review letters*, 123(1):013401, 2019.

[65] Arthur Christianen, Gerrit C Groenenboom, and Tijs Karman. Lossy quantum defect theory of ultracold molecular collisions. *Physical Review A*, 104(4):043327, 2021.

[66] C Chin, T Kraemer, M Mark, J Herbig, P Waldburger, H-C Nägerl, and R Grimm. Observation of feshbach-like resonances in collisions between ultracold molecules. *Physical review letters*, 94(12):123201, 2005.

[67] S Knoop, F Ferlaino, M Mark, M Berninger, H Schöbel, H-C Nägerl, and R Grimm. Observation of an efimov-like trimer resonance in ultracold atom–dimer scattering. *Nature Physics*, 5(3):227–230, 2009.

[68] Alessandro Zenesini, Bo Huang, Martin Berninger, H-C Nägerl, Francesca Ferlaino, and Rudolf Grimm. Resonant atom-dimer collisions in cesium: Testing universality at positive scattering lengths. *Physical Review A*, 90(2):022704, 2014.

[69] Fudong Wang, Xin Ye, Mingyang Guo, D Blume, and Dajun Wang. Observation of resonant scattering between ultracold heteronuclear feshbach molecules. *Physical Review A*, 100(4):042706, 2019.

[70] Huan Yang, De-Chao Zhang, Lan Liu, Ya-Xiong Liu, Jue Nan, Bo Zhao, and Jian-Wei Pan. Observation of magnetically tunable feshbach resonances in ultracold ^{23}Na^{40}K $+^{40}$ K collisions. *Science*, 363(6424):261–264, 2019.

[71] Xin-Yao Wang, Matthew D Frye, Zhen Su, Jin Cao, Lan Liu, De-Chao Zhang, Huan Yang, Jeremy M Hutson, Bo Zhao, Chun-Li Bai, et al. Magnetic feshbach resonances in collisions of ^{23}Na^{40}K with^{40}K. *New Journal of Physics*, 23(11):115010, 2021.

[72] Hyungmok Son, Juliana J. Park, Wolfgang Ketterle, and Alan O. Jamison. Collisional cooling of ultracold molecules. *Nature*, 580(7802):197–200, Apr 2020.

[73] Juliana J Park, Yu-Kun Lu, Alan O Jamison, Timur Tscherbul, and Wolfgang Ketterle. A feshbach resonance in collisions between ultracold ground state molecules. *arXiv preprint arXiv:2208.05557*, 2022.

[74] Rebekah Hermsmeier, Jacek Kłos, Svetlana Kotochigova, and Timur V Tscherbul. Quantum spin state selectivity and magnetic tuning of ultracold chemical reactions of triplet alkali-metal dimers with alkali-metal atoms. *Physical review letters*, 127(10):103402, 2021.

[75] Eugene P Wigner. On a class of analytic functions from the quantum theory of collisions. In *The Collected Works of Eugene Paul Wigner*, pages 409–440. Springer, 1993.

[76] Freeman J Dyson. Statistical theory of the energy levels of complex systems. i. *Journal of Mathematical Physics*, 3(1):140–156, 1962.

[77] TA Brody. A statistical measure for the repulsion of energy levels. *Lettere al Nuovo Cimento (1971-1985)*, 7(12):482–484, 1973.

[78] Tómas A Brody, Jorge Flores, J Bruce French, PA Mello, A Pandey, and Samuel SM Wong. Random-matrix physics: spectrum and strength fluctuations. *Reviews of Modern Physics*, 53(3):385, 1981.

[79] Charles E Porter and Robert G Thomas. Fluctuations of nuclear reaction widths. *Physical Review*, 104(2):483, 1956.

[80] F Ferlaino, S Knoop, M Berninger, M Mark, H-C Nägerl, and R Grimm. Collisions of ultracold trapped cesium feshbach molecules. *Laser Physics*, 20(1):23–31, 2010.

[81] Eugene P Wigner. On the behavior of cross sections near thresholds. *Physical Review*, 73(9):1002, 1948.

[82] Paul S Julienne, Thomas M Hanna, and Zbigniew Idziaszek. Universal ultracold collision rates for polar molecules of two alkali-metal atoms. *Physical Chemistry Chemical Physics*, 13(42):19114–19124, 2011.

[83] A Derevianko, JF Babb, and A Dalgarno. High-precision calculations of van der waals coefficients for heteronuclear alkali-metal dimers. *Physical Review A*, 63(5):052704, 2001.

[84] J. Zhang, E. G. M. van Kempen, T. Bourdel, L. Khaykovich, J. Cubizolles, F. Chevy, M. Teichmann, L. Tarruell, S. J. J. M. F. Kokkelmans, and C. Salomon. p-wave feshbach resonances of ultracold ^{6}Li. *Phys. Rev. A*, 70:030702, Sep 2004.

[85] Nur Ismail, Cristine Calil Kores, Dimitri Geskus, and Markus Pollnau. Fabry-pérot resonator: spectral line shapes, generic and related airy distributions, linewidths, finesses, and performance at low or frequency-dependent reflectivity. *Optics express*, 24(15):16366–16389, 2016.

[86] Frédéric Chevy, EGM Van Kempen, Thomas Bourdel, J Zhang, L Khaykovich, M Teichmann, L Tarruell, SJJMF Kokkelmans, and C Salomon. Resonant scattering properties close to a p-wave feshbach resonance. *Physical Review A*, 71(6):062710, 2005.

[87] Yan-Peng Bai, Jing-Lun Li, Gao-Ren Wang, and Shu-Lin Cong. Model for investigating quantum reflection and quantum coherence in ultracold molecular collisions. *Physical Review A*, 100(1):012705, 2019.

[88] Zbigniew Idziaszek and Paul S Julienne. Universal rate constants for reactive collisions of ultracold molecules. *Physical review letters*, 104(11):113202, 2010.

[89] Arthur Christianen, Martin W Zwierlein, Gerrit C Groenenboom, and Tijs Karman. Photoinduced two-body loss of ultracold molecules. *Physical Review Letters*, 123(12):123402, 2019.

[90] Jonathan D Weinstein, Robert DeCarvalho, Thierry Guillet, Bretislav Friedrich, and John M Doyle. Magnetic trapping of calcium monohydride molecules at millikelvin temperatures. *Nature*, 395(6698):148–150, 1998.

[91] Wesley C Campbell, Edem Tsikata, Hsin-I Lu, Laurens D van Buuren, and John M Doyle. Magnetic trapping and zeeman relaxation of NH ($X^3\Sigma^-$). *Physical review letters*, 98(21):213001, 2007.

[92] Hsin-I Lu, Ivan Kozyryev, Boerge Hemmerling, Julia Piskorski, and John M Doyle. Magnetic trapping of molecules via optical loading and magnetic slowing. *Physical review letters*, 112(11):113006, 2014.

[93] Edem Tsikata, WC Campbell, MT Hummon, Hsin-I Lu, and John M Doyle. Magnetic trapping of nh molecules with 20 s lifetimes. *New Journal of Physics*, 12(6):065028, 2010.

[94] Yang Liu, Sida Zhou, Wei Zhong, Pavle Djuricanin, and Takamasa Momose. One-dimensional confinement of magnetically decelerated supersonic beams of O_2 molecules. *Physical Review A*, 91(2):021403, 2015.

[95] Yang Liu, Manish Vashishta, Pavle Djuricanin, Sida Zhou, Wei Zhong, Tony Mittertreiner, David Carty, and Takamasa Momose. Magnetic trapping of cold methyl radicals. *Physical review letters*, 118(9):093201, 2017.

[96] Jens Riedel, Steven Hoekstra, Wolfgang Jäger, Joop J Gilijamse, Sebastiaan YT van de Meerakker, and Gerard Meijer. Accumulation of stark-decelerated NH molecules in a magnetic trap. *The European physical journal D*, 65(1):161–166, 2011.

[97] Yair Segev, Martin Pitzer, Michael Karpov, Nitzan Akerman, Julia Narevicius, and Edvardas Narevicius. Collisions between cold molecules in a superconducting magnetic trap. *Nature*, 572(7768):189–193, 2019.

[98] M. Koller, F. Jung, J. Phrompao, M. Zeppenfeld, I. M. Rabey, and G. Rempe. Electric-field-controlled cold dipolar collisions between trapped CH_3F molecules. *Phys. Rev. Lett.*, 128:203401, May 2022.

[99] David Reens, Hao Wu, Tim Langen, and Jun Ye. Controlling spin flips of molecules in an electromagnetic trap. *Physical Review A*, 96(6):063420, 2017.

[100] HJ Williams, L Caldwell, NJ Fitch, S Truppe, J Rodewald, EA Hinds, BE Sauer, and MR Tarbutt. Magnetic trapping and coherent control of laser-cooled molecules. *Physical review letters*, 120(16):163201, 2018.

[101] Yu Liu and Kang-Kuen Ni. Bimolecular chemistry in the ultracold regime. *Annual review of physical chemistry*, 73:73–96, 2022.

[102] Philip D Gregory, Jacob A Blackmore, Sarah L Bromley, and Simon L Cornish. Loss of ultracold $Rb^{87}Cs^{133}$ molecules via optical excitation of long-lived two-body collision complexes. *Physical Review Letters*, 124(16):163402, 2020.

[103] Philipp Gersema, Kai K. Voges, Mara Meyer zum Alten Borgloh, Leon Koch, Torsten Hartmann, Alessandro Zenesini, Silke Ospelkaus, Junyu Lin, Junyu He, and Dajun Wang. Probing photoinduced two-body loss of ultracold nonreactive bosonic $^{23}Na^{87}Rb$ and $^{23}Na^{39}K$ molecules. *Phys. Rev. Lett.*, 127:163401, Oct 2021.

[104] Roman Bause, Andreas Schindewolf, Renhao Tao, Marcel Duda, Xing-Yan Chen, Goulven Quéméner, Tijs Karman, Arthur Christianen, Immanuel Bloch, and Xin-Yu Luo. Collisions of ultracold molecules in bright and dark optical dipole traps. *Physical Review Research*, 3(3):033013, 2021.

[105] Manuel Lara, John L Bohn, Daniel Potter, Pavel Soldán, and Jeremy M Hutson. Ultracold Rb-OH collisions and prospects for sympathetic cooling. *Physical review letters*, 97(18):183201, 2006.

[106] Piotr S Żuchowski and Jeremy M Hutson. Prospects for producing ultracold NH_3 molecules by sympathetic cooling: A survey of interaction potentials. *Physical Review A*, 78(2):022701, 2008.

[107] Matthew T Hummon, Timur V Tscherbul, Jacek Kłos, Hsin-I Lu, Edem Tsikata, Wesley C Campbell, Alexander Dalgarno, and John M Doyle. Cold N + NH collisions in a magnetic trap. *Physical review letters*, 106(5):053201, 2011.

[108] S Jurgilas, A Chakraborty, CJH Rich, L Caldwell, HJ Williams, NJ Fitch, BE Sauer, Matthew D Frye, Jeremy M Hutson, and MR Tarbutt. Collisions between ultracold molecules and atoms in a magnetic trap. *Physical Review Letters*, 126(15):153401, 2021.

[109] Nitzan Akerman, Michael Karpov, Yair Segev, Natan Bibelnik, Julia Narevicius, and Edvardas Narevicius. Trapping of molecular oxygen together with lithium atoms. *Physical review letters*, 119(7):073204, 2017.

[110] A. Mosk, S. Kraft, M. Mudrich, K. Singer, W. Wohlleben, R. Grimm, and M. Weidemüller. Mixture of ultracold lithium and cesium atoms in an optical dipole trap. *Applied Physics B*, 73(8):791–799, Dec 2001.

[111] Eite Tiesinga, Carl J Williams, Paul S Julienne, Kevin M Jones, Paul D Lett, and William D Phillips. A spectroscopic determination of scattering lengths for sodium atom collisions. *Journal of research of the National Institute of Standards and Technology*, 101(4):505, 1996.

[112] Kai K Voges, Philipp Gersema, Torsten Hartmann, Silke Ospelkaus, and Alessandro Zenesini. Hyperfine dependent atom-molecule loss analyzed by the analytic solution of few-body loss equations. *Physical Review Research*, 4(2):023184, 2022.

[113] Alessio Ciamei, Alex Bayerle, Chun-Chia Chen, Benjamin Pasquiou, and Florian Schreck. Efficient production of long-lived ultracold Sr_2 molecules. *Physical Review A*, 96(1):013406, 2017.

[114] KH Leung, E Tiberi, B Iritani, I Majewska, R Moszynski, and T Zelevinsky. Ultracold $^{88}Sr_2$ molecules in the absolute ground state. *New Journal of Physics*, 23(11):115002, 2021.

[115] Jeremy M Sage, Sunil Sainis, Thomas Bergeman, and David DeMille. Optical production of ultracold polar molecules. *Physical review letters*, 94(20):203001, 2005.

[116] CD Bruzewicz, Mattias Gustavsson, Toshihiko Shimasaki, and D DeMille. Continuous formation of vibronic ground state rbcs molecules via photoassociation. *New Journal of Physics*, 16(2):023018, 2014.

[117] Toshihiko Shimasaki, Michael Bellos, CD Bruzewicz, Zack Lasner, and David DeMille. Production of rovibronic-ground-state rbcs molecules via two-photon-cascade decay. *Physical Review A*, 91(2):021401, 2015.

[118] Toshihiko Shimasaki, Jin-Tae Kim, and David DeMille. Production of rbcs molecules in the rovibronic ground state via short-range photoassociation to the $2^1\Pi_1$ $2^3\Pi_1$ and $3^3\Sigma$ states. *ChemPhysChem*, 17(22):3677–3682, 2016.

[119] Toshihiko Shimasaki, Jin-Tae Kim, Yuqi Zhu, and David DeMille. Continuous production of rovibronic-ground-state rbcs molecules via short-range photoassociation to the $b^3\Pi_1$ $c^3\Sigma_1^+$ $B^1\Pi_1$ states. *Physical Review A*, 98(4):043423, 2018.

[120] T.M. Rvachov and Massachusetts Institute of Technology. Department of Physics. *Ultracold $^{23}Na^6Li$ Molecules in the Triplet Ground State*. Massachusetts Institute of Technology, Department of Physics, 2018.

[121] Michael E Gehm. Properties of ^{6}Li. *Jetlab*, 2003.

[122] Sean Burchesky, Loïc Anderegg, Yicheng Bao, S Yu Scarlett, Eunmi Chae, Wolfgang Ketterle, Kang-Kuen Ni, and John M Doyle. Rotational coherence times of polar molecules in optical tweezers. *Physical Review Letters*, 127(12):123202, 2021.

[123] Rodney Avram Brooks, CH Anderson, and NF Ramsey. Rotational magnetic moments of diatomic alkalis. *Physical Review Letters*, 10(10):441, 1963.

[124] S Knoop, T Schuster, R Scelle, A Trautmann, J Appmeier, MK Oberthaler, E Tiesinga, and E Tiemann. Feshbach spectroscopy and analysis of the interaction potentials of ultracold sodium. *Physical Review A*, 83(4):042704, 2011.

[125] Michael Steinke, Horst Knöckel, and Eberhard Tiemann. (X)$1^1\Sigma^+$ state of LiNa studied by fourier-transform spectroscopy. *Physical Review A*, 85(4):042720, 2012.

[126] Tijs Karman and et al. Paper on Na + NaLi scattering calculations.

[127] Zbigniew Idziaszek, Krzysztof Jachymski, and Paul S Julienne. Reactive collisions in confined geometries. *New Journal of Physics*, 17(3):035007, 2015.

[128] Frederick H Mies, Carl J Williams, Paul S Julienne, and Morris Krauss. Estimating bounds on collisional relaxation rates of spin-polarized ^{87}Rb atoms at ultracold temperatures. *Journal of research of the National Institute of Standards and Technology*, 101(4):521, 1996.

[129] RV Krems and A Dalgarno. Quantum-mechanical theory of atom-molecule and molecular collisions in a magnetic field: Spin depolarization. *The Journal of chemical physics*, 120(5):2296–2307, 2004.

[130] TV Tscherbul, Yu V Suleimanov, V Aquilanti, and RV Krems. Magnetic field modification of ultracold molecule–molecule collisions. *New Journal of Physics*, 11(5):055021, 2009.

[131] Anthony Stone. *The Theory of Intermolecular Forces*. Oxford University Press, Oxford, 2013.

[132] Marcin Gronowski, Adam M Koza, and Michał Tomza. Ab initio properties of the NaLi molecule in the $a^3\Sigma^+$ electronic state. *Physical Review A*, 102(2):020801, 2020.

[133] James F Harrison and Daniel B Lawson. Quadrupole moments of the alkali dimers, Li_2, Na_2, and K_2. *International journal of quantum chemistry*, 102(6):1087–1091, 2005.

[134] Rebekah Hermsmeier, Jacek Kłos, Svetlana Kotochigova, and Timur V Tscherbul. Quantum spin state selectivity and magnetic tuning of ultracold chemical reactions of triplet alkali-metal dimers with alkali-metal atoms. *Physical review letters*, 127(10):103402, 2021.

[135] Harald Friedrich. *Theoretical Atomic Physics*. Springer International, New York, 4 edition, 2017.